Tectono-thermal evolution of a long-lived Paleozoic accretionary margin: insights from the Famatinian orogeny, NW Argentina

by

Pablo Farias

PhD Thesis

Submitted in fulfilment of the requirement for the degree of Doctor of Philosophy

Supervisors:

Roberto Weinberg

Alexander Cruden

School of Earth, Atmosphere and Environment

Monash University, Clayton, Victoria, Australia

2019

Copyright notice

Abstract

Accretionary orogens are dynamic plate margins that are susceptible to record different tectono-metamorphic events. The metamorphic conditions in the core and mid-crustal sections of these orogens can trigger the partial melting of metasedimentary rocks, which in turn, will change the rheology and structural behaviour of the orogen. The structural response of the thermally mature sections, to tectonic and gravitational forces, and the time frame involved are not fully understood. This thesis contributes to the understanding of the structural and thermal evolution of the Ordovician Famatinian accretionary orogen, in NW Argentina, focused on the Sierra de Quilmes that exposes mid-crustal levels of the orogen.

The Sierra de Quilmes is composed of three high-temperature and low-pressure metamorphic complexes dominated by migmatites and juxtaposed by thrusting on remarkably thick shear zones following the 470 ± 10 Ma mountain-building phase. Crustal thickening, driven by E-W shortening, became counterbalanced by gravity. This led to a period of post-anatectic constriction, recorded by a southward escape, parallel to the orogen, of the thermally weakened footwall complex. This lateral flow suggests that the orogen was unfit to support significant vertical thickening and failed to grow.

Geochronology of zircon, monazite, and titanite indicates that the complexes were hot and partially molten over a ~60 Myr period, from ~500-440 Ma. However, the footwall complex sustained high-temperatures for another 60 Myr, cooling slowly through the 750 °C to 700 °C isograds between 440-380 Ma, as indicated by Zr-in-titanite temperature record. The gradual cooling recorded by titanite coincided with the growth of allanite and epidote in the retrograde path, as indicated by the REE patterns in titanite grains. Also, amphibolite facies shearing in one of the complex-bounding shear zones involved in the southern escape of the footwall triggered new high-REE monazite grain growth and partially reset pre-existing ones at ~407 Ma.

The behaviour and nature of the time record of zircon, monazite, and titanite in the different metamorphic complexes and sometimes in rocks of similar grade and composition, are varied. Their distinct behaviour is controlled dominantly by temperature differences, but also by other factors like rock fabric (grain size) and deformation. Thus, the analysis of various geochronometers from all complexes and several samples within the same complex is the most efficient way to obtain the most accurate and comprehensive record of the evolution of such terranes.

The thesis concludes that this long-lived hot system most likely undermined the stability of the orogenic edifice and contributed to the mentioned lateral escape. The Famatinian orogen, similar to the Variscan orogen, was a large-hot orogen that failed to grow because of being too hot to do so. These findings provide new insights into the behaviour of mountains and geochronometers during long-lived high-temperature metamorphic events.

Declaration

This thesis is an original work of my research and contains no material which has been accepted for the award of any other degree or diploma at any university or equivalent institution and that, to the best of my knowledge and belief, this thesis contains no material previously published or written by another person, except where due reference is made in the text of the thesis.

Signature: ……………………… Pablo Farias

Print Name: ……Pablo Farias…………….

Date: …………22/12/2019……………….

Table of contents

Preliminary pages

Chapter 1 Research aims and geology background

Chapter 3 Untangling the protracted thermal evolution of a migmatitic terrane by means of multiple geochronometers: insights from the Sierra de Quilmes

List of figures

Chapter 1

Chapter 2

Chapter 3

Chapter 4

List of tables

Acknowledgements

I wish to thank, first and foremost, my supervisor Roberto Weinberg for his wise guidance and companionship. He patiently crafted me into a better scientist and field geologist. I am grateful for his high level of support and contagious enthusiasm that kept me going through this windy rollercoaster called PhD. Also, for the time, discussions, ideas, and resources that Roberto invested in me during these years. He taught me to see through complex geology and distillate the essence of it, and most importantly, how to communicate it. For all that, I am extremely grateful.

I gratefully thank my PhD panel, Fabio Capitanio, Laurent Ailleres, Steven Micklethwaite, also to Peter Betts, David Moore, Andy Tompkins, Oliver Nebel and co-supervisor Sandy Cruden, and all the brilliant minds of Monash University for the stimulating discussions that improved my work. I want to thank all the people at Monash that gave me the chance to work as a TA. Teaching and supporting other students kept my technical knowledge fresh and improved my communication and people skills. The Argentinian team at Universidad Nacional de Salta led by the great Raúl "Tato" Becchio and Alfonso Sola, was always supportive at all stages of my PhD. I thank Alejandro Nievas, Victor and my brother Juan Manuel for the technical support during sample preparation and fieldwork in Salta.

Also, I want to recognise and acknowledge all the researchers in Argentina that worked and toiled to understand the geology of the Sierras Pampeanas for the last 20 years. That knowledge was essential to this work. Massimo Raveggi and all the Isotopia Laboratory crew were always available and ready to teach and support me during the analytical work in Monash. Massimo taught me the insights of analytical work and made me understand that an analytical result is more than a number. I am also very thankful to all my friends at Monash, especially Marianne, Martin, Saskia, Nathan and Prasanna that supported me in the last and hardest stages of my PhD, thank you all for your friendship and stimulating philosophical conversations. Likewise, to all my friends outside Monash, my friends from the Tango community that helped me disconnect when I needed.

Finally, I want to thank my beautiful family. Without their love and support, this would be impossible.

To all my inspiring mentors in geology

"All my life through, the new sights of Nature made me rejoice like a child."

--Marie Curie--

Chapter 1

Research aims and geology background

1– Introduction

During orogenesis, rocks move through evolving thermal and structural fields within the orogen (Jamieson and Beaumont, 2013). In particular, in subduction–related, accretionary orogens the mid–crustal levels of the continental back–arc are characterised by long–lasting high–temperature and low–pressure (HT–LP) metamorphism spread along broad zones due to the thinner lithosphere interacting with the asthenosphere (Heuret et al., 2007; Heuret and Lallemand, 2005; Hyndman et al., 2005). This thermally weakened crustal section is susceptible to a record of deformational events associated with the subduction dynamics (Curie and Hyndman, 2006; Heuret and Lallemand, 2005; Jamieson and Beaumont, 2013; Lister and Forster, 2009), regardless of its tectonic mode (e.g., extension or shortening (Lister and Forster, 2009). Although there are many well studied accretionary orogens (Bouhallier et al., 1995; Chardon et al., 1996; Fergusson and Henderson, 2015; Franke, 2014; Hajná et al., 2012; Rubio Pascual et al., 2016), most of the understanding about dynamics of their mid–crustal sections is based on numerical or analogue models (Chardon and Jayananda, 2008; Chardon et al., 2011; Cruden et al., 2006; Jamieson et al., 2007; Jamieson et al., 2010; Parsons et al., 2016), supported by inferences based on fieldwork. These models have defined processes and inspire interpretation of major tectonic features observed in nature, and to a lesser extent the time scales involved in such processes. Here we investigate a pristine section of an exposed mid–crustal section, allowing us a direct view into the roots of an orogen and more specifically into the pre–Andean Famatinian back–arc currently exposed in the Sierra de Quilmes, NW of Argentina.

The Famatinian orogen was a long–lived wide (~400 km) and hot accretionary orogeny associated with wide shear zones (Finch et al., 2015; Finch et al., 2017; Larrovere et al., 2016; Larrovere et al., 2008) that records about 60 million years (c. 500–440 Ma) of magmatism and metamorphism (Büttner et al., 2005; Finch et al., 2017; Ortiz et al., 2019; Sola et al., 2013; Sola et al., 2017; Wolfram et al., 2019). The Famatinian orogenic cycle is one of three major accretionary orogenies that occurred in the Western Gondwana margin during the Paleozoic. These consecutive orogenic cycles reworked the rocks of the Sierra de Quilmes resulting in a long–lived poly–deformed terrane. The understanding of the Famatinian structural and thermal evolution will give us insights into processes acting in the mid–crustal sections of ongoing accretionary orogens like the neighbouring central Andes or the North American Cordillera, and more specifically their back–arc sections.

2– Rationale of the thesis and research questions

This project aims to better understand the nature of deformation and mass transfer in the ductile mid–crustal levels of the wide and hot Famatinian back–arc, and the time scales involved in the process. In order to better understand how the Famatinian back–arc, represented in the Sierra de Quilmes operated, we raised the following questions:

1) How and why is deformation partitioned in the mid–crustal levels of a continental back–arc?

2) What is the temporal relationship between the different deformational phases and the protracted anatexis documented in the Sierra de Quilmes?

3) Are the multiple anatectic events recorded in zircon from a metamorphic complex in the northern Sierra de Quilmes (Wolfram et al., 2019) reflected in the southern complexes investigated here?

4) How do the U–Pb systematic and elemental composition of zircon, monazite, and titanite change in the different metamorphic complexes?

3– Structure of the thesis

This thesis builds on three PhD theses carried out in the Sierra de Quilmes (Finch, 2016; Wolfram, 2017; Fuentes, 2017), which provide a substantial background to build on and complete the picture of the complex architecture of this Paleozoic back–arc. This chapter details the research questions and provides the geological background necessary to understand and contextualise the study area. This is followed by the research chapters that are divided into two main parts. The first part focusses on understanding the evolution and nature of deformation of the long–lived high–temperature and low–pressure (HT–LP) continental back–arc terrane (Chapter 2). The second part of the work aims to constrain the time scales at which the terrane was active and also to explore the different behaviour of three geochronometers (zircon, monazite, and titanite) on the different complexes (Chapters 3 and 4). Finally, in the last Chapter 5, results and conclusions are brought together and future research directions provided.

Research chapters:

Chapter 2: "Orogen–parallel stretching of a HT–LP back–arc terrane: insights from the Ordovician Famatinian orogeny, NW Argentina." This chapter introduces the newly defined metamorphic complexes located south of previously studied areas. The structures in these complexes are notably different from the ones in the north. During the Famatinain crustal thickening stage, the east–west convergence was resolved first as thrusting with overall top–to–west kinematics and tectonic transport towards the orogenic front. After reaching a critical point in which the tectonic forces equilibrated with gravitational forces, the thermally–weakened footwall complex, the area studied here, reacted by escaping to the south, parallel to the orogen, under non–coaxial constriction. This evolution and the structures described here are an excellent example of lateral mass flow during mountain building.

Chapter 3: "Untangling the protracted thermal evolution of a migmatitic terrane using multiple geochronometers. Insights from the Sierra de Quilmes". This chapter builds upon the previous chapter. The objective is to constrain the timing of anatexis, peak metamorphism, and cooling history in the footwall complex, and link it with different deformational events. We found that peak metamorphism and anatexis happened at around 460 Ma across all complexes during W–directed thrusting. This implies that the younger non–coaxial constriction event (D2), that strongly overprinted anatectic structures in the footwall complex was active after 460 Ma. Also, titanite U-Pb dates are coupled with compositional variations (LREE), revealing the progressive modal increases of allanite during the protracted metamorphic retrogression. We found that the footwall complex, unlike the hanging wall complex, remained above 700 °C for c. 60 Myr after the metamorphic peak, suggesting a slow cooling of c. 1 °C/Ma that started at 440 Ma to at least 380 Ma.

Chapter 4: "Exploring the different behaviour of geochronometers in migmatites to unravel 120 Ma of orogeny". This chapter aims to integrate the geochronology results of the footwall complex (Chapter 3) with the geochronology of the hanging wall complexes in order to evaluate and compare the behaviour of the three geochronometers in different P–T conditions and strain regimes. This chapter builds on chapters 2 and 3, and previous work (Büttner et al., 2005; Finch et al., 2017; Wolfram et al., 2017) in the Tolombon complex and reports new geochronological data from the newly defined Tolombon West complex in the hanging wall. The results show that the U-Pb isotopic system of the different geochronometers responded differently to the slightly different metamorphic history of each complex during the Famatinian orogeny. Zircon reacted by forming entirely new grains in the granulite facies of the Tolombon complex where the temperature reached 800 °C, and metamorphic rims formed on partially dissolved detrital zircon in terranes with similar lithology but maximum temperature of c. 750 °C. Monazite remained stable during peak metamorphism in all complexes and was affected by coupled dissolution–precipitation that obliterated its U-Pb systematics. New high–REE monazite formed at c. 407 Ma assisted by shearing. Titanite stopped forming in the hanging wall at 440 Ma and continued forming in the footwall complex below its closure temperature, probably assisted by shearing (D2). We learned that in this long–lived terrane, not only do minerals change behaviour with temperature and shearing conditions, they are also not homogenised in either a single sample or in the same complex, even when submitted to nominally similar evolution. Therefore, analyses of several accessory phases from a number of samples are the most efficient way to get a more complete overview of the evolution of a terrane.

4– Methods

Two field trips were carried out with the support of researchers from the Universidad Nacional de Salta (UNSa) in Argentina to map the southern block of the Sierra de Quilmes. The first campaign led to a fundamental understanding of the structures and the nature of the rocks, and the second one targeted specific places to link large–scale structural features. In addition to that, aeromagnetic data from the SEGEMAR (the Argentinian geological service) were used to interpret structures and major lithological groups across the range, presented in Chapter 2. We collected samples from specific locations for petrological studies, fabric analysis, whole–rock geochemistry, and geochronology. The petrology and microstructures were analysed in oriented petrographic thin sections. The CPO (quartz c–axis crystallographic preferred orientation) from quartz–rich rocks was analysed, using the G50 Fabric Analyser at Monash University. Whole–rock geochemistry including major elements (done at the University of Tasmania) and trace elements (done at Monash University) from specific lithologies was used to discriminate the lithological groups, and together with their mineral composition from microprobe mineral analysis (done at the University of Melbourne), a thermodynamic model and pseudosection was done to constrain P–T conditions. In regards to geochronological studies, after sample preparation, SEM imaging (done at the MCEM at Monash

University) and cathodoluminescence images (University of Melbourne) of zircon, monazite, and titanite were done to identify mineral zonation and target accordingly. The dating of those minerals was done at the Monash Isotopia Facility at Monash University using Laser ablation ICP–MS, and Laser ablation Split Stream (LASS) ICP–MS for coupled U-Pb age and trace element composition.

Terminology

For migmatites, we follow the terminology of Sawyer (2008) and use the term *migmatite* for any partially melted rock, *metatexite* for those migmatites that preserve the original fabric, *stromatic metatexite* for migmatites with a layered fabric, *diatexite* for migmatites that lost coherence due to high fraction of melt, *neosome* for the sections that underwent partial melting, *leucosome* for the light–coloured, crystallised product of partial melting, and *melanosome* for the residual part of the neosome from which melt was extracted. Mineral abbreviations are after Whitney (2010). When dealing with geochronology, we follow Horstwood (2016) and Schoene (2013) for terminology and use “date” to refer to the calculated number from measured isotopic ratios, and “age” when the date or dates have a geological significance.

5– Geological background

The Sierra de Quilmes is located in the NW of Argentina, in the Sierras Pampeanas geological province (Fig. 1a). This province encompasses a series of north–south trending mountain ranges located in the current Andean foreland that were uplifted by the flat–slab subduction of the Pacific plate (Caminos, 1999; Casquet et al., 2008; González Bonorio, 1950). Deeper levels of the crust are exposed in the south and shallower in the north of the Sierras Pampeanas (Büttner et al., 2005; Pankhurst et al., 1998; Rapela et al., 1998a; Rapela et al., 2015; Whitmeyer and Simpson, 2003). The rocks of the Sierras Pampeanas were shaped during three consecutive Paleozoic orogenies that were once part of the Western Gondwana active margin, and part of the 18,000 km long and 1600 km wide Terra Australis Orogen (TAO) (Fig. 1b)(Cawood, 2005; Pankhurst and Vaughan, 2009). The TAO represents the active margin of Gondwana that commenced soon after the Neoproterozoic breakup of Rodinia and opening of the Iapetus and the Pacific Ocean along the eastern and western Gondwana respectively (Goodge et al., 2010; Jacobs, 2009). It encompasses the Tasman orogen of Australia, Ross orogen of Antarctica and Tuhua orogen of New Zealand, the Cape orogen of Southern Africa and the Neoproterozoic and Paleozoic orogens of South America (Cawood, 2005; Schwartz et al., 2008).

The establishment of the active margin and the TAO in Western Gondwana was interrupted by three consecutive Paleozoic accretions of microcontinents of Laurentian affinity that in turn controlled the evolution of these orogenic cycles (Cawood, 2005; Dalla Salda et al., 1998; Ramos, 2004; Ramos et al., 1986). Every orogenic cycle started with E–dipping subduction of oceanic crust under the western continental margin of Gondwana, resulting in a continental magmatic arc and an accretionary orogen. This was followed by crustal thickening and thermal maturation. The accretion of microcontinents into the active margin drove the end of the orogenic cycle and the reorganisation of the subduction system. Every orogenic cycle accreted new material to the continent either as large turbidite fans or as exotic terranes.

The first of these orogenic cycles was the Pampean (c. 550-530 Ma) followed by the Famatinian (c. 500-440 Ma) and Achalian/Chanic (c. 400-350 Ma) orogenic cycles (e.g. Ramos et al. (1998) and Rapela et al. (1998c). These orogenic cycles reworked vast volumes of turbidites with minor carbonates and volcanic rocks deposited during the Neoproterozoic and Early Cambrian in the passive margin of Western Gondwana and sourced from the Gondwana continent. This extensive package of metasedimentary rocks is known as the Puncoviscana sequence (Aceñolaza and Aceñolaza, 2007b; Adams et al., 2011; Turner, 1960), which is the regional basement and protolith of most of the Sierras Pampeanas metamorphic and igneous rocks. The Sierras Pampeanas is divided into two major blocks, the Western and Eastern Sierras Pampeanas (Caminos, 1979; Rapela et al., 2015). The Eastern Sierras Pampeanas, where the Sierra de Quilmes is located, represents the reworked rocks of the Puncoviscana sequence accreted into the continental margin and flanked to the east by the Rio de la Plata craton. The Western Sierras Pampeanas encompasses the exotic Laurentian blocks accreted to the Gondwana margin during the first two orogenic cycles. Most of the elements presented in this chapter are discussed in more details in Weinberg (2018). We start the next section with a review of the Sierra de Quilmes, followed by the regional Puncoviscana sequence and the evolution of the accretionary orogenic cycles that added to the growth of the continental margin.

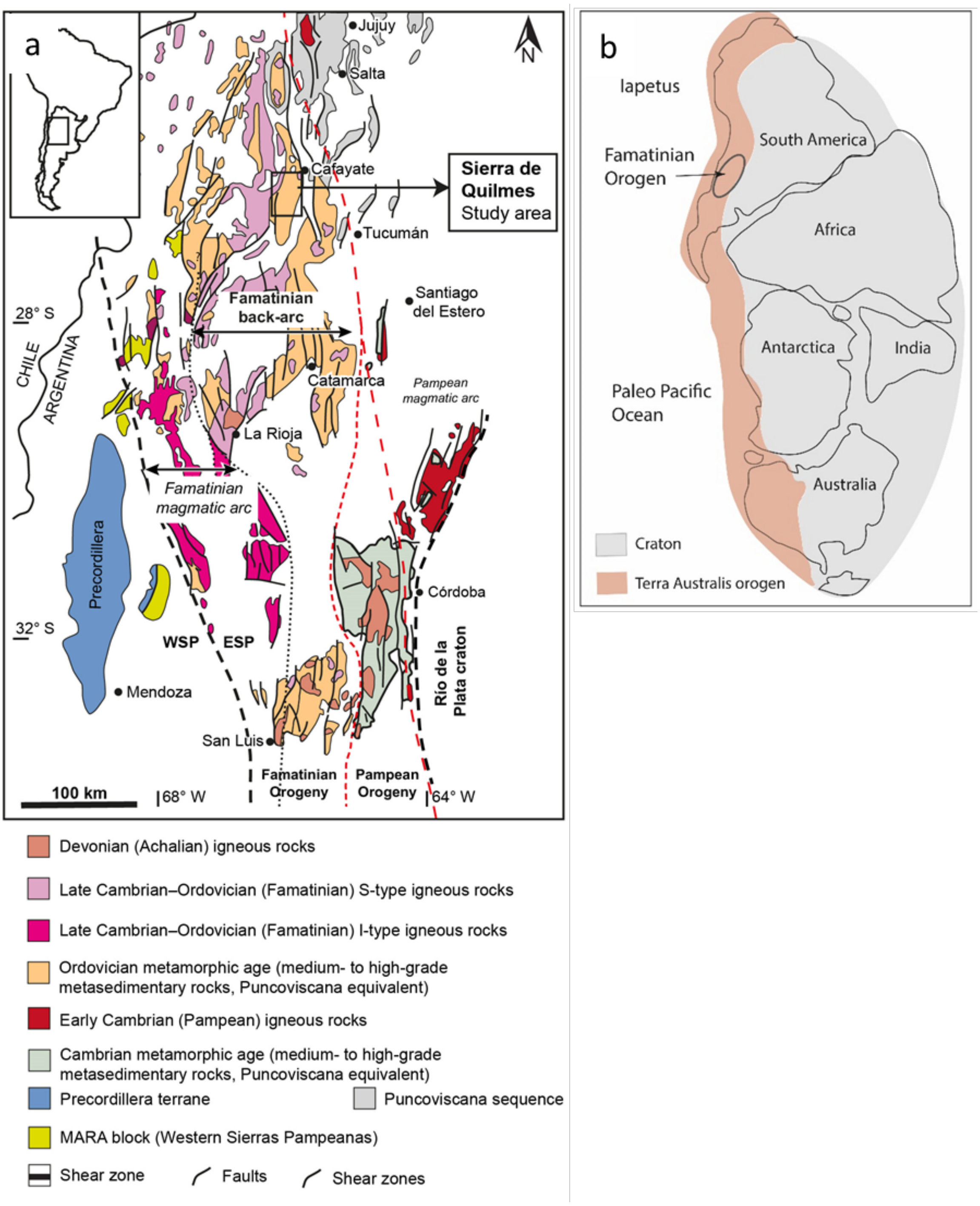

Figure 1. (a) The Sierra Pampeanas geological map with the location of the study area. (b) The Terra Australis orogen during the Ordovician, modified after Cawood (2005).

5.1– The Sierra de Quilmes, the study area

The Sierra de Quilmes is a 130 by 30 km, north–south trending range located in the northern part of the Eastern Sierras Pampeanas (Fig. 1a). It comprises the turbiditic Puncoviscana sequence reworked by the Pampean, Famatinian and possibly the Achalian orogenic cycles, but mostly by the protracted high–temperature and low–pressure (HT–LP) metamorphism of the Famatinian back–arc (Büttner et al., 2005; Wolfram et al., 2019), and its unusually wide shear zones developed during the Oclóyic phase of the Famatinian orogeny (Finch et al., 2017). The Sierra de Quilmes represents the exposed mid–crust levels of a long–lived polydeformed terrane, a perfect natural laboratory for understanding the evolution of deeper parts of orogens.

5.2– The Puncoviscana sequence. The protolith of Eastern Sierras Pampeanas

The Puncoviscana sequence extends over an area of 800 km north–south and around 150 km east–west (Ramos, 2008), and is at least 3 km thick with no exposed basement (Aceñolaza and Aceñolaza, 2007c; Adams et al., 2011). It is interpreted to be the bulk protolith and basement of the Eastern Sierras Pampeanas. Low metamorphic grades of this sequence are exposed in the north, and high–grade equivalents in the south of the Sierras Pampeanas (Moya, 2015; Zimmermann, 2005a).

The Puncoviscana sequence has traditionally been associated to Precambrian turbidites in NW Argentina (Omarini et al., 1999), but its lithological correlation with other formations, absolute age, source, and tectonic setting have been debated for a long time. Simplified, the Puncoviscana sequence is considered to be part of a continental margin wedge that was deposited during the Neoproterozoic to Cambrian times and typically composed of shelf and slope deposits with a trend to deeper environments towards the west (Aceñolaza et al., 2002; Aceñolaza and Aceñolaza, 2007a; JeŽek et al., 1985; Zimmermann, 2005b). In NW Argentina, the Puncoviscana type locality is described as “monotonous outcrops of coarse–grained turbiditic sandstones of flysch type, thick and monotonous strata of diamictites and polymictic conglomerates and isolated but thick strata of shallow–water micritic limestones.” (Omarini et al., 1999).

The source of these sediments is considered to be from the cratonic parts of Gondwana (Aceñolaza and Aceñolaza, 2007c). More specifically, from the Neoproterozoic Braziliano and Mesoproterozoic Sunsás Orogens (Adams et al., 2011; Miller et al., 2011). This interpretation is based on the detrital zircon signature of the Puncoviscana sequence that is characterised by two dominant age groups: 670–545 Ma and 1200–900 Ma (Miller et al., 2011), which are typical of those orogens.

The age range of this sequence varies across the literature. It has been interpreted that the sediments were deposited between >600 and 520 Ma (Drobe et al., 2009; Omarini et al., 1999; Rapela et al., 1998a; Schwartz and Gromet, 2004; Sims et al., 1998b; Zimmermann, 2005b), but since the base of the sequence has not yet been found, it is speculated it could be as old as 650 Ma contemporary with the breakup of Rodinia (Aceñolaza and Aceñolaza, 2007c; Omarini et al., 1999). However, Do Campo (2005) presented K–Ar ages of authigenic mica interpreted to represent diagenesis at 670 ± 27 Ma. Aceñolaza and Toselli, (2009) found Ediacaran fossil traces in NW Argentina that tend to be younger towards the south where they can be as young as Early Cambrian. The youngest zircon age, indicating the maximum depositional age, varies from 520 Ma (Adams et al., 2011), to 517 Ma (Aparicio González et al., 2014) to 509 Ma (Pearson et al., 2012). Escayola et al. (2011) proposed that the end of sedimentation of the Puncoviscana sequence was before the deposition of the overlaying, unconformable Cambrian Mesón Group, which has a maximum deposition age of 513 ± 2 Ma, defined by the four concordant zircon ages (Aparicio González et al., 2014). The overlapping of the younger detrital zircon in the Puncoviscana sediments and the Mesón Group does not allow a clear distinction of the time gap between them. Also, Escayola (2011) reports U–Pb zircon ages from felsic volcanic layers from the NW Puncoviscana sequence that yield 537 ± 1

Ma, nearby a pluton of 523.7 ± 0.8 Ma intruding the folded sequence, suggesting a deformational event between 537 and 524 Ma.

The similarities between turbidite deposits across the Sierras Pampeanas make it challenging to separate them so that they are commonly grouped as the Puncoviscana sequence. Therefore, some of the turbidites that were once considered to be part of the Puncoviscana sequence have now been redefined. This is in part because of the improved understanding of turbidite systems (Posamentier and Walker, 2006; Posamentier et al., 2014; Reading, 1996), more detailed mapping, and the use of tools like detrital zircon (e.g., (Collo and Astini, 2008).

There is still controversy about the tectonic setting of the Puncoviscana sequence (Quenardelle and Ramos, 1999). It has been interpreted as deposited in the Western Gondwana passive margin (Aceñolaza et al., 2002; Adams et al., 2011; JeŽek et al., 1985; Rapela et al., 1998c; Schwartz et al., 2008), a rift sequence (Omarini et al., 1999; Ramos, 2008), a foreland basin (Escayola et al., 2011; Keppie and Bahlburg, 1999), or a fore–arc basin (Einhorn et al., 2015; Hauser et al., 2011; Rapela et al., 2007). The presence of interbedded amphibolites with MORB geochemical signature, in the deeper sections of the Puncoviscana basin, suggest that the extension that drove the deposition of the sequence may have led to the formation of an ocean floor (Baldo et al., 1996; Rapela et al., 1998b). Escayola et al. (2011) have a more integral theory of evolution that is based on time of deposition, deformation, and magmatism. They argue that the sediments were first deposited at around 540 Ma in the fore–arc and /or trench of the Pampean arc. This was followed by syn–orogenic foreland sedimentation when a Laurentia–derived continental terrane (the MARA block (Rapela et al., 2015), (Fig. 1a) arrived at the western margin of Gondwana at c. 530 Ma. Collo et al. (2009), and Weinberg et al. (2018) argued for the need to separate the sequence in two, based on detrital zircon evidence from a section in the southern Sierras Pampeanas. The older part of the sequence was deposited in the passive margin before the onset of the Pampean magmatic arc, thus being a pre–orogenic turbiditic sequence. This sequence is unconformably overlain by a younger turbiditic sequence with detrital zircon of Pampean age, suggesting a syn–orogenic deposition. As we will argue in Chapter 3, new detrital zircon and whole–rock geochemistry in the Sierra de Quilmes support this division of the Puncoviscana sequence in pre– and syn–orogenic.

5.3– Pampean orogenic cycle (c. 550–530 Ma)

The Pampean orogenic cycle (Pampean cycle for short), is the first tectono–thermal event recorded in the Sierras Pampeanas (Fig. 2). It involved the accretion of large volumes of continental detritus (turbidites from the Puncoviscana sequence), similar to many other contemporary turbidite–dominated accretionary orogens along the Eastern Gondwana of the TAO (Cawood, 2005; Foster et al., 2009; Gray et al., 2007). The Pampean cycle has been associated with subduction processes followed by accretion of a continental ribbon (Escayola et al., 2011; Rapela et al., 1998b; Rapela et al., 2015). The Pampean cycle was defined and studied dominantly in the Córdoba province, where metamorphism reached granulite facies, and there is no strong overprint of younger orogenic cycles.

The Pampean cycle is represented by a discontinuous magmatic arc that trends N–S flanking the Rio de la Plata craton, separated by the Córdoba fault (Peri et al., 2013), and continues to NW Argentina as isolated magmatic bodies (Dahlquist et al., 2016). The magmatic arc is represented by a series of subduction–related belts of metaluminous calk–alkaline granitoids and dacite–rhyolite (Lira et al., 1996; Rapela et al., 1998c), flanked by a peraluminous magmatic belt to the west (Rapela et al., 1998c).

The Pampean calc–alkaline magmatism started at 555 Ma (Rapela et al., 2015; Schwartz et al., 2008) and peaked at 540–530 Ma (Rapela et al., 1998b), followed by extensive low–pressure anatexis and peraluminous magmatism in the fore–arc that peaked at 520 Ma (Iannizzotto et al., 2013; Rapela et al., 1998b; Rapela et al., 1998c) and isothermal decompression and exhumation (Baldo et al., 1996;

Otamendi et al., 2004; Rapela et al., 2015). A rapid cooling inferred from U-Pb titanite, and apatite ages, and $^{40}Ar/^{39}Ar$ muscovite cooling ages, mark the end of the Pampean cycle between 510 and 500 Ma (Simpson et al., 2003).

Pampean metamorphism reached maximum P–T conditions in the southern Sierras Pampeanas, where the crustal thickening and burial resulted in granulite facies conditions (8.6 kbar, 810 °C) defining a clockwise P–T–t path (Baldo et al., 1996; Otamendi et al., 2001; Rapela et al., 1998b; Schwartz et al., 2008; Steenken et al., 2011). In the NW Argentina, the Puncoviscana sequence reached lower metamorphic conditions than in the south, with maximum P–T of 9 kbar and 250 °C during the Pampean cycle (Do Campo et al., 2014). Pampean–age metamorphism was described in areas far outside the arc and surroundings. For example, Lucassen (2011) described in the Puna region, high–temperature and low to medium–P metamorphism (600–750 °C, and 4–8 kbar) associated to Pampean peraluminous magmatism (Escayola et al., 2011; Ortiz et al., 2017; Ortiz et al., 2019; Zimmermann et al., 2014). This Pampean–age block is separated from the main Pampean arc by a large younger Famatinian–age metamorphic block. The link between this Pampean–age block in the west and the main Pampean arc region in the east is detailed in Weinberg (2018).

Middle–Cambrian deformation and exhumation of the Puncoviscana sequence are attributed to the Pampean cycle. The main deformation event is the Tilcara–Pampean or Tilcarian Orogeny, first described in the lower grade Puncoviscana sequence (Aceñolaza and Aceñolaza, 2007c; Adams et al., 2011; Bahlburg and Breitkreuz, 1991; Escayola et al., 2011; Omarini et al., 1999; Ramos et al., 2010). This event caused the regional angular unconformity that separates the Puncoviscana sequence from the overlying Late Cambrian–Early Ordovician undeformed quartzites of the Mesón Group. This event relates to the accretion of the exotic MARA block (Rapela et al., 2015). This block is a composite of amalgamated terranes that includes the Sierra de Maz, Arequipa–Antofalla, and the Rio Apa blocks. The MARA block is interpreted to have rifted out of the eastern margin of Laurentia, based mainly on detrital zircon signature and lithological correlations with the Grenville orogen counterparts (Murra et al., 2016; Rapela et al., 2015).

The transition to the Famatinian orogenic cycle is characterised by a tectonic and magmatic lull. This is first evidenced by the shallow–marine sedimentary sequences deposited after the Tilcara event between c. 520 and 500 Ma. These sequences are represented by the Mesón Group in the north (Astini, 2008; Omarini et al., 1999), the Negro Peinado and Achavil Formations of the Famatina Range (Collo and Astini, 2008; Collo et al., 2009), and the La Cébila and Ambato Metamorphic Complexes in the Sierra de Velasco and Ambato (Rapela et al., 2015). These sedimentary basins lack evidence of contemporaneous volcanism (Weinberg et al., 2018) and they seem to have a reduced number of detrital zircon of ages between 490–515 Ma (Einhorn et al., 2015). Altogether they mark a regional reorganisation of the subduction dynamics, with renewed extension after the Pampean shortening associated with a tectonic and magmatic quiescence following the accretion of the MARA block (Weinberg et al., 2018).

5.4– Famatinian orogenic cycle (c. 500–440 Ma)

This orogen (Famatinian cycle for short) started at c. 505–500 Ma (Bahlburg and Berndt, 2016; Wolfram et al., 2019) after the Late Cambrian–Early Ordovician Pampean magmatic lull, when subduction restarted west of MARA, forming a new magmatic arc paired with an extensional back–arc to the east, in the previous Pampean fore–arc (Fig. 2).

The Famatinian orogen has two paired magmatic belts. A magmatic arc with rocks of calc–alkaline character dominated by I–type granodiorites trending NW–SE and alongside the MARA block, in the south, and it continues to the north to northern Chile and onto the Arequipa block in Peru (Chew et al., 2016; Ramos, 2008). Southwards it extends to the margin of the Patagonian massif (Chernicoff et al., 2010). In the Puna region, the calc–alkaline magmatic arc is interpreted by Weinberg (2018) to be represented in the "Faja Eruptiva Occidental" (Coira et al., 2009b). This arc is paired to the east with a 200–300 km–wide peraluminous belt with S–type granites and dominant high–temperature, low–pressure migmatites, as result of intense crustal anatexis and paleo–depths no greater than c. 25 km (Otamendi et al., 2012; Pankhurst et al., 2000a; Rapela et al., 1992). This peraluminous belt is interpreted to represent the deep levels of the Famatinian back–arc (Weinberg et al., 2018) with typical bimodal magmatism (Coira et al., 2009a).

The climax of arc magmatism was between c. 480 and c. 465 Ma peaking at c. 470 Ma (Bellos et al., 2015; Castro et al., 2014; Ducea et al., 2017; Ducea et al., 2010; Mulcahy et al., 2014; Mulcahy et al., 2007; Ortiz et al., 2019; Otamendi et al., 2017; Pankhurst et al., 2000b; Pankhurst et al., 1998; Quenardelle and Ramos, 1999) coeval with peak metamorphism and anatexis in the extensional back–arc (Büttner et al., 2005; Finch et al., 2017; Sola et al., 2013; Sola et al., 2017; Wolfram et al., 2019). The Famatinian magmatic belt has been studied by several authors (Alasino et al., 2016; Astini and Dávila, 2004; Bahlburg et al., 2016; Bellos et al., 2015; Dahlquist et al., 2008; Ducea et al., 2017; Lucassen and Franz, 2005; Ortiz et al., 2017; Otamendi et al., 2012; Otamendi et al., 2017; Otamendi et al., 2009; Pankhurst and Rapela, 1998; Pankhurst et al., 2000a; Rapela et al., 1998c; Saavedra et al., 1998; Sato et al., 2004; Struart-Smith et al., 1999; Suzaño et al., 2015; Suzaño et al., 2017; Tibaldi et al., 2013; Toselli et al., 2002; Toselli et al., 1996; Von Gosen and Prozzi, 1998; Zimmermann and Bahlburg, 2003), however, interpretations of its tectonic settings and age are still debated. The end of magmatism is interpreted to happen at some point between 465 and 440 Ma. Otamendi et al. (2017) argued that the end of the calc–alkaline magmatism occurred at c. 465 Ma because of the Cuyania/Precordillera accretion. Castro et al. (2014) reported younger zircon overgrowth at 450 Ma, and Wolfram (2019) argued that the end of arc magmatism ended with the back–arc anatexis at c. 440 Ma. The available crystallization ages from the magmatic arc seems to indicate its westward migration. The older ages (from ca. 490 to 480 Ma) are represented in the Sierras de Córdoba, San

Luis, Sierras de Chepes and Eastern Cordillera, and younger (480–470 Ma) ages more common in the Famatina ranges and Puna to the east, presumably due to a retreat or roll–back of the subducting slab (Ramos et al., 2010).

Famatinian extensional phase (c. 500–460 Ma)

The extensional phase of the Famatinian cycle is marked by the formation of large marine basins in the surface coupled with anatexis and peraluminous magmatism in the mid–crustal levels of the back–arc (Büttner, 2009). The Famatinian–age mafic magmatic rocks exposed east of the magmatic arc, suggests that extension was more prominent in the north compared to the south (Weinberg et al., 2018). This interpretation is based on the geochemical and isotopic nature of these rocks. In the southern section, the rocks are isotopically homogeneous and derived from lithospheric–sourced evolved magmas, suggesting hybridisation between primitive magmas with upper crustal material (Dahlquist and Galindo, 2004; Ducea et al., 2010; Grosse et al., 2011; Pankhurst et al., 2000a). In contrast, in NW Argentina mafic rocks have more juvenile mantle isotopic compositions, reflecting a more significant asthenospheric input (Franz et al., 2006; Ortiz et al., 2017; Suzaño et al., 2017; Zimmermann et al., 2014).

The extensional regime of the Famatinian cycle resulted in large Ordovician marine basins, exposed in NW Argentina. The depocentres of these basins are consistently deeper towards the north (Astini and Dávila, 2004). Based on the sedimentary rock record, deposition started at c. 490 Ma and continued until 470–460 Ma (e.g. (Astini, 2008; Bahlburg and Breitkreuz, 1991; Büttner, 2009; Cisterna et al., 2017; Hauser et al., 2011) suggesting that the area was under sea level for more than 30 Myr.

The Ordovician sedimentary sequence represented in NW Argentina by the Santa Victoria Group was deposited unconformably over the Meson Group. The unconformity between the Groups represents the basin inversion after the onset of the Famatinian cycle, referred as to the Iruya event (Astini, 2008; Bahlburg and Breitkreuz, 1991; Ramos et al., 2010; Turner, 1975; Zimmermann and Bahlburg, 2003). The Santa Victoria Group represents volcanoclastic deposits interlayered with deep–marine turbidites (Astini, 2008; Bahlburg and Breitkreuz, 1991; Turner, 1975). The base of the Santa Victoria Group was dated as Late Cambrian (Furongian Stage 10 that begins at 492 Ma) (Buatois and Mángano, 2003; Buatois et al., 2006; J Zeballo and Albanesi, 2009; Tortello and Esteban, 2016). Sedimentation continued until at least 460 Ma, and ended with the onset of the Oclóyic tectonic phase (Astini and Dávila, 2004; Rapela et al., 1998a; Turner, 1975).

In summary, the Late Cambrian – Early Ordovician Mesón Group represents the renewed extension that followed the Pampean cycle. These sediments were rapidly buried and later exhumed during the onset of the Famatinian cycle, which is marked by the Iruya unconformity. The marine deposits of the Santa Victoria Group were deposited over this unconformity, suggesting subsidence in the extensional continental back–arc of the Famatinian cycle, that ends with the Oclóyic phase after c. 460 Ma.

The Oclóyic phase (c. 460–440 Ma?)

The arrival of the Laurentian–derived terrane of Cuyania/Precordillera to the active margin triggered a phase of shortening and mountain building, known as the Oclóyic Orogeny or Oclóyic phase (Astini and Dávila, 2004; Rapela et al., 1998a; Turner, 1975). This accretion may have started at 470 Ma (Ramos et al., 1986) or slightly later (Otamendi et al., 2017; Ramos, 2004) and it is evidenced by the closure of the Ordovician marine basins (Aceñolaza and Aceñolaza, 2007c). This phase is characterized by folding and thrusting (Astini and Dávila, 2004; Finch et al., 2015; Rapela et al., 1998c; Semenov and Weinberg, 2017; Whitmeyer and Simpson, 2003). It lasted until 440–435 Ma when peraluminous magmatism and anatexis in the back–arc waned (Bahlburg and Berndt, 2016;

Bahlburg et al., 2016; Büttner et al., 2005; Mulcahy et al., 2014; Wolfram et al., 2019). Titanite ages in the Puna region, suggest that metamorphism lasted until 430–420 Ma (Lucassen and Becchio, 2003; Lucassen et al., 2011).

Some of the Famatinian shear zones are unusually wide. For example the 3 km–wide mylonitic–ultramylonitic Pichao shear zone in the Sierra de Quilmes (Finch et al., 2015), the 1 to 4 km–wide La Chilca shear zone (Larrovere et al., 2008), the 2 km–wide TIPA (Tinogasta–Pituil–Antinaco) shear zone (López and Toselli, 1993) that can be traced over 200 km (Höckenreiner et al., 2003), and the 10–15 km–wide Guacha Corral shear zone (Martino, 2003; Otamendi et al., 2004; Semenov and Weinberg, 2017; Simpson et al., 2003; Whitmeyer and Simpson, 2003). These shear zones represent mostly west–verging thrusts, towards the arc, with a few east–verging (Astini and Dávila, 2004; Collo and Astini, 2008). They record high–temperature and low–pressure metamorphism with mineral associations comprising cordierite–sillimanite–garnet in migmatites, with high–grade rocks thrusted over lower–grade rocks, suggesting exhumation of deeper and hotter rocks.

5.5– Achalian orogeny (c. 400–350 Ma)

The c. 400–350 Ma Achalian orogenic cycle (Aceñolaza and Toselli, 1981; De Luchi et al., 2007; Drobe et al., 2010; Drobe et al., 2009; Rapela et al., 1998a; Siegesmund et al., 2009; Sims et al., 1998b; Steenken et al., 2006; Struart-Smith et al., 1999), also known as Chanic orogeny (Ramos et al., 1986) started when subduction resumed after the accretion of the Precordillera/Cuyania block (Fig. 2). Unlike the previous ones, the Achalian orogeny does not have paired magmatic belts. Instead, this orogenic cycle is characterised by scattered voluminous granite batholiths and reactivated shear zones overprinting the older orogenies across the Sierras Pampeanas. Similar to the previous orogenic cycles, the shortening phase and termination of the magmatic activity are associated with the docking of a new block to the active margin: the Chilenia block (Quenardelle and Ramos, 1999;

Ramos et al., 1986; Sims et al., 1998b; Steven Davis et al., 1999). Ramos et al. (1986) argue that the collision between Chilenia and Precordillera occurred before the Late Devonian because of the onlap of Carboniferous strata from Precordillera over the Chilenian block.

Constraints on the time of Achalian cycle initiation are difficult, as there seems to be a gradual transition between the Famatinian and Achalian orogenic cycles. Ramos et al. (1998) argued that the collision between the Chilenia block with the proto–margin of Gondwana finished by 394 Ma, based on $^{40}Ar/^{39}Ar$ muscovite ages from shear zones in the Sierra de Palo (part of the MARA block). In a nearby location, within the MARA block, Mulcahy (2014) reported anatectic and shearing events of around 410 Ma suggesting that there were caused by a plate boundary reorganization during the Chilenia block collision. The sheared Escalerilla granite in the Sierra de San Luis yields U–Pb zircon age of 403 ± 6 Ma, interpreted as one of the first intrusions of the Achalian cycle (Sims et al., 1997).

A suite of middle Devonian to Lower Carboniferous batholiths in the Sierras de Cordoba and San Luis represents the largest evidence of Achalian magmatism (De Luchi et al., 2007; Pinotti et al., 2002; Pinotti et al., 2006; Rapela et al., 1998a; Struart-Smith et al., 1999). The Devonian peraluminous Achala granitoid (Rapela et al., 2008), and the Cerro Aspero batholith (Pinotti et al., 2002; Pinotti et al., 2006) in Córdoba are the largest. To the north of the Sierras Pampeanas, in the Sierra de Velazco, in La Rioja (Fig. 1a), there are isolated granites of Lower Carboniferous age (Báez et al., 2005; Dahlquist et al., 2008; Grosse et al., 2008). The Achalian intrusions have several common features. They are all nearly circular, discordant with the host, shallow intrusions, and syeno– to monzogranitic compositions (Steenken et al., 2011). Moreover, Steenken (2011), argue based on εNd values, that unlike in the Famatinian times, the Achalian magmatism reflects major input of juvenile sources. Dahlquist et al. (2010) argued that the emplacement of A–type granitoids with asthenospheric signatures at the end of the orogeny was strongly controlled by pre–existing crustal–scale structures.

The causes of voluminous magmatism are still debated. Thomas and Astini (2003) refer to the Devonian magmatism as the product of gravitational collapse, or back–arc extension of a distant subduction zone. De Luchi et al. (2007) proposed that the magmatism was a result of mafic underplating or a slab break–off during the late stages of subduction that ended with the collision of Chilenia. Miller and Sollner (2005), Dalla Salda et al. (1998), and Llambias et al. (1998) proposed that the Carboniferous magmatism was post–kinematic and associated with regional crustal heating after an orogenic collapse. Grosse et al. (2008) interpreted the gradual younging of magmatic bodies from south to north as evidence of progressive delamination of the lower crust that resulted in upwelling of the upper mantle from south to north.

Several transpressional shear zones were active during the Achalian cycle. Sims et al. (1998) mention shear zones in the Sierras de Córdoba that yield 358 ± 2 Ma (Ar/Ar in biotite), and between 351–361 Ma in the Sierra de San Luis. All of these shear zones overprint granites with Early Devonian U–Pb zircon ages, like the 403 ± 6 Ma Escalerilla granite, therefore constraining the maximum age of shearing (Sims et al., 1998a).

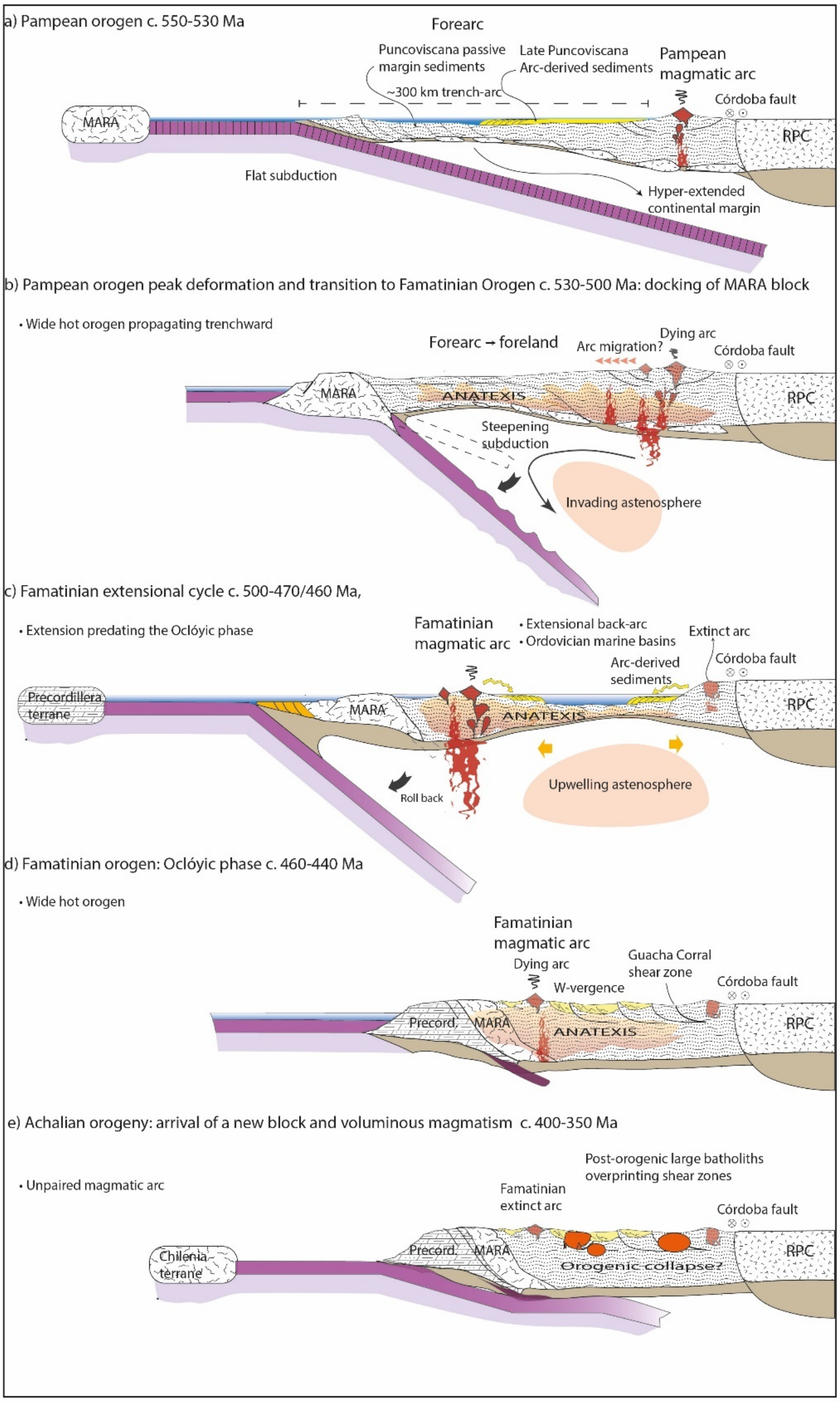

Figure 2. a-b) Different stages of the Pampean orogeny. Started as an hyperextended passive margin overlain by the turbidites of the Puncoviscana sequence. The arrival of the MARA block triggered the steepening of the subdicted slab, and extensive anatexis in the middle crust. c-d) The Famatinian orogenic cycle with the extensional phase and associated anatexis and marine basisns. During the accretion of the Precordillera terrane, the orogenic cycle switches to shortening (Ocloyic phase). This phase is characterized by trench-verging wide shear zones. After c. 440 Ma, the Famatinian magmatism wanes. e) Initiation of subduction after the accretion of the Precordillera terrane and inauguration of the Achalian orogenic cycle. Modified from Weinberg (2018).

6- Aim of the thesis

In order to understand the nature of deformation and mass transfer in the ductile mid–crustal levels of the Famatinian back–arc, we will first characterize the structural evolution of the unexplored sections of the Sierra de Quilmes. To understand the time scales involved in the process, and the behaviour of zircon, monazite and titanite in the different high-grade complexes, we will use U-Pb geochronology combined with their mineral composition, supported by Zr-in-titanite thermometry, and other techniques mentioned in section 4 of this chapter. The new findings will challenge the current ideas about the duration and thermal evolution of the Famatinian orogenic cycle.

References

Aceñolaza, F., and A. Toselli, 1981, Geología del Noroeste Argentino: Publicación Especial de la Facultad de Ciencias Naturales, Universidad Nacional de Tucumán., p. 1-212.

Aceñolaza, F. G., H. Miller, and A. J. Toselli, 2002, Proterozoic - Early Paleozoic evolution in western South America - A discussion: Tectonophysics, v. 354, p. 121-137.

Aceñolaza, G., and F. Aceñolaza, 2007a, Insights in the Neoproterozoic-Early Cambrian transition of NW Argentina: Facies, environments and fossils in the proto-margin of western Gondwana, *in* P. Vickers-Rich, and P. Komarower, eds., Geological Society Special Publication, p. 1-13.

Aceñolaza, G., and F. Aceñolaza, 2007b, Insights in the Neoproterozoic-Early Cambrian transition of NW Argentina: Facies, environments and fossils in the proto-margin of western Gondwana, *in* P. Vickers-Rich, and P. Komarower, eds., Geological Society Special Publication, p. 1-13.

Aceñolaza, G., and F. Aceñolaza, 2007c, Insights in the Neoproterozoic–Early Cambrian transition of NW Argentina: facies, environments and fossils in the proto-margin of western Gondwana: Geological Society, London, Special Publications, v. 286, p. 1-13.

Adams, C. J., H. Miller, F. G. Aceñolaza, A. J. Toselli, and W. L. Griffin, 2011, The Pacific Gondwana margin in the late Neoproterozoic–early Paleozoic: Detrital zircon U–Pb ages from metasediments in northwest Argentina reveal their maximum age, provenance and tectonic setting: Gondwana Research, v. 19, p. 71-83.

Alasino, P. H., C. Casquet, R. J. Pankhurst, C. W. Rapela, J. A. Dahlquist, C. Galindo, M. A. Larrovere, C. Recio, S. R. Paterson, F. Colombo, and E. G. Baldo, 2016, Mafic rocks of the Ordovician Famatinian magmatic arc (NW Argentina): New insights into the mantle contribution: Bulletin of the Geological Society of America, v. 128, p. 1105-1120.

Aparicio González, P. A., M. M. Pimentel, N. Hauser, and M. C. Moya, 2014, U–Pb LA-ICP-MS geochronology of detrital zircon grains from low-grade metasedimentary rocks (Neoproterozoic – Cambrian) of the Mojotoro Range, northwest Argentina: Journal of South American Earth Sciences, v. 49, p. 39-50.

Astini, R., 2008, Sedimentación, facies, discordancias y evolución paleoambiental durante el Cambro-Ordovícico, Revista de la Asociacion Geologica Argentina, 50-73 p.

Astini, R. A., and F. M. Dávila, 2004, Ordovician back arc foreland and Ocloyic thrust belt development on the western Gondwana margin as a response to Precordillera terrane accretion: Tectonics, v. 23, p. TC4008 1-19.

Báez, M., L. Bellos, P. Grosse, and F. Sardi, 2005, Caracterización petrológica de la sierra de Velasco, 123-130 p.

Bahlburg, H., and J. Berndt, 2016, Provenance from zircon U-Pb age distributions in crustally contaminated granitoids: Sedimentary Geology, v. 336, p. 161-170.

Bahlburg, H., J. Berndt, and A. Gerdes, 2016, The ages and tectonic setting of the Faja Eruptiva de la Puna Oriental, Ordovician, NW Argentina: Lithos, v. 256-257, p. 41-54.

Bahlburg, H., and C. Breitkreuz, 1991, Paleozoic evolution of active margin basins in the southern Central Andes (northwestern Argentina and northern Chile): Journal of South American Earth Sciences, v. 4, p. 171-188.

Baldo, E. G., M. Demange, and R. D. Martino, 1996, Evolution of the Sierras de Córdoba, Argentina: Tectonophysics, v. 267, p. 121-142.

Bellos, L. I., A. Castro, J. Díaz-Alvarado, and A. Toselli, 2015, Multi-pulse cotectic evolution and in-situ fractionation of calc-alkaline tonalite–granodiorite rocks, Sierra de Velasco batholith, Famatinian belt, Argentina: Gondwana Research, v. 27, p. 258-280.

Bouhallier, H., D. Chardon, and P. Choukroune, 1995, Strain patterns in Archaean dome-and-basin structures: The Dharwar craton (Karnataka, South India): Earth and Planetary Science Letters, v. 135, p. 57-75.
Buatois, L. A., and M. G. Mángano, 2003, Sedimentary facies, depositional evolution of the Upper Cambrian-Lower Ordovician Santa Rosita formation in northwest Argentina: Journal of South American Earth Sciences, v. 16, p. 343-363.
Buatois, L. A., F. J. Zeballo, G. L. Albanesi, G. Ortega, N. E. Vaccari, and M. G. Mangano, 2006, Depositional environments and stratigraphy of the upper Cambrian-lower Ordovician Santa Rosita Formation at the Alfarcito area, Cordillera Oriental, Argentina: Integration of biostratigraphic data within a sequence stratigraphic framework: Latin American Journal of Sedimentology and Basin Analysis, v. 13, p. 1-29.
Büttner, S. H., 2009, The Ordovician Sierras Pampeanas–Puna basin connection: Basement thinning and basin formation in the Proto-Andean back-arc: Tectonophysics, v. 477, p. 278-291.
Büttner, S. H., J. Glodny, F. Lucassen, K. Wemmer, S. Erdmann, R. Handler, and G. Franz, 2005, Ordovician metamorphism and plutonism in the Sierra de Quilmes metamorphic complex: Implications for the tectonic setting of the northern Sierras Pampeanas (NW Argentina): Lithos, v. 83, p. 143-181.
Caminos, R., 1979, Sierras Pampeanas Noroccidentales Salta, Tucumán, Catamarca, La Rioja y San Juan: Geología Regional Argentina, Academia Nacional de Ciencias, v. 5, p. 225-291.
Caminos, R., 1999, Geologia Regional Argentina: SEGEMAR.
Casquet, C., R. J. Pankhurst, C. W. Rapela, C. Galindo, C. M. Fanning, M. Chiaradia, E. Baldo, J. M. González-Casado, and J. A. Dahlquist, 2008, The Mesoproterozoic Maz terrane in the Western Sierras Pampeanas, Argentina, equivalent to the Arequipa-Antofalla block of southern Peru? Implications for West Gondwana margin evolution: Gondwana Research, v. 13, p. 163-175.
Castro, A., J. Díaz-Alvarado, and C. Fernández, 2014, Fractionation and incipient self-granulitization during deep-crust emplacement of Lower Ordovician Valle Fértil batholith at the Gondwana active margin of South America: Gondwana Research, v. 25, p. 685-706.
Cawood, P. A., 2005, Terra Australis Orogen: Rodinia breakup and development of the Pacific and Iapetus margins of Gondwana during the Neoproterozoic and Paleozoic: Earth-Science Reviews, v. 69, p. 249-279.
Chardon, D., P. Choukroune, and M. Jayananda, 1996, Strain patterns, décollement and incipient sagducted greenstone terrains in the Archaean Dharwar craton (south India): Journal of Structural Geology, v. 18, p. 991-1004.
Chardon, D., and M. Jayananda, 2008, Three-dimensional field perspective on deformation, flow, and growth of the lower continental crust (Dharwar craton, India): Tectonics, v. 27.
Chardon, D., M. Jayananda, and J. J. Peucat, 2011, Lateral constrictional flow of hot orogenic crust: Insights from the Neoarchean of south India, geological and geophysical implications for orogenic plateaux: Geochemistry, Geophysics, Geosystems, v. 12.
Chernicoff, C. J., E. O. Zappettini, J. O. S. Santos, S. Allchurch, and N. J. McNaughton, 2010, The southern segment of the Famatinian magmatic arc, La Pampa Province, Argentina: Gondwana Research, v. 17, p. 662-675.
Chew, D. M., G. Pedemonte, and E. Corbett, 2016, Proto-Andean evolution of the Eastern Cordillera of Peru: Gondwana Research, v. 35, p. 59-78.
Cisterna, C. E., M. Koukharsky, B. Coira, C. Günter, and H. H. Ulbrich, 2017, Arenigian tholeiitic basalts in the Famatina Ordovician basin, northwestern Argentina: emplacement conditions and their tectonic significance: Andean Geology, v. 44, p. 123-146.

Coira, B., A. Kirschbaum, F. Hongn, B. Pérez, and N. Menegatti, 2009a, Basic magmatism in northeastern Puna, Argentina: Chemical composition and tectonic setting in the Ordovician back-arc: Journal of South American Earth Sciences, v. 28, p. 374-382.

Coira, B., M. Koukharsky, S. R. Guevara, and C. E. Cisterna, 2009b, Puna (Argentina) and northern Chile Ordovician basic magmatism: A contribution to the tectonic setting: Journal of South American Earth Sciences, v. 27, p. 24-35.

Collo, G., and R. A. Astini, 2008, The Achavil Formation: A new low-grade metamorphic unit in the Upper Cambrian evolution of Famatina: Revista de la Asociacion Geologica Argentina, v. 63, p. 344-362.

Collo, G., R. A. Astini, P. A. Cawood, C. Buchan, and M. Pimentel, 2009, U-Pb detrital zircon ages and Sm-Nd isotopic features in low-grade metasedimentary rocks of the Famatina belt: implications for late Neoproterozoic-early Palaeozoic evolution of the proto-Andean margin of Gondwana: Journal of the Geological Society, v. 166, p. 303-319.

Cruden, A. R., M. H. B. Nasseri, and R. Pysklywec, 2006, Surface topography and internal strain variation in wide hot orogens from three-dimensional analogue and two-dimensional numerical vice models, Geological Society Special Publication, p. 79-104.

Curie, C. A., and R. D. Hyndman, 2006, The thermal structure of subduction zone back arcs: Journal of Geophysical Research: Solid Earth, v. 111.

Dahlquist, J., and C. Galindo, 2004, Geoquímica isotópica de los granitoides de la sierra de Chepes: un modelo geotectónico y termal, implicancias para el orógeno famatiniano, v. 59, 57-69 p.

Dahlquist, J., S. O. Verdecchia, E. Baldo, M. Basei, P. Alasino, C. W. Rapela, M. d. C. Campos Neto, P. Zandomeni, and G. Uran, 2016, Early Cambrian U-Pb zircon age and Hf-isotope data from the Guasayán pluton, Sierras Pampeanas, Argentina: implications for the northwestern boundary of the Pampean arc: Andean Geology, v. 1, p. 137-150.

Dahlquist, J. A., R. J. Pankhurst, C. W. Rapela, C. Galindo, P. Alasino, C. M. Fanning, J. Saavedra, and E. Baldo, 2008, New SHRIMP U-Pb data from the Famatina Complex: Constraining Early-Mid Ordovician Famatinian magmatism in the Sierras Pampeanas, Argentina: Geologica Acta, v. 6, p. 319-333.

Dalla Salda, L. H., M. G. Lopez de Luchi, C. A. Cingolani, and R. Varela, 1998, Laurentia-Gondwana collision: the origin of the Famatinian-Appalachian Orogenic Belt (a review): Geological Society, London, Special Publications, v. 142, p. 219-234.

De Luchi, M. G. L., S. Siegesmund, K. Wemmer, A. Steenken, and R. Naumann, 2007, Geochemical constraints on the petrogenesis of the Paleozoic granitoids of the Sierra de San Luis, Sierras Pampeanas, Argentina: Journal of South American Earth Sciences, v. 24, p. 138-166.

Do Campo, M., G. Collo, and F. Nieto García, 2014, Geothermobarometry of very low-grade metamorphic pelites of the Vendian–Early Cambrian Puncoviscana Formation (NW Argentina), v. 25, 429-451 p.

Do Campo, M., and S. R. Guevara, 2005, Provenance analysis and tectonic setting of late Neoproterozoic metasedimentary successions in NW Argentina: Journal of South American Earth Sciences, v. 19, p. 143-153.

Drobe, M., M. L. de Luchi, A. Steenken, K. Wemmer, R. Naumann, R. Frei, and S. Siegesmund, 2010, Geodynamic evolution of the Eastern Sierras Pampeanas (Central Argentina) based on geochemical, Sm–Nd, Pb–Pb and SHRIMP data: International Journal of Earth Sciences, v. 100, p. 631-657.

Drobe, M., M. G. López de Luchi, A. Steenken, R. Frei, R. Naumann, S. Siegesmund, and K. Wemmer, 2009, Provenance of the late Proterozoic to early Cambrian metaclastic sediments of the Sierra de San Luis (Eastern Sierras Pampeanas) and Cordillera Oriental, Argentina: Journal of South American Earth Sciences, v. 28, p. 239-262.

Ducea, M. N., G. W. Bergantz, J. L. Crowley, and J. Otamendi, 2017, Ultrafast magmatic buildup and diversification to produce continental crust during subduction: Geology, v. 45, p. 235-238.

Ducea, M. N., J. E. Otamendi, G. Bergantz, K. M. Stair, V. A. Valencia, and G. E. Gehrels, 2010, Timing constraints on building an intermediate plutonic arc crustal section: U- Pb zircon geochronology of the Sierra Valle Fértil-La Huerta, Famatinian arc, Argentina: Tectonics, v. 29, p. n/a-n/a.

Einhorn, J. C., G. E. Gehrels, A. Vernon, and P. G. DeCelles, 2015, U-Pb zircon geochronology of Neoproterozoic-Paleozoic sandstones and Paleozoic plutonic rocks in the Central Andes (21°S-26°S), *in* M. N. Ducea, M. N. Ducea, P. G. DeCelles, P. A. Kapp, and B. Carrapa, eds., Memoir of the Geological Society of America, Geological Society of America, p. 115-124.

Escayola, M. P., C. R. van Staal, and W. J. Davis, 2011, The age and tectonic setting of the Puncoviscana Formation in northwestern Argentina: An accretionary complex related to Early Cambrian closure of the Puncoviscana Ocean and accretion of the Arequipa-Antofalla block: Journal of South American Earth Sciences, v. 32, p. 438-459.

Fergusson, C. L., and R. A. Henderson, 2015, Early Palaeozoic continental growth in the Tasmanides of northeast Gondwana and its implications for Rodinia assembly and rifting: Gondwana Research, v. 28, p. 933-953.

Finch, M. A., R. F. Weinberg, M. G. Fuentes, P. Hasalová, and R. Becchio, 2015, One kilometre-thick ultramylonite, Sierra de Quilmes, Sierras Pampeanas, NW Argentina: Journal of Structural Geology, v. 72, p. 33-54.

Finch, M. A., R. F. Weinberg, P. Hasalová, R. Becchio, M. G. Fuentes, and A. Kennedy, 2017, Tectono-metamorphic evolution of a convergent back-arc: The Famatinian orogen, Sierra de Quilmes, Sierras Pampeanas, NW Argentina: Bulletin of the Geological Society of America, v. 129, p. 1602–1621.

Foster, D. A., D. R. Gray, C. Spaggiari, G. Kamenov, and F. P. Bierlein, 2009, Palaeozoic Lachlan orogen, Australia; accretion and construction of continental crust in a marginal ocean setting: Isotopic evidence from Cambrian metavolcanic rocks, Geological Society Special Publication, p. 329-349.

Franke, W., 2014, Topography of the Variscan orogen in Europe: Failed-not collapsed: International Journal of Earth Sciences, v. 103, p. 1471-1499.

Franz, G., F. Lucassen, W. Kramer, R. Trumbull, R. L. Romer, H.-G. Wilke, J. Viramonte, R. Becchio, and W. Siebel, 2006, Crustal Evolution at the Central Andean Continental Margin: a Geochemical Record of Crustal Growth, Recycling and Destruction, v. 1, p. 45-64.

González Bonorio, F., 1950, Algunos problemas geológicos de las Sierras Pampeanas: Revista de la Asociacion Geologica Argentina, v. 3, p. 81-110.

Goodge, J., C. Fanning, D. M. Brecke, K. Licht, and E. F. Palmer, 2010, Continuation of the Laurentian Grenville Province across the Ross Sea Margin of East Antarctica, v. 118, 601-619 p.

Gray, D. R., D. A. Foster, R. Maas, C. V. Spaggiari, R. T. Gregory, B. Goscombe, and K. H. Hoffmann, 2007, Continental growth and recycling by accretion of deformed turbidite fans and remnant ocean basins: Examples from Neoproterozoic and Phanerozoic orogens, Memoir of the Geological Society of America, p. 63-92.

Grosse, P., L. I. Bellos, C. R. de los Hoyos, M. A. Larrovere, J. N. Rossi, and A. J. Toselli, 2011, Across-arc variation of the Famatinian magmatic arc (NW Argentina) exemplified by I-, S- and transitional I/S-type Early Ordovician granitoids of the Sierra de Velasco: Journal of South American Earth Sciences, v. 32, p. 110-126.

Grosse, P., F. Söllner, M. A. Báez, A. Toselli, J. N. Rossi, and J. D. de la Rosa, 2008, Lower Carboniferous post-orogenic granites in central-eastern Sierra de Velasco, Sierras Pampeanas, Argentina: U–Pb monazite geochronology, geochemistry and Sr–Nd isotopes, v. 98, 1001-1025 p.

Hajná, J., J. Žák, V. Kachlík, and M. Chadima, 2012, Deciphering the Variscan tectonothermal overprint and deformation partitioning in the Cadomian basement of the Teplá-Barrandian unit, Bohemian Massif: International Journal of Earth Sciences, v. 101, p. 1855-1873.
Hauser, N., M. Matteini, R. H. Omarini, and M. M. Pimentel, 2011, Combined U–Pb and Lu–Hf isotope data on turbidites of the Paleozoic basement of NW Argentina and petrology of associated igneous rocks: Implications for the tectonic evolution of western Gondwana between 560 and 460Ma: Gondwana Research, v. 19, p. 100-127.
Heuret, A., F. Funiciello, C. Faccenna, and S. Lallemand, 2007, Plate kinematics, slab shape and back-arc stress: A comparison between laboratory models and current subduction zones: Earth and Planetary Science Letters, v. 256, p. 473-483.
Heuret, A., and S. Lallemand, 2005, Plate motions, slab dynamics and back-arc deformation: Physics of the Earth and Planetary Interiors, v. 149, p. 31-51.
Höckenreiner, M., F. Söllner, and H. Miller, 2003, Dating the TIPA shear zone: An Early Devonian terrane boundary between the Famatinian and Pampean systems (NW Argentina): Journal of South American Earth Sciences, v. 16, p. 45-66.
Horstwood, M. S. A., J. Košler, G. Gehrels, S. E. Jackson, N. M. McLean, C. Paton, N. J. Pearson, K. Sircombe, P. Sylvester, P. Vermeesch, J. F. Bowring, D. J. Condon, and B. Schoene, 2016, Community-Derived Standards for LA-ICP-MS U-(Th-)Pb Geochronology – Uncertainty Propagation, Age Interpretation and Data Reporting: Geostandards and Geoanalytical Research, v. 40, p. 311-332.
Hyndman, R. D., C. A. Currie, and S. P. Mazzotti, 2005, Subduction zone backarcs, mobile belts, and orogenic heat: GSA Today, v. 15, p. 4-10.
Iannizzotto, N. F., C. W. Rapela, E. G. A. Baldo, C. Galindo, C. M. Fanning, and R. J. Pankhurst, 2013, The Sierra Norte-Ambargasta batholith: Late Ediacaran–Early Cambrian magmatism associated with Pampean transpressional tectonics: Journal of South American Earth Sciences, v. 42, p. 127-143.
J Zeballo, F., and G. Albanesi, 2009, Conodontes cámbricos y Jujuyaspis keideli Kobayashi (Trilobita) en el Miembro Alfarcito de la Formación Santa Rosita, quebrada de Humahuaca, Cordillera Oriental de Jujuy, v. 46, 537-556 p.
Jacobs, J., 2009, A review of two decades (1986 – 2008) of geochronological work in Heimefrontfjella, and geotectonic Interpretation of western Dronning Maud Land, East Antarctica, v. 79, 47-57 p.
Jamieson, R. A., and C. Beaumont, 2013, On the origin of orogens: Bulletin of the Geological Society of America, v. 125, p. 1671-1702.
Jamieson, R. A., C. Beaumont, M. H. Nguyen, and N. G. Culshaw, 2007, Synconvergent ductile flow in variable-strength continental crust: Numerical models with application to the western Grenville orogen: Tectonics, v. 26.
Jamieson, R. A., C. Beaumont, C. J. Warren, and M. H. Nguyen, 2010, The Grenville Orogen explained? Applications and limitations of integrating numerical models with geological and geophysical data: Canadian Journal of Earth Sciences, v. 47, p. 517-539.
JeŽek, P., A. P. Willner, F. G. AceÑolaza, and H. Miller, 1985, The Puncoviscana trough — a large basin of Late Precambrian to Early Cambrian age on the pacific edge of the Brazilian shield: Geologische Rundschau, v. 74, p. 573-584.
Keppie, J. D., and H. Bahlburg, 1999, Puncoviscana Formation of northwestern and central Argentina: Passive margin or foreland basin deposit?, Special Paper of the Geological Society of America, p. 139-143.
Larrovere, M. A., P. H. Alasino, and E. G. Baldo, 2016, The double-vergent ductile shear zone of northwestern sierra de Velasco: Deformation of the middle crust during the Famatinian orogeny: Revista de la Asociacion Geologica Argentina, v. 73, p. 117-133.

Larrovere, M. A., A. Toselli, and J. N. Rossi De Toselli, 2008, Petrology and structure of La Chilca Shear Zone, Catamarca, v. 63, 254-263 p.

Lira, R., E. M. Ripley, and I. A. Españón, 1996, Meteoric water induced selvage-style greisen alteration in the Achala Batholith, central Argentina: Chemical Geology, v. 133, p. 261-277.

Lister, G., and M. Forster, 2009, Tectonic mode switches and the nature of orogenesis: Lithos, v. 113, p. 274-291.

López, J., and A. Toselli, 1993, La faja milonítica Tipa: faldeo oriental del Sistema de Famatina, Argentina, v. 3, 39-42 p.

Lucassen, F., and R. Becchio, 2003, Timing of high-grade metamorphism: Early Palaeozoic U-Pb formation ages of titanite indicate long-standing high-T conditions at the western margin of Gondwana (Argentina, 26-29°S): Journal of Metamorphic Geology, v. 21, p. 649-662.

Lucassen, F., R. Becchio, and G. Franz, 2011, The early Palaeozoic high-grade metamorphism at the active continental margin of West Gondwana in the Andes (NW Argentina/N Chile): International Journal of Earth Sciences, v. 100, p. 445-463.

Lucassen, F., and G. Franz, 2005, The early Palaeozoic Orogen in the Central Andes: a non-collisional orogen comparable to the Cenozoic high plateau?: Geological Society, London, Special Publications, v. 246, p. 257-273.

Martino, R. D., 2003, Ductile deformation shear belts at Pampean Ranges near Córdoba, Central Argentina: A review: Revista de la Asociacion Geologica Argentina, v. 58, p. 549-571.

Miller, H., C. Adams, F. G. Aceñolaza, and A. J. Toselli, 2011, Evolution of exhumation and erosion in western West Gondwanaland as recorded by detrital zircons of late Neoproterozoic and Cambrian sedimentary rocks of NW and Central Argentina: International Journal of Earth Sciences, v. 100, p. 619-629.

Moya, M., 2015, La Fase Ocloyica (Ordovicico Superior) en el noroeste argentino. Interpretacion historica y evidencias en contrario: Serie Correlacion Geologica, v. 3, p. 73-110.

Mulcahy, S. R., S. M. Roeske, W. C. McClelland, J. R. Ellis, F. Jourdan, P. R. Renne, J. D. Vervoort, and G. I. Vujovich, 2014, Multiple migmatite events and cooling from granulite facies metamorphism within the Famatina arc margin of northwest Argentina: Tectonics, v. 33, p. 1-25.

Mulcahy, S. R., S. M. Roeske, W. C. McClelland, S. Nomade, and P. R. Renne, 2007, Cambrian initiation of the Las Pirquitas thrust of the western Sierras Pampeanas, Argentina: Implications for the tectonic evolution of the proto-Andean margin of South America: Geology, v. 35, p. 443.

Murra, J. A., C. Casquet, F. Locati, C. Galindo, E. G. Baldo, R. J. Pankhurst, and C. W. Rapela, 2016, Isotope (Sr, C) and U–Pb SHRIMP zircon geochronology of marble-bearing sedimentary series in the Eastern Sierras Pampeanas, Argentina. Constraining the SW Gondwana margin in Ediacaran to early Cambrian times: Precambrian Research, v. 281, p. 602-617.

Omarini, R. H., R. J. Sureda, H. J. Götze, A. Seilacher, and F. Pflüger, 1999, Puncoviscana folded belt in northwestern Argentina: Testimony of Late Proterozoic Rodinia fragmentation and pre-Gondwana collisional episodes: International Journal of Earth Sciences, v. 88, p. 76-97.

Ortiz, A., N. Hauser, R. Becchio, N. Suzaño, A. Nieves, A. Sola, M. Pimentel, and W. Reimold, 2017, Zircon U-Pb ages and Hf isotopes for the Diablillos Intrusive Complex, Southern Puna, Argentina: Crustal evolution of the Lower Paleozoic Orogen, Southwestern Gondwana margin: Journal of South American Earth Sciences, v. 80, p. 316-339.

Ortiz, A., N. Suzaño, N. Hauser, R. Becchio, and A. Nieves, 2019, New hints on the evolution of the Eastern Magmatic Belt, Puna Argentina. SW Gondwana margin: Zircon U-Pb ages and Hf isotopes in the Pachamama Igneous-Metamorphic Complex: Journal of South American Earth Sciences, v. 94, p. 102246.

Otamendi, J., A. Patiño Douce, and A. Demichelis, 2001, Amphibolite to granulite transition in aluminous greywackes from the Sierra de Comechingones, C??rdoba, Argentina, v. 17, 415-434 p.
Otamendi, J. E., P. A. Castellarini, M. R. Fagiano, A. H. Demichelis, and A. M. Tibaldi, 2004, Cambrian to Devonian Geologic Evolution of the Sierra de Comechingones, Eastern Sierras Pampeanas, Argentina: Evidence for the Development and Exhumation of Continental Crust on the Proto-Pacific Margin of Gondwana: Gondwana Research, v. 7, p. 1143-1155.
Otamendi, J. E., M. N. Ducea, and G. W. Bergantz, 2012, Geological, Petrological and Geochemical Evidence for Progressive Construction of an Arc Crustal Section, Sierra de Valle Fertil, Famatinian Arc, Argentina: Journal of Petrology, v. 53, p. 761-800.
Otamendi, J. E., M. N. Ducea, E. A. Cristofolini, A. M. Tibaldi, G. C. Camilletti, and G. W. Bergantz, 2017, U-Pb ages and Hf isotope compositions of zircons in plutonic rocks from the central Famatinian arc, Argentina: Journal of South American Earth Sciences, v. 76, p. 412-426.
Otamendi, J. E., M. N. Ducea, A. M. Tibaldi, G. W. Bergantz, J. D. de la Rosa, and G. I. Vujovich, 2009, Generation of Tonalitic and Dioritic Magmas by Coupled Partial Melting of Gabbroic and Metasedimentary Rocks within the Deep Crust of the Famatinian Magmatic Arc, Argentina: Journal of Petrology, v. 50, p. 841-873.
Pankhurst, R. J., and C. W. Rapela, 1998, The proto-Andean margin of Gondwana: an introduction: Geological Society, London, Special Publications, v. 142, p. 1-9.
Pankhurst, R. J., C. W. Rapela, and C. M. Fanning, 2000a, Age and origin of coeval TTG, I- and S-type granites in the Famatinian belt of NW Argentina, Special Paper of the Geological Society of America, p. 151-168.
Pankhurst, R. J., C. W. Rapela, and C. M. Fanning, 2000b, Age and origin of coeval TTG, I- and S-type granites in the Famatinian belt of NW Argentina, Special Paper of the Geological Society of America, p. 151-168.
Pankhurst, R. J., C. W. Rapela, J. Saavedra, E. Baldo, J. Dahlquist, I. Pascua, and C. M. Fanning, 1998, The Famatinian magmatic arc in the central Sierras Pampeanas: an Early to Mid-Ordovician continental arc on the Gondwana margin: Geological Society, London, Special Publications, v. 142, p. 343-367.
Pankhurst, R. J., and A. P. M. Vaughan, 2009, The tectonic context of the Early Palaeozoic southern margin of Gondwana, Geological Society Special Publication, p. 171-176.
Parsons, A. J., E. C. Ferré, R. D. Law, G. E. Lloyd, R. J. Phillips, and M. P. Searle, 2016, Orogen-parallel deformation of the Himalayan midcrust: Insights from structural and magnetic fabric analyses of the Greater Himalayan Sequence, Annapurna-Dhaulagiri Himalaya, central Nepal: Tectonics, v. 35, p. 2515-2537.
Pearson, D., P. Kapp, P. W. Reiners, G. E. Gehrels, M. N. Ducea, A. Pullen, J. E. Otamendi, and R. N. Alonso, 2012, Major Miocene exhumation by fault - propagation folding within a metamorphosed, early Paleozoic thrust belt: Northwestern Argentina: Tectonics, v. 31.
Peri, V. G., M. C. Pomposiello, A. Favetto, H. Barcelona, and E. A. Rossello, 2013, Magnetotelluric evidence of the tectonic boundary between the Río de La Plata Craton and the Pampean terrane (Chaco-Pampean Plain, Argentina): The extension of the Transbrasiliano Lineament: Tectonophysics, v. 608, p. 685-699.
Pinotti, L., J. E. Coniglio, A. M. Esparza, F. D'Eramo, and E. Llambías, 2002, Nearly circular plutons emplaced by stoping at shallow crustal levels, Cerro Aspero batholith, Sierras Pampeanas de C??rdoba, Argentina, v. 15, 251-265 p.
Pinotti, L., J. M. Tubía, F. D'Eramo, N. Vegas, A. M. Sato, J. Coniglio, and A. Aranguren, 2006, Structural interplay between plutons during the construction of a batholith (Cerro Aspero batholith, Sierras de Córdoba, Argentina): Journal of Structural Geology, v. 28, p. 834-849.

Posamentier, H. W., and R. G. Walker, 2006, Deep-Water Turbidites and Submarine Fans Facies Models Revisited, *in* H. W. Posamentier, and R. G. Walker, eds., v. 84, SEPM Society for Sedimentary Geology, p. 0.

Posamentier, H. W., R. G. Walker, and Sepm, 2014, Facies models revisited.

Quenardelle, S. M., and V. A. Ramos, 1999, Ordovician western Sierras Pampeanas magmatic belt: Record of Precordillera accretion in Argentina

Laurentia-Gondwana connections before Pangea, *in* V. A. Ramos, and J. D. Keppie, eds., v. 336, Geological Society of America, p. 0.

Ramos, V. A., 2004, Cuyania, an exotic block to Gondwana: Review of a historical success and the present problems: Gondwana Research, v. 7, p. 1009-1026.

Ramos, V. A., 2008, The basement of the Central Andes: The arequipa and related terranes, *in* R. Jeanloz, A. L. Albee, K. C. Burke, and K. H. Freeman, eds., Annual Review of Earth and Planetary Sciences, p. 289-324.

Ramos, V. A., R. D. Dallmeyer, and G. Vujovich, 1998, Time constraints on the Early Palaeozoic docking of the Precordillera, central Argentina, Geological Society Special Publication, p. 143-158.

Ramos, V. A., T. E. Jordan, R. W. Allmendinger, C. Mpodozis, S. M. Kay, J. M. Cortés, and M. Palma, 1986, Paleozoic terranes of the central Argentine-Chilean Andes: Tectonics, v. 5, p. 855-880.

Ramos, V. A., G. Vujovich, R. Martino, and J. Otamendi, 2010, Pampia: A large cratonic block missing in the Rodinia supercontinent: Journal of Geodynamics, v. 50, p. 243-255.

Rapela, C., E. Baldo, R. Pankhurst, and C. Fanning, 2008, The Devonian Achala Batholith of the Sierras Pampeanas: F-rich, aluminous A-type granites, v. 1.

Rapela, C. W., B. Coira, A. Toselli, and J. Saavedra, 1992, The lower paleozoic magmatism of southwestern gondwana and the evolution of the famatinian orogen: International Geology Review, v. 34, p. 1081-1142.

Rapela, C. W., R. J. Pankhurst, C. Casquet, E. Baldo, J. Saavedra, and C. Galindo, 1998a, Early evolution of the Proto-Andean margin of South America: Geology, v. 26, p. 707.

Rapela, C. W., R. J. Pankhurst, C. Casquet, E. Baldo, J. Saavedra, C. Galindo, and C. M. Fanning, 1998b, The Pampean Orogeny of the southern proto-Andes: Cambrian continental collision in the Sierras de Cordoba: Geological Society, London, Special Publications, v. 142, p. 181-217.

Rapela, C. W., R. J. Pankhurst, C. Casquet, C. M. Fanning, E. G. Baldo, J. M. González-Casado, C. Galindo, and J. Dahlquist, 2007, The Río de la Plata craton and the assembly of SW Gondwana: Earth-Science Reviews, v. 83, p. 49-82.

Rapela, C. W., R. J. Pankhurst, J. Saavedra, and C. Galindo, 1998c, Early evolution of the proto-andean margin of South America: Geology, v. 26, p. 707-710.

Rapela, C. W., S. O. Verdecchia, C. Casquet, R. J. Pankhurst, E. G. Baldo, C. Galindo, J. A. Murra, J. A. Dahlquist, and C. M. Fanning, 2015, Identifying Laurentian and SW Gondwana sources in the Neoproterozoic to Early Paleozoic metasedimentary rocks of the Sierras Pampeanas: Paleogeographic and tectonic implications: Gondwana Research.

Reading, H. G., 1996, Sedimentary environments : processes, facies, and stratigraphy: Cambridge, Mass.; Oxford, Blackwell Science.

Rubio Pascual, F. J., A. López-Carmona, and R. Arenas, 2016, Thickening vs. extension in the Variscan belt: P–T modelling in the Central Iberian autochthon: Tectonophysics, v. 681, p. 144-158.

Saavedra, J., A. Toselli, J. Rossi, E. Pellitero, and F. Durand, 1998, The Early Palaeozoic magmatic record of the Famatina System: a review: Geological Society, London, Special Publications, v. 142, p. 283-295.

Sato, A. M., H. Tickyj, E. J. Llambías, M. A. Stipp Basei, and P. D. González, 2004, Las Matras Block, Central Argentina (37°S-67°W): the Southernmost Cuyania Terrane and its Relationship with the Famatinian Orogeny: Gondwana Research, v. 7, p. 1077-1087.

Sawyer, E. W., 2008, Atlas of Migmatites, NRC Research Press and Mineralogical Association of Canada, 387 p.
Schoene, B., D. J. Condon, L. Morgan, and N. McLean, 2013, Precision and accuracy in geochronology: Elements, v. 9, p. 19-24.
Schwartz, J. J., and L. P. Gromet, 2004, Provenance of a late Proterozoic–early Cambrian basin, Sierras de Córdoba, Argentina: Precambrian Research, v. 129, p. 1-21.
Schwartz, J. J., L. P. Gromet, and R. Miró, 2008, Timing and duration of the calc-alkaline arc of the pampean orogeny: Implications for the late neoproterozoic to cambrian evolution of Western Gondwana: Journal of Geology, v. 116, p. 39-61.
Semenov, I., and R. F. Weinberg, 2017, A major mid-crustal decollement of the Paleozoic convergent margin of western Gondwana: The Guacha Corral shear zone, Argentina: Journal of Structural Geology, v. 103, p. 75-99.
Siegesmund, S., A. Steenken, R. D. Martino, K. Wemmer, M. G. López de Luchi, R. Frei, S. Presnyakov, and A. Guereschi, 2009, Time constraints on the tectonic evolution of the Eastern Sierras Pampeanas (Central Argentina): International Journal of Earth Sciences, v. 99, p. 1199-1226.
Simpson, C., R. D. Law, L. P. Gromet, R. Miro, and C. J. Northrup, 2003, Paleozoic deformation in the Sierras de Cordoba and Sierra de Las Minas, eastern Sierras Pampeanas, Argentina: Journal of South American Earth Sciences, v. 15, p. 749-764.
Sims, J. P., T. R. Ireland, A. Camacho, P. Lyons, P. E. Pieters, R. G. Skirrow, P. G. Stuart-Smith, and R. Miró, 1998a, U-Pb, Th-Pb and Ar-Ar geochronology from the southern Sierras Pampeanas, Argentina: implications for the Palaeozoic tectonic evolution of the western Gondwana margin, Geological Society Special Publication, p. 259-281.
Sims, J. P., T. R. Ireland, A. Camacho, P. Lyons, P. E. Pieters, R. G. Skirrow, P. G. Stuart-Smith, and R. Miró, 1998b, U-Pb, Th-Pb and Ar-Ar geochronology from the southern Sierras Pampeanas, Argentina: implications for the Palaeozoic tectonic evolution of the western Gondwana margin, Geological Society Special Publication, p. 259-281.
Sims, J. P., R. G. Skirrow, P. G. Stuart-Smith, and P. Lyons, 1997, Informe geologico y metalogenico de las Sierras de San Luis y Comechingones (provincias de San Luis y Cordoba). 1:250000: Anales XXVIII, Instituto de Geologia y Recursos Minerales, SEGEMAR.
Sola, A. M., R. A. Becchio, and M. M. Pimentel, 2013, Petrogenesis of migmatites and leucogranites from Sierra de Molinos, Salta, Northwest Argentina: A petrologic and geochemical study: Lithos, v. 177, p. 470-491.
Sola, A. M., P. Hasalová, R. F. Weinberg, N. O. Suzaño, R. A. Becchio, F. D. Hongn, and N. Botelho, 2017, Low-P melting of metapelitic rocks and the role of H2O: Insights from phase equilibria modelling: Journal of Metamorphic Geology, v. 35, p. 1131-1159.
Steenken, A., M. G. López de Luchi, C. M. Dopico, M. Drobe, K. Wemmer, and S. Siegesmund, 2011, The Neoproterozoic-early Paleozoic metamorphic and magmatic evolution of the Eastern Sierras Pampeanas: An overview: International Journal of Earth Sciences, v. 100, p. 465-488.
Steenken, A., S. Siegesmund, M. López de Luchi, R. Frei, and K. Wemmer, 2006, Neoproterozoic to Early Palaeozoic events in the Sierra de San Luis: Implications for the Famatinian geodynamics in the Eastern Sierras Pampeanas (Argentina), v. 163, 965-982 p.
Steven Davis, J., S. Roeske, W. C. McClelland, and L. W. Snee, 1999, Closing the ocean between the Precordillera terrane and Chilenia: Early Devonian ophiolite emplacement and deformation in the southwest Precordillera, v. 336, 115-138 p.
Struart-Smith, P., A. Camacho, J. P. Sims, R. Skirrow, P. Lyons, P. E. Pieters, L. P. Black, and R. Miró, 1999, Uranium-lead dating of felsic magmatic cycles in the southern Sierras Pampeanas, Argentina; Implications for the tectonic development of the proto-Andean Gondwana margin, v. Special Paper.

Suzaño, N., R. Becchio, A. Nieves, A. Sola, and A. Ortiz, 2015, Mezcla de magmas en el arco magmático Famatiniano del noroeste de Argentina: Ejemplo en el complejo intrusivo Diablillos, Puna Austral: Revista Mexicana de Ciencias Geologicas, v. 32, p. 433-454.
Suzaño, N., R. Becchio, A. Sola, A. Ortiz, A. Nieves, M. Quiroga, and G. Fuentes, 2017, The role of magma mixing in the evolution of the Early Paleozoic calc-alkaline granitoid suites. Eastern magmatic belt, Puna, NW Argentina: Journal of South American Earth Sciences, v. 76, p. 25-46.
Tibaldi, A. M., J. E. Otamendi, E. A. Cristofolini, I. Baliani, B. A. Walker Jr, and G. W. Bergantz, 2013, Reconstruction of the early ordovician famatinian arc through thermobarometry in lower and middle crustal exposures, sierra de valle fértil, argentina: Tectonophysics, v. 589, p. 151-166.
Tortello, M. F., and S. B. Esteban, 2016, Early Ordovician trilobites from the Iruya area (Cordillera Oriental, northwestern Argentina) and their stratigraphic significance: Journal of Paleontology, v. 90, p. 923-958.
Toselli, A., A. Sial, and J. N. Rossi, 2002, Ordovician magmatism of the Sierras Pampeanas, Sistema de Famatina and Cordillera Oriental, NW of Argentina, v. 16, 313-326 p.
Toselli, A. J., A. N. Sial, J. Saavedra, J. N. R. De Toselli, and V. P. Ferreira, 1996, Geochemistry and genesis of the S-type, cordierite-andalusite-bearing capillitas batholith, Argentina: International Geology Review, v. 38, p. 1040-1053.
Turner, J. C. M., 1960, Estratigrafía de la Sierra de Santa Victoria y adyacencias: Boletín de la Academia Nacional de Ciencias, p. 163–196.
Turner, J. C. M., 1975, Geología del sector oriental de los Departamentos de Santa Victoria e Iruya, Provincia de Salta. República Argentina: Boletín de la Academia Nacional de Ciencias: Boletín de la Academia Nacional de Ciencias, v. 51, p. 11-24.
Von Gosen, W., and C. Prozzi, 1998, Structural evolution of the Sierra de San Luis (Eastern Sierras Pampeanas, Argentina): implications for the Proto-Andean Margin of Gondwana: Geological Society, London, Special Publications, v. 142, p. 235-258.
Weinberg, R. F., R. Becchio, P. Farias, N. Suzaño, and A. Sola, 2018, Early paleozoic accretionary orogenies in NW Argentina: Growth of West Gondwana: Earth-Science Reviews, v. 187, p. 219-247.
Whitmeyer, S. J., and C. Simpson, 2003, High strain-rate deformation fabrics characterize a kilometers-thick Paleozoic fault zone in the Eastern Sierras Pampeanas, central Argentina: Journal of Structural Geology, v. 25, p. 909-922.
Whitney, D. L., and B. W. Evans, 2010, Abbreviations for names of rock-forming minerals: American Mineralogist, v. 95, p. 185-187.
Wolfram, L. C., R. F. Weinberg, P. Hasalová, and R. Becchio, 2017, How melt segregation affects granite chemistry: Migmatites from the Sierra de Quilmes, NW Argentina: Journal of Petrology, v. 58, p. 2339-2364.
Wolfram, L. C., R. F. Weinberg, O. Nebel, K. Hamza, P. Hasalová, J. Míková, and R. Becchio, 2019, A 60-Myr record of continental back-arc differentiation through cyclic melting: Nature Geoscience, v. 12, p. 215-219.
Zimmermann, U., 2005a, Provenance studies of very low- to low-grade metasedimentary rocks of the Puncoviscana complex, northwest Argentina, Geological Society Special Publication, p. 381-416.
Zimmermann, U., 2005b, Provenance studies of very low- to low-grade metasedimentary rocks of the Puncoviscana complex, northwest Argentina, Geological Society Special Publication, p. 381-416.

Zimmermann, U., and H. Bahlburg, 2003, Provenance analysis and tectonic setting of the Ordovician clastic deposits in the southern Puna Basin, NW Argentina: Sedimentology, v. 50, p. 1079-1104.

Zimmermann, U., H. Bahlburg, K. Mezger, J. Berndt, and S. M. Kay, 2014, Origin and age of ultramafic rocks and gabbros in the southern Puna of Argentina: an alleged Ordovician suture revisited: International Journal of Earth Sciences, v. 103, p. 1023-1036.

Chapter 2

Orogen parallel stretching of a HT–LP back–arc terrane: insights from the Ordovician Famatinian orogeny, NW Argentina

Abstract

Most orogenies are characterised by shortening perpendicular to the orogenic front. Here, we describe a mid–crustal section of the accretionary c. 470 Ma Famatinian orogeny that evolves from plane strain to constriction, with a non–coaxial component associated with stretching parallel to the orogen. This section of the crust, currently exposed in the Sierra de Quilmes, represents the thermally–weakened back–arc that evolves to foreland during a shortening phase of the orogenic cycle as a result of the accretion of the Laurentian–derived Precordillera terrane to the western margin of Gondwana.

In this area, three metamorphic complexes were juxtaposed by thrusting on remarkably thick shear zones. Two of them, the Tolombon and Tolombon West complex, are structurally part of the hanging wall and dominated by migmatites with Al–rich turbidite protoliths. The third complex, the Agua del Sapo complex is part of the footwall and composed mostly of Al–poor, Ca–rich turbidites, now schists, gneisses, and migmatites. All three complexes record a high–T/low–P (HT–LP) metamorphic history.

Although the east–west shortening of the orogen was continuous and unidirectional, the style/mode of deformation of the footwall was different from the hanging wall, developing and recording a significantly different late phase of high–T deformation. We argue that the east–west convergence was resolved first as thrusting with overall top–to–west kinematics and tectonic transport towards the orogenic front and plane strain associated with crustal thickening and regional W–verging folding. After reaching a critical point when the thrusting to the west was impeded and the rock mass started to fold, the vertical gravitational and horizontal tectonic forces became balanced, and the thermally–weakened footwall complex reacted by shearing under a non–coaxial constrictional regime, assisting the escape to the south, parallel to the orogen, of the hanging wall complexes. This

later event is characterised by syn–folding shearing with consistent top–to–south kinematics that resulted in an intense stretching lineation, large L–tectonite domains, and sheath folding subparallel to the transport direction. In other words, the east–west shortening resolved first as thickening was counterbalanced by an element of orogen–parallel extension. This work describes a case in which crustal thickening of hot rock masses reached equilibrium and where continued shortening forced lateral escape parallel to the length of the orogen under constriction.

1 Introduction

Orogens grow by accretion and burial of rock masses. During orogenesis, rocks move through evolving thermal and structural fields within the orogen (Jamieson and Beaumont, 2013). In particular, in subduction–related, accretionary orogens, the mid–crustal levels of the continental back–arc are characterised by long–lasting high temperature, and low pressure (HT–LP) metamorphism spread along broad zones due to the thinner lithosphere interacting with the asthenosphere (Hyndman et al., 2005). These HT–LP systems are associated with large zones of partial melting that creates heterogeneities and represent weaker parts of the crust (Ellis et al., 1998). Although extensional back–arcs are associated with a higher thermal influx, most of the current back–arcs are under shortening, and also have high geothermal gradients (Curie and Hyndman, 2006; Hyndman et al., 2005). Regardless of the tectonic mode (extension versus shortening (Lister and Forster, 2009), temperature plays a vital role in crustal rheology, making the back–arc potentially an extremely sensitive record of different deformational phases focusing a significant part of the deformation associated with subduction or terrane collision in an active margin (Collins, 2002; Curie and Hyndman, 2006; Heuret and Lallemand, 2005; Hyndman et al., 2005; Jamieson and Beaumont, 2013; Lister and Forster, 2009; Thompson et al., 2001).

Most accretionary orogenies are dominated by shortening perpendicular to the orogeny with a defined tectonic transport direction governed by an essentially 2D deformation (Burg and Ford, 1997; Dewey, 2002; Jamieson and Beaumont, 2013). However because of factors like heterogeneous lithology, rheology, boundary conditions and stress orientation, the bulk strain can be partitioned into different domains (i.e. simple / pure shear, or oblate / prolate strain) at different scales (Carreras et al., 2013; Jones and Tanner, 1995; Passchier and Trouw, 2005; Tikoff and Teyssier, 1994). Examples of strain partitioning within accretionary orogens include: the Archean Dharwar craton south of India, where (Bouhallier et al., 1995; Chardon et al., 1996; Chardon et al., 2011) found that domains of pure shear developed as the result of the interplay of horizontal regional shortening with diapiric forces. Hajná (2012) and (Rubio Pascual et al., 2016) mapped the ancient collisional Variscan orogen and described cases where pure shear domains are separated by domains of simple shear, that in combination accommodated the orogen–perpendicular shortening. (Braathen et al., 2000; Fletcher and Bartley, 1994; Malavieille, 1993; Sullivan, 2009; Sullivan and Law, 2007) documented major thrusts exposed in the North American Cordillera and Norwegian Caledonides where the strain was partitioned as simple shear coupled with constrictional, pure shear domains in the footwall rocks of major trusts. Furthermore, strain partitioning is not exclusive of compressional regimes. A good example of that is Mancktelow (1994) who studied fold–shear zones relationships in low–angle detachment systems of the Simplon region of the Alps and Death Valley regions and concluded that these high strain zones developed large constrictional domains parallel to the extensional direction, similar to the case of strain partitioning in the extensional metamorphic domes in the Aegean Sea (Jolivet et al., 2004). In terms of tectonic transport direction, large volumes of ductile rock can flow in directions that deviate from the direction perpendicular to the orogen. For example Chardon (2009) reviewed several Precambrian accretionary orogens such as the Birimian of West Africa, the Svecofennian of Finland and Sweden, the Trans–Hudson orogen of Canada, the Yavapai of SW United States, and the Arabo–Nubian shield (Condie, 2007; Windley, 1992). In all these cases, the lateral flow of discrete zones within wide high–temperature, low–pressure metamorphic belts is the response to tectonic shortening. They suggested that this may be analogous to what happens in current, wide hot orogens, like the Cordilleran or Tibetan belts. For the latter Chardon (2008; Chardon et al., 2011; Parsons et al., 2016) used numerical modelling of the mid–crustal levels which led to several scenarios of orogen–parallel lateral flow.

Cases of orogen–scale lateral flow are sometimes accompanied by a change in the strain regime. Cruden (2006) and Bajolet (2015) by means of analogue and numerical modelling, and Handy (2005) by structural mapping, found that weaker zones within accretionary, hot and wide orogens can develop different strain regimes in response to the heterogeneous rheological architecture and the interplay of tectonic and gravitational forces. In cases, the decoupling of the weaker orogenic lithosphere with respect to converging stronger block(s) resulted in the stretching and lateral escape, parallel to the orogen of the lower weaker section. In all cases, it is postulated that the orogenic crustal thickening is partially inhibited by the lateral redistribution of ductile rock masses from the deeper sections of the crust.

In the examples above based on field evidence, they tend to focus on some of the specific aspects of the structural architecture of orogens (i.e., strain regime or tectonic transport). So far, only analogue and numerical modelling of orogens have been able to link all aspects and show the bigger picture. Here, we report on the exhumed Ordovician Famatinian orogen in the Sierra de Quilmes, NW Argentina. In this region, we document the ductile lateral escape of the footwall at mid–crustal conditions following a large–scale thrust. The process was likely a response to topography build–up and led to a homogenization of crustal thickness along the length of the orogen. The findings illustrate how a crustal–scale, arc–verging thrust thickened the crust to its limit, after which continued orogeny–perpendicular shortening caused folding of the thrust system and an orogen–parallel, south–directed flow of the footwall under intense constriction. This paper starts with a description of the regional geology, including the tectonic framework of the Famatinian Orogeny. This is followed by a description of the results of the geological and structural mapping of the Sierras de Quilmes, followed by interpretation of the results and discussion where a model for the evolution of the deformation is proposed.

2 Regional Geology

2.1 Sierras Pampeanas and Paleozoic orogenies of NW Argentina

The Sierra de Quilmes, our primary focus here, is part of a larger geological province called Sierras Pampeanas (Fig 1), which comprise a number of north–south trending mountain ranges located between 24° and 34°S and 64° and 68°W in the current Andean foreland of west Argentina (Büttner et al., 2005). These mountains are interpreted to have been part of an accretionary margin developed along West Gondwana during Paleozoic times, as part of the Terra Australis Orogen (Cawood, 2005; Schwartz et al., 2008). Due to the current flat–slab subduction of the Andean orogen, the Sierras Pampeanas were uplifted exposing different crustal levels along the current foreland of the Andes (Büttner et al., 2005; Pankhurst and Rapela, 1998; Rapela et al., 1998a; Rapela et al., 2015). In general, deeper sections of the crust are better exposed in the south of Sierras Pampeanas and shallower levels in the north (Büttner, 2005; Rapela et al., 1998), where the Sierra de Quilmes is located.

The Sierras Pampeanas are composed almost exclusively of Paleozoic meta–sedimentary and igneous rocks shaped and formed during the Pampean (c. 540–520 Ma), Famatinian (c. 490–440 Ma) and Achalian (c. 410–350 Ma) orogenies. The history of these orogenies was controlled by subduction–accretion episodes into the western margin of Gondwana (Astini, 1998; Escayola et al., 2011; Omarini et al., 1999; Ramos, 2004; Ramos, 2008; Ramos et al., 1998; Ramos et al., 2000;

Ramos et al., 1986; Ramos et al., 2010; Rapela et al., 1998a; Rapela et al., 1998b; Rapela et al., 2015; Vaughan and Pankhurst, 2008). The Sierras Pampeanas are divided into the Western and Eastern Sierras Pampeanas, based on the provenance of the basement rocks. The Western Sierras Pampeanas are dominated by a wide range of metasedimentary rocks and meta–basic and ultrabasic domains with isotopic compositions and age distribution of Laurentian affinity (Casquet et al., 2012; Dalla Salda et al., 1998; Rapela et al., 2015). It is a composite of two major blocks (Fig. 1). The MARA block to the east (Rapela et al., 2015) representing high–grade crystalline rocks and to the west, the Precordillera block, that represents a Paleozoic carbonate platform (Astini et al., 1995; Ramos, 2004). Both represent Laurentian blocks that rifted, drifted and were accreted to the margin of Gondwana where they caused the end of the Pampean and Famatinian subduction systems, respectively (Weinberg et al., 2018). These exotic terranes contrast to the autochthonous Eastern Sierras Pampeanas. This terrane is associated with a suite of deformed metamorphic rocks derived from the turbidites of the Puncoviscana Formation, which are intruded by an extensive suite of Paleozoic igneous rocks. The Puncoviscana Formation turbidites were deposited on the Western Gondwana margin and sourced from the Natal–Namaqua belt and/or the Dom Feliciano belt of Brazil and Uruguay (Rapela et al., 2015) between c. 670 and 520 Ma (Adams et al., 2011; Rapela et al., 1998b), just before the onset of the Cambrian Pampean orogeny. Hence, the Eastern Sierras Pampeanas record events that affected the Paleo–Pacific margin of Gondwana during the Cambrian Pampean orogeny, and later overprinted by the metamorphism and arc magmatism of the younger Famatinian and Achalian orogenies. The Sierra de Quilmes, our subject of study, is part of the Eastern Sierras Pampeanas and it records different aspects of the three orogenies, of which the Famatinian is the most intense of all (Büttner et al., 2005; Finch et al., 2015; Finch et al., 2017; Lucassen et al., 2000; Wolfram et al., 2017; Wolfram et al., 2019).

2.1.1 Famatinian orogeny

The Famatinian orogenic cycle is an Ordovician subduction–related Andean–type continental orogeny. The Famatinian magmatic arc and continental back–arc (Figure 1a) developed in the fore–arc of the previous Cambrian Pampean orogeny, and induced extensive areas of high-grade metamorphism and magmatism between c. 500 Ma to c. 440 Ma, with a climax at c. 470 Ma (Bahlburg et al., 2016; Ducea et al., 2017; Lucassen et al., 2000; Wolfram et al., 2017; Wolfram et al., 2019). A metaluminous I–type magmatic arc developed along the western edge of the Eastern Sierras Pampeanas and paired with a peraluminous S–type magmatic belt immediately to the east, associated with the anatexis and reworking of the metasedimentary rocks in the mid–crustal sections of the back–arc (Büttner et al., 2005; Pankhurst and Rapela, 1998; Pankhurst et al., 2000; Pankhurst et al., 1998; Rapela et al., 1992).

The Famatinian orogeny eventually finished as a result of the docking of the exotic Precordillera terrane, with Laurentian affinities, into the western margin of Gondwana at c. 450–440 Ma. The docking process may have caused a change from regional extension and back–arc sedimentation to shortening and mountain building that characterised the Oclóyic tectonic phase, (Turner, 1975), hence the Famatinian back–arc switches to a foreland after the accretion (Bahlburg and Breitkreuz, 1991). This event lead to shortening across the Famatinian foreland up to c. 440 Ma (Aceñolaza et al., 2002; Astini, 1998; Astini et al., 1995; Thomas and Astini, 2003) when crustal anatexis ended (Bahlburg and Berndt, 2016; Büttner et al., 2005; Mulcahy et al., 2014; Wolfram et al., 2017). This phase is characterised by several km–wide west–verging shear zones, such as the Pichao Shear Zone in the Sierra de Quilmes (Finch et al., 2015), La Chilca shear zone (Larrovere et al., 2016; Larrovere et al., 2011), the TIPA shear zone (Höckenreiner et al., 2003), or the Guacha Corral shear zone (Martino, 2003; Semenov and Weinberg, 2017), among others (Piñán-Llamas and Simpson, 2006; Simpson et al., 2001; Wegmann et al., 2008; Weinberg et al., 2018) (Fig. 1b) that accommodated the east–west convergence, stacking high–grade rocks over lower–grade rocks. Rocks of the Famatinian belt were finally exhumed at upper crustal levels in the Carboniferous–Permian limit (De Los Hoyos et al., 2011).

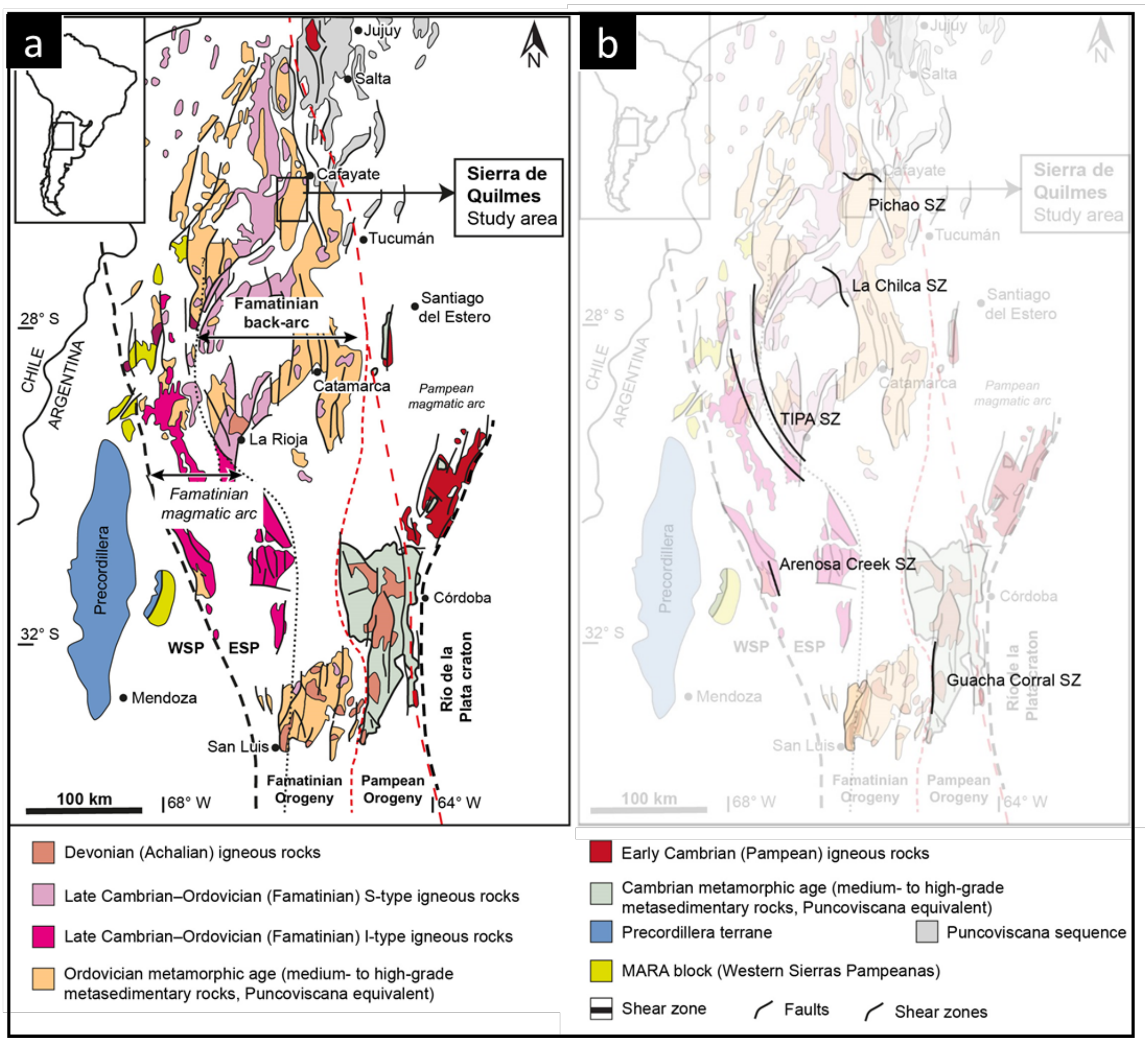

Figure 1– (a) Regional map of Sierras Pampeanas and (b) Famatinian shear zones mentioned in the text.

2.2 Geology of the Sierra de Quilmes

In the Famatinian orogeny context, the Sierra de Quilmes represents the mid–crustal section of what was an extensional back–arc at the start of the orogeny from c. 500 to 470 Ma, to the east of the main Famatinian arc. The back–arc evolved to a compressional foreland terrane during the Oclóyic stage of the orogenic cycle from c. 470 to 440 Ma (Weinberg et al., 2018). The Sierra de Quilmes (Fig. 2) is a 130 by 30 km, north–south trending range which encompasses a composite of polydeformed metasedimentary and igneous rocks. Furthermore, the protolith of all rocks in the area is interpreted to be the Neoproterozoic to Cambrian turbidite sequence of the Puncoviscana Formation (Adams et al., 2011; Rapela, 1976; Toselli et al., 1978). The metamorphism of the Sierra de Quilmes represents a regional high–T/low–P (HT–LP) sequence that reached granulite facies and underwent melting forming vast migmatites and some granite intrusions (Büttner et al., 2005; Finch et al., 2015; Finch et al., 2016). Several workers have studied the northern sectors of the Sierra de Quilmes (Büttner, 2009; Büttner et al., 2005; Finch et al., 2015; Finch et al., 2016; Rossi and Toselli, 1976; Toselli et al., 1978; Wolfram et al., 2017), leaving the southern part of the ranges relatively unexplored.

The geology of the Sierra de Quilmes is defined by a collage of large metamorphic complexes composed of metasedimentary rocks, intruded by large peraluminous plutons and separated by ductile shear zones (Fig. 2). Toselli (1978) and Rapela (1976) first defined the Tolombon and the Agua del Sapo complexes and noticed that they record different metamorphic conditions and that they are separated by a thick shear zone.

2.2.1 Tolombon complex

The Tolombon complex is defined by a metasedimentary package comprising typical Al–rich siliciclastic rocks derived from turbidites. The package is intruded by peraluminous granitic rocks and different generations of pegmatites (Büttner et al., 2005; Finch et al., 2015; Toselli et al., 1978).

Wolfram submitted (2017) divided the Tolombon complex in two based on the volume and nature of diatexites. The Ovejeria complex to the east and the Tolombon complex proper to the west. For the sake of simplicity and due to their geological similarities, we merge the Ovejeria and Tolombon complexes, into a single block named Tolombon complex.

The metamorphic facies in this complex increases over short distances from the chlorite zone at low greenschist facies in the northeast corner, grading to the biotite–muscovite zone, then into the garnet–cordierite–sillimanite zone, and lastly into the orthopyroxene zone under granulite facies in the south–west, immediately above the complex–bounding shear zone. The isograds run parallel to the dominant metamorphic foliation (Büttner et al., 2005; Finch et al., 2015). The mineral paragenesis across all facies is associated to high–temperature and low–pressure (HT–LP) conditions that in the high grades lead to extensive partial melting, with peak metamorphic conditions estimated in <6 kbar and 800 °C (Büttner et al., 2005; Finch et al., 2017). Migmatites range from metatexite to diatexite, and they are the source of the large leucogranitic plutons found in the area (Toselli et al., 1978). The HT–LP anatectic conditions of the Tolombon complex lasted for a notably long period of c. 70 Ma, between c. 510 and c. 440 Ma, indicated by zircon and monazite geochronology (U/Pb LA–ICPMS) of migmatites (Wolfram et al., 2019).

The main foliation in the complex strikes NW–SE and dips moderately northeast, parallel to the bedding and the metamorphic isograds. In the migmatitic zone towards the shear zone, this foliation defines the axial planar foliation of asymmetric isoclinal west–verging folds (F1) with fold axes trending roughly north–south. Many of these F1 folds are intruded by leucosomes along the axial plane, indicative of syn–anatectic folding (Finch et al., 2017). Also, the tightening of F1 folds and shearing strain increases towards the contact with the Agua del Sapo complex giving place to the Pichao shear zone separating the two metamorphic complexes.

2.2.2 Pichao shear zone and Agua del Sapo complex

Finch (2015) detailed the nature of the tectonic contact between the Tolombon and the Agua del Sapo complexes, defining the Pichao shear zone (PSZ). This shear zone is a 3km–wide high strain zone that runs parallel to the main foliation (Fig. 2). The strain intensity increases towards the footwall reaching ultramylonites of up to 1 km thick (Fig. 2). Finch (2015) and Finch (2016) report that the Pichao shear zone is characterised by: (i) microstructural features, and mineral paragenesis that constrain the bulk of the deformation to the temperature range between 500–700 °C; (ii) pervasive top–to–west kinematics suggesting the thrusting of the Tolombon complex (hanging wall) over the Agua del Sapo complex (footwall). The main trend, in the west, undulates, and occasionally strikes nearly E–W, moderately dipping to the north, when it becomes a sinistral shear zone, still accommodating the westward motion of the hanging wall; and (iii) mineralogy of porphyroclasts and geochemical signature of ultramylonite that indicate that the protolith of the shear zone is the diatexite migmatite of the Tolombon complex. They also inferred that the unusual thickness of the ultramylonite is due to the outward migration of intracrystalline water in the high–strain zone that facilitated deformation in its margins while hardening the ultramylonite itself (Finch et al., 2016). The U–Pb dating of monazite in syn–kinematic leucosomes indicates that shearing within the Tolombon complex lasted for a notably long period of c. 40 Ma, with at least two episodes of monazite growth, the first between 497–482 Ma and a later one between 472–461 Ma (Finch et al., 2017). The longevity of the shearing might be also due to elevated radiogenic heat production that kept the complexes thermo-tectonically active (Alessio et al., 2018; Wolfram et al., 2017).

The footwall of the Pichao shear zone is the Agua del Sapo complex, first defined by Toselli (1978). They noticed that unlike the granulite facies of the hanging wall, the immediate footwall of the shear zone is composed by amphibolite facies rocks. Piñán-Llamas (2009) investigated the structural makeup of these turbidite–derived metamorphic rocks suggesting that they were only deformed during the Cambrian Pampean orogeny, and Acosta Nagle (2014) reported a small pluton of Achalian age in the southern tip of the ranges. Despite these preliminary descriptions of the south–eastern side of the Sierra de Quilmes, where the some of the Agua del Sapo complex crops out, its boundaries with other complexes and most of its hinterland remain unmapped.

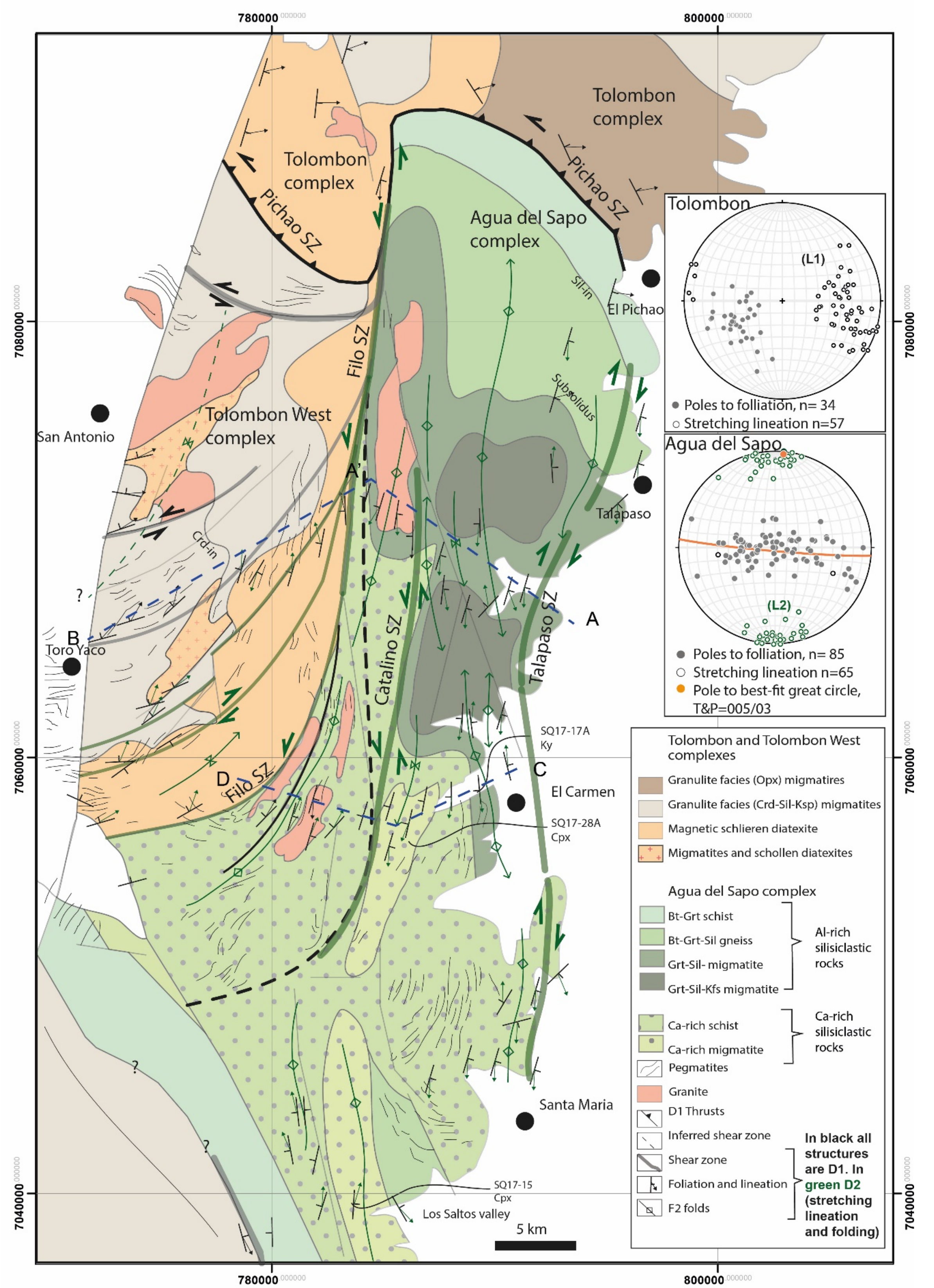

Figure 2– Geological map of the Sierra de Quilmes and its three complexes. The different generation of structures (L1, L2) will be explained in further sections. Rectangle refers to position of Fig. 19.

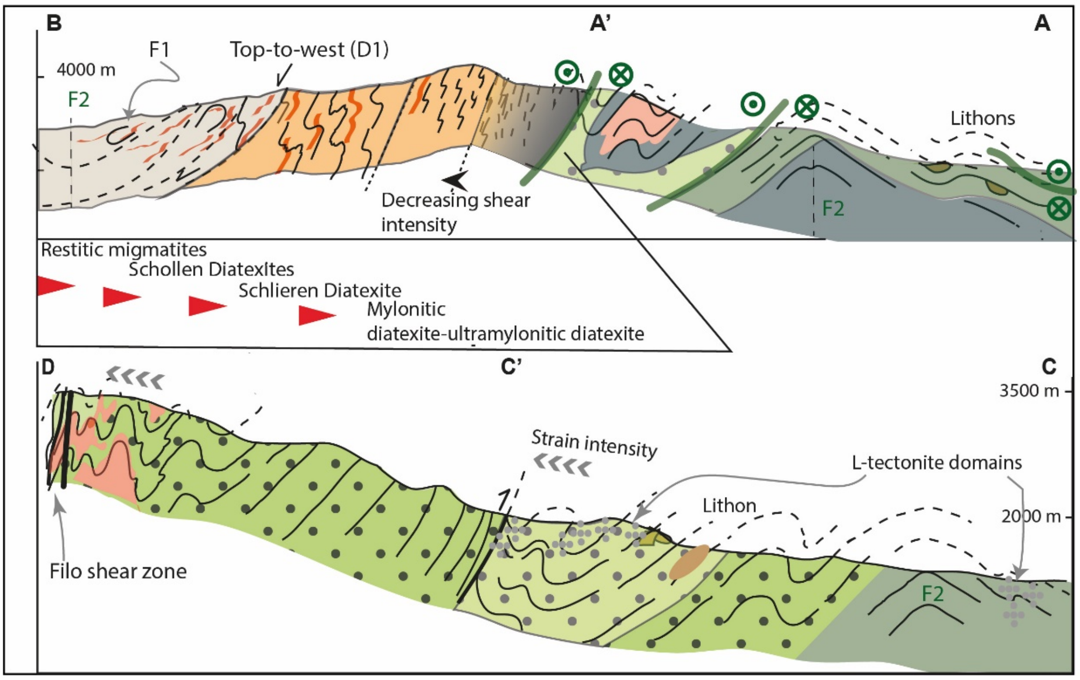

Figure 3– Two cross sections in Fig. 2. On top, north section showing dextral and sinistral shear zones and upright folding in the Agua del Sapo complex. The apparent normal structure in Tolombon West represents a folded (F2) top–to–west thrust. On the bottom, southern section of the Agua del Sapo complex. The strain intensity increases towards the west in the vicinity of a major shear zone as recorded by tightening of upright F2 folds. See Fig. 2 for references.

3 Method

3.1 Aeromagnetic data

Aeromagnetic data were used to interpret and follow structures and major lithological groups in the field. The survey, designed by SEGEMAR (the Argentinian geological service), was commissioned to *Sander Geophysics Limited* and completed in July 1998. It was designed with N–S flight lines with a 1000 m of separation between lines and tie lines every 7500 m. The total magnetic intensity (TMI) grid after corrections was provided by the SEGEMAR. The total magnetic intensity grid was processed to generate the reduced to the pole grid (RTP; Fig. 4a). From the RTP, and using different filters, other grids were generated (Fig. 4). Among them, the first vertical derivative (RTP–1VD) and the tilt derivative (RTP–TDR) that allow us to interpret more precisely the distribution and orientation of shallow high–frequency structures. Also, the analytical signal (AS), which is independent of the magnetic field orientation was useful to map out the outline of the Agua del Sapo complex.

3.2 Crystallographic preferred orientation (CPO)

The G50 Fabric Analyser at Monash University was used to measure individual quartz grain c–axis orientation in thin sections. The c–axes were used to determine the CPO pattern (Peternell et al., 2010; Wilson et al., 2007). The raw data from the Fabric Analyser was processed in the crystal imaging system *INVESTIGATOR G50 v5.9* software to select the c–axis orientation of specific quartz grains within mono–mineralic quartz ribbons or quartz–rich areas. The quality and accuracy of the resulting data are assessed by two factors with every data point: the geometric and retardation quality. The first is a measure of the closeness of the extinction planes from the different light directions, and the second evaluates the usefulness of the c–axis azimuths. Following procedures in Peternell (2010) and Hunter (2016), values in geometric and retardation <75 were excluded from the analysis. Equal area stereo diagrams were created for every sample.

4 Results

4.1 The southern section of the Sierra de Quilmes: the Agua del Sapo and Tolombon West complexes

In this paper, we have focused on the region south of the Pichao Shear Zone, comprised by the Agua del Sapo complex. As a result of geological mapping, we have divided it into two distinct regions: the Agua del Sapo complex proper, to the east of the mountain divide, and the Tolombon West complex to the west. The two are separated by a newly mapped N–S trending shear zone up to 2 km–wide, that crops out along the ridge of the chain and displaces the trend of the Pichao Shear Zone sinistrally with a heave of 7 km (Fig. 2). There are thus three metamorphic complexes identified in the Sierra de Quilmes: the Tolombon, Tolombon West and Agua del Sapo complexes, separated by the two interconnected, thick shear zones the Pichao and Filo shear zones. This division is based on a combination of geological features and supported by satellite and aeromagnetic images. In this section, we describe these complexes, their boundaries, and their expression in aeromagnetic images. Before describing the lithologies and structures of the area, we provide a broad interpretation of the aeromagnetic images.

4.2 Interpretation of aeromagnetic images

The first–order feature of the aeromagnetic images (Fig. 4) is that they show two fields with different aeromagnetic signatures, corresponding to the Agua del Sapo complex in the east and the Tolombon West complex in the west. These two are separated by a north–south corridor of high magnetic values over the Tolombon West complex, which has a sharp boundary against the Agua del Sapo Complex corresponding to the eastern limit of the Filo Shear Zone that will be described below. The Agua del Sapo complex is characterised by lower magnetic values and a smoother magnetic texture with longer wavelength variations in the RTP–TDR and RTP–1VD images compared to the Tolombon West complex, indicating the relatively low dip angles of the stratigraphy. The Tolombon West complex is characterised by a mottled (in RTP–1VD and RTP–AS images) to stippled (RTP–TDR images) texture, reflecting overall higher magnetic intensities (RTP–AS images) and steeper gradients with shorter wavelength patterns indicating a more heterogeneous distribution of magnetic rocks and steeper dip angles. To the north, the Pichao Shear Zone is characterised by a low magnetic intensity corridor that contrasts with the higher magnetic values of the granulite facies rocks of the Tolombon complex.

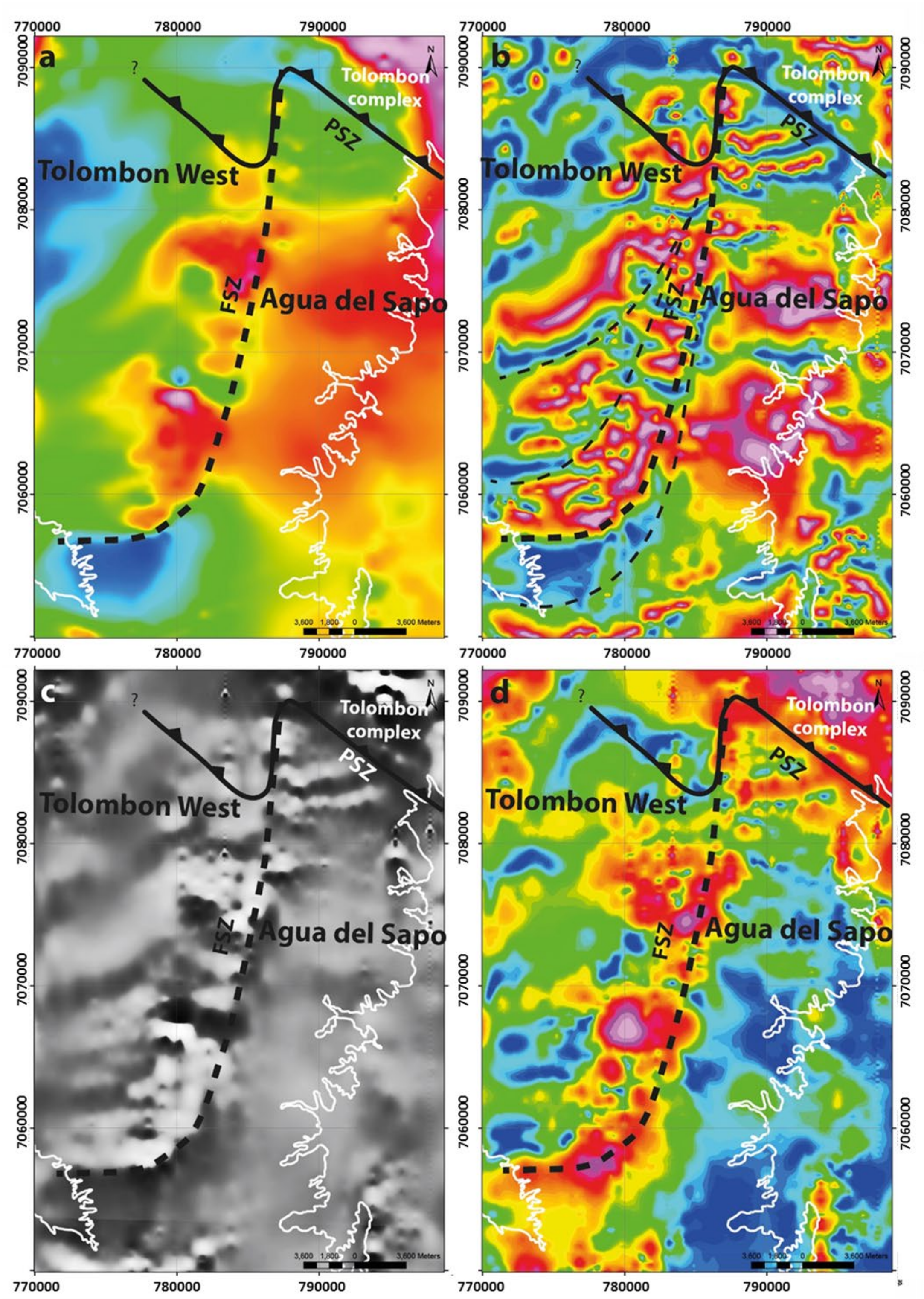

Figure 4– Aeromagnetic images of a section of the Sierra de Quilmes showing the contacts between the three complexes in Fig. 2. White lines are the outline of the Sierra de Quilmes. Interpretation of major structures from: a) Total magnetic intensity (TMI). b) Reduced to pole–tilt derivative (RTP–TD). c) Reduced to pole– first vertical derivative (RTP–1VD). Note the asymmetric magnetic gradient of rocks dipping NW in the Tolombon West complex. d) Reduced to pole– analytical signal (RTP–AS).

Note the distinct change in the magnetic signal across the mountain range from west to east, with the Agua del Sapo complex having lower magnetic values in contact with an irregular N–S band of high magnetic rocks following the Filo Shear Zone in the RTP–1VD. Aeromagnetic data provided by SEGEMAR, the Argentinian Geological Service.

4.3 Tolombon West complex

This complex is separated from the Tolombon complex by the western section of the Pichao Shear Zone (PSZ), and from the Agua del Sapo complex by the north–south striking Filo Shear Zone (FSZ). The rock types here are dominated by migmatites and minor calc–silicate rocks, comprising a similar Al–rich siliciclastic package as the Tolombon complex. The migmatites record a gradual increase of leucosomes and irregular granite from west to east alongside with an increase of finite strain marked by a more intense foliation development.

In the western part of the complex, most of the migmatites are melanocratic, restitic metatexites interlayered with 5–10 m wide bands of nebulitic metatexites and mesocratic schollen diatexites. The restitic metatexites are folded and preserve the original compositional layering characteristic of the turbiditic protolith, and some of the interlayered psammitic and calc–silicate rocks are particularly refractory, thus preserving their sedimentary structures (Fig. 5a). In areas where the restitic metatexites are dominant, there are regularly–spaced lenses of leucosome oriented subparallel to the axial surface of N–S trending folds (Fig. 5b). These residual metatexites are dominated by biotite, cordierite, sillimanite, plagioclase, and K–feldspar with c. 20% of quartz and rare scattered garnet.

The rock has 1mm porphyroblasts of K–feldspar (Fig. 6c), cordierite and large 2–3 mm polymineralic nodules. The K–feldspar is mostly poikiloblastic with aligned inclusions of rounded quartz and subhedral biotite (Fig. 6d), and commonly with less abundant or inclusion–free outer zones. The cordierite is poikiloblastic with a similar suite of inclusions. The nodules are composed of fine–grained quartz–feldspar–biotite–sillimanite and rarely garnet in the centre of the nodule. The garnet is ameboidal and is always in contact with biotite and sillimanite. Sillimanite is present as fibrolite and mostly associated with fine–grained biotite in the form of isolated 1–2 cm nodules in the coarse–grained quartz–feldspar–rich matrix, and as coronas (or rims) around the biotite–rich nodules and cordierite (Fig. 6e). Some cordierite blasts are up to 3 cm and usually with small garnet cores. These cordierites are in thin layers of leucosome, and the relation between cordierite size and leucosome volume suggest that a large volume of melt was lost, leaving restitic cordierites behind (Fig. 6g). An interesting feature in some melanosomes is the presence of small cuspate quartz pockets in the triple junction of larger grains (Fig. 6f). These irregular quartz pockets have inclusions of small corroded biotite and plagioclase, and they are distinguished from the granular matrix by their interstitial shape. There are also leucosome lenses composed by Qtz+Pl+Feldspar+Bt with an equigranular texture and average grain size of 1mm.

Towards the east of the complex, some metatexite migmatites present a net–veined structure and a dilatant fabric characterised by the lack of systematic orientation of leucosomes, suggesting low syn–anatectic differential stress (Fig. 5c). Other metatexites have small anastomosed shear zones controlling the orientation of the leucosomes (Fig. 5d) establishing rhomb–shaped paleosome blocks. In these sheared migmatites, there are 2–10 cm wide veins composed mainly of sillimanite (> 90%) which are parallel to leucosome veins (Fig. 5e). In some areas, stromatic metatexites are overprinted by a second set of leucosomes with different composition and orientation (Fig. 5f). In these rocks, the leucosome stroma are subparallel to the compositional layering, granitic in composition and with a mafic selvage. The cross–cutting leucosomes are narrower, randomly oriented and tonalitic, lacking the mafic selvages and with diffuse transitional contacts to the host rock.

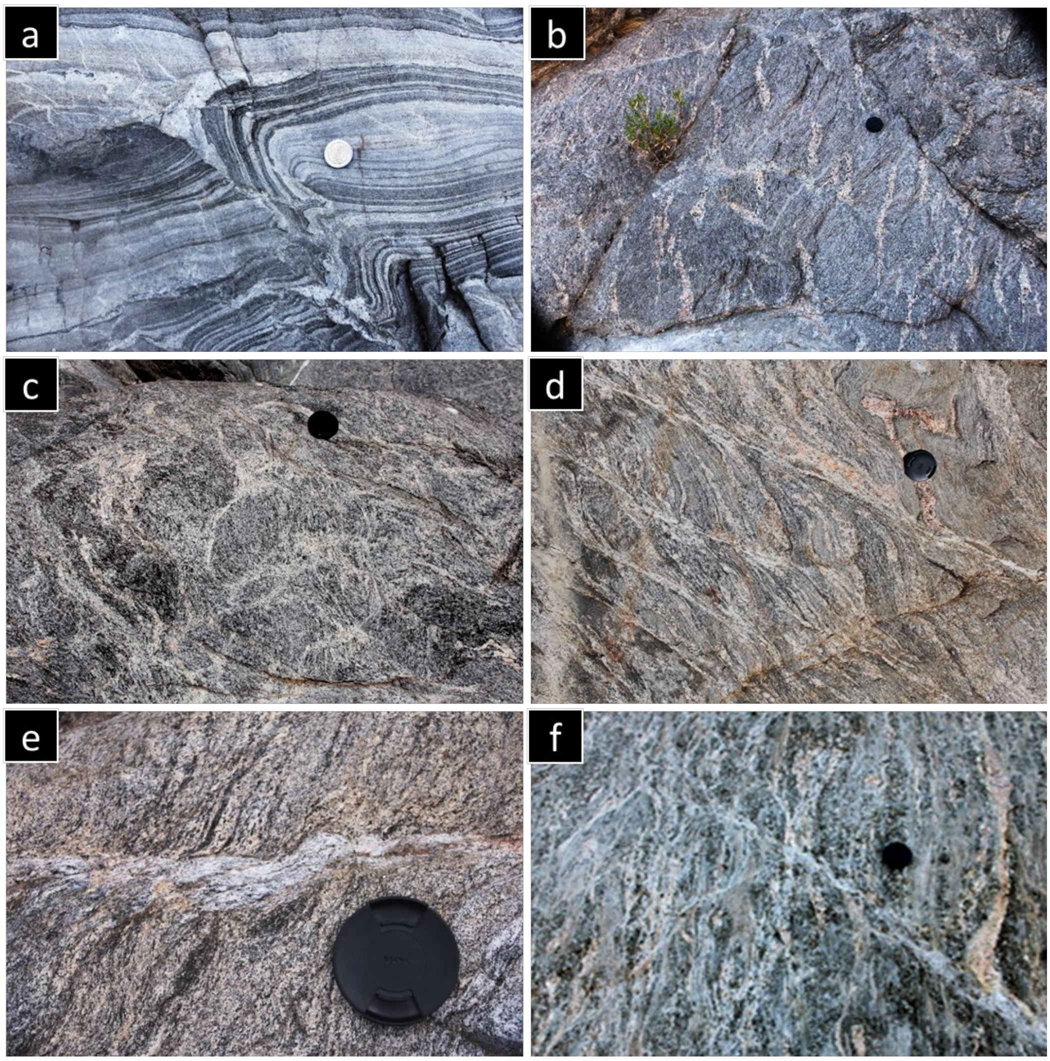

Figure 5– Tolombon West migmatites. (a) Boudinaged metapsammite with evidence for partial melting with leucosomes focused in the boudin neck. (b) Restitic migmatite with a conspicuous set of regularly spaced leucosomes 20–25 cm long, oriented sub–parallel to the axial surface of folds (vertical in the photograph). (c) Net–veined migmatite with dilatant fabric characterised by a lack of systematic orientation of leucosomes. (d) Sheared metatexite. The bedding–parallel stromatitic neosomes are linked seamlessly with oblique leucosomes in shear planes, defining a rhomb–shaped fabric. (e) Sillimanite–rich leucosome in sheared stromatic migmatite. (f) Migmatite showing early foliation–parallel granitic leucosomes overprinted by later thinner, tonalitic, net–veined leucosomes.

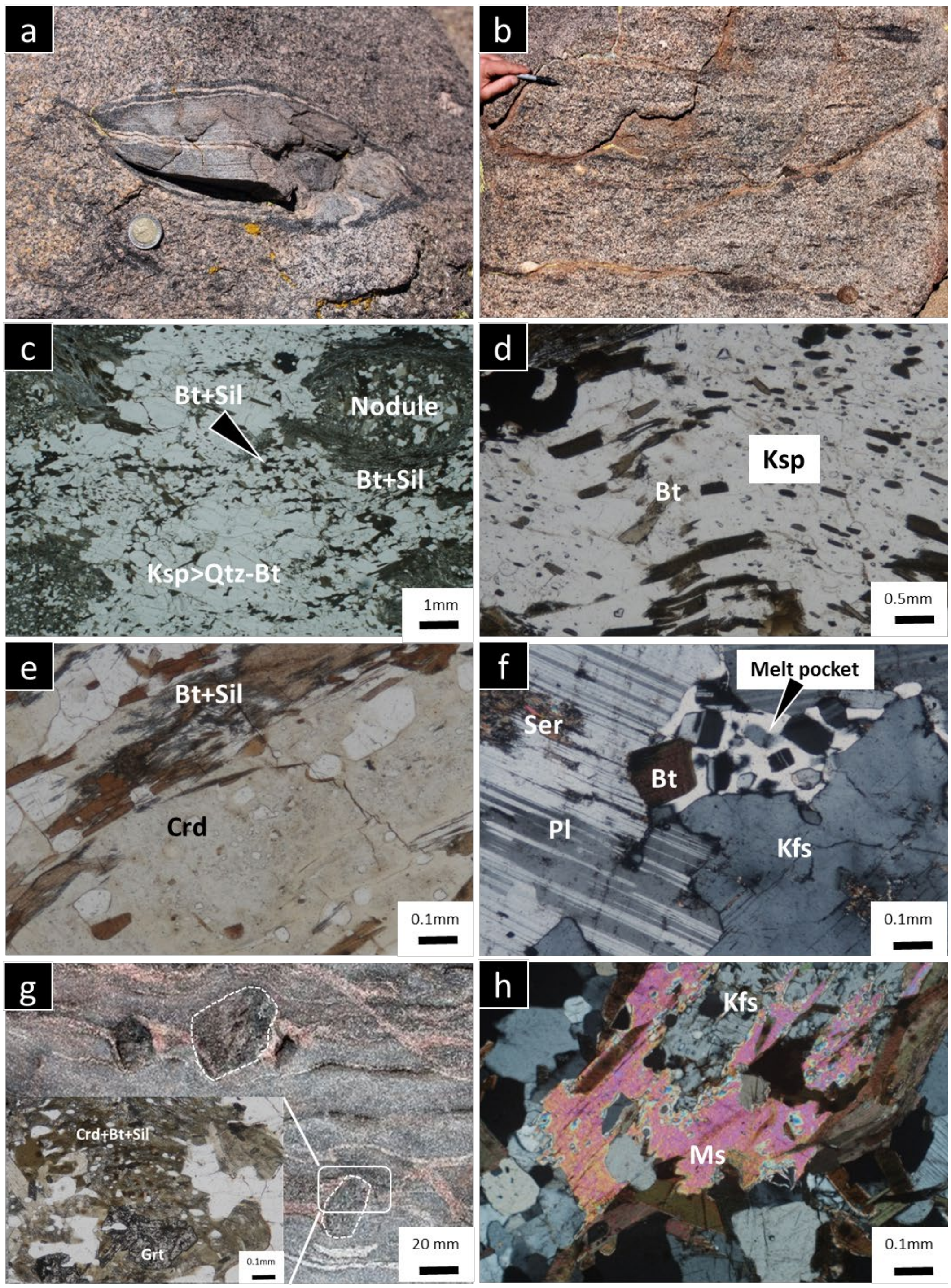

Figure 6– Tolombon West diatexites. (a) Coarse–grained diatexite with a raft of psammitic migmatite source rock. (b) Flow–induced schlieren typical of evolved diatexites. (c–e) photomicrographs in PPL, (f and h) in XPL. (c) Nodules of Bt–Sil–Feldspar–Grt in melanosome of stromatitic metatexites, possibly after retrogression of cordierite. (d) Large poikiloblastic Feldspar with aligned inclusions of biotite and quartz defining a folded internal foliation. (e) Poikiloblastic cordierite with inclusions of biotite and quartz. Biotite–sillimanite is common at the edge of the cordierite. (f) Irregular interstitial quartz grain with multiple inclusions of euhedral biotite and plagioclase. The quartz is interpreted to

be a pseudomorph of a melt pool and evidence for final interstitial melt. (g) Retrogressed cordierite porphyroblasts now biotite–sillimanite cored by garnet. Note the thin layer of leucosome surrounding the large spots. (h) Feldspar altered to muscovite.

In the eastern domain, the metatexites transition to diatexite migmatites. This is coupled with the disappearance of cordierite from the mineral paragenesis and an increase in the modal content of garnet. There are, however, nodules of Sil+Bt that could represent pseudomorphs after cordierite. There is also a gradational change in the fabric of these diatexites: coarse–grained leucocratic diatexites with schollen or rafts of source rock (Fig. 6a) tend to become more homogeneous and include flow–induced schlieren when approaching the eastern boundary of the complex close to the Filo SZ (Fig. 6b). In this area, magnetite–rich diatexite migmatites dominate (Fig. 2) and are accompanied by magnetite–rich pegmatites, which are reflected in the high magnetic susceptibility values of this area (Fig. 4). These diatexites have a sheeted geometry concordant to the regional foliation that trends NNE–SSW and dips steeply west (Fig. 2).

Pegmatites and irregular granitic bodies are parallel to the main NNE–SSW foliation (Fig. 2). Most of the pegmatites are deformed, and their mineralogy is defined by quartz, K–feldspar, plagioclase, muscovite, tourmaline, and accessory magnetite and garnet. Interestingly some of the largest pegmatites in the SE section of the Tolombon West complex have 10–20 cm clots of magnetite. As is common throughout the Sierra de Quilmes, pegmatites have a well–developed alteration rim about 20–30cm wide of 0.1–0.5 cm crystals of muscovite. Large bodies of low–magnetic leucogranite are emplaced within migmatites of Tolombon West, similar to those of the Tolombon complex (Wolfram et al., 2017). The largest body is the San Antonio garnet, two–mica granite, a 7 km long body emplaced north of the complex (Fig. 2).

The migmatites across the Tolombon West complex reached the garnet–cordierite–sillimanite metamorphic zone, similar to the one described by previous authors in the neighbouring Tolombon complex, suggesting temperatures between 650–750 ºC and pressures below 5 kbar (Büttner et al., 2005). Unlike the Tolombon, in the Tolombon West complex, there is no evidence of orthopyroxene. A key feature of all rocks within the Tolombon West complex is a strong retrogression of peak metamorphic assemblages: cordierite and garnet are partially replaced by biotite–sillimanite (Fig. 6g), and sillimanite and K–feldspar are commonly replaced by 2–3 cm poikiloblasts of muscovite (Fig. 6h).

In–situ magnetic susceptibility measurements taken across the complex agree with the regional aeromagnetic data that show higher values in the eastern part of the complex, matching the pattern observed in (Fig. 4c). However, the magnetic susceptibility values are heterogeneous at the outcrop scale, ranging from 200 to 5000 units. The highest in–situ magnetic susceptibility values are correlated with the magnetite clots in pegmatites, and in meter–scale fold hinges in schollen diatexites across the complex.

4.4 Agua del Sapo complex

The Agua del Sapo complex is the footwall of the Pichao shear zone to the south and east of the other two complexes (Fig. 2). As described in section 3.2, the Agua del Sapo complex differs from the other complexes in the aeromagnetic images by a smooth magnetic texture and generally lower magnetic amplitude (Fig. 4b–d). The complex encompasses a suite of strongly deformed metasedimentary rocks. The bulk composition and the metamorphic nature of these rocks vary from north to south. In the northern part, in the immediate footwall of the Pichao Shear Zone, the rocks are garnet–biotite schists and sillimanite paragneisses of amphibolite facies similar to the sub–solidus rocks of the Tolombon complex. This group of rocks is referred to as Al–rich siliciclastic rocks. Some 20 km to the south, these rocks give way transitionally to Hbl+Ep+Aln+Ttn–bearing meta–sedimentary rocks with graded–bedding and variable but relatively limited volumes of leucosomes (from a few to 10–15% in area). These more calcic and ferromagnesian rocks dominate between

Ruinas de Quilmes and Santa Maria (Fig. 1) and had previously been recognized by Toselli (1978), who assigned them to the Puncoviscana Formation. They are presumably marls and will be referred to as Ca–rich siliciclastic rocks. Inspection of Table 1 shows that they typically have CaO > 2%, compared to much lower values for the Al–rich, Sil+Crd bearing metasedimentary rocks to the north. Note that these Ca–rich rocks also have bulk compositions that match a typical metaluminous igneous composition (Fig. 7). Similar Ca–rich rocks have been described in the Cumbre de Calchaquies, immediately to the east of the Sierra de Quilmes and associated with a marly protolith (López et al., 2019). We describe these rock types separately below.

Table 1– Whole–rock composition of samples from Agua del Sapo complex (AdS) and Tolombon West complex (TW). Note that the Ca–rich siliciclastic rocks have > 2% CaO (in red) in comparison with lower values in Al–rich siliciclastic rocks (CaO < 2% in blue). Also one tonalitic has CaO > 2 % in the Tolombon West complex.

Sample ID	Complex	Lithology	SiO_2	TiO_2	Al_2O_3	Fe_2O_3	MnO	MgO	CaO	Na_2O	K_2O	P_2O_5	LOI
SM005_1	AdS	Ca-Ep migmatite	59.13	0.79	14.83	6.43	0.12	3.98	5.46	1.75	6.14	0.20	0.79
SM005_2	AdS	Ca-Ep migmatite	67.93	0.82	12.61	4.51	0.09	2.69	5.76	2.62	1.33	0.29	0.84
SM005_3	AdS	Ca-rich schist	72.36	0.61	12.72	4.15	0.08	1.69	2.27	3.25	2.18	0.19	0.75
SQ17-25A	AdS	Ca-Ep migmatite	70.37	0.63	12.04	4.07	0.07	2.30	3.95	2.41	2.75	0.20	1.28
SQ17-46C	AdS	Amphibolite	57.41	1.14	13.52	6.68	0.16	6.94	11.52	0.75	0.29	0.50	0.94
SQ17-015	AdS	Ca-Ep schist	62.52	0.78	14.23	5.63	0.11	4.14	5.83	1.37	3.74	0.19	1.45
SQ17-34B	AdS	Metapsammite	66.44	0.69	15.20	5.59	0.09	2.29	1.82	3.29	2.97	0.19	0.94
SQ17-34A	AdS	Metapeilte	58.75	0.24	23.07	4.70	0.08	2.47	0.88	2.28	6.34	0.08	1.49
SQ17-022	AdS	Leucosome	67.56	0.69	14.80	5.23	0.06	2.05	0.96	2.04	4.46	0.18	1.57
SQ17-049	AdS	Granite	70.78	0.51	13.65	4.17	0.08	1.74	1.04	2.24	3.94	0.11	1.18
SQ17-56	AdS	Diatexite	69.64	0.54	14.53	4.37	0.10	1.94	1.18	2.47	3.30	0.08	1.36
SM003	AdS	Gneiss	60.78	0.90	16.86	7.47	0.12	3.64	0.98	1.74	4.83	0.17	2.12
SQ17-65B	TW	Residual diatexite	63.04	0.75	16.77	6.99	0.11	2.65	0.53	1.76	5.54	0.17	1.50
SQ17-066	TW	Residual diatexite	62.39	0.76	16.99	7.91	0.11	2.79	0.52	1.83	5.06	0.14	1.08
SQ17-076	TW	Diatexite	71.76	0.50	13.48	3.72	0.07	1.45	1.00	2.43	4.01	0.16	0.89
SQ17-077	TW	Residual diatexite	68.08	0.69	15.78	5.45	0.10	2.38	0.95	2.07	3.26	0.16	1.36
SQ17-88A	TW	Residual diatexite	62.15	0.82	17.71	6.69	0.13	3.08	0.72	1.97	5.00	0.13	1.71
SQ17-88B	TW	Residual diatexite	64.39	0.79	16.40	6.39	0.11	2.75	0.73	2.15	4.43	0.15	1.75
TY071	TW	Granite	69.78	0.57	14.00	4.24	0.07	1.78	1.41	2.47	3.89	0.27	1.13
TY081	TW	Granite	62.96	0.55	17.03	4.70	0.09	2.95	4.14	3.47	2.30	0.32	1.07
TY089	TW	Residual diatexite	61.90	0.81	17.83	6.66	0.11	3.01	0.63	2.09	5.20	0.16	1.70
LC066	TW	Diatexite	67.21	0.69	15.09	5.50	0.11	2.35	1.51	2.62	3.40	0.25	1.20
LC065	TW	Diatexite	71.10	0.47	14.09	3.61	0.07	1.38	1.15	2.51	4.13	0.21	1.71

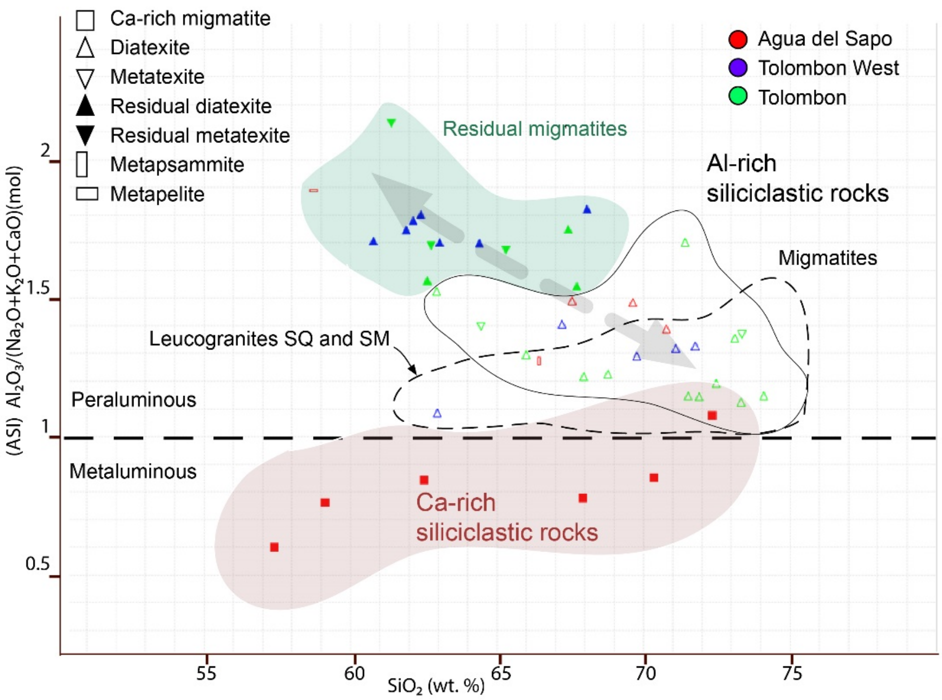

Figure 7– Bivariate major element plot for Sierra de Quilmes migmatites and granite plotting in the peraluminous field and the Ca–rich siliciclastic rocks from the Agua del Sapo complex in the metaluminous field. Leucogranite field based on data from NE Sierra de Quilmes (SQ) (Wolfram et al., 2017), and from Sierra de Molinos (SM) (Sola et al., 2013). Modified after Wolfram (2017).

4.4.1 Al–rich siliciclastic rocks

Biotite–garnet schist

These rocks crop out in the north, immediately below the PSZ and are similar to schists in the Tolombon complex (Büttner et al., 2005; Finch et al., 2017) and Tolombon West complex. They are pelitic rocks interlayered with rare psammitic rocks (Fig. 8a). Their mineral paragenesis is defined by biotite, quartz, plagioclase, muscovite, and garnet in the pelitic domains, and more quartz and feldspar with less micaceous minerals in the psammitic layers. Tourmaline, apatite, zircon, monazite, and opaques are the common accessory minerals. Biotite is partly retrogressed to chlorite. Also, it is common to find strongly stretched calc–silicate nodules or layers, and pegmatites stretched into isolated boudins interconnected by thin trails of the same material.

Grt–Sil paragneiss

Some 5 km south of the PSZ, the schist transitionally grades to coarser–grained paragneisses with a slightly higher magnetic signature than the schist. This change in the magnetic intensity is recorded in the RTP image (Fig. 4a). The transition from schist to paragneiss is coupled with the first appearance of sillimanite, which increases in modal content towards the south. Sillimanite is retrogressed to muscovite which forms large 2–3 mm porphyroblasts. Porphyroblasts of garnet have small quartz and opaque inclusions that form sigmoidal patterns in the core with inclusion–free rims.

Grt–Sil–Ky metatexite migmatite

South of the paragneiss, c. 10 km south of the PSZ, near Talapaso village (Fig. 2), metatexite migmatites mark the onset of partial melting evidenced by 2–5 cm discrete leucosome lenses at a high angle to the bedding (Fig. 8b). Despite the anatexis, graded–bedding is still well preserved. However, metamorphism has given rise to inverted coarsening, with the pelitic layers now being coarser than the psammitic. Coupled with the change in metamorphism, there is an increase in the magnetic intensity in the reduced–to–pole magnetic intensity (RTP) and the reduced–to–pole tilt derivative (RTP–TD) of the magnetic images (Fig. 4).

Although a strong pervasive shearing overprinted most of the migmatitic fabric in the complex, there are discrete, low strain lithons, 5 to 10 metre–wide. These lithons preserve the delicate structures associated with partial melting (Fig. 8d, f) and earlier structures, such as an earlier stretching lineation, described in the structural section below. The lithons become rarer to the south, where the intensity of deformation is stronger.

Leucosomes are comprised of quartz, K–feldspar, plagioclase, fibrolitic sillimanite, garnet, and minor biotite plus monazite, zircon, tourmaline and apatite as accessory minerals. The melanosome is characterised by a similar paragenesis but with the addition of kyanite (Fig. 8i), and an increased percentage of biotite and sillimanite and diminished amounts of quartz and feldspars, developing a more lepidoblastic texture. The presence of Kyanite may indicate the continuation of the retrograde P-T path crossing the Sil-Ky isograd when cooling below 500 °C, like in Büttner (2005) for the granulites of the hanging wall Tolombon complex. The peritectic minerals garnet and K–feldspar have inclusions of sillimanite and biotite without any preferred orientation. Fibrolite forms aggregates with biotite, and in many cases, they form isolated nodules or coronas around small garnet cores (Fig. 8g). Garnet is strongly replaced by biotite–sillimanite forming cm–scale grey nodules characteristic of these rocks. Also, large blasts of late muscovite typically replace sillimanite (Fig. 8j). The main foliation is defined by the preferred orientation of biotite, muscovite, and sillimanite.

Grt–Sil–Feldspar metatexite migmatite

Towards the centre of the magnetic high in the RTP–TD image (Fig. 4b), the volume of neosome increases (Fig. 2). Their mineral paragenesis is similar to the previous migmatite except for the occurrence of 2–3 cm poikiloblasts of K–feldspar, and the lack of Ky. These poikiloblasts are interpreted to be peritectic K–feldspar because of their corroded inclusions of biotite and quartz. Sometimes they have inclusion–free rims (Fig. 8h). Garnet is 1–3 cm in diameter, anhedral, with sillimanite inclusions. Also, there are 1–3 cm nodules of biotite–sillimanite–quartz with small garnets in the core which form spots in the outcrops (Fig. 8c, f). These spots represent the retrogression of cordierite, and they are sometimes elongated, parallel to the axial planar foliation of upright folds or the stretching lineation. As in the other high–grade rocks in the complex, sillimanite and K–feldspar are retrogressed to muscovite blasts 1–2 cm in length.

At the outcrop scale, the presence of at least two leucosome veins cross–cutting each other is noticeable. One set is typically strongly folded, sub–parallel to bedding, coarse–grained and with a mafic selvedge. The other set overprints the first, is relatively undeformed, fine–grained and lacks the mafic selvedge (Fig. 8d). The fact that the second set of veins cross–cut these migmatites indicates that the melt–escape threshold (MET) (Sawyer, 2008) was reached within the complex.

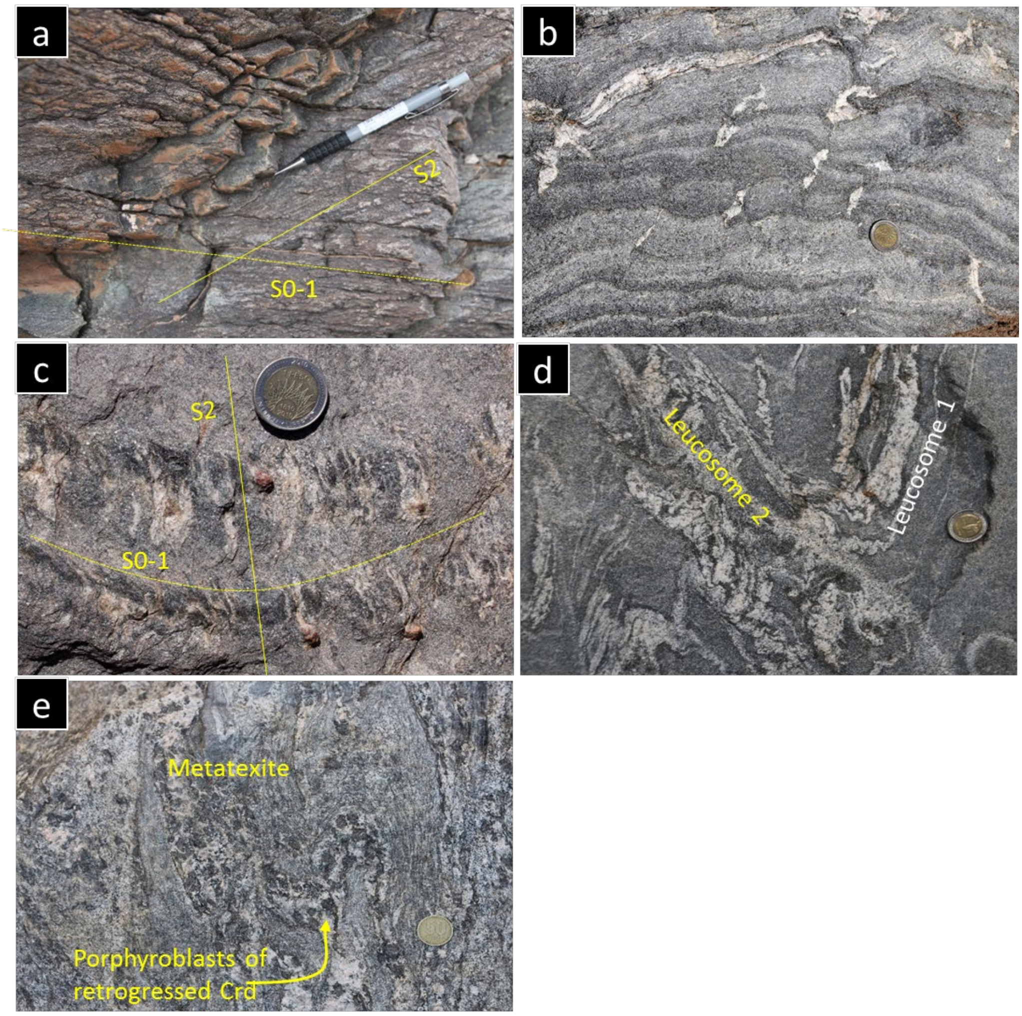

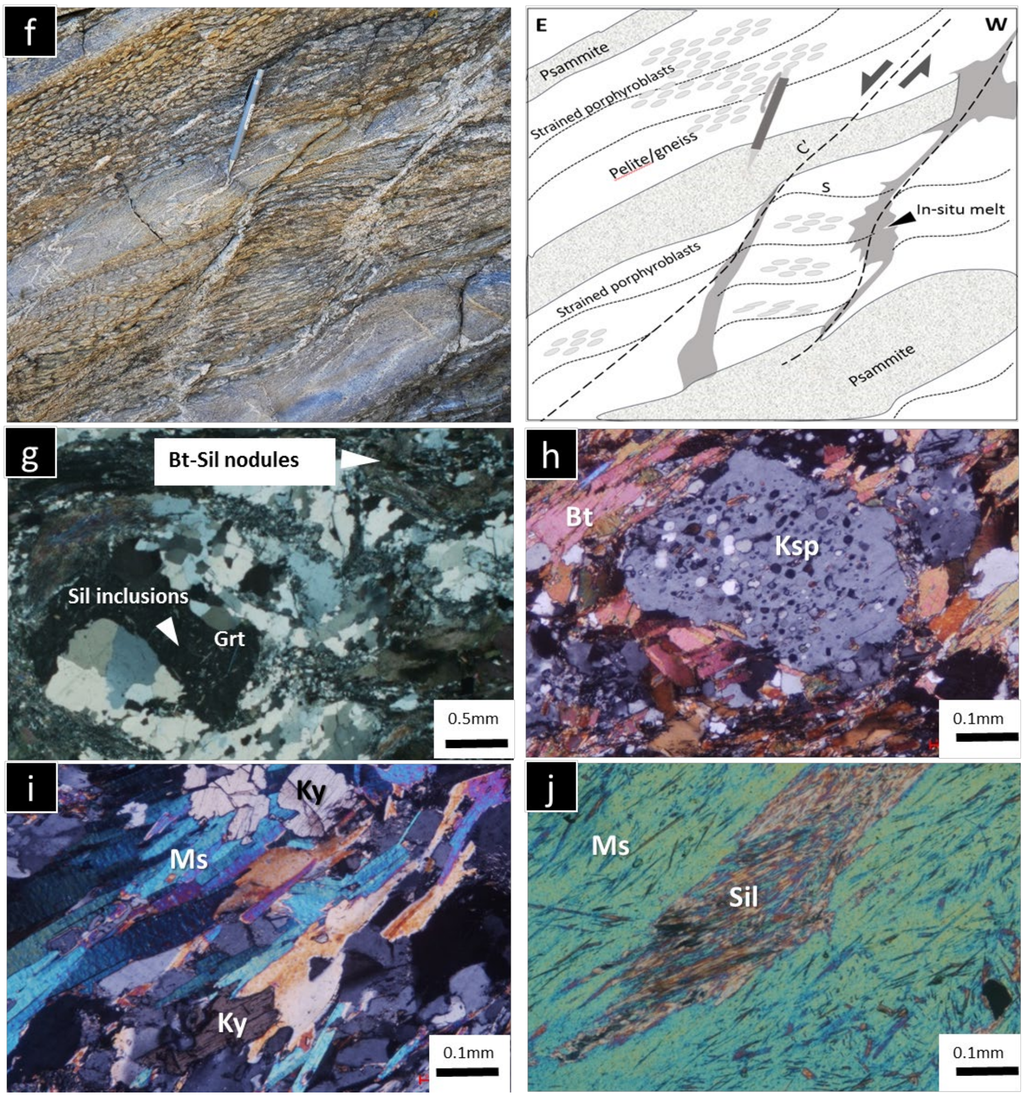

Figure 8– Features from Al–rich siliciclastic rocks in the north part of the Agua del Sapo complex. (a) Bt–Grt schist with compositional layering parallel to main foliation (S0/1) overprinted by a weaker S2 foliation. (b) Onset of partial melting marked by discrete cm–size leucosome lenses at an angle to bedding parallel to S2. (c) Grt–Bt–Sil aggregates aligned parallel to S2, at a high angle to bedding. (d) Two sets of leucosome overprint each other in migmatites. Leucosome 1 is parallel to bedding and leucosome 2 crosscuts all structures and has diffuse margins against host rocks. (e) Folded metatexite with dark–coloured nodules of Bt–Sil, presumably after cordierite retrogression, surrounding a core of garnet). (f) Left. Leucosomes in relatively undeformed lithons. Right. Line–drawing showing the main features in f). (g) Garnet with sillimanite inclusions and Bt–Sil nodules in melanosome. (h) Poikiloblastic Feldspar with inclusions of Qtz and Bt in melanosome. (i) Ky associated with muscovite. (j) Sillimanite partly retrogressed to muscovite porphyroblast. (g–j are photomicrographs in XPL.

S–type granites

Peraluminous two–mica granites, similar those in the Tolombon West complex, are common in the vicinity of the Filo SZ in the west part of the complex (Fig. 2). These granites are elongated in the north–south direction, weakly foliated and concordant with the country–rock foliation. They have a low–magnetic signature in the aeromagnetic images; however, they have a wide range of magnetic susceptibility values measured in–situ, between 10 and 200, but typically 20. The high magnetic values are associated with biotite–magnetite–rich clots of restitic material. The mineralogy is simple and characterised by quartz, plagioclase, K–feldspar, garnet, biotite, sillimanite and muscovite, with accessory zircon, monazite, and rare apatite. These granites have aligned biotite–garnet–rich schlieren and sometimes 1 cm–long phenocrysts of K–feldspar with abundant inclusions of biotite and rounded quartz, similar to those in the migmatites, suggesting that they were sourced from the anatectic metasedimentary rocks. As in the migmatites, the sillimanite and K–feldspars are replaced by late muscovite that forms large inclusion–rich porphyroblasts.

4.4.2 Ca–rich siliciclastic rocks

As mentioned before, the Al–rich siliciclastic rocks transition southwards to the Ca–rich siliciclastic rocks. The areas where these rocks dominate have a widespread and smooth magnetic pattern associated with low magnetic intensities (Fig. 4) and in–situ magnetic susceptibility of < 20. They have typical interlayered pelitic–psammitic bedding with preservation of graded bedding and are interpreted to represent turbidites. The psammitic layers have a coarse–grained (0.5–1 mm) and equigranular texture with a mineral assemblage characterised by Qtz+Pl+Feldspar+Hbl+Bt+Ep±Grt and accessory alanite, titanite, and apatite (Fig. 9e). The pelitic layers, with overall finer grain size, have a similar mineral paragenesis but are richer in biotite, muscovite and hornblende. Some bands are rich in biotite, and lack hornblende, and some have both minerals. This variable hornblende/biotite ratio reflects the primary compositional layering, and it can be observed at the thin section scale (Fig. 9c). Hornblende is 0.5–2 mm, subhedral and usually overgrows titanite and epidote–allanite. In some cases, in the psammitic layers, hornblende is found as isolated large 1–3 cm euhedral poikiloblasts with inclusions of quartz and plagioclase (Fig. 9b). Plagioclase shows in some cases diffuse concentric zoning and is also found forming myrmekite in contact with microcline. K–feldspar, less abundant than plagioclase, forms porphyroclasts when the rock is sheared and recrystallization is common along the edges of these porphyroclasts. Garnet is rare and usually located at the contact of the Hornblende–rich and Biotite–rich layer (Fig. 9c). They are anhedral poikiloblasts 1–3 cm in diameter with inclusions of quartz, plagioclase, biotite, and epidote–allanite (Fig. 9d). Epidote is abundant (c. 20%), typically subhedral to euhedral 0.5–1 mm and occasionally intergrown with plagioclase (Fig. 9f), garnet or biotite, and commonly have rounded allanite cores. Titanite is euhedral and abundant in the Hornblende–rich layers (Fig. 9e). Feldspars are altered to sericite along the edges and as patches within the crystals.

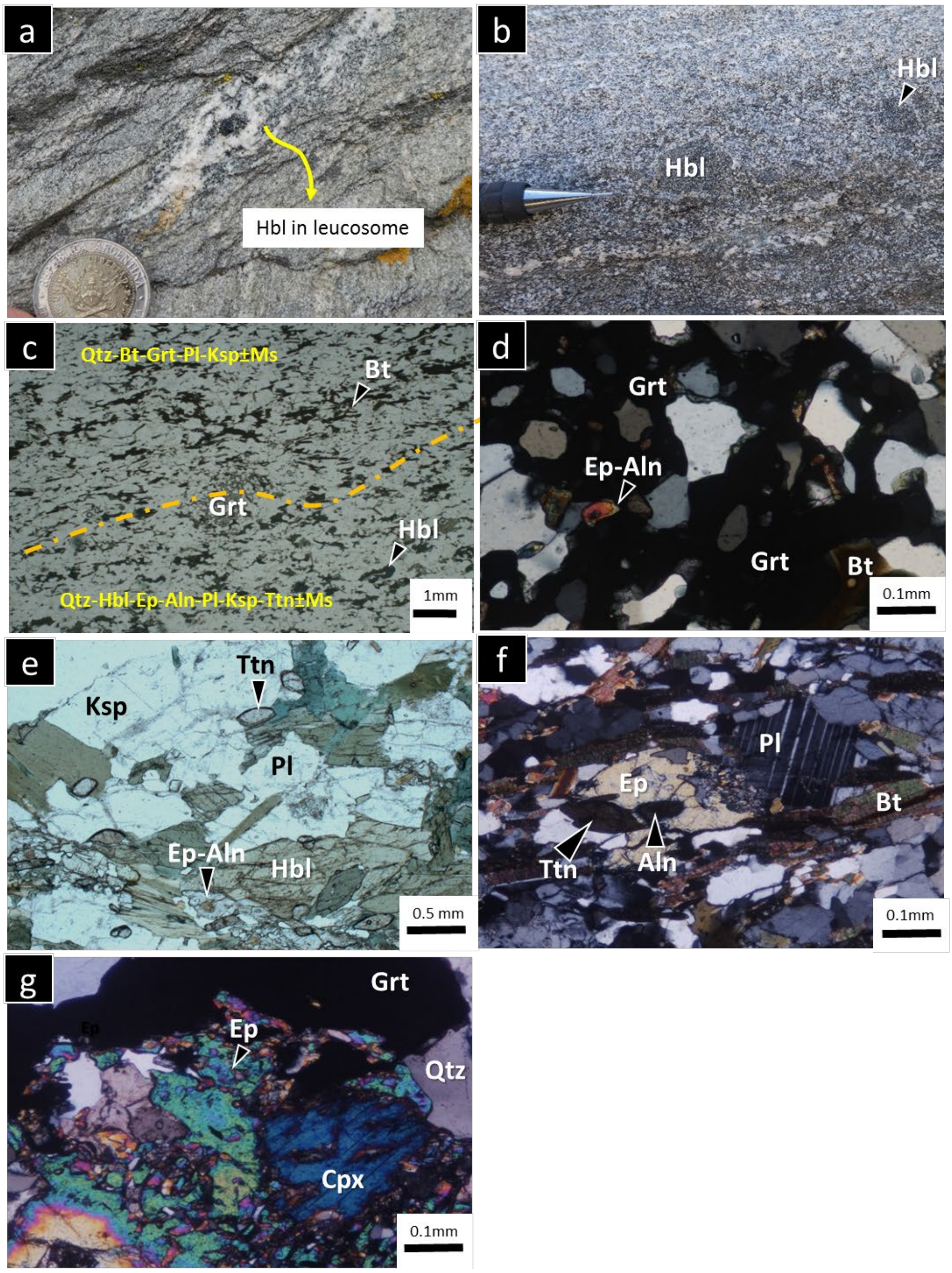

Figure 9– Petrographic features of the Agua del Sapo Ca–rich siliciclastic rocks. (a) Qtz+Mc+Hbl leucosome in sheared migmatite. Peritectic Hbl is larger and euhedral if compared to grains in surrounding rock. (b) Poikiloblastic Hbl in mesosome. (c) Compositional layering reflected as Hbl– rich and Bt–rich bands. Note that poikiloblastic garnet is at the contact between the layers. (d) Close up of poikiloblastic garnet with inclusions of epidote–allanite, quartz and biotite. (e) Typical mineral paragenesis and texture of migmatite. (f) Epidote with allanite core intergrown with Pl and Bt in contact with titanite. (g) Cpx and Ep in contact with garnet. (c) and (e) are photomicrographs in PPL, (d, f, and g), in XPL.

Ca–rich migmatite

The map in Fig. 2 marks where the onset of partial melting on these Ca–rich siliciclastic rocks, indicated by the increase of leucosomes and grain size to an average of 1–2 mm (Fig. 9a). The bulk mineralogy is similar to the unmelted rocks, with the difference in the modal content of some minerals and the presence of clinopyroxene (Fig. 9g) and rare Ca–rich scapolite (meionite). The modal content of epidote with allanite cores decreases here to less than 10%, and when present, it is in contact with hornblende or biotite. Clinopyroxene is 0.1–0.5 mm long, subhedral to euhedral in direct contact with hornblende and epidote, and it overgrows titanite and apatite. Meionite is scattered in these rocks and typically as 0.5 mm euhedral grains in the psammitic layers. The hornblende–rich layers have a coarse–grained granoblastic texture where the euhedral hornblende usually have inclusions of rounded quartz, and it is intergrown with biotite.

These migmatites are characterised by conspicuous Qtz–rich leucosome patches and lenses concentrated in boudin necks and other dilatant sites along the Hbl–rich beds. Leucosomes have an overall coarser grain size compared with the paleosome, and a thin melanosome edge composed by Hbl+Bt±Feldspar. Leucosomes comprise Qtz+Mc+Pl+Hbl±Bt. Quartz is the dominant mineral (80%) followed by the microcline (c. 15%) which is preferably located at the margins of leucosomes. The peritectic porphyroblasts of hornblende of up to 2 cm long have quartz and plagioclase inclusions and are mostly located near the edges of the leucosomes, but sometimes are found as isolated crystals in the centre of the lenses (Fig. 9a).

These lenses are mostly located in the psammitic layers. Although, thin leucosome veinlet swarms cross–cut pelites, tending to define a new foliation. Their orientation changes systematically as they cross over from hornblende–rich beds, where they usually are at a high angle to bedding, to more pelitic biotite–rich beds, where they are at lower angles, suggesting foliation refraction.

4.5 Summary

The Sierra de Quilmes is composed of three metamorphic complexes derived from the Neoproterozoic turbidites of the Puncoviscana formation and separated by thick shear zones. The Tolombon and Tolombon West complexes are dominated by migmatites with an Al–rich bulk composition and variable degrees of partial melting. The former, reached peak metamorphic conditions of granulite facies at 6 kbar and 800ºC in the orthopyroxene zone (Büttner et al., 2005), and the latter is estimated to have reached 5 kbar and >700ºC based on the garnet–cordierite–sillimanite paragenesis in rocks that underwent partial melting. The Agua del Sapo complex is different in that the Al–rich metasedimentary rocks in the north give way to Ca–rich compositions in the south. This compositional change is coupled with an increase in metamorphic conditions from the biotite–garnet zone in the north, to anatectic rocks with peritectic Hbl in Ca–rich migmatites in the south. Furthermore, there is a pervasive retrogression affecting the high–grade paragenesis of the Tolombon West and Agua del Sapo complexes: biotite and sillimanite partly retrogress cordierite, and sillimanite retrogresses to muscovite blasts in both complexes and K–feldspars in the Tolombon West complex. Muscovite in the Agua del Sapo complex is strongly stretched along the main foliation, unlike the large muscovite blasts from Tolombon West migmatites that are randomly oriented.

4.6 Structures

Here we focus on the ductile structural evolution of the Tolombon West and Agua del Sapo complexes, that is complementary to the record in the Tolombon complex documented in the literature and where west–verging thrust coeval with anatexis dominates (Fig. 10a)(Finch et al., 2017). The structural record of the Tolombon West is dominated by folds with local shear zones, whereas that of the Agua del Sapo complex is dominated by a very distinctive prolate deformation and simple shear.

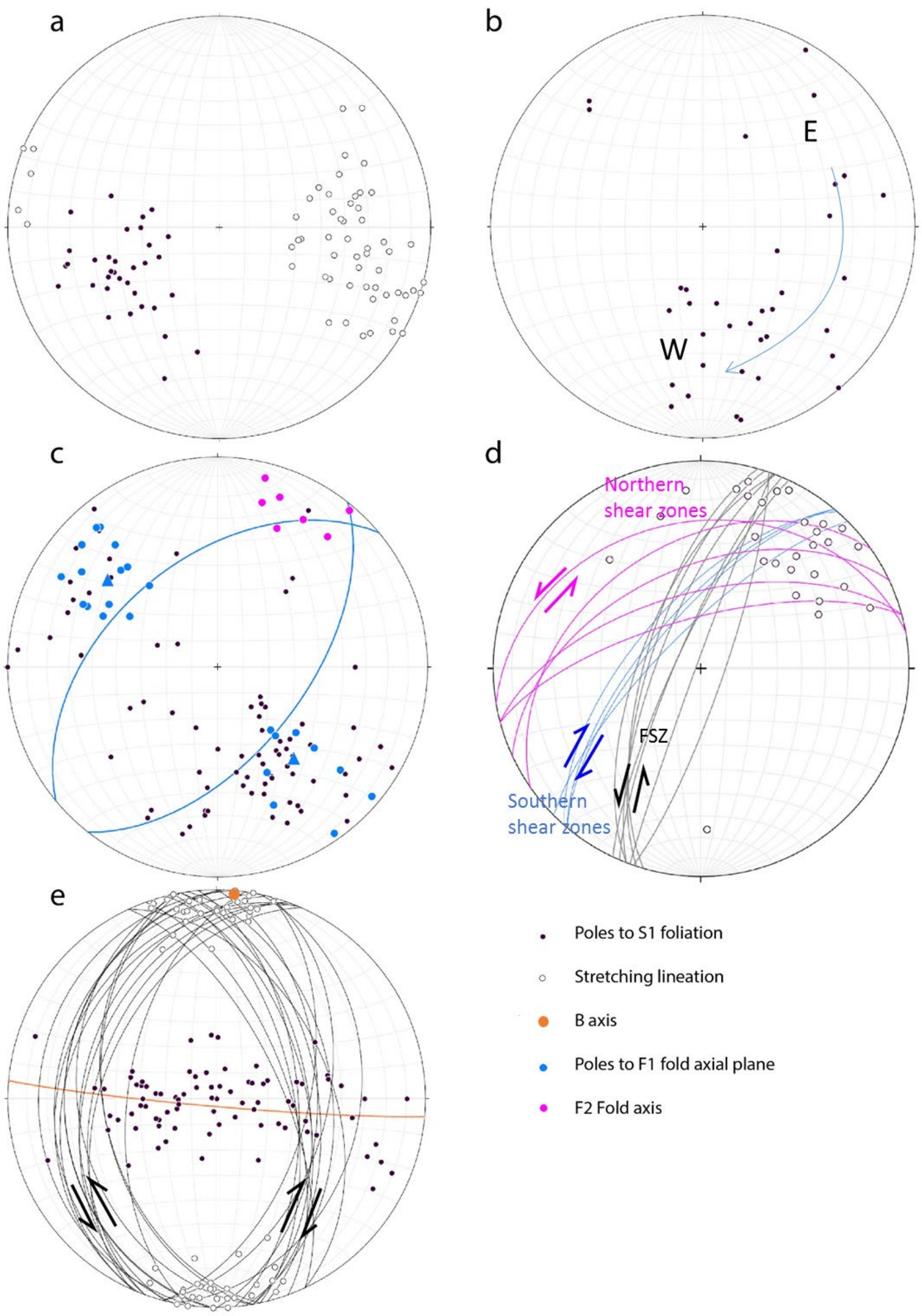

Figure 10– Stereonet projections of foliation and lineation from the Sierra de Quilmes. (a) Data from Tolombon complex from (Finch et al., 2015) showing a well–defined lineation associated with W–verging thrusts. (b) North section of the Tolombon West. The west–dipping foliation is from areas

near the Filo shear zone and the north–dipping structures from the western edge of the complex defining a foliation curvature away from the FSZ in Figure 2. (c) South part of the Tolombon West complex. The poles to fold axial planes with leucosomes (blue dots) clustered in two groups indicating that they were folded and define the two limbs of F2. Blue great circles are the mean plane from the pole clusters which intersect in the NE close to the shallow plunging F2 fold axis. (d) Shear zones in Tolombon West complex. Blue great circles indicate dextral shear zones, purple ones indicate sinistral shear zones and black ones indicate the sinistral splays from the Filo shear zone. (e) Agua del Sapo complex. Black great circles are dextral and sinistral shear zones. Note that the B axis is parallel to the stretching lineation.

4.6.1 Tolombon West complex

The western section of the Pichao shear zone places the Tolombon over the Tolombon West complex, and the N–S trending Filo shear zone separates the Tolombon West from the Agua del Sapo complex (Fig. 2). The Tolombon West complex can be divided into two sections based on its structural style: the northern and the southern section. The limit between the northern and southern zone is diffuse and around the Toro Yaco town (Fig. 2).

4.6.1.1 Structures in the northern section

The structures in the north are similar to those of the Tolombon complex, dominated by syn–anatectic fold and thrusting to the west. The dominant foliation is S1 parallel to bedding, associated with F1 isoclinal folds and top–to–west shear zones. The F1 folds have west vergence and are associated with magma escape paths parallel to the axial planes (Fig. 10a), suggesting that they are syn–anatectic. Unlike the Tolombon complex, there are sinistral shear zones dipping moderately to the NW with an associated mineral lineation, mostly composed of sillimanite, that plunges between 10–30° to the NE (Fig. 10d). These shear zones are relatively narrow (2–5 m wide) mylonitic to proto–mylonitic corridors, and a few of them have 20–30 cm thick ultramylonitic bands (Fig. 11b). Their kinematics suggests a tectonic transport to the west, as in a sinistral strike-slip shear zone, and the presence of sillimanite on the shear planes indicates high–grade metamorphic conditions, as with the thrusting in the Tolombon complex (Büttner et al., 2005; Finch et al., 2015).

The F1 axial planar foliation and the shear zones are parallel to the metamorphic foliation (S1) and the bedding. This fabric dips steeply to the west near the Filo shear zone and progressively changes to a northwest dip towards the west away from the Filo shear zones (Fig. 10b). This trend is depicted in the aeromagnetic images by the low magnetic corridors splaying out from the Filo SZ (see Fig. 4c).

In the west, where the S1 dips northwest, there are rare metric–scale N–S trending upright open folds with leucosomes in their axial planes (Fig. 5b) parallel to a weak S2 foliation, hence evidence of a second folding event (F2).

4.6.1.2 Structures in the southern section

Like the northern section, the fabric rotates from N–S to NE–SW following the trace of the Filo shear zone (Fig. 2). Also, the F1 isoclinal folds are similar to the north, as they typically have axial planar leucosome veins and cuspate fold hinges and are sub–parallel to S1. Unlike the northern section, F1 and S1, are overprinted by F2 in a moderately different orientation. The stereonet projections (Fig. 10c), shows two clusters defining the later F2 folding event rarely observed in the north. These F2 folds are km–scale upright folds with fold axis plunging 5–10° to the NE, and an inter–limb angle of c. 75°. The F2 axial planes are marked by the orientation of elongated porphyroblasts of cordierite, fibrolite sillimanite, and biotite that form S2 (Fig. 11c). Sometimes F2 axial planar foliation is coupled with leucosomes (Fig. 11d). The graded bedding, still evident in some migmatites, was used to reconstruct the younging direction of these km–scale F2 folds.

There are also shear zones parallel to S1 similar to those in the northern area in terms of metamorphic grade; however their kinematic is variable. Some 5 km to the south of Toro Yaco town (Fig. 2) there are 1–2 m–thick sillimanite–bearing dextral shear zones that dip steeply (c. 70º) to the NW and that overprints F2, deflecting their trace by few centimetres. To the east and south of these dextral shear zones, there are sub–vertical sinistral shear zones that are part of the splays of the Filo shear zone. Both sets of shear zones are parallel to the F2 axial planes and their mineral stretching lineation, mostly defined by sillimanite and stretched mineral aggregates, plunge c. 30º NE. This is depicted in the map (Fig.2) and the stereonet projections (Fig. 10d).

4.6.1.3 Summary

The structures of the Tolombon West complex are similar to those of the Tolombon complex as there is a dominant foliation parallel to bedding (S1), syn–anatectic isoclinal folds (F1) and high–grade shear zones in the northern area indicating tectonic transport to the west. However, in contrast to the Tolombon complex, in the Tolombon West complex there are N-S trending upright F2 folds and sinistral shear zones that are splays from the Filo Shear Zone. Further to that, the entire fabric is rotated from a N-S to a NE-SW direction in the southern part of the complex, where there are some dextral shear zones. Therefore, in the Tolombon West complex there is evidence of a second deformational event, and a more complex tectonic history than the one recorded in the hanging wall Tolombon complex.

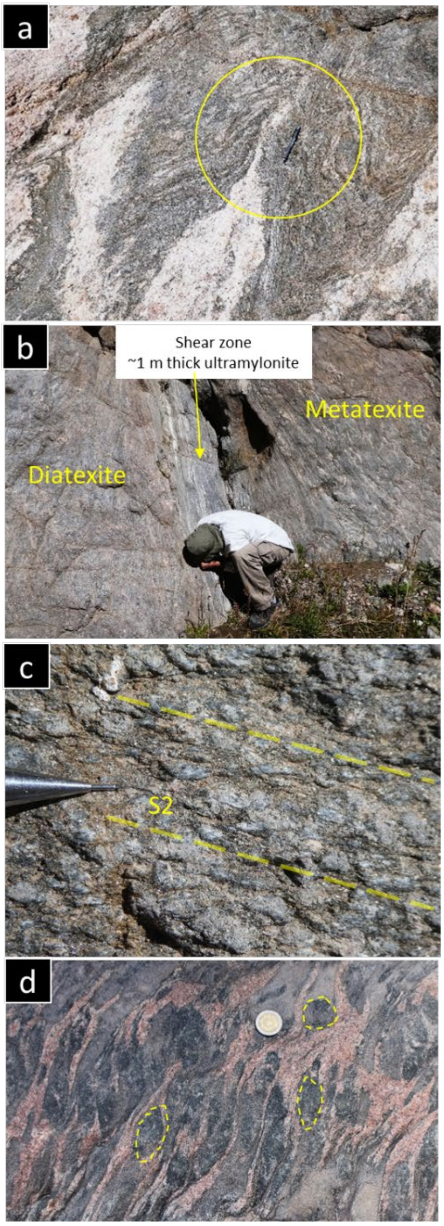

Figure 11– Structures in the Tolombon West complex. (a) F1 cuspate hinge in isoclinal folds with leucosome on the axial surfaces. (b) c. 1 m thick, NE–SW trending, ultramylonite at the contact diatexite–metatexite showing sinistral kinematics. (c) Aligned Crd–Sil porphyroblasts parallel to the axial surface of F2 folds. (d) Leucosome controlled by S2 wrapping cordierite, marked in dotted lines.

4.6.2 Filo shear zone

The trace of the sub–vertical Filo shear zone is clearly shown in the aeromagnetic images (Fig. 4). It has a broad, curved shape, rotating gradually from its north–south trend in the north to an east–

west trend in the south, where it splays into numerous smaller shear zones that were described above (Fig. 2). In the northern sector, its width is c. 500 m, and it ends where intersects the Pichao shear zone with no continuation to the north, to the Tolombon complex. It also deflects the Pichao shear zone by c. 7 km sinistrally. In the southern sector, where it trends E–W, there is a significant decrease in its width to around 2–5 m–thick mylonitic bands.

This shear zone, similar to the Pichao shear zone, records intense deformation producing a c. 200 m thick black, ultramylonitic rock with naked clasts (clasts without tails/wings around them) in the northern sector, similar to the main features of the Pichao shear zone (Fig. 12a). The sinistral kinematics (Fig. 10d) are indicated by σ–shaped porphyroclasts of feldspar and garnet, S–C' shear bands formed by biotite–sillimanite; and muscovite fish. Along most of its length the rocks have lower amphibolite facies parageneses, and deforms both the Al–rich and the Ca–rich siliciclastic rocks of the Agua del Sapo complex, the latter showing stretched hornblende, epidote and allanite. At its northern end, where it deflects and merges with the Pichao shear zone, there is a greenschist facies overprint with chlorite in the matrix, as it is also found in some samples of the Pichao ultramylonites (Finch et al., 2015). In this region, the core of the shear zone has a gently NE–plunging lineation in a steep sinistral shear zone. Outwards from the core of the Filo Shear Zone, the lineation rotates towards W or E plunging, and the ultramylonitic foliation becomes moderately dipping and recording top–to–W motion, suggesting that the earlier, top–to–W Pichao shear zone was rotated and overprinted by the sinistral motion in the NNE–striking Filo shear zone.

The microstructures in the ultramylonites are varied. The typical ones are characterised by 90% matrix and 10% feldspars porphyroclasts. The matrix is reasonably homogeneous with only short quartz ribbons in a homogenized matrix (Kilian et al., 2011) while the feldspar porphyroclasts are mantled by recrystallized K–feldspar and myrmekites. Quartz shows dominant recrystallisation by grain boundary migration (GBM), and in the same sample, there are examples of low temperature budging (BLG). GBM is associated with c. 200–300 µm recrystallised quartz grains with lobate boundaries (Fig. 12b) and strong crystallographic preferred orientation (CPO) of the grains. BLG is evidenced by small lobate grains concentrated in the boundaries of parental larger quartz grains (Fig. 12c).

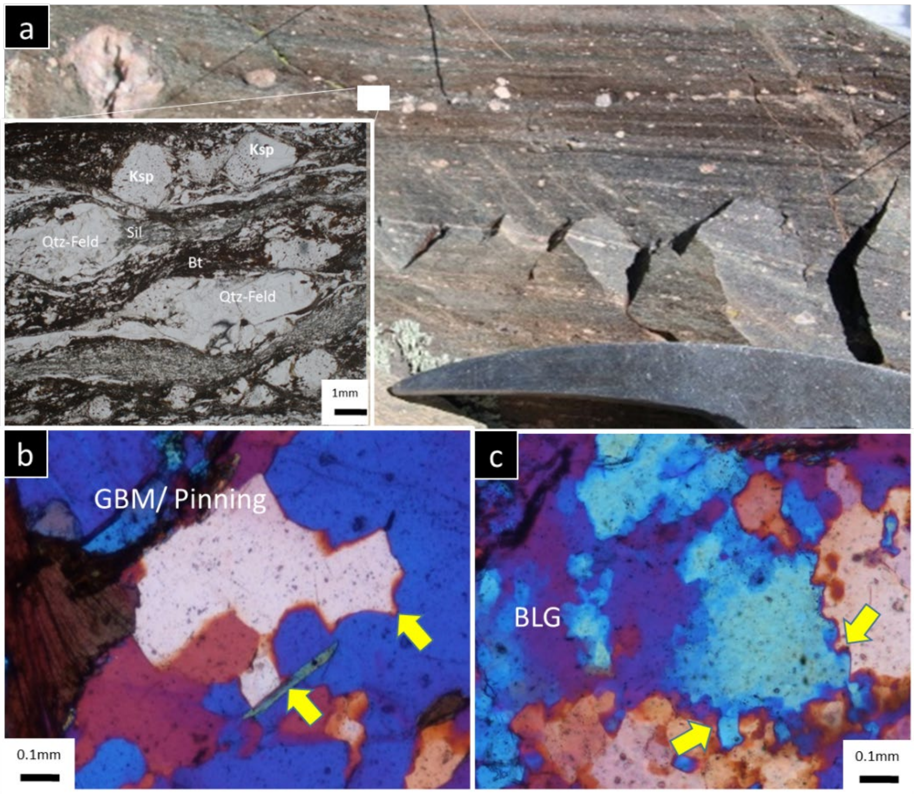

Figure 12– Filo shear zone structures. (a) Ultramylonite with details in photomicrograph in plane–polarized light. Quartz–feldspar aggregates are strained with recrystallized tails together with bands of biotite–sillimanite, shown in inset. (b) Grain boundary migration (GBM) of quartz evidenced by cuspate and lobate borders and pinning by mica grain (yellow arrows). (c) Lobate margins of recrystallised quartz, suggesting the onset of bulging (BLG). They are smaller in size and more irregular when compared to GBM lobate borders in (b).

4.6.3 Agua del Sapo complex: the footwall complex

The nature of the deformation in the Agua del Sapo complex is different from the other complexes. The dominant structural feature in this complex is an intense sub–horizontal N–S trending lineation that can be seen in the rocks from a distance and is associated with intense shearing. These structures overprint earlier ones that are typical of the hanging wall (D1), and therefore considered here as D2. This D2 is the last major event and is followed by a much weaker D3 event represented as a set of 1–5 m wide, sub–vertical greenschist facies dextral shear zones striking north–south, located in the eastern edge of the complex (Fig. 2). In the next section, we will describe the nature of the two major deformational events, D1 and D2.

4.6.3.1 D1 structures

The earliest structure in rocks of this complex is a metamorphic foliation parallel to bedding (S1), defined by muscovite, biotite and sillimanite in the Al–rich siliciclastic rocks, and biotite and hornblende plus elongated epidote–allanite grains in the Ca–rich rocks. There are also early isoclinal folds (F1) which have axial planar leucosomes parallel to S1 suggesting that F1 was contemporaneous to peak metamorphism and anatexis. Because of the very intense D2 deformation, these structures are generally obliterated, except in some lithons such as the well–preserved km–scale lithons near the Pichao shear zone in the north of the Agua del Sapo complex (Fig. 13). The size and frequency of these lithons decrease from north to south, where D2 becomes more intense. Within these lithons, the stretching lineation plunges east and records the same top–to–west kinematics as the hanging wall Tolombon complex. Because these are the earliest structures recorded in the Agua del Sapo complex we label these structures L1 and D1 and interpret them to be similar to the dominant structure in the Tolombon complex. In some lithons, there are also leucosomes that preserve delicate melt extraction structures, which are generally absent or unclear in rocks strongly deformed by later deformation. Outside the lithons the highly–strained rocks have a sub–horizontal stretching lineation trending N–S and associated with strike–slip shear zones which we describe in the next subsection. The transition between the lithons and the country rock is sharp (1–2 meters), and defined by the progressive rotation of the stretching lineation from moderately E-plunging within the lithon to N-S sub horizontal in the sheared country rock.

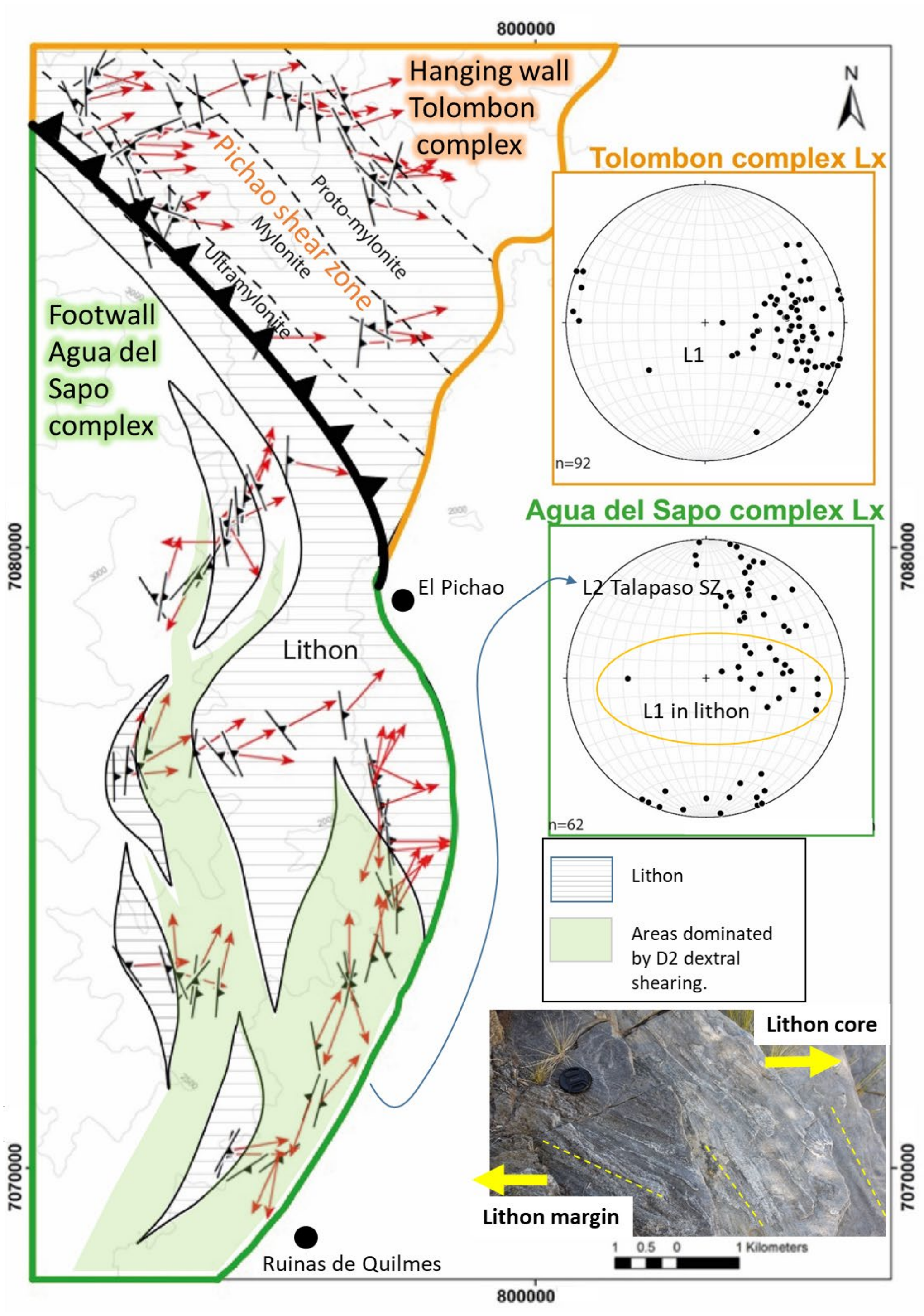

Figure 13– Lithons in the footwall Agua del Sapo complex immediately structurally below the Pichao Shear Zone (see rectangle in Fig. 2 for location). Outlined in green is the strongly deformed rocks (D2) and in grey with horizontal stripes, the less deformed lithons preserving the older top–to–west sense of shear dominant in the Tolombon Complex and the Pichao Shear Zone. Stereographic projections show stretching lineation for both complexes. In the Agua del Sapo complex lithons (lower-right inset) preserve east plunging lineation similar to those in the Pichao Shear Zone and with a similar thrusting movement sense.

4.6.3.2 D2 Structures

The dominant structures in this complex overprint D1 and are related to a D2 event, characterised by a pervasive shearing with a strong N–S sub–horizontal stretching lineation (L2) (Fig. 10e). There are also km–scale N–S trending upright doubly–plunging folds (F2), with the axial planar foliation (S2) overprinting F1 and S1. F2 folds are associated with constrictional structures like L and L>S tectonites, and tubular sheath folds with their axis subparallel to the F2 fold axis and the stretching lineation of the shear zones. All of these structures are described below.

Shear zones and stretching lineation (L2)

The entire complex is generally strongly sheared with a well–defined lineation that trends N–S (Fig. 2). Given the rock type, particularly the psammites, it is not always possible to ascertain strain intensity. However, markers like pegmatites and leucosome veins are strongly stretched (Fig. 14 a–c) and tend to be mylonitic, making it easier to identify high–strain zones. We have tentatively defined two main strain corridors parallel to the Filo shear zone, the Talapaso shear zone to the east and the Catalino shear zone to the west (Fig. 2). The Talapaso shear zone dips c. 45° to the east and has a dextral shear sense. The Catalino shear zone dips c. 35–40° to the west and has a sinistral shear sense. Like with the Filo shear zone, the Catalino shear zone ends when it intersects the Pichao shear zone with no continuation into the Tolombon complex. The Talapaso and Catalino shear zones are typically 500 m wide mylonitic zones that transition into proto–mylonites across strike. The strain profile in all these shear zones appears asymmetric with a sharp strain gradient in the footwall and a wider hanging wall. In between these major shear zones, there are several parallel proto–mylonitic corridors with top–to–south movement, expressed as dextral kinematics in planes that dip east and sinistral when they dip west. The most typical kinematic indicators are σ–shaped porphyroclasts of K–feldspar or plagioclase, muscovite fish (Fig. 14e), asymmetric strain shadows around garnet and other mineral aggregates, and S–C' shear bands formed by biotite–sillimanite. The mineral lineation (L2) in all shear zones plunges 0 to 10° to the north or south (Fig. 10) and is defined by strained quartz–felspathic aggregates, micas, and tourmaline.

The shear zones have strongly strained pegmatites and leucosomes where quartz and feldspars are both ductily stretched. At the microscopic level, quartz is recrystallised by sub–grain rotation (SGR), characterised by a strong oblique fabric defined by the sharp undulose extinction in quartz grains (Passchier and Trouw, 2005). There are also quartz ribbons along the main mylonitic foliation and areas where quartz crystals have straight grain boundaries and lack undulose extinction typical of static recrystallisation, or grain boundary area reduction (GBAR). The feldspar porphyroclasts are mantled by smaller grains of recrystallised feldspar and typically with myrmekites that form on the face of Feldspar facing the shortening direction (Fig. 14g).

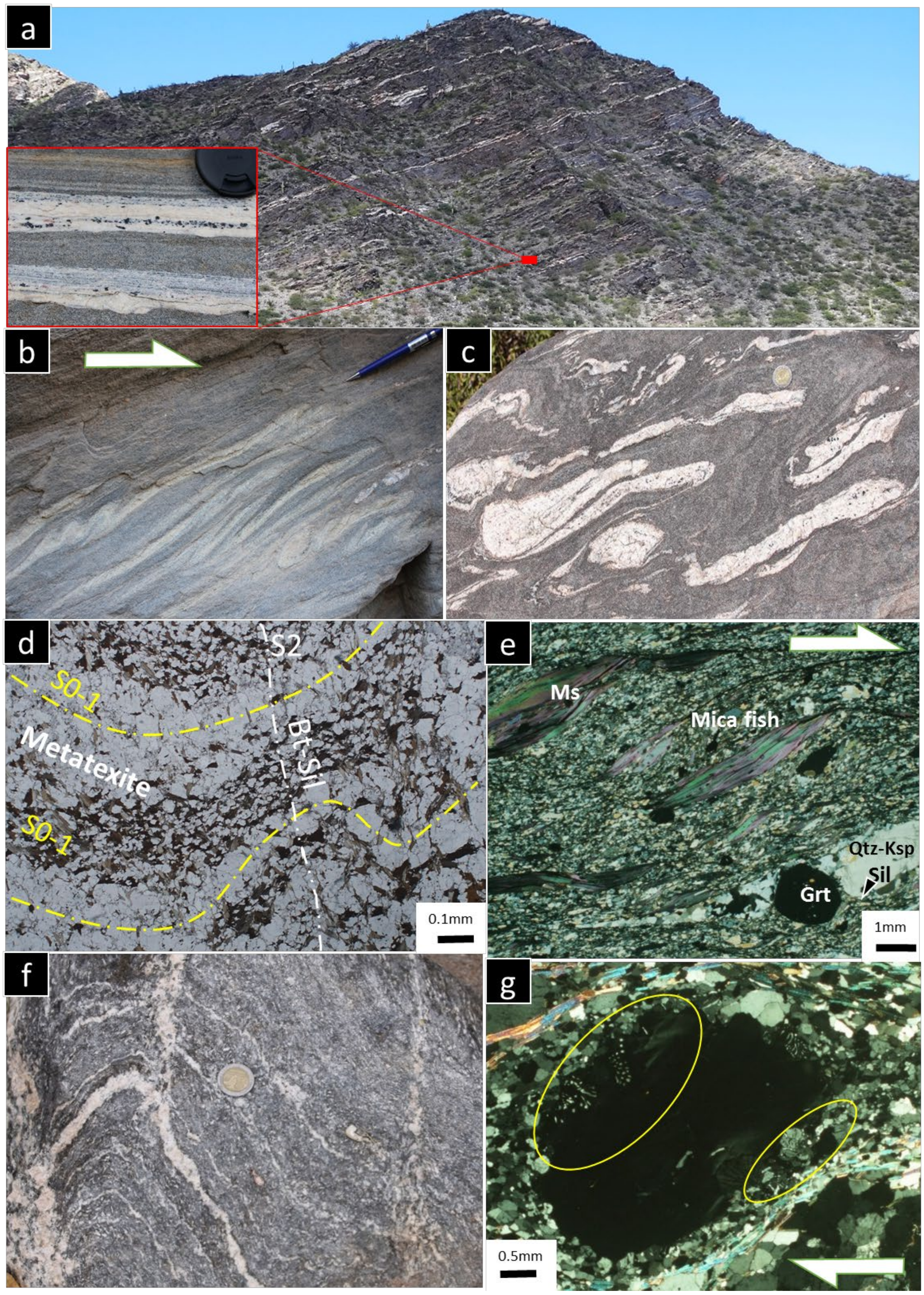

Figure 14– Structures of the Agua del Sapo complex. (a) Strong fabric defined by sheared leucogranitic pegmatites. Inset shows mylonitic pegmatite. Qtz and Feldspar were both deformed in the ductile regime. (b) Tight fold train with vergence to the right (top–to–south) in amphibolite facies metasedimentary rock. (c) Strained and disaggregated pegmatites. Some are still linked by very thin stretched sections. (d) Photomicrograph of folded metatexite showing S2 defined by Bt+Sil. (e) Dextral motion indicated by mica fish and asymmetric trails around garnet. (f) F2 fold with leucosome in axial planar foliation. (g) Feldspar porphyroclast with asymmetric recrystallised mantle

and myrmekites (marked by yellow ellipses). All photographs were taken on planes perpendicular to foliation and parallel to lineation.

Upright folds (F2) and axial planar foliation (S2)

There are km–scale N–S trending open upright folds (F2) that overprint earlier structures, similar to the ones in the southern Tolombon West. They are open folds, with a 2–5 km wavelength in the eastern half of the complex, transitionally changing to close folds with a 0.5–0.1 km wavelength in the western side of the complex and near the Filo shear zone. The F2 fold axes trends north–south and plunge shallowly to both north and south, defining large scale doubly–dipping folds or elongated domes (Fig. 2). The core of these domes are marked by the exposure of the higher grade rocks in the complex, and coincide with the two large magnetic anomalies in the RTP_TD (Fig. 4). The axial planar foliation (S2)cross–cuts S0–1, and this overprinting relationship can be observed at different scales, from satellite to the microscope. The mineral paragenesis associated with S2 in the Al–rich siliciclastic rocks is defined by biotite and sillimanite (Fig. 14d) and elongated mineral aggregates (Bt–Sil rimming Grt) (Fig. 8c, g). In some outcrops, the F2 axial plane has leucosome veins (Fig. 14f). The intensity of S2 foliation increases from east to west coupled with the tightening of fold inter–limb angle.

L and L>S tectonites

The high strain zones in between the Talapaso and Catalino shear zones are associated with a lack of foliation and kilometric domains of L– and L>S tectonites (Fig. 15a, b). The L–tectonites trend N–S parallel to the stretching lineation. In these rocks, long minerals such as amphibole, tourmaline (Fig. 15c) and sillimanite are oriented such that their basal sections dominate in lineation–normal faces, and there is no defined foliation, as the basal cleavage of micas have no preferred orientation.

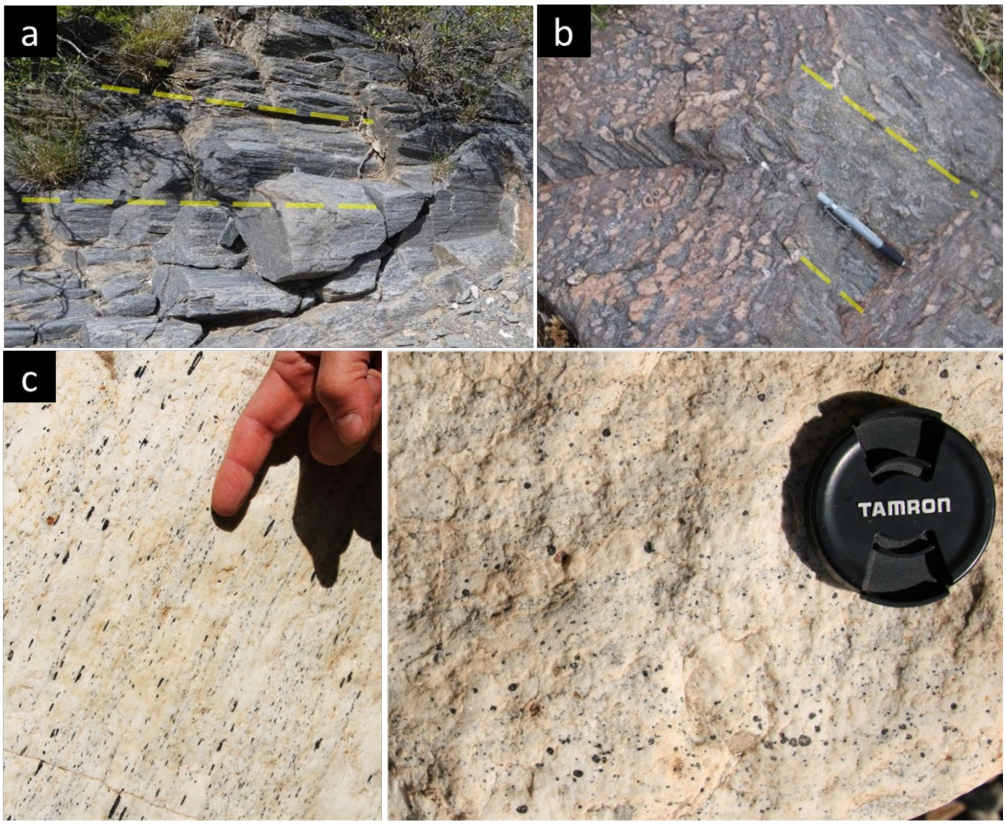

Figure 15– L–tectonites in different rock–types: a) metapsammite, b) metapelite, and c) leucogranite seen along lineation defined by tourmaline grains and stretched quartz and feldspars (left) and normal to lineation showing the absence of a foliation (right).

CPO in Agua del Sapo quartz–rich samples

In order to determine whether the linear fabric is a result of constriction or another mechanism such as overprinting deformation phases (Ramsay and Huber, 1983), we analyzed the crystallographic preferred orientation (CPO) of quartz–rich bands (> 90% quartz) of L–tectonites. Quartz c–axis orientation after deformation is a result of the activation of different slip systems and the final pattern of axis distribution is related to specific finite strain geometries that can be used to discriminate between constrictional and plane strain (Heilbronner and Tullis, 2006; Lister and Hobbs, 1980; Lister and Williams, 1979; Pennacchioni et al., 2010; Sullivan, 2013; Sullivan and Beane, 2010).

In quartz–rich L–tectonites like the ones in (Fig. 16 a,b,c), the pattern of crystallographic preferred orientation of quartz c–axis corresponds to constriction (Lister and Hobbs, 1980; Sullivan, 2009, 2013). In samples with >10 % mica the CPO pattern becomes diffuse (Fig. 16 d and e). The CPO pattern of quartz–rich layers shows a vertical single–girdle or cleft–girdles. The difference between those two patterns reflects the variable c–axis opening angle which increases as a function of deformation temperatures as rhomb <a> and basal <a> slip become more important (Sullivan, 2013; Sullivan and Beane, 2010). Also, the single–girdle is typically oblique, suggesting that the quartz was affected by a component of non–coaxial deformation (Lister and Hobbs, 1980; Passchier and Trouw, 2005; Sullivan and Beane, 2010). In summary, the CPO pattern of quartz–rich layers suggests constrictional regime with a component of simple–shear.

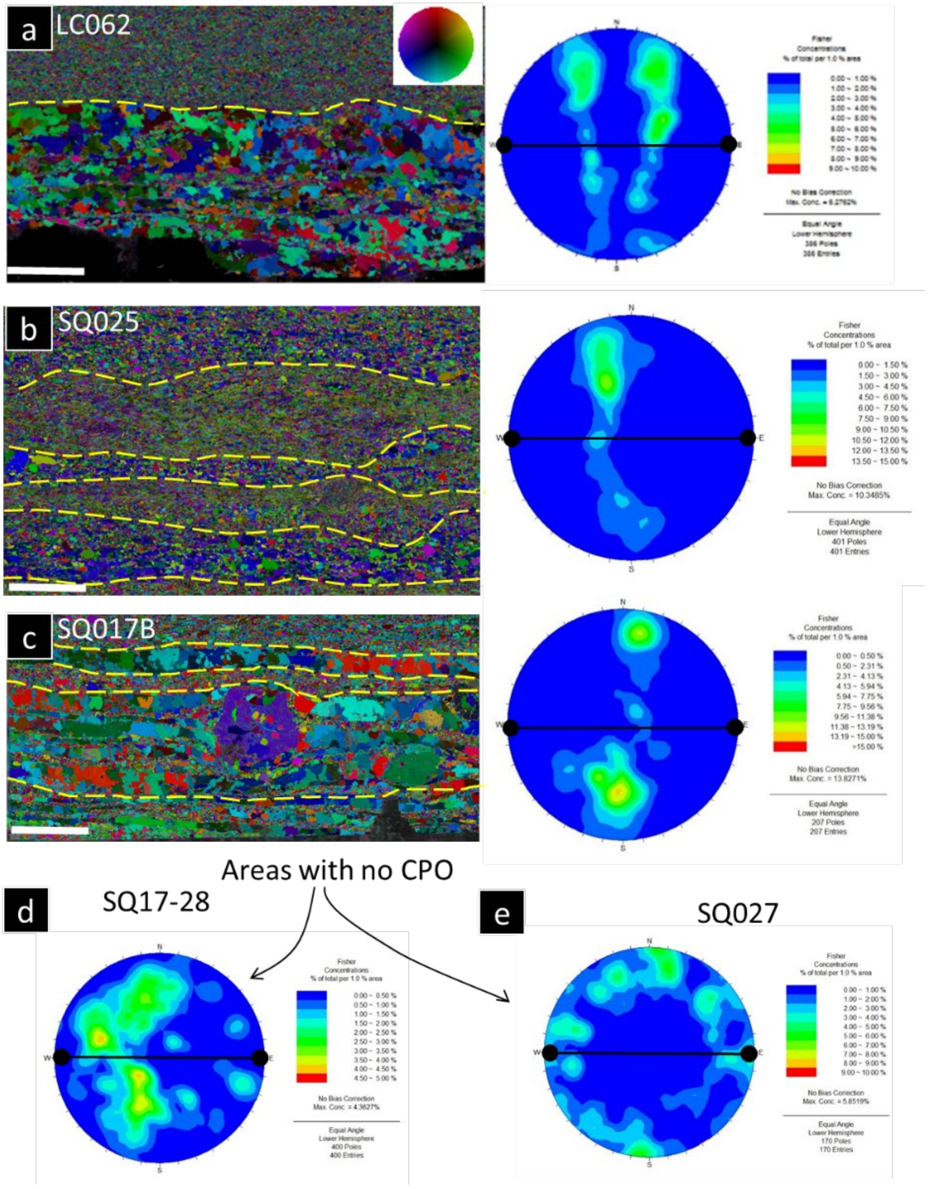

Figure 16– CPO pattern for samples of quartz–rich L–tectonites. Data collected in thin sections cut parallel to lineation and perpendicular to the foliation. (a, b, and c) C–axis orientation image of thin sections to the left and stereograms of the c–axis to the right. The colour of every grain represents its c–axis orientation in space (top right corner colour–coded circle). The sections analysed in every sample are the coarser–grained quartz–rich layers marked by yellow dotted lines. These layers contained < 10 % of other mineral phases and was several quartz grains in width. The reference frame in the stereograms is defined by the E–W vertical foliation plane (black line) and the horizontal lineation represented as black dots. (a) This sample shows two parallel single–girdles or "cleft girdle" typical of constrictional strain. (b, c) Slightly oblique single–girdle, typical of simple shear. (d and e) Stereogram from samples with > 10% mica and feldspar is showing an ill–defined CPO (d), or no CPO at all (e).

Sheath and tubular folds

In areas where L–tectonites are common, there are sheath folds (Ramsay and Huber, 1983) that are variable in size (3 to 0.5 m) and shape, and the vast majority are strongly strained and stretched parallel to the L–tectonites. Many of these folds have an acute hinge angle ω lower than 20º and an x:y ratio >1. This kind of tight sheath fold is called tubular fold (Skjernaa, 1989), and it is the end member of the sheath fold spectrum. For the definition of these fold parametres refer to (Fig. 17). These tubular folds have their fold hinge pointing to the south, and they are associated with smaller ptygmatic and buckled folds of leucocratic veins (Fig. 17).

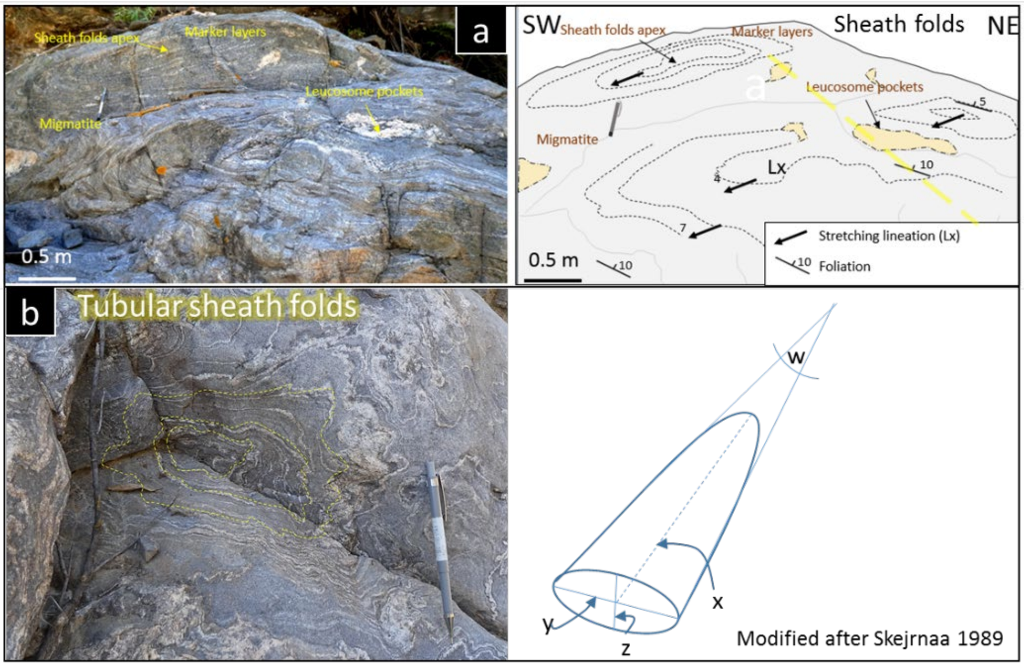

Figure 17– Sheath folds in the Agua del Sapo complex. (a) Sheath folds seen parallel to stretching lineation and diagram to the right showing details. (b) Tubular sheath folds and sketch showing sheath fold angle and axis mentioned in the text.

5 Discussion

5.1 Pichao–Filo Thrust System

Mapping shows that that the Filo shear zone merges with rather than cross–cuts the Pichao shear zone (Fig. 2), with no continuation in the Tolombon complex. These two shear zones have also a number of similarities that suggest they formed as an interconnected thrust system: (i) they are both wide (>3 km) mylonite–ultramylonite shear zones, (ii) their strain profile is asymmetric, with sharp strain gradient against the lower–grade Agua del Sapo complex rocks of the footwall, and wider in the higher–grade hanging wall, and (iii) they have syn–kinematic sillimanite and dynamically recrystallized quartz and Feldspar suggesting high–grade metamorphic conditions of deformation (Finch et al., 2015).

Against this background, we argue that the Filo shear zone together with the eastern section of the Pichao shear zone form the basal decollement of a thrust system, and the Tolombon West complex is a horse that is bound by the Filo shear zone and the western section of the Pichao shear zone (Fig. 17). This thrust system, called here the Pichao–Filo thrust system, placed the Tolombon over the Tolombon West complex, and both were thrusted over the Agua del Sapo complex. In the next sections, we will refer to the Tolombon and Tolombon West as the hanging wall complexes, and the Agua del Sapo complex the footwall of this decollement.

The Pichao–Filo thrust system is folded, as depicted in the map (Fig. 2), forming a broad antiform and an apparent synform in the east and west side of the Pichao shear zone respectively (Fig. 18), suggesting that at some point the thrusting to the west (D1) was impeded, causing buckling of the entire thrust system. Also, in the region where the two shear zones merge, the Pichao shear zone is deflected sinistrally by ~7 km. The stretching lineation of the Pichao shear zone is rotated from the typical E–W trend (D1) to sub–horizontal N–S trend in the core of the Filo shear zone (section 4.6.2). Similarly, the trace of the Pichao shear zone merges with the N–S trending dextral Talapaso shear zone that drags the Pichao shear zone to the south. This deflection to the south of the Pichao shear zone relates to reactivation after the thrust system was folded. In other words, the sinistral Filo and dextral Catalino shear zones mark a D2 event that overprints the D1 Pichao shear zone.

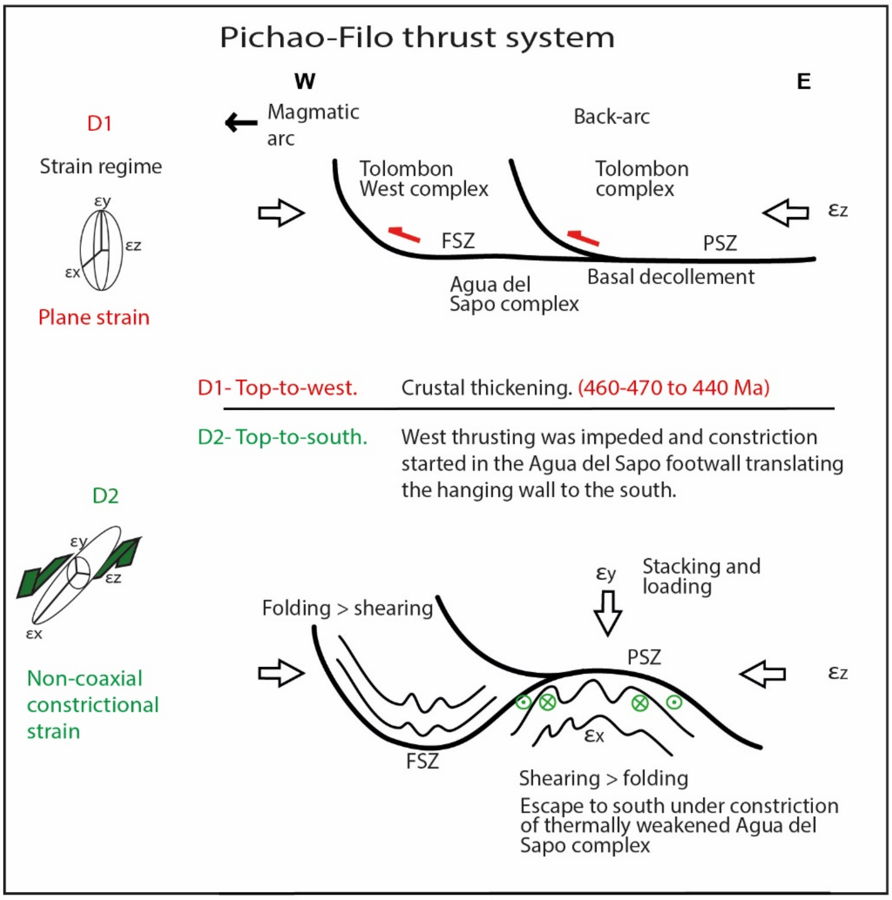

Figure 18– Pichao–Filo thrust system, and interpretation of its evolution on cross sections with the list of events. First, top–to–west thrusting (D1) thickened the crust and transported material to the west, towards the magmatic arc. At some point this thrusting is impeded, and the Agua del Sapo complex reacted by shearing with a top-to-south sense, parallel to the orogen in a non–coaxial constrictional regime (D2).

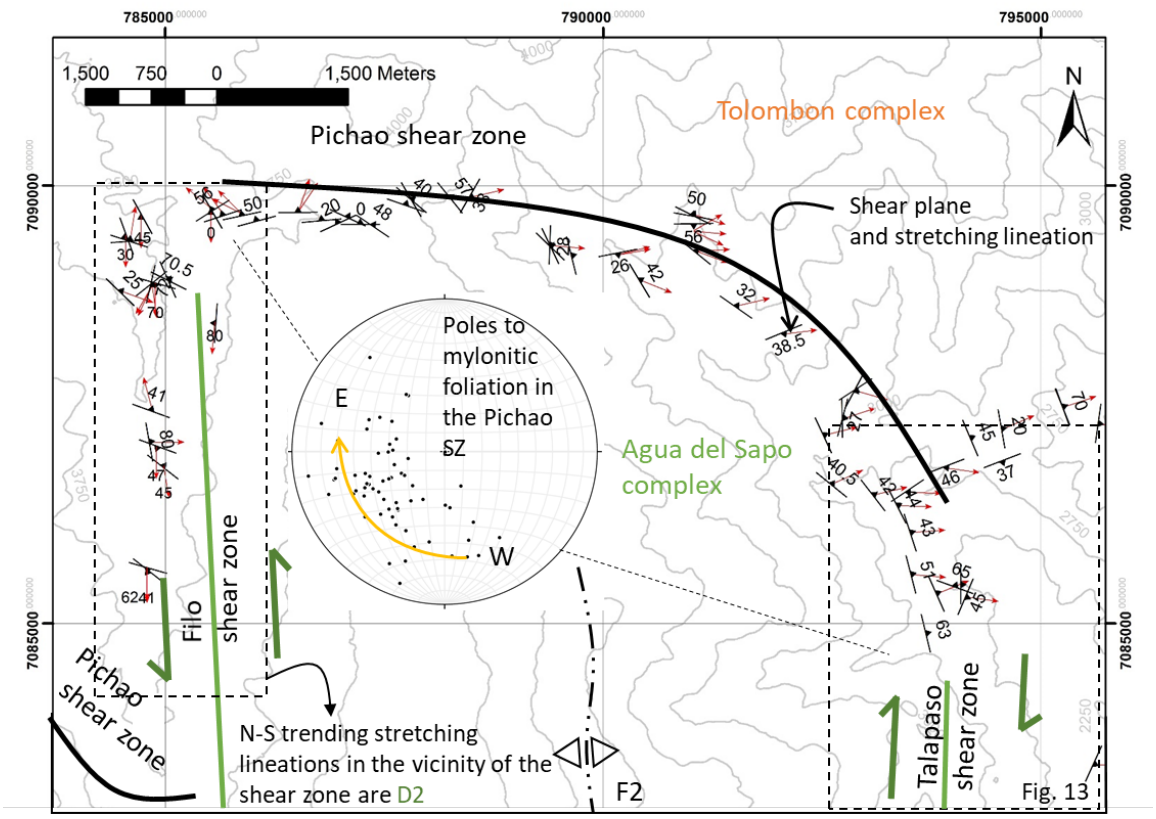

Figure 19– Pichao shear zone intersected by the Talapaso and Filo shear zones. Shear planes and stretching lineations depicting gentle folding of the Pichao shear zone and dragging by the N–S trending Filo and Talapaso shear zones. The stereonet shows the rotation of mylonitic foliation in the Pichao shear zone from west where it dips north, to east where it dips to the east, like the Talapaso SZ. The intersection of Pichao and Talapaso shear zones are detailed in Fig. 13.

Larrovere (2016) reported a similar case of branching of a thrust in the Sierra de Velasco, 270 Km south of the Sierra de Quilmes, in rocks of similar metamorphic conditions and within the frame of the Famatinian orogeny. They argued that the E–W shortening was accommodated and nucleated in a major thrust with top–to–west kinematics with discrete minor splays that diverge towards shallower levels. However, they do not report a later tectonic reactivation.

5.2 The nature of D2

As we have shown the nature of the structures in the Sierra de Quilmes varies across the different complexes. In the hanging wall of the Pichao shear zone, in the granulite to greenschist facies rocks of the Tolombon complex the structural record is dominated by D1, a high–temperature syn–anatectic thrust to the west, which is also recorded in the Pichao shear zone. This contrasts with the two–phase history of the other complexes. In the northern part of the Tolombon West complex, D1 structures like the isoclinal F1 folds and northwest–dipping shear zones with top–to–west kinematics, are preserved away from the Filo shear zone. In the Agua del Sapo complex, D1 structures are only preserved in lithons near the Pichao shear zone (section 4.6.3.1). D2 overprints D1 in both complexes; however, they are very distinct: while in the Tolombon West complex D2 is dominated by folding, in the Agua del Sapo complex is dominated by shearing. In the following section, we describe the nature of D2 in each complex.

D2 in the Tolombon West complex

In the Tolombon West, D2 is expressed mostly as folding with subordinate shearing focused around the Filo shear zone in the southern part of the complex. The D2 sinistral Filo shear zone impacts strongly in this complex. It rotates the foliation from gently northwest–dipping in the west away from the shear zone, to steeply west–dipping and N–S striking near the Filo shear zone. This regional rotation is accompanied by metric–scale syn–anatectic upright F2 folds that trend parallel to the Filo shear zone trace and becomes more intense in the south, where they trend NE–SW. Theses syn–anatectic F2 upright folds are overprinting S1 and F1. This overprinting relationship is depicted in Figure 10c. Also in the southern section of the complex, narrow sillimanite–bearing dextral shear zones are parallel to the F2 axial planar foliation, and they deflect F2 folds by few centimetres.

We interpret the deflection of the entire fabric in the south of the complex as the response of some buttress further south of the complex that disturbed the stress field from E–W to an NW–SE directed shortening (Fig. 20). The intensification of F2 in this area may have happened as the result of the sinistral shearing that transferred the Tolombon West complex to the south (as evidenced in the c. 7

km sinistral displacement of the Filo shear zone in the northern sector) causing compression of the complex against this buttress. At some point before the metamorphic retrogression of the complex, a renewed E–W shortening triggered minor dextral shearing (Fig. 20).

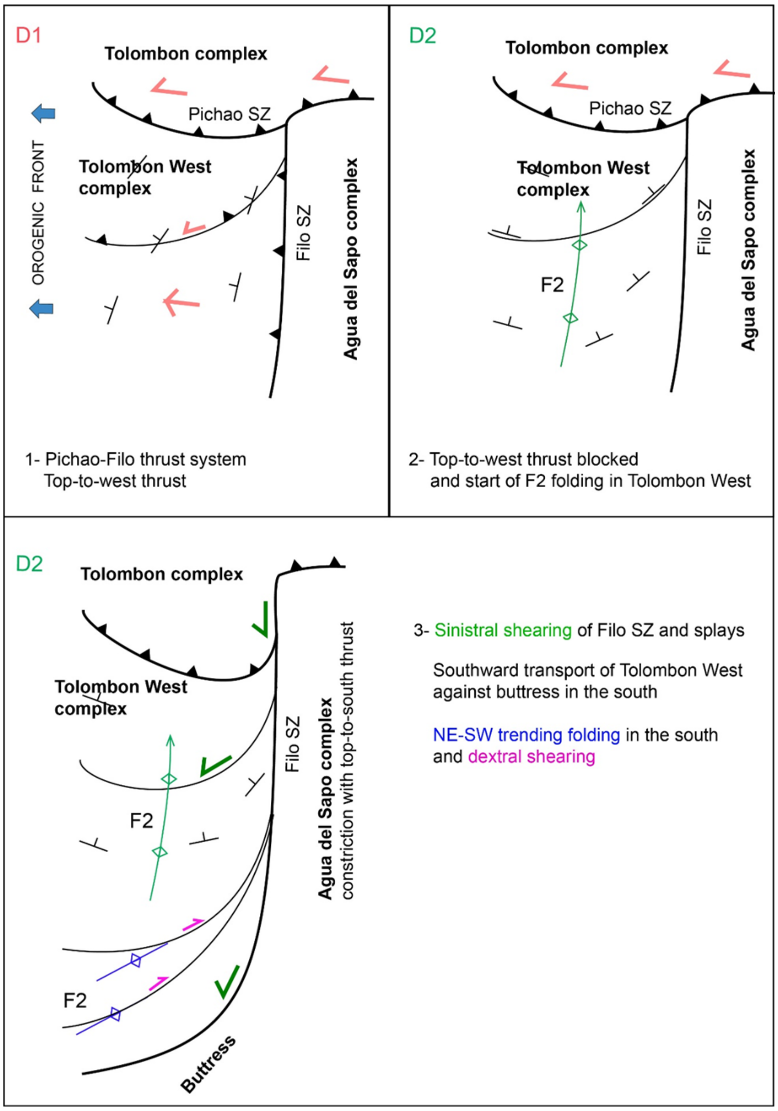

Figure 20– D1 and D2 in the Tolombon West complex. Upper half of figure showing Filo shear zone with top–to–west kinematics during D1. Top–to–west is blocked by the orogenic front, and the entire complex started to fold (F2). Lower half of figure showing D2 manifested first as sinistral shearing and southern transport of the complex. The southern transport against buttress trigger NE–SW folds and minor dextral shearing.

D2 in the Agua del Sapo complex

Unlike the Tolombon West complex, D2 in the Agua del Sapo complex is expressed as an intensive and pervasive shearing coupled with folding that strongly overprinted D1 structures. Most of the rocks are strongly sheared with a well–developed stretching lineation. These shear zones trend N–S, subparallel to the Filo shear zone, and have a similar N–S trending sub–horizontal stretching lineation. We have found that when shear zones dip east, they are dextral and when they dip west, they are sinistral, such as the dextral Talapaso and sinistral Catalino shear zones (Fig. 2). Thus, irrespective of their dip direction, they all record a top–to–south transport direction (Fig. 21). Also, these shear zones are parallel to the F2 open fold limbs, suggesting that they may represent a series of thrusts with top–to–south kinematics that were either folded during or after shearing.

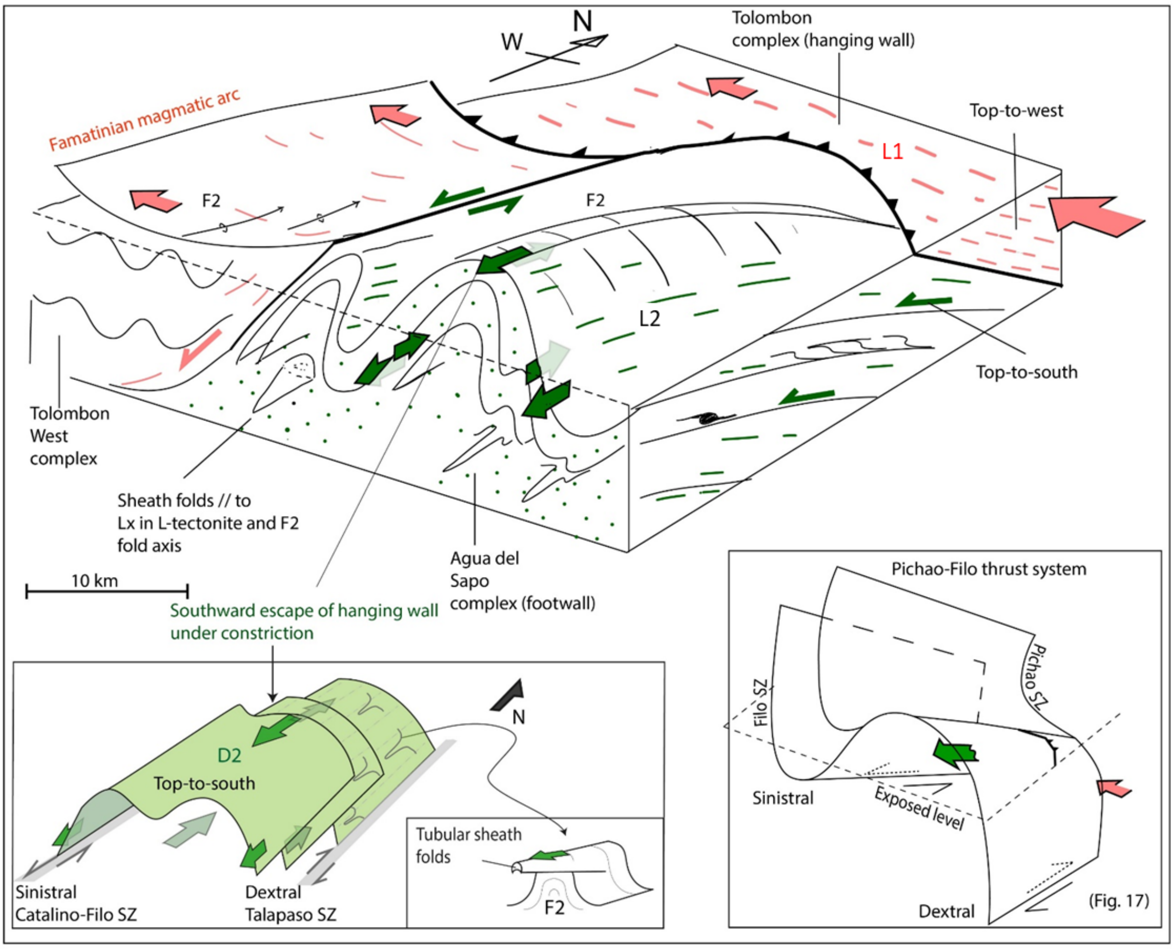

Figure 21– Kinematics of D2 in the Sierra de Quilmes with details of the Agua del Sapo complex structures. Open upright F2 folds with dextral and sinistral shear zones in both limbs defining a southward tectonic transport. F2 fold axis is parallel to L2 and L–tectonites indicating a non–coaxial constrictional regime. Inset in lower right corner depicts the complete Pichao–Filo thrust system (Fig. 18) folded and dipping to the north.

This top–to–south shearing is associated with L–tectonites and tubular sheath folds. L and L>S tectonites can be formed either by overprinting events with different maximum shortening directions (Ramsay and Huber, 1983) or by constriction (Sullivan, 2013). In our case, the orientation of anisotropic minerals (section 4.6.3.2) in combination with the quartz c–axis CPO pattern of their monomineralic domains, suggest constrictional conditions. In addition to that, tubular sheath folds have been also linked with coaxial or constrictional strain within shear zones (Sullivan, 2013). The bulk strain under which the sheath folds are formed (e.g., coaxial or non–coaxial strain) can be discriminated based on simple geometric parameters like the R' ratio, which express the ellipticity measured from the outer to the inner–most elliptical "rings" of individual fold closures (Alsop and Holdsworth, 2006). In areas where the tubular sheath folds dominate, the R' is > 1, suggesting pure shear or constrictional strain (Alsop and Holdsworth, 2012). Skjernaa (1989) proposed a model in which the formation of tubular folds is conditioned by the presence of non–cylindrical parent structures whose long axes are parallel to the later shearing direction. Following this concept, we suggest that the progenitor of the tubular folds in the complex was the N–S oriented F1 folds that progressively developed into sheath folds when overprinted by the D2 shearing event (Fig. 22).

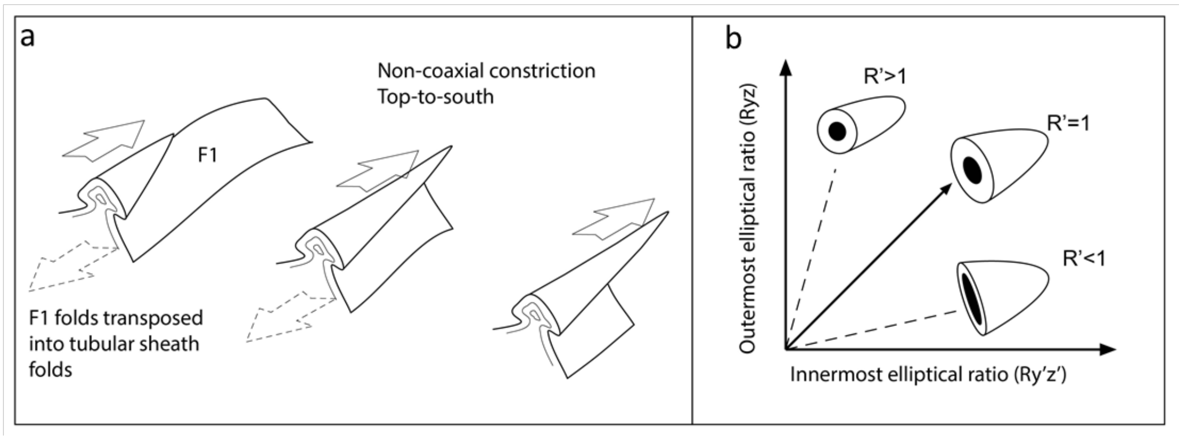

Figure 22– (a) Tubular sheath folds nucleated in F1 that is amplified during top–to–south shearing. Modified from Skjernaa (1989). (b) Diagram showing the relation between R' and bulk strain. Modified from Alsop (2006).

We conclude that the south–verging thrusts developed during a constrictional event, with a south directed stretching axis that is not only the transport direction of the thrusts but also the axes of sheath folds as well as of the F2 upright folds (Fig. 21). Therefore, D2 in this complex represents a case of non–coaxial constriction (Fletcher and Bartley, 1994). An analogy of this orogenic non–coaxial constriction is found in current glacial sheets. Bons (2016) mapped internal features in mechanically anisotropic ice sheets that form cylindrical and sheath folds sub–parallel to the ice flow when the glacier is channelled (constricted) into narrow valleys.

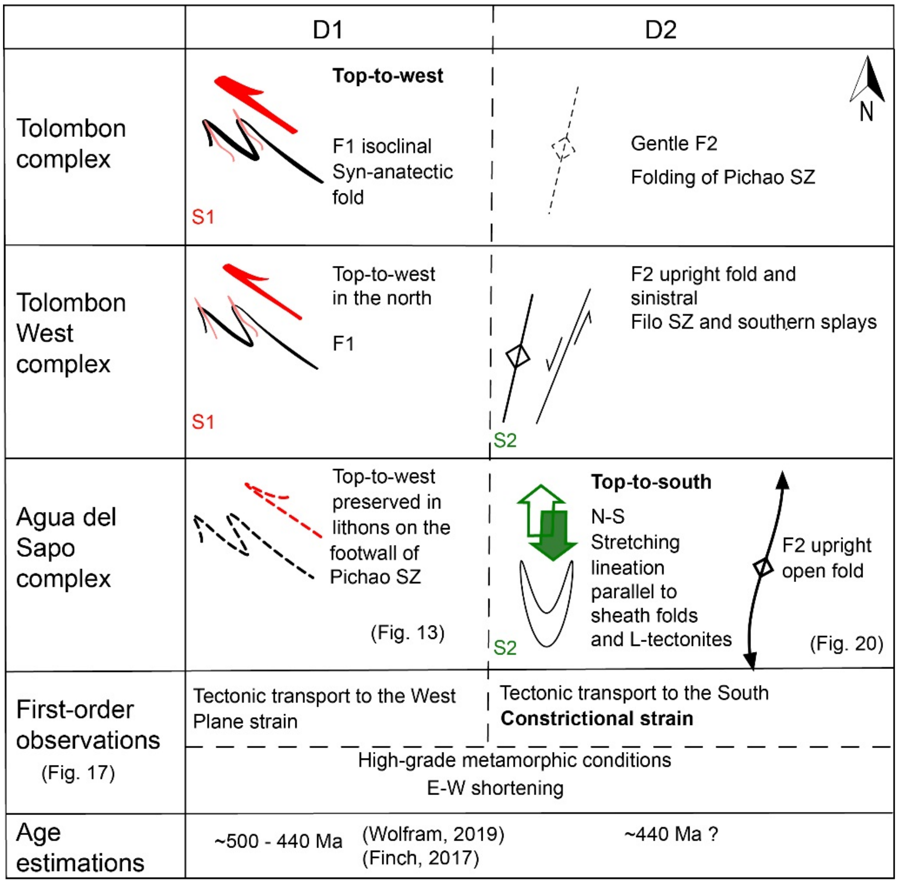

Figure 23– Summary of D1 and D2 in the three complexes. The age estimations are based on zircon ages from Wolfram (2019) on the Tolombon complex where anatexis lasted c. 60 Myr from c. 500–440 Ma.

5.3 Metamorphic conditions during D1 and D2

D1 was contemporaneous with anatexis in all complexes. In the Tolombon complex, the D1 top–to–west thrusting and folding are associated with peak metamorphic conditions and anatexis (Finch et al., 2015; Finch et al., 2016). This is supported by the presence of leucosomes parallel to the F1 axial planar foliation and shear planes, suggesting that folding and shearing controlled the orientation of leucosomes and melt migration paths, hence demonstrating anatexis coeval with E–W shortening. Finch (2017) envisaged a scenario where the rate of compaction of migmatites was faster than the melt flow, resulting in bands of increased porosity perpendicular to σ_1 that focused the melt, a mechanism studied and demonstrated by Weinberg (2015) in migmatites under shortening regimes. The same syn–anatectic features are also observed in the other complexes. In the northern part of the Tolombon West, where top–to–west shearing is preserved, leucosomes are focused in the shear planes (Fig. 5d), and F1 folds have leucosomes in their axial surface (Fig. 11a). In the Agua del Sapo complex D1 structures are strongly obliterated by D2, however there is evidence of the shear–assisted melt migration within lithons that preserve D1 structures (Fig. 8f).

D2 was also contemporaneous with anatexis in the Tolombon West and Agua del Sapo complexes. This is evidenced in leucosomes preferably oriented parallel to the upright F2 axial planar foliation in both complexes (Fig. 5b and Fig. 11d for Tolombon West and Fig. 8b and Fig. 14f for Agua del Sapo complex) and as melt pathways focused in the sillimanite–bearing sinistral shear zones in the Tolombon West complex. There are also several cases of later undeformed leucosome cross–cutting deformed metatexites (Fig. 5f for Tolombon West and Fig. 8d for Agua del Sapo complex). The mineral paragenesis associated with the F2 axial planar foliation (S_2) in both complexes is composed by biotite and sillimanite (Fig. 8c and Fig. 14d) supporting the idea that D2 evolved under high–grade conditions. Although the syn–anatectic D1 and D2 suggest protracted supra–solidus conditions in the Sierra de Quilmes, the record in the D2 shear zones extends this long record with evidence for lower temperature. D2 top–to–south shearing was active after peak metamorphism, during retrogression, as evidenced in the retrogressed mica fish (Fig. 14e).

Pichao shear zone

Microstructures and syn–kinematic mineral paragenesis of the Pichao shear zone and its sinistral splays in the Tolombon West complex can be used to qualitatively estimate the temperature of shearing. The record of grain boundary migration (GBM) in quartz from mylonite (Fig. 12b) suggests a range of temperatures between 500–700 °C (Passchier and Trouw, 2005; Stipp et al., 2002). Also, the size of the recrystallised grains of quartz and feldspar are expected to increase as a function of temperature. In the same mylonite that records GBM, the recrystallised quartz grain–size ranges between c. 200–400 µm, which is common in mylonite developed over c. 650 °C (Rosenberg and Handy, 2005; Rosenberg and Stünitz, 2003) or over c. 550 °C according to Stipp (2002). The coexistence of quartz GBM and bulging (BLG) in the same sample (Fig. 12c), suggest also shearing at lower temperatures (< 400 °C (Stipp et al., 2002). However, caution must be taken as the recrystallisation mechanism is strongly influenced by the presence of fluids, differential stress, and variable strain rate (Law, 2014; Passchier and Trouw, 2005).

The presence of stable syn–kinematic sillimanite in the shear zone suggests that shearing was active at upper amphibolite conditions (Büttner et al., 2005; Larrovere et al., 2008). We also found that the Ca–rich metasedimentary sequence was sheared by the Filo shear zone. The same epidote with allanite cores that we found in the Agua del Sapo complex was stable during sinistral shearing. This paragenesis is characteristic of retrogressed Ca–rich metasedimentary rocks where allanite and REE–rich epidote become stable below 700–750 °C (Budzyń et al., 2017; Budzyn et al., 2011; Janots et al., 2008; Wing et al., 2003).

Based on the combination of quartz microstructures and syn–kinematic mineral paragenesis, we estimate that the mylonite of the Filo shear zone developed under high–grade metamorphic conditions with temperatures over 550 °C suggested by the GBM of quartz and stable sillimanite. The shear zone was later reactivated or continuously sheared down to lower temperatures, probably during metamorphic retrogression as indicated by the sheared epidote–allanite, and through c. 400 °C as evidenced by the BLG of quartz. Important to note that the low–temperature shearing was probably weak and insufficient to completely erase the GBM features on the mylonite. Also, the thick ultramylonite in the Filo shear zone and its splays in the Tolombon West complex may represent a localisation of the strain after the high–temperature shearing. This is possibly the result of protracted shearing during cooling and exhumation of the whole package, similar to the case of the c. 1 km thick ultramylonite of the Pichao shear zone (Finch et al., 2015; Finch et al., 2017).

Tolombon West shear zones

The sinistral shear zones in the southern part of the complex are interpreted to be splays of the Pichao shear zone (section 4.2). These shear zones share the same characteristics in terms of microstructures and syn–kinematic mineral paragenesis, reflecting similar temperatures. The difference is naturally the thickness if compared with the Filo shear zone (Fig. 11b). Unlike these sinistral shear zones, the dextral shear zones in the southern part of the Tolombon West complex, developed under high–temperature amphibolite conditions as evidenced by the abundant syn–kinematic sillimanite but they do not record syn–kinematic retrogression mineralogy or formation of ultramylonite, suggesting that they were high–temperature, short–lived and lower strain structures.

Agua del Sapo shear zones

Similar temperature estimations can be done in the D2 shears of the Agua del Sapo complex. Here we noticed that K–feldspar is ductilely stretched, and when forming porphyroclasts it shows core–and–mantle textures with myrmekite in the interphase core–mantle (Fig. 14g). The core–mantle myrmekite texture is reported in granitic mylonites that underwent temperatures in the range of 450–600 °C (Passchier and Trouw, 2005; Rosenberg and Stünitz, 2003; Simpson, 1985; Simpson and Wintsch, 1989; Tullis and Yund, 1991). In terms of quartz microstructures, there is evidence for quartz sub–grain rotation (SGR) indicating temperatures between 400–500 °C (Passchier and Trouw, 2005; Stipp et al., 2002). Sometimes SGR progress to an oblique foliation, which develops mainly in the combined SGR and GBM recrystallisation regime (Passchier and Trouw, 2005). There are also more cases of quartz BLG than in the Filo shear zone, and quartz ribbons along the main mylonitic foliation and areas where quartz crystals have straight grain boundaries and lack undulose extinction which is typical of static recrystallisation, or grain boundary area reduction (GBAR). The CPO pattern of quartz–rich domains is strong, and it tends to form narrow single–girdles. Estimations of deformation temperature from quartz CPO from mylonites show that the quartz c–axis girdles evolve from wide double–girdle in greenschist facies to narrow single–girdles in amphibolite facies (Barth et al., 2010; Sullivan and Beane, 2010), hence allowing us to infer temperature strain conditions. Like in the Pichao shear zone, sillimanite forms S/C shear bands, and allanite–cored epidote is strained in the Ca–rich rocks. Also, in this complex, the shear zones have abundant mica fish of muscovite (Fig. 14e).

Based on the above, the D2 shear zones in the Agua del Sapo complex record temperatures ranging from c. 600 ºC, expressed by the recrystallised K–feldspars and syn–kinematic sillimanite to c. 400 ºC based on the BLG of quartz, similar to the Filo shear zone. However, unlike in the Filo shear zone, BLG is more frequent, and the quartz seems to have recovered by static recrystallisation as evidenced by GBAR. The latter will take place in quartz towards lower internal energy configurations, common in rocks that went through protracted high temperatures after deformation stopped or water was present along grain boundaries (Heilbronner and Tullis, 2006; Passchier and Trouw, 2005). Also, the syn–kinematic muscovite suggest that these shear zones were active during the later retrogression of the complex.

5.4 Origin of D2

The Sierra de Quilmes represents the mid–crustal levels of the Ordovician Famatinian back–arc. Back–arcs, regardless of their tectonic regime (e.g., extension or shortening), are wide hot and rheological weak parts of the crust, dominated by HT–LP metamorphic conditions, susceptible to localise the deformation from convergence (Hyndman et al., 2005). When in a shortening tectonic mode, back–arcs may be too weak to build up a thick crust and high orogens (Jamieson and

Beaumont, 2013). Instead, these hot and weak sections of the crust are prone to lateral and transversal spread (Beaumont et al., 2010; Cruden et al., 2006; Jamieson and Beaumont, 2013) and maintain a subdued topography. The magnitude of this flow depends on a delicate balance between crustal thickening and gravity–driven flattening (Jamieson et al., 2011). For example, if the force from shortening rate is greater than the vertical gravitational forces, crustal thickening and topographic growth would take place, and the opposite will happen in hot orogens where lateral flow tends to maintain a subdued topography forming plateaus underlain by a weak ductile crust (Hyndman and Currie, 2011). A classic example of this is the thermally softened Variscan orogen that Franke (2014) described as “failed” orogen that was unfit for stacking and isostatic uplift.

The Sierra de Quilmes records protracted high–temperature conditions that were probably inherited from a previous extensional phase of the back–arc (Weinberg et al., 2018). These high–temperatures are well documented in the hanging wall Tolombon complex where 60 Myr of crustal melting are inferred from zircon U/Pb ages (505–440 Ma) (Wolfram et al., 2019). At some point during that time, the Famatinian back–arc switched from extension to the shortening phase (the Oclóyic phase), which is represented by our D1 and D2 deformational events. Finch (2017) demonstrated that the transport to the west in the hanging wall Tolombon complex (D1), was syn–anatectic and that the thermal peak was between c. 490–460 Ma, as indicated by U/Pb ages of monazite.

We argue that the Sierra de Quilmes represents a mid–crustal section of the thermally–mature Famatinian continental back–arc that during the Oclóyic phase evolved from a stage of crustal thickening (D1) where the three HT–LP complexes were stacked over each other. This was followed by a second event (D2) that started after the thrust–to–west was impeded, most likely by the thicker crust of the Famatinian magmatic arc located to the west (Fig. 1), and the entire thrust system started to fold. We propose that this second event was restricted to the Tolombon West and Agua del Sapo complexes. In the former manifested mostly by folding, and in the latter by top-to-south shearing, parallel to the orogen and under a constrictional regime. The constriction in the Agua del Sapo complex was caused by the interplay of equivalent tectonic forces (E–W horizontal shortening), and gravitational forces (vertical load of the hanging wall complexes). The top-to-south shearing under constriction (D2) was, therefore, the structural response of the weaker and ductile footwall Agua del Sapo complex to the persistent E–W shortening convergence forces combined with the loading of the more competent granulite facies Tolombon complex.

5.5 The Pichao–Filo thrust system within the Famatinian orogeny context

The Pichao–Filo thrust system shares some characteristics with other Oclóyic shear zones (Fig. 1b). They are all unusually wide, like the 10–15 km–wide Guacha Corral shear zone (Martino, 2003; Otamendi et al., 2004; Semenov and Weinberg, 2017; Whitmeyer and Simpson, 2003), the 1–4 km–wide La Chilca shear zone (Larrovere et al., 2008), the 3 km–wide Pichao shear zone (Finch et al., 2015), or the 2 km–wide TIPA shear zone (Höckenreiner et al., 2003). They have west vergence and record tectonic transport to the magmatic arc and trench, and they thrust deeper hotter HT–LP blocks over shallower and colder rocks, with no evidence of high–pressure metamorphism. The unusual widths of these shear zones suggest they were long–lived structures (Semenov and Weinberg, 2017; Weinberg et al., 2018). Also, Finch (2016) found that hydrolytic weakening was the mechanism that promoted the development of the 1–km–thick ultramylonite in the Pichao shear zone. As with some of the other Oclóyic shear zones, the Pichao–Filo thrust system could have inherited the west vergence from the previous Pampean forearc (Weinberg et al., 2018), or from the extensional phase of the Famatinian orogenic cycle (Büttner, 2009).

6 Conclusion

The Sierra de Quilmes reflects two major deformational events that occurred during the shortening stage of the Famatinian orogenic cycle, the Oclóyic phase. The first event, D1, is characterised by a high–temperature syn–anatectic thrust to the west, defined as the Pichao–Filo thrust system that juxtaposed three HT–LP metamorphic complexes. This thrusting to the west was at some point impeded, probably by the thicker crust to the west where the magmatic arc was, and the entire package started to fold, leading to the second event, D2. The nature of this event changes across the complexes. While it is not recognised in the hanging wall Tolombon complex, it is dominated by syn–anatectic folding in the diatexite–rich Tolombon West complex, and by intense shearing in the footwall Agua del Sapo complex. This shearing represents south–verging thrusts that were coeval with upright syn–anatectic folding under a constrictional regime, as indicated by the stretching lineation–parallel tubular sheath folds and L–tectonites, thus defining a non–coaxial constrictional event. We argue that the continuous and unidirectional east–west convergence was resolved first as a west–verging thrusting that thickened the crust to a point where the orogenic edifice could no longer sustain thickening. At this point, the deeper section, represented here in the Agua del Sapo complex, reacted by shearing with a top-to-south sense under constriction, parallel to the orogen. Hence the footwall was structurally active after the hanging wall ceased, recording a different late phase of high–T deformation.

This is the first reported case of decoupling of deformation at this scale in the Famatinian orogen. We envisage the Oclóyic phase of the Famatinian orogen as a case of long–lived large–hot orogen that was not able to sustain high topography as it was too weak, forcing the orogen to spread laterally similar to the case of the thermally weaken Grenvillian or Variscan orogens (Beaumont et al., 2010; Jamieson and Beaumont, 2013).

References

Aceñolaza, F. G., H. Miller, and A. J. Toselli, 2002, Proterozoic - Early Paleozoic evolution in western South America - A discussion: Tectonophysics, v. 354, p. 121-137.

Acosta Nagle, A. E., and J. P. López, 2014, Geology and Petrology of Tres Cerritos Granite, Southern Extreme Of The Quilmes Range, Catamarca Province: Revista de la Asociacion Geologica Argentina, v. 71, p. 434-443.

Adams, C. J., H. Miller, F. G. Aceñolaza, A. J. Toselli, and W. L. Griffin, 2011, The Pacific Gondwana margin in the late Neoproterozoic–early Paleozoic: Detrital zircon U–Pb ages from metasediments in northwest Argentina reveal their maximum age, provenance and tectonic setting: Gondwana Research, v. 19, p. 71-83.

Alessio, K. L., M. Hand, D. E. Kelsey, M. A. Williams, L. J. Morrissey, and K. Barovich, 2018, Conservation of deep crustal heat production: Geology, v. 46, p. 335-338.

Alsop, G. I., and R. E. Holdsworth, 2006, Sheath folds as discriminators of bulk strain type: Journal of Structural Geology, v. 28, p. 1588-1606.

Alsop, G. I., and R. E. Holdsworth, 2012, The three dimensional shape and localisation of deformation within multilayer sheath folds: Journal of Structural Geology, v. 44, p. 110-128.

Astini, R. A., 1998, Stratigraphical evidence supporting the rifting, drifting and collision of the Laurentian Precordillera terrane of western Argentina.: The Geological Society.

Astini, R. A., J. L. Benedetto, and N. E. Vaccari, 1995, The early Paleozoic evolution of the Argentine Precordillera as a Laurentian rifted, drifted, and collided terrane: A geodynamic model: Geological Society of America Bulletin, v. 107, p. 253-273.

Bahlburg, H., and J. Berndt, 2016, Provenance from zircon U-Pb age distributions in crustally contaminated granitoids: Sedimentary Geology, v. 336, p. 161-170.

Bahlburg, H., J. Berndt, and A. Gerdes, 2016, The ages and tectonic setting of the Faja Eruptiva de la Puna Oriental, Ordovician, NW Argentina: Lithos, v. 256-257, p. 41-54.

Bahlburg, H., and C. Breitkreuz, 1991, Paleozoic evolution of active margin basins in the southern Central Andes (northwestern Argentina and northern Chile): Journal of South American Earth Sciences, v. 4, p. 171-188.

Bajolet, F., D. Chardon, J. Martinod, D. Gapais, and J. J. Kermarrec, 2015, Synconvergence flow inside and at the margin of orogenic plateaus: Lithospheric-scale experimental approach: Journal of Geophysical Research B: Solid Earth, v. 120, p. 6634-6657.

Barth, N. C., B. R. Hacker, G. G. E. Seward, E. O. Walsh, D. Young, and S. Johnston, 2010, Strain within the ultrahigh-pressure Western Gneiss region of Norway recorded by quartz CPOs, Geological Society Special Publication, p. 663-685.

Beaumont, C., R. Jamieson, and M. Nguyen, 2010, Models of large, hot orogens containing a collage of reworked and accreted terranes: Canadian Journal of Earth Sciences, v. 47, p. 485-515.

Bons, P. D., D. Jansen, F. Mundel, C. C. Bauer, T. Binder, O. Eisen, M. W. Jessell, M. G. Llorens, F. Steinbach, D. Steinhage, and I. Weikusat, 2016, Converging flow and anisotropy cause large-scale folding in Greenland's ice sheet: Nature Communications, v. 7.

Bouhallier, H., D. Chardon, and P. Choukroune, 1995, Strain patterns in Archaean dome-and-basin structures: The Dharwar craton (Karnataka, South India): Earth and Planetary Science Letters, v. 135, p. 57-75.

Braathen, A., O. Nordgulen, P. T. Osmundsen, T. B. Andersen, A. Solli, and D. Roberts, 2000, Devonian, orogen-parallel, opposed extension in the Central Norwegian Caledonides: Geology, v. 28, p. 615-618.

Budzyń, B., D. E. Harlov, G. A. Kozub-Budzyń, and J. Majka, 2017, Experimental constraints on the relative stabilities of the two systems monazite-(Ce) – allanite-(Ce) – fluorapatite and xenotime-(Y) – (Y,HREE)-rich epidote – (Y,HREE)-rich fluorapatite, in high Ca and Na-Ca environments under P-T conditions of 200–1000 MPa and 450–750 °C: Mineralogy and Petrology, v. 111, p. 183-217.

Budzyn, B., D. E. Harlov, M. L. Williams, and M. J. Jercinovic, 2011, Experimental determination of stability relations between monazite, fluorapatite, allanite, and REE-epidote as a function of pressure, temperature, and fluid composition: American Mineralogist, v. 96, p. 1547-1567.

Burg, J. P., and M. Ford, 1997, Orogeny through time: An overview, Geological Society Special Publication, p. 1-17.

Büttner, S. H., 2009, The Ordovician Sierras Pampeanas–Puna basin connection: Basement thinning and basin formation in the Proto-Andean back-arc: Tectonophysics, v. 477, p. 278-291.

Büttner, S. H., J. Glodny, F. Lucassen, K. Wemmer, S. Erdmann, R. Handler, and G. Franz, 2005, Ordovician metamorphism and plutonism in the Sierra de Quilmes metamorphic complex: Implications for the tectonic setting of the northern Sierras Pampeanas (NW Argentina): Lithos, v. 83, p. 143-181.

Carreras, J., J. W. Cosgrove, and E. Druguet, 2013, Strain partitioning in banded and/or anisotropic rocks: Implications for inferring tectonic regimes: Journal of Structural Geology, v. 50, p. 7-21.

Casquet, C., C. W. Rapela, R. J. Pankhurst, E. G. Baldo, C. Galindo, C. M. Fanning, J. A. Dahlquist, and J. Saavedra, 2012, A history of Proterozoic terranes in southern South America: From Rodinia to Gondwana: Geoscience Frontiers, v. 3, p. 137-145.

Cawood, P. A., 2005, Terra Australis Orogen: Rodinia breakup and development of the Pacific and Iapetus margins of Gondwana during the Neoproterozoic and Paleozoic: Earth-Science Reviews, v. 69, p. 249-279.

Chardon, D., P. Choukroune, and M. Jayananda, 1996, Strain patterns, décollement and incipient sagducted greenstone terrains in the Archaean Dharwar craton (south India): Journal of Structural Geology, v. 18, p. 991-1004.

Chardon, D., D. Gapais, and F. Cagnard, 2009, Flow of ultra-hot orogens: A view from the Precambrian, clues for the Phanerozoic: Tectonophysics, v. 477, p. 105-118.

Chardon, D., and M. Jayananda, 2008, Three-dimensional field perspective on deformation, flow, and growth of the lower continental crust (Dharwar craton, India): Tectonics, v. 27.

Chardon, D., M. Jayananda, and J. J. Peucat, 2011, Lateral constrictional flow of hot orogenic crust: Insights from the Neoarchean of south India, geological and geophysical implications for orogenic plateaux: Geochemistry, Geophysics, Geosystems, v. 12.

Collins, W. J., 2002, Hot orogens, tectonic switching, and creation of continental crust: Geology, v. 30, p. 535-538.

Condie, K. C., 2007, Accretionary orogens in space and time, Memoir of the Geological Society of America, p. 145-158.

Cruden, A. R., M. H. B. Nasseri, and R. Pysklywec, 2006, Surface topography and internal strain variation in wide hot orogens from three-dimensional analogue and two-dimensional numerical vice models, Geological Society Special Publication, p. 79-104.

Curie, C. A., and R. D. Hyndman, 2006, The thermal structure of subduction zone back arcs: Journal of Geophysical Research: Solid Earth, v. 111.

Dalla Salda, L. H., M. G. Lopez de Luchi, C. A. Cingolani, and R. Varela, 1998, Laurentia-Gondwana collision: the origin of the Famatinian-Appalachian Orogenic Belt (a review): Geological Society, London, Special Publications, v. 142, p. 219-234.

De Los Hoyos, C. R., A. P. Willner, M. A. Larrovere, J. N. Rossi, A. J. Toselli, and M. A. S. Basei, 2011, Tectonothermal evolution and exhumation history of the paleozoic Proto-andean gondwana margin crust: The famatinian belt in NW argentina: Gondwana Research, v. 20, p. 309-324.

Dewey, J. F., 2002, Transtension in arcs and orogens: International Geology Review, v. 44, p. 402-439.

Ducea, M. N., G. W. Bergantz, J. L. Crowley, and J. Otamendi, 2017, Ultrafast magmatic buildup and diversification to produce continental crust during subduction: Geology, v. 45, p. 235-238.

Ellis, S., C. Beaumont, R. A. Jamieson, and G. Quinlan, 1998, Continental collision including a weak zone: The vise model and its application to the Newfoundland Appalachians: Canadian Journal of Earth Sciences, v. 35, p. 1323-1346.

Escayola, M. P., C. R. van Staal, and W. J. Davis, 2011, The age and tectonic setting of the Puncoviscana Formation in northwestern Argentina: An accretionary complex related to Early Cambrian closure of the Puncoviscana Ocean and accretion of the Arequipa-Antofalla block: Journal of South American Earth Sciences, v. 32, p. 438-459.

Finch, M. A., R. F. Weinberg, M. G. Fuentes, P. Hasalová, and R. Becchio, 2015, One kilometre-thick ultramylonite, Sierra de Quilmes, Sierras Pampeanas, NW Argentina: Journal of Structural Geology, v. 72, p. 33-54.

Finch, M. A., R. F. Weinberg, P. Hasalová, R. Becchio, M. G. Fuentes, and A. Kennedy, 2017, Tectono-metamorphic evolution of a convergent back-arc: The Famatinian orogen, Sierra de Quilmes, Sierras Pampeanas, NW Argentina: Bulletin of the Geological Society of America, v. 129, p. 1602–1621.

Finch, M. A., R. F. Weinberg, and N. J. R. Hunter, 2016, Water loss and the origin of thick ultramylonites: Geology, v. 44, p. 599-602.

Fletcher, J. M., and J. M. Bartley, 1994, Constrictional strain in a non-coaxial shear zone: implications for fold and rock fabric development, central mojave metamorphic core complex, california: Journal of Structural Geology, v. 16, p. 555-570.

Franke, W., 2014, Topography of the Variscan orogen in Europe: Failed-not collapsed: International Journal of Earth Sciences, v. 103, p. 1471-1499.

Hajná, J., J. Žák, V. Kachlík, and M. Chadima, 2012, Deciphering the Variscan tectonothermal overprint and deformation partitioning in the Cadomian basement of the Teplá-Barrandian unit, Bohemian Massif: International Journal of Earth Sciences, v. 101, p. 1855-1873.

Handy, M. R., J. Babist, R. Wagner, C. Rosenberg, and M. Konrad, 2005, Decoupling and its relation to strain partitioning in continental lithosphere: Insight from the Periadriatic fault system (European Alps), Geological Society Special Publication, p. 249-276.

Heilbronner, R., and J. Tullis, 2006, Evolution of c axis pole figures and grain size during dynamic recrystallization: Results from experimentally sheared quartzite: Journal of Geophysical Research: Solid Earth, v. 111.

Heuret, A., and S. Lallemand, 2005, Plate motions, slab dynamics and back-arc deformation: Physics of the Earth and Planetary Interiors, v. 149, p. 31-51.

Höckenreiner, M., F. Söllner, and H. Miller, 2003, Dating the TIPA shear zone: An Early Devonian terrane boundary between the Famatinian and Pampean systems (NW Argentina): Journal of South American Earth Sciences, v. 16, p. 45-66.

Hunter, N. J. R., P. Hasalová, R. F. Weinberg, and C. J. L. Wilson, 2016, Fabric controls on strain accommodation in naturally deformed mylonites: The influence of interconnected micaceous layers: Journal of Structural Geology, v. 83, p. 180-193.

Hyndman, R., and C. Currie, 2011, Why is the North America Cordillera high? Hot backarcs, thermal isostasy, and mountain belts: Geology, v. 39, p. 783-786.

Hyndman, R. D., C. A. Currie, and S. P. Mazzotti, 2005, Subduction zone backarcs, mobile belts, and orogenic heat: GSA Today, v. 15, p. 4-10.

Jamieson, R. A., and C. Beaumont, 2013, On the origin of orogens: Bulletin of the Geological Society of America, v. 125, p. 1671-1702.

Jamieson, R. A., M. J. Unsworth, N. B. W. Harris, C. L. Rosenberg, and K. Schulmann, 2011, Crustal melting and the flow of mountains: Elements, v. 7, p. 253-260.

Janots, E., M. Engi, A. Berger, J. Allaz, J. O. Schwarz, and C. Spandler, 2008, Prograde metamorphic sequence of REE minerals in pelitic rocks of the Central Alps: Implications for allanite-monazite-xenotime phase relations from 250 to 610°C: Journal of Metamorphic Geology, v. 26, p. 509-526.

Jolivet, L., V. Famin, C. Mehl, T. Parra, C. Aubourg, R. Hébert, and P. Philippot, 2004, Strain localization during crustal-scale boudinage to form extensional metamorphic domes in the Aegean Sea, v. 380.

Jones, R., and P. W. Tanner, 1995, Strain partitioning in transpression zones: Journal of Structural Geology, v. 17, p. 793-802.

Kilian, R., R. Heilbronner, and H. Stünitz, 2011, Quartz grain size reduction in a granitoid rock and the transition from dislocation to diffusion creep: Journal of Structural Geology, v. 33, p. 1265-1284.

Larrovere, M. A., P. H. Alasino, and E. G. Baldo, 2016, The double-vergent ductile shear zone of northwestern sierra de Velasco: Deformation of the middle crust during the Famatinian orogeny: Revista de la Asociacion Geologica Argentina, v. 73, p. 117-133.

Larrovere, M. A., C. R. de los Hoyos, A. J. Toselli, J. N. Rossi, M. A. S. Basei, and M. E. Belmar, 2011, High T/P evolution and metamorphic ages of the migmatitic basement of northern Sierras Pampeanas, Argentina: Characterization of a mid-crustal segment of the Famatinian belt: Journal of South American Earth Sciences, v. 31, p. 279-297.

Larrovere, M. A., A. Toselli, and J. N. Rossi De Toselli, 2008, Petrology and structure of La Chilca Shear Zone, Catamarca, v. 63, 254-263 p.

Law, R. D., 2014, Deformation thermometry based on quartz c-axis fabrics and recrystallization microstructures: A review: Journal of Structural Geology, v. 66, p. 129-161.

Lister, G., and M. Forster, 2009, Tectonic mode switches and the nature of orogenesis: Lithos, v. 113, p. 274-291.

Lister, G. S., and B. E. Hobbs, 1980, The simulation of fabric development during plastic deformation and its application to quartzite: the influence of deformation history: Journal of Structural Geology, v. 2, p. 355-370.

Lister, G. S., and P. F. Williams, 1979, Fabric development in shear zones: theoretical controls and observed phenomena: Journal of Structural Geology, v. 1, p. 283-297.

López, J. P., U. Altenberger, L. I. Bellos, and C. Günter, 2019, The Cumbres Calchaquíes Range (NW-Argentina). Geochemical sedimentary provenance, tectonic setting and metamorphic evolution of a Neoproterozoic sedimentary basin: Journal of South American Earth Sciences.

Lucassen, F., R. Becchio, H. G. Wilke, G. Franz, M. F. Thirlwall, J. Viramonte, and K. Wemmer, 2000, Proterozoic-Paleozoic development of the basement of the Central Andes (18-26°S) - A mobile belt of the South American craton: Journal of South American Earth Sciences, v. 13, p. 697-715.

Malavieille, J., 1993, Late Orogenic extension in mountain belts: Insights from the basin and range and the Late Paleozoic Variscan Belt: Tectonics, v. 12, p. 1115-1130.

Mancktelow, N. S., and T. L. Pavlis, 1994, Fold‐fault relationships in low‐angle detachment systems: Tectonics, v. 13, p. 668-685.

Martino, R. D., 2003, Ductile deformation shear belts at Pampean Ranges near Córdoba, Central Argentina: A review: Revista de la Asociacion Geologica Argentina, v. 58, p. 549-571.

Mulcahy, S. R., S. M. Roeske, W. C. McClelland, J. R. Ellis, F. Jourdan, P. R. Renne, J. D. Vervoort, and G. I. Vujovich, 2014, Multiple migmatite events and cooling from granulite facies metamorphism within the Famatina arc margin of northwest Argentina: Tectonics, v. 33, p. 1-25.

Omarini, R. H., R. J. Sureda, H. J. Götze, A. Seilacher, and F. Pflüger, 1999, Puncoviscana folded belt in northwestern Argentina: Testimony of Late Proterozoic Rodinia fragmentation and pre-Gondwana collisional episodes: International Journal of Earth Sciences, v. 88, p. 76-97.

Otamendi, J. E., P. A. Castellarini, M. R. Fagiano, A. H. Demichelis, and A. M. Tibaldi, 2004, Cambrian to Devonian Geologic Evolution of the Sierra de Comechingones, Eastern Sierras Pampeanas, Argentina: Evidence for the Development and Exhumation of Continental Crust on the Proto-Pacific Margin of Gondwana: Gondwana Research, v. 7, p. 1143-1155.

Pankhurst, R. J., and C. W. Rapela, 1998, The proto-Andean margin of Gondwana: an introduction: Geological Society, London, Special Publications, v. 142, p. 1-9.

Pankhurst, R. J., C. W. Rapela, and C. M. Fanning, 2000, Age and origin of coeval TTG, I- and S-type granites in the Famatinian belt of NW Argentina, Special Paper of the Geological Society of America, p. 151-168.

Pankhurst, R. J., C. W. Rapela, J. Saavedra, E. Baldo, J. Dahlquist, I. Pascua, and C. M. Fanning, 1998, The Famatinian magmatic arc in the central Sierras Pampeanas: an Early to Mid-Ordovician continental arc on the Gondwana margin: Geological Society, London, Special Publications, v. 142, p. 343-367.

Parsons, A. J., E. C. Ferré, R. D. Law, G. E. Lloyd, R. J. Phillips, and M. P. Searle, 2016, Orogen-parallel deformation of the Himalayan midcrust: Insights from structural and magnetic fabric analyses of the Greater Himalayan Sequence, Annapurna-Dhaulagiri Himalaya, central Nepal: Tectonics, v. 35, p. 2515-2537.

Passchier, C. W., and R. A. J. Trouw, 2005, Microtectonics: Microtectonics, Springer Berlin Heidelberg, 1-366 p.

Pennacchioni, G., L. Menegon, B. Leiss, F. Nestola, and G. Bromiley, 2010, Development of crystallographic preferred orientation and microstructure during plastic deformation of natural coarse-grained quartz veins: Journal of Geophysical Research: Solid Earth, v. 115.

Peternell, M., P. Hasalová, C. J. L. Wilson, S. Piazolo, and K. Schulmann, 2010, Evaluating quartz crystallographic preferred orientations and the role of deformation partitioning using EBSD and fabric analyser techniques: Journal of Structural Geology, v. 32, p. 803-817.

Piñán-Llamas, A., and C. Simpson, 2006, Deformation of Gondwana margin turbidites during the Pampean orogeny, north-central Argentina: Bulletin of the Geological Society of America, v. 118, p. 1270-1279.

Piñán-Llamas, A., and C. Simpson, 2009, Primary structure influence on compositional banding in psammites: Examples from the Puncoviscana Formation, north-central Argentina: Journal of Structural Geology, v. 31, p. 55-71.

Ramos, V. A., 2004, Cuyania, an Exotic Block to Gondwana: Review of a Historical Success and the Present Problems: Gondwana Research, v. 7, p. 1009-1026.

Ramos, V. A., 2008, The basement of the Central Andes: The arequipa and related terranes, *in* R. Jeanloz, A. L. Albee, K. C. Burke, and K. H. Freeman, eds., Annual Review of Earth and Planetary Sciences, p. 289-324.

Ramos, V. A., R. D. Dallmeyer, and G. Vujovich, 1998, Time constraints on the Early Palaeozoic docking of the Precordillera, central Argentina, Geological Society Special Publication, p. 143-158.

Ramos, V. A., M. Escayola, D. I. Mutti, and G. I. Vujovich, 2000, Proterozoic-early Paleozoic ophiolites of the Andean basement of southern South America, Special Paper of the Geological Society of America, p. 331-349.

Ramos, V. A., T. E. Jordan, R. W. Allmendinger, C. Mpodozis, S. M. Kay, J. M. Cortés, and M. Palma, 1986, Paleozoic terranes of the central Argentine-Chilean Andes: Tectonics, v. 5, p. 855-880.

Ramos, V. A., G. Vujovich, R. Martino, and J. Otamendi, 2010, Pampia: A large cratonic block missing in the Rodinia supercontinent: Journal of Geodynamics, v. 50, p. 243-255.

Ramsay, J. G., and M. I. Huber, 1983, The techniques of modern structural geology. Volume 1: strain analysis: The techniques of modern structural geology. Volume 1: strain analysis.

Rapela, C. W., 1976, El Basamento Metamorfico de la Region de Cafayate, Provincia de Salta. Aspectos Petrologicos y Geoquimicos: Revista de la Asociacion Geologica Argentina, v. 3, p. 203-222.

Rapela, C. W., B. Coira, A. Toselli, and J. Saavedra, 1992, The lower paleozoic magmatism of southwestern gondwana and the evolution of the famatinian orogen: International Geology Review, v. 34, p. 1081-1142.

Rapela, C. W., R. J. Pankhurst, C. Casquet, E. Baldo, J. Saavedra, and C. Galindo, 1998a, Early evolution of the Proto-Andean margin of South America: Geology, v. 26, p. 707.

Rapela, C. W., R. J. Pankhurst, C. Casquet, E. Baldo, J. Saavedra, C. Galindo, and C. M. Fanning, 1998b, The Pampean Orogeny of the southern proto-Andes: Cambrian continental collision in the Sierras de Cordoba: Geological Society, London, Special Publications, v. 142, p. 181-217.

Rapela, C. W., S. O. Verdecchia, C. Casquet, R. J. Pankhurst, E. G. Baldo, C. Galindo, J. A. Murra, J. A. Dahlquist, and C. M. Fanning, 2015, Identifying Laurentian and SW Gondwana sources in the Neoproterozoic to Early Paleozoic metasedimentary rocks of the Sierras Pampeanas: Paleogeographic and tectonic implications: Gondwana Research.

Rosenberg, C. L., and M. R. Handy, 2005, Experimental deformation of partially melted granite revisited: Implications for the continental crust: Journal of Metamorphic Geology, v. 23, p. 19-28.

Rosenberg, C. L., and H. Stünitz, 2003, Deformation and recrystallization of plagioclase along a temperature gradient: An example from the Bergell tonalite: Journal of Structural Geology, v. 25, p. 389-408.

Rossi, J., and A. Toselli, 1976, Migmatization y Metamorfismo en el basamento de la Sierra de Quilmes, al Oeste de Colalao del Valle, Tucuman: Revista de la Asociacion Geologica Argentina, v. 2, p. 83-94.

Rubio Pascual, F. J., A. López-Carmona, and R. Arenas, 2016, Thickening vs. extension in the Variscan belt: P–T modelling in the Central Iberian autochthon: Tectonophysics, v. 681, p. 144-158.

Sawyer, E. W., 2008, Atlas of Migmatites, NRC Research Press and Mineralogical Association of Canada, 387 p.

Schwartz, J. J., L. P. Gromet, and R. Miró, 2008, Timing and duration of the calc-alkaline arc of the pampean orogeny: Implications for the late neoproterozoic to cambrian evolution of Western Gondwana: Journal of Geology, v. 116, p. 39-61.

Semenov, I., and R. F. Weinberg, 2017, A major mid-crustal decollement of the Paleozoic convergent margin of western Gondwana: The Guacha Corral shear zone, Argentina: Journal of Structural Geology, v. 103, p. 75-99.

Simpson, C., 1985, Deformation of granitic rocks across the brittle-ductile transition: Journal of Structural Geology, v. 7, p. 503-511.

Simpson, C., S. J. Whitmeyer, D. G. De Paor, L. P. Gromet, R. Miro, M. A. Krol, and H. Short, 2001, Sequential ductile to brittle reactivation of major fault zones along the accretionary margin of Gondwana in Central Argentina: Geological Society, London, Special Publications, v. 186, p. 233-255.

Simpson, C., and R. P. Wintsch, 1989, Evidence for deformation ‐ induced K ‐ feldspar replacement by myrmekite: Journal of Metamorphic Geology, v. 7, p. 261-275.

Skjernaa, L., 1989, Tubular folds and sheath folds: definitions and conceptual models for their development, with examples from the Grapesvare area, northern Sweden: Journal of Structural Geology, v. 11, p. 689-703.

Sola, A. M., R. A. Becchio, and M. M. Pimentel, 2013, Petrogenesis of migmatites and leucogranites from Sierra de Molinos, Salta, Northwest Argentina: A petrologic and geochemical study: Lithos, v. 177, p. 470-491.
Stipp, M., H. Stünitz, R. Heilbronner, and S. M. Schmid, 2002, The eastern Tonale fault zone: A 'natural laboratory' for crystal plastic deformation of quartz over a temperature range from 250 to 700 °C: Journal of Structural Geology, v. 24, p. 1861-1884.
Sullivan, W. A., 2009, Kinematic significance of L tectonites in the footwall of a major terrane-bounding thrust fault, Klamath Mountains, California, USA: Journal of Structural Geology, v. 31, p. 1197-1211.
Sullivan, W. A., 2013, L tectonites: Journal of Structural Geology, v. 50, p. 161-175.
Sullivan, W. A., and R. J. Beane, 2010, Asymmetrical quartz crystallographic fabrics formed during constrictional deformation: Journal of Structural Geology, v. 32, p. 1430-1443.
Sullivan, W. A., and R. D. Law, 2007, Deformation path partitioning within the transpressional White Mountain shear zone, California and Nevada: Journal of Structural Geology, v. 29, p. 583-599.
Thomas, W. A., and R. A. Astini, 2003, Ordovician accretion of the Argentine Precordillera terrane to Gondwana: A review: Journal of South American Earth Sciences, v. 16, p. 67-79.
Thompson, A. B., K. Schulmann, J. Jezek, and V. Tolar, 2001, Thermally softened continental extensional zones (arcs and rifts)as precursors to thickened orogenic belts: Tectonophysics, v. 332, p. 115-141.
Tikoff, B., and C. Teyssier, 1994, Strain modeling of displacement-field partitioning in transpressional orogens: Journal of Structural Geology, v. 16, p. 1575-1588.
Toselli, A., J. Rossi, and C. W. Rapela, 1978, El Basamento Metamorfico de la Sierra de Quilmes, Republica Argentina: Revista de la Asociacion Geologica Argentina, v. 33, p. 105-121.
Tullis, J., and R. A. Yund, 1991, Diffusion creep in feldspar aggregates: experimental evidence: Journal of Structural Geology, v. 13, p. 987-1000.
Turner, J. C. M., 1975, Geología del sector oriental de los Departamentos de Santa Victoria e Iruya, Provincia de Salta. República Argentina. : Boletín de la Academia Nacional de Ciencias p. 11–24
Vaughan, A. P. M., and R. J. Pankhurst, 2008, Tectonic overview of the West Gondwana margin: Gondwana Research, v. 13, p. 150-162.
Wegmann, M. I., U. Riller, F. D. Hongn, J. Glodny, and O. Oncken, 2008, Age and kinematics of ductile deformation in the Cerro Durazno area, NW Argentina: Significance for orogenic processes operating at the western margin of Gondwana during Ordovician – Silurian times: Journal of South American Earth Sciences, v. 26, p. 78-90.
Weinberg, R., M. Veveakis, and K. Regenauer-Lieb, 2015, Compaction-driven melt segregation in migmatites, v. 43, 471-474 p.
Weinberg, R. F., R. Becchio, P. Farias, N. Suzaño, and A. Sola, 2018, Early paleozoic accretionary orogenies in NW Argentina: Growth of West Gondwana: Earth-Science Reviews.
Whitmeyer, S. J., and C. Simpson, 2003, High strain-rate deformation fabrics characterize a kilometers-thick Paleozoic fault zone in the Eastern Sierras Pampeanas, central Argentina: Journal of Structural Geology, v. 25, p. 909-922.
Wilson, C. J. L., D. S. Russell-Head, K. Kunze, and G. Viola, 2007, The analysis of quartz c-axis fabrics using a modified optical microscope: Journal of Microscopy, v. 227, p. 30-41.
Windley, B., 1992, Chapter 11 proterozoic collisional and accretionary orogens, Developments in Precambrian Geology, p. 419-446.
Wing, B. A., J. M. Ferry, and T. M. Harrison, 2003, Prograde destruction and formation of monazite and allanite during contact and regional metamorphism of pelites: Petrology and geochronology: Contributions to Mineralogy and Petrology, v. 145, p. 228-250.

Wolfram, L. C., R. F. Weinberg, P. Hasalová, and R. Becchio, 2017, How melt segregation affects granite chemistry: Migmatites from the Sierra de Quilmes, NW Argentina: Journal of Petrology, v. 58, p. 2339-2364.
Wolfram, L. C., R. F. Weinberg, O. Nebel, K. Hamza, P. Hasalová, J. Míková, and R. Becchio, 2019, A 60-Myr record of continental back-arc differentiation through cyclic melting: Nature Geoscience, v. 12, p. 215-219.

Chapter 3

Untangling the protracted thermal evolution of a migmatitic terrane by means of multiple geochronometers: insights from the Sierra de Quilmes

Abstract

The combination of U–Pb ages and trace element composition of zircon, monazite, and titanite derived from laser–ablation split stream analyses allow us to delineate the thermal evolution of the polydeformed, upper–amphibolite facies, turbidite–derived Agua del Sapo metamorphic complex in NW Argentina. This complex records two consecutive Paleozoic orogenies lasting c. 160 Ma: the Pampean and Famatinian orogenies. The latter was known to occur between c. 500 to 440 Ma, but the combination of new titanite and monazite U-Pb dates extend its duration another c. 60 Myr to 380 Ma. The study area is located in the footwall of a thrust that placed granulite facies rocks over it. The sedimentary protolith of these rocks is part of the extensive Neoproterozoic – Early Cambrian Puncoviscana sequence, mostly comprised of turbidites. U–Pb dating on detrital zircon grains indicates a maximum depositional age of 560 Ma for these rocks. These rocks were intruded by an S–type granite dated here at 540 Ma, contemporaneous with the magmatic climax of the Pampean orogeny. Between 500–440 Ma the Famatinian orogeny caused anatexis of the metasedimentary rocks forming voluminous migmatites and granites, and triggered the growth of thin metamorphic rims over detrital zircon. Monazite of the same rocks shows the same age span as the metamorphic zircon dates, with a major frequency peak at c. 460 Ma, hence resolving the time of the metamorphic climax. We also found that monazite behaviour depends on rock type and fabric: leucosomes and granites show a well–defined single peak at 460 Ma, unlike the migmatitic metasedimentary sequence that shows a broader age spread, including younger ages scattered between 440–425 Ma, with no significant accompanying changes in monazite chemistry. Titanite dates from Ca–rich siliciclastic rocks showed a more complex history. Like for monazite, some samples showed a single age peak concentrated at 460 Ma, others showed a broadly distributed age population with some analyses at 460 Ma, but most scattered between c. 440–380 Ma. The younger titanite group has lower LREE contents, interpreted to be due to the formation of LREE–rich allanite–

epidote after the breakdown of monazite during high–temperature retrogression. The temperature of this retrogression reaction is compatible with T–estimates based on Zr–in–titanite that indicate cooling of the rocks from temperatures in excess of 750 °C at c. 460 Ma to 700 °C at 380 Ma. Thus titanite records the effects of retrogression during prolonged cooling of < 1 °C/Ma and the stabilisation of allanite in the retrograde path. With this work we have unraveled the protracted tectono–thermal evolution of the complex by using the three geochronometers. We speculate that the protracted cooling at the end of the Famatinian orogeny that caused the partial resetting of titanite, and increased modal content of allanite and epidote may be linked to the thrusting of the granulite facies rocks over the Agua del Sapo complex, that kept the complex hot for loger if compared with the hanging wall complex. A key finding is that the Famatinian record lasted from the first zircon and monazite ages at c. 500 Ma representing the start of a high–T metamorphic event that peaked at 460 Ma and then cooled slowly through the 750 °C to 700 °C isograd between 440–380 Ma marked by the low–LREE young titanite, recording a nearly c. 120 Ma high–T metamorphic event.

1 Introduction

Accessory minerals like zircon ($ZrSiO_4$), monazite ((Ce,La) PO_4), and titanite ($CaTiSiO_4$) are well–known geochronometers that can provide a record of dynamic long–term geological events. Each of these minerals has been traditionally associated to different closure temperatures below which they close their U–Pb isotopic system and start working as geochronometers (Braun et al., 2006; Kirkland et al., 2017; Rollinson, 1995; Turekian and Holland, 2013). For any mineral, the closure temperature (T_c) depends on factors like diffusivity for a particular element (D), effective diffusion radius, grain radius, and cooling rate (Dodson, 1973). Zircon and monazite closure temperatures are >900 °C (Cherniak and Pyle, 2008; Cherniak and Watson, 2001; Cherniak et al., 2004; Gardés et al., 2007; Kelsey et al., 2008; Lee et al., 1997), and titanite vary from 450–500 °C (Mattinson, 1978) to over 825 °C (Gao et al., 2012) but most recent studies agree that its closure temperature is typically above 660 °C, possibly over 700 °C (Kohn, 2017). Therefore, the combined use of these geochronometers should cover a wider temperature range around peak metamorphic conditions allowing a more refined and complete picture of the thermal history of hot orogens.

Zoning within these accessory phases is a common feature in host rocks subjected to complex geological histories. This zoning reflects changes in composition, pressure and/or temperature of the host rock that may trigger regrowth, dissolution–reprecipitation, recrystallisation, diffusion, or a combination of all. Improvements of analytical tools like *laser ablation split stream* (LASS–ICP–MS) allow us to investigate the U–Pb age and composition of the same spot in a single zone within the grain. This allows investigation of the temporal evolution in composition across different ages that ultimately can lead to inferences of the temporal evolution of petrogenetic processes.

One of the most studied geochronometers is zircon. This mineral can be used to trace the formation and/or destruction of other phases like monazite or garnet (Taylor et al., 2016, and references within). For example, the depletion of heavy rare earth elements (HREE) in zircon is usually associated with prograde growth of garnet (Rubatto, 2002; Whitehouse and Platt, 2003). Similarly, Eu content in monazite is a useful tracer of K–feldspar formation in the host rock during prograde metamorphism (Rubatto et al., 2013). Titanite trace–element composition has been recently used to trace other mineral growth. For example, variations of HREE in titanite, like in the zircon, are linked to garnet formation (Scibiorski et al., 2019b). However, variations in other elements in titanite, like the LREE, have so far not been fully understood. The integration of trace–element geochemistry and U–Pb geochronology of zircon, monazite, and titanite makes these minerals powerful tracers of petrogenetic processes.

In this work, we report new geochronological and mineral composition data that aim to better understand the thermal evolution of the high–temperature and low–pressure mid–crustal sections of an Ordovician continental back–arc currently represented in the Agua del Sapo complex. We were able not only to constrain the evolution of the terrane better but also to better understand the behaviour of the different geochronometers. This paper starts with a summary of the geology of NW Argentina and the Paleozoic orogens that affected the region, and that of the Agua del Sapo metamorphic complex, our focus here. The paper then describes the petrography of the different rock types, followed by the results from geochronology and mineral chemistry. We discuss the behaviour of the different accessories during crustal evolution and conclude by integrating the geochronology results and mineral chemistry of the three geochronometers to propose a tectono–metamorphic evolution for the complex.

2 Geology background

2.1 Sierras Pampeanas and the Palaeozoic orogenies

The area of study is located in the Sierra de Quilmes. This mountain range is part of a larger geological province called Sierras Pampeanas that encompasses a series of north–south trending mountain ranges located in the north–west of Argentina, in the current Andean foreland (Fig. 1). Due to the current flat–slab subduction of the Andean orogeny, the Sierras Pampeanas were uplifted, exposing different crustal levels (Büttner et al., 2005; Pankhurst et al., 1998; Rapela et al., 1998c; Rapela et al., 2015; Whitmeyer and Simpson, 2003). Deeper sections of the crust are better exposed in the south of Sierras Pampeanas and shallower levels in the north (Büttner et al., 2005; Rapela et al., 1998b), where the Sierra de Quilmes is located.

The Sierras Pampeanas are part of a Palaeozoic accretionary margin that was once part of the Western Gondwana supercontinent, and the Terra Australis orogen (Cawood, 2005). The Sierras Pampeanas are composed mainly of Palaeozoic metamorphic and igneous rocks that were formed and deformed by the Pampean (c. 540–520 Ma), Famatinian (c. 500–440 Ma) and Achalian (c. 400–350 Ma) orogenies (see Weinberg (2018b) for a comprehensive review). The development of these orogenies was controlled by subduction and accretion of different Laurentian–derived terranes (Aceñolaza et al., 2002; Aceñolaza and Toselli, 2009; Astini, 1998; Escayola et al., 2011; Omarini et al., 1999; Ramos, 2004, 2008; Ramos et al., 1998; Ramos et al., 2000; Ramos et al., 1986; Ramos et al., 2010; Rapela et al., 1998c; Rapela et al., 2015; Vaughan and Pankhurst, 2008). The amalgamation of these exotic terranes into the accretionary margin outlines a composite block that is currently known as the Western Sierras Pampeanas (WSP) (Fig. 1). To the east of the WSP and west of the Rio de la Plata craton, there is the Eastern Sierras Pampeanas (ESP) where the study area is located. This block is composed largely by metasedimentary and igneous rocks derived from the turbidite sequence of the Puncoviscana Formation (Adams et al., 2011). These turbidites were first deposited in the passive margin of Western Gondwana between c. 670 and 520 Ma (Adams et al., 2011; Omarini et al., 1999; Rapela et al., 1998c), initially in the passive margin with sediments sourced from the craton and later during the Pampean orogeny, in the fore–arc of an active accretionary margin and with sediments sourced from the Pampean magmatic arc. The Pampean arc is oriented N–S and crops out discontinuously from the Sierra de Córdoba in the south to the Cordillera Oriental in the north of Argentina (Dahlquist et al., 2016; Weinberg et al., 2018b). Schwartz (2008a) divided the Pampean arc into a calc–alkaline belt in the east paired with a peraluminous high–temperature medium to high–pressure migmatitic belt to the west. The Pampean arc and its peraluminous margin have been associated with a continent–continent collision (Martino, 2003; Otamendi et al., 2004; Pankhurst et al., 2000; Rapela et al., 1998a; Schwartz et al., 2008b; Semenov and Weinberg, 2017; Weinberg and Geordie, 2008). After the Pampean orogenic cycle finished at c. 520 Ma, subduction restarted in the west and initiated the Famatinian orogenic cycle forcing the migration of the subduction–related magmatic arc some 200km towards the trench.

Famatinian orogenic cycle and the Oclóyic phase

The Famatinian orogenic cycle was a subduction–related, Andean–type continental orogeny that initiated at c. 505–500 Ma as suggested by U–Pb zircon ages in S–type magmatic rocks of the back–arc (Bahlburg et al., 2016; Wolfram et al., 2017). This orogeny resulted in a north–south striking, and 1600 km–long I–type dominated magmatic arc coupled to the east with an S–type dominated back–arc developed over the previous Pampean fore–arc. The arc magmatism occurred between c. 490 and c. 440 Ma with a peak at 470 Ma (Bellos et al., 2015; Ducea et al., 2017; Ducea et al., 2010; Mulcahy et al., 2014; Pankhurst et al., 2000; Pankhurst et al., 1998; Rapela et al., 2018; Weinberg et al., 2018b; Wolfram et al., 2017) coeval with peak metamorphism and extensive anatexis in the back–arc (Büttner et al., 2005; Finch et al., 2017; Lucassen et al., 2010; Sola et al., 2013; Sola et al., 2017; Wolfram et al., 2017).

The tectonic regime in the Famatinian back–arc changed from extensional to compressional when the Laurentian–derived micro–continent known as the Precordillera terrane/block approached and docked to the western margin of Gondwana in the Late Ordovician (c. 458–449 Ma) (Astini, 1998; Astini et al., 1995; Thomas and Astini, 2003). This accretion triggered a phase of crustal shortening known as the Oclóyic phase (Turner, 1975). This phase had implications for the upper crust as most of the marine basins developed during the extensional period were closed, folded, and partly eroded. This event is marked by regional unconformities (Astini and Dávila, 2004; Bahlburg and Hervé, 1997; Davila et al., 2003) and is associated with anomalously wide mylonitic–ultramylonitic thrust zones (Finch et al., 2015; Larrovere et al., 2016; Rapela et al., 1998b; Semenov and Weinberg, 2017). The Famatinian cycle finished at around 440–435 Ma when magmatism and anatexis diminished (2009; Bahlburg et al., 2016; Büttner et al., 2005; Mulcahy et al., 2014; Wolfram et al., 2017).

Based on the cooling history of many locations across the Northern Sierras Pampeanas, it is suggested that the mid–crustal sections were exhumed close to the present erosional surface between 400 and 300 Ma. For example, K–Ar ages indicate that the rocks passed the closure temperature of ca. 530 °C for hornblende at 480–450 Ma and the closure temperature of ca. 350 °C for biotite at ca. 400 Ma in many locations (Lucassen et al., 2000). Reheating at around 300 Ma was variable and partially reset the K–Ar system (Larrovere et al., 2016; Lucassen et al., 2000).

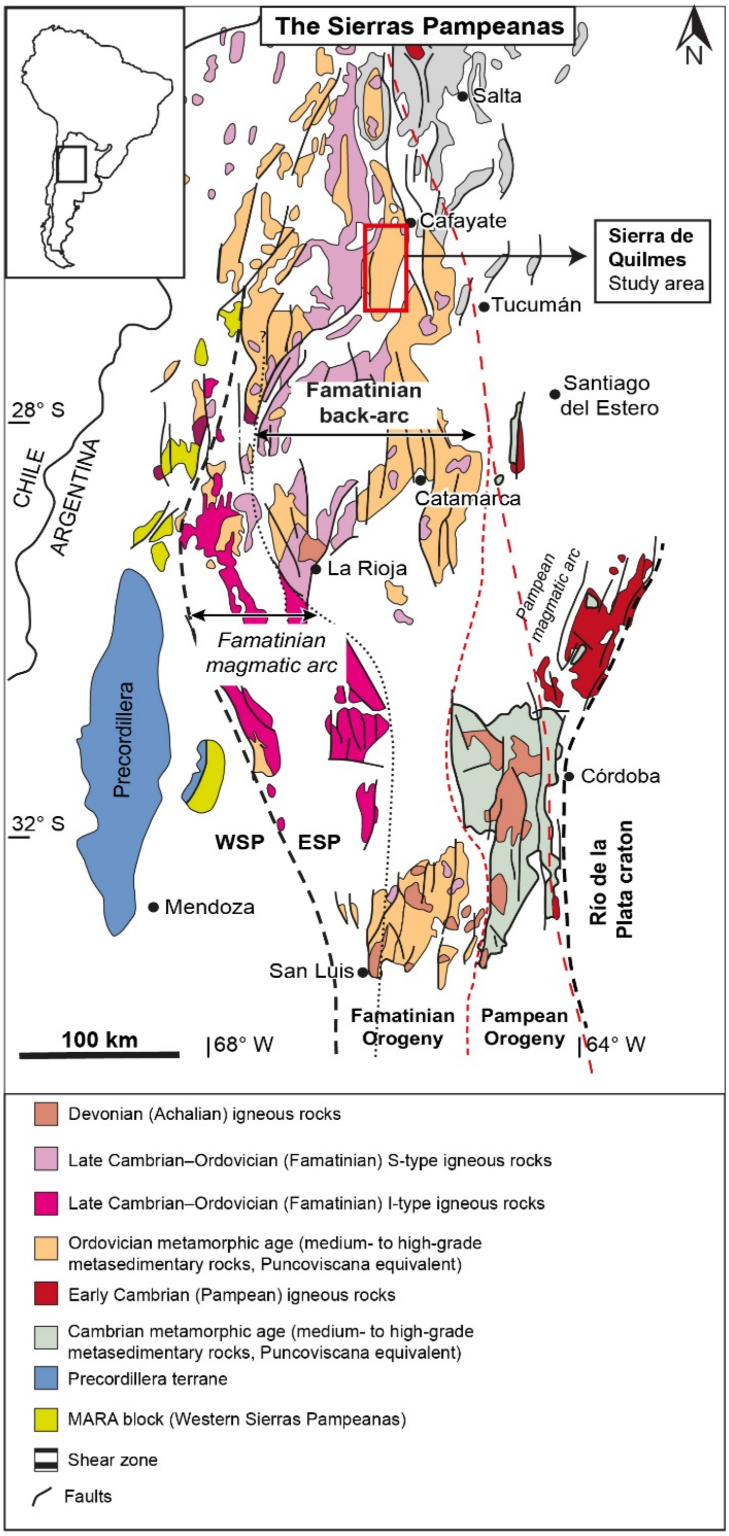

Figure 1– Map of the Sierras Pampeanas and location of the Sierra de Quilmes.

2.2 Geology of the Sierra de Quilmes: three metamorphic complexes

The Sierra de Quilmes is located in the north of the Eastern Sierras Pampeanas province. It is a mountain range that extends c. 130 km in the north–south direction and approximately 30 km wide (Fig. 2). The protolith of all the metasedimentary and igneous rocks in the Sierra de Quilmes is the extensive turbiditic sequence of the Puncoviscana Formation (Büttner et al., 2005; Rapela, 1976a, b; Toselli et al., 1978). Although the rocks in this area were affected by all the Palaeozoic orogenies, the Ordovician Famatinian orogenic cycle was the most intense of all. Hence, the geology of the Sierra de Quilmes represents the mid–crustal section of the Famatinian back–arc, which was dominated by a high temperature and low pressure (HT–LP) metamorphic regime (Büttner, 2009; Büttner et al., 2005; Finch et al., 2015; Finch et al., 2017; Finch et al., 2016; Rapela, 1976a, b; Rossi and Toselli, 1976; Toselli et al., 1978; Wolfram et al., 2017) that was established at the beginning of the orogenic cycle during its extensional phase. Also, there are anomalously wide and intense shear zones, such as the Pichao Shear Zone, that are associated with crustal shortening and orogenesis during the Oclóyic phase (Finch et al., 2015).

The Sierra de Quilmes is composed of three metamorphic complexes intruded by peraluminous igneous rocks. The Tolombon complex in the north, the Tolombon West complex in the southwest, and the Agua del Sapo complex in the southeast (Fig. 2). These complexes are separated by two major interconnected high–grade shear zones. The Filo shear zone that strikes roughly north–south along the ridge of the range and dips steeply to the west separates the Agua del Sapo complex in the east from the Tolombon West complex in the west. The Filo shear zone has sinistral kinematics with a sub–horizontal stretching lineation (Chapter 2). This shear zone links northwards to the curved but generally NE dipping Pichao shear zone (Finch et al., 2015). The two interconnected shear zones form the Pichao–Filo thrust system. This thrust system juxtaposes, as thrust–bound horses within a thrust duplex system, the Tolombon over the Tolombon West complex, which in turn are thrusted over the Agua del Sapo complex. We will consider the Tolombon and Tolombon West complexes, as the hanging wall complexes of the Agua del Sapo complex, which is the area of interest.

Hanging wall complexes

The metasedimentary rocks of the Tolombon complex that form the hanging wall of the Pichao shear zone are dominated by migmatites that reached granulite facies conditions in the orthopyroxene zone under granulite facies conditions (Finch et al., 2015; Finch et al., 2017). The peak metamorphic conditions were constrained to c. 6 kbar and 800 °C with a mineral paragenesis associated with HT–LP conditions (Büttner et al., 2005; Finch et al., 2017). This high–grade metamorphism resulted in extensive partial melting and formation of diatexites and S–type leucogranitic plutons that dominates most of the exposed regions of the complex (Wolfram et al., 2017). The Tolombon West complex is similar to the Tolombon complex in terms of lithology, but it lacks the Opx–zone and is dominated by a garnet–cordierite–sillimanite zone, similar to that of the eastern Tolombon complex where Büttner (2005) established metamorphic conditions of 650–750°C and pressures < 5 kbar. The peritectic mineral paragenesis is retrogressed: cordierite and garnet are partially replaced by biotite–sillimanite, and sillimanite and feldspar are commonly replaced by large poikiloblasts of muscovite. As we defined in Chapter 2, these two high–grade complexes were thrusted over each other with a top–to–west kinematics (D1). This event represents the syn–anatectic shortening of the Famatinian back–arc.

Agua del Sapo complex: the study area

This complex, first described by Rossi (1976; Toselli et al., 1978), represents the footwall of the Pichao–Filo thrust system. This complex is different from the hanging wall complexes both in terms of lithology and structures. In the northern part of the complex, in the immediate footwall of the Pichao shear zone, the rocks are similar to the hanging wall complexes in that they derive from the same Al–rich siliciclastic turbiditic sequence and have Al–rich minerals like cordierite and sillimanite. However, some 20 km to the south (Fig. 2), these rocks transition to Ca–rich siliciclastic metasedimentary rocks with hornblende, titanite, allanite, and epidote in the mineral paragenesis. The metamorphic grade also increases from north to south, from amphibolite facies Bt–Grt–Sil mineral paragenesis, lacking evidence of anatexis, to migmatites with a Grt–Sil–Kfs mineral paragenesis towards the south. Interlayered with the latter, the Ca–rich siliciclastic rocks are dominated by hornblende–bearing migmatites with titanite–epidote–allanite and occasionally clinopyroxene and scapolite. As described in Chapter 2, the structural architecture of the Agua del Sapo complex is also different from the hanging wall complexes. Here, the top–to–west D1 thrusts are overprinted by a pervasive top–to–south shearing with a strong sub–horizontal, north–south trending stretching lineation parallel to constrictional sheath folds and upright open folds (D2). The D2 event in this complex is interpreted as the non-coaxial constriction of the migmatitic rocks due to the interplay of E–W and vertical shortening leading to constriction. D2 started when the crust achieved a critical thickness and the horizontal tectonic forces equilibrated with vertical gravitational forces, forcing the lateral stretching of the constricted complex.

Summary

The Sierra de Quilmes represents the mid–crustal levels of the back–arc of the c. 500–440 Ma Famatinian orogeny. This area was affected by long–term high heat flux and HT–LP metamorphic conditions that resulted in widespread cyclical anatexis and magmatism lasting over c. 60 Ma (Weinberg et al., 2018a; b, and references therein). The Sierra de Quilmes is composed of three high–grade metamorphic complexes separated by the wide shear zones of the Pichao–Filo thrust system. In the footwall Agua del Sapo complex the initial D1 thrusting is strongly overprinted by a D2 top–to–south shearing during constriction of the thermally–weakened rocks, as a response to the crustal thickening and continuous east–west shortening (see Chapter 2).

2.3 Previous geochronology

Most of the dating effort so far has been focused on the Tolombon complex (Büttner et al., 2005; Finch et al., 2017; Lucassen et al., 2000; Wolfram et al., 2019), with a few samples from the north end of the Agua del Sapo complex (Finch et al., 2017). Results from the Tolombon and Agua del Sapo complexes reveal Famatinian ages of magma crystallisation and metamorphism (Table 1). In the Tolombon complex Wolfram (2019) obtained melt crystallisation ages of diatexites and leucocratic granites by means of SHRIMP U–Pb ages in zircon. The results show cyclical zircon–growth events that span the entire Famatinian orogeny with a recurrence of c. 10–15 Myr, between 505 and 440 Ma, suggesting protracted high–temperature conditions and multiple anatectic events. The hihest density of dates are centred at 470–460 Ma (Wolfram et al., 2019). Lucassen (2000) estimated the age of high–grade metamorphism to be ca. 440 Ma based on the Sm/Nd age of calc–silicate rocks in the granulite facies Tolombon complex. This age is significantly younger than the 477 ± 11 Ma Sm/Nd age based on a garnet aplite whole–rock isochron of Büttner (2005). Monazite ages in the Tolombon complex yield ages ranging between 490–440 Ma. Büttner (2005) obtained U–Pb TIMS monazite ages of c. 470 Ma. However, the total dissolution of grains used in this technique could potentially produce mixed ages. Finch (2017) reported two monazite U–Pb SHRIMP age populations at 484.8 ± 2.3 and 470.7 ± 2.2 Ma from sheared migmatites of the Pichao shear zone. Later Wolfram (2017) obtained U–Pb SHRIMP monazite ages of migmatites that spread between 500–440 Ma (similar age range as the zircon U–Pb ages of the same rocks). They found that monazite in the Tolombon complex was zoned but found no core–rim systematics, and argued that U–Pb ages were decoupled from the mineral chemistry responsible for the zonation. The Ar–Ar age of muscovite from pegmatites yielded ages of 442 ± 11 Ma for coarse grained grains and 408 ± 7 Ma for fine–grain muscovite in small shear zones (Büttner et al., 2005).

In the Agua del Sapo complex, (Finch et al., 2017) reported monazite U–Pb ages from a mylonitic Bt–Grt schist sample collected right at the base of the Pichao shear zone. This sample yielded monazite ages of c. 470 Ma, which are comparable with the monazite ages of the hanging wall Tolombon complex. This rock contains Bt + Qtz + Kfs + Pl + Grt, and there is no evidence of retrogression. However, a Bt + Ms + Grt schist sampled c. 1 km south of the previous sample, records younger monazite ages between 435–420 Ma. This rock contains Bt + Qtz + Kfs + Pl + Ms + Grt + Tur where the garnet is partially retrogressed to Bt + Chl, and biotite is partially replaced by chlorite. Finch (2017) argued that the younger ages are the result of heating of the amphibolite–facies rocks in the footwall after the thrusting of the granulite–facies Tolombon complex.

In order to better understand the thermal response to the thrusting on the footwall complex and to determine the timing of anatexis, we sampled a variety of rocks across the Agua del Sapo complex. The complex is particularly well–suited for the comparison of U–Pb dating results because rocks typically have pairs of datable accessory phases: the Al–rich siliciclastic rocks generally have Zrn+Mnz whereas the Ca–rich ones have Zrn+Ttn. We dated these minerals by means of LASS–ICP–MS (laser ablation split stream inductively coupled plasma mass spectrometry) and LA–ICP–MS for two monazite samples. The new data is integrated into available data to interpret the tectono–thermal history of the complex and critically assess the response of each of these geochronometers to the long–lasting hot metamorphic conditions of this orogeny. The geochronology of the Tolombon West complex will be presented and disussed in Chapter 4, where I compare the results and behaviour of geochronometres in all complexes of the Sierra de Quilmes.

Table 1– Summary of geochronological data from previous studies in the Sierra de Quilmes (Büttner et al., 2005; Finch et al., 2017; Lucassen et al., 2000; Wolfram et al., 2017)

	Zircon (U–Pb) (Ma)	*Monazite (U–Pb)(Ma)**	*Titanite (U–Pb)(Ma)*	*Muscovite (Ar–Ar)(Ma)**	*Sm/Nd (Ma)**	*Rb/Sr (Ma)**
Tolombon Complex	c. 505[a] c. 490[a] c. 475–465[a] c. 460[a] c. 450–445[a]	c. 470[b] c. 460[c] 473 ± 4[d] 468 ± 2[d] 484.8 ± 2.3[g] 470.7 ± 2.2[g]	459–468[n] (TIMS)	442 ± 11[e] 408 ± 7[f]	442 ± 9[j] 477 ± 11[K]	450 ± 7[l] 416 6[m]
Agua del Sapo Complex		463.6 ± 2.2[h] 484.6 ± 2.6[h] 420.8 ± 1.8[i] 435.2 ± 1.9[i]				

**All uncertainties are 2σ*

[a] Five different age peaks were determined between c. 500 and c. 445 Ma with the most intense peaks at 474 ± 1.8 Ma and 459 ± 1.3 Ma (SHRIMP)(Wolfram et al., 2019)
[b] Schlieren diatexite. Monazite ages between 450–490 Ma with a central age at c. 470 Ma (SHRIMP) (Wolfram et al., 2017)
[c] Pink leucogranite. Monazite ages between 440–480 Ma with a central age at c. 460 Ma (SHRIMP) (Wolfram et al., 2017)
[d] Bt–Grt–Crd migmatite (TIMS) (Büttner et al., 2005)
[e] Large muscovite grains (Büttner et al., 2005)
[f] Small muscovite in shear zone (Büttner et al., 2005)
[g] Pichao shear zone (SHRIMP) (Finch et al., 2017)
[h] Schist at base of Pichao shear zone (SHRIMP) (Finch et al., 2017)
[i] Schist at the immediate footwall of the Pichao shear zone (SHRIMP) (Finch et al., 2017)
[j] Isochron (Grt–Pl–WR) in calc–silicate rock at granulite facies (Lucassen et al., 2000)
[k] Isochron (Grt–Ap–WR) in garnet aplite (Büttner et al., 2005)
[l] Retrograde muscovite from migmatite (Büttner et al., 2005)
[m] Fine–grained syn–kinematic muscovite. Maximum age of deformation (Büttner et al., 2005)
[n] Calc–silicate in migmatites near Cafayate (Büttner et al., 2005)

3 Analytical methods

3.1 LA–ICP–MS and LASS–ICP–MS

3.1.1 Sample preparation

Samples were crushed and milled. From the total, an aliquot was separated for geochemical analysis and the rest for mineral separation. The latter was sieved and the fraction finer than >355 µm was washed, and the heaviest fraction was separated by panning. After drying the sample, the magnetic minerals were separated with a rare earth hand–magnet. The final fraction was further fractionated by washing and panning in a watch glass with ethylic alcohol. Following initial Frantz separation, the less magnetic fraction was treated in heavy liquid DIM (Di–iodomethane, density 3.3 g/cm^3) to separate the heaviest minerals like zircon and monazite, and the magnetic fraction was further fractionated using different values of tilt and voltages in the Frantz for titanite separation. The heaviest fraction from the heavy liquids and the separates from the Frantz were used for hand–picking under a stereo binocular microscope. The zircon, monazite and titanite grains were grouped based on morphology and colour and mounted in 25 mm epoxy resin discs.

The epoxy mounts were polished, and the minerals photographed under reflected light in an optic microscope, followed by backscattered electrons (BSE) images at the Centre for Electron Microscopy at Monas University using an MCEM JEOL 7001F scanning electron microscope. Zircon was imaged using cathode–luminescence (CL) on the Philips (FEI) XL30 ESEM TMP electron microscope with a Gatan CL detector at the scanning electron microscope facility at Melbourne University. For in–situ LASS–ICP–MS, the selected thin sections were polished and the target mineral grains mapped before BSE imaging.

The U–Pb zircon, monazite and titanite dating was carried out at the School of Earth, Atmosphere and Environment, Monash University, by means of LA–ICP–MS and LA–ICP–Ms in a split stream mode (LASS–ICP–MS). The first two samples (Table 2) were analysed by LA–ICP–MS where U/Pb and trace elements were analysed separately using a Thermo ICAPTQ triple quadrupole ICP–MS coupled with an ASI Resolution 193 nm excimer laser equipped with a dual volume Laurin Technic S155 ablation cell. For the rest of the samples, the LASS–ICP–MS was used. This allowed to obtain U/Pb and trace elements from the same spot. The minerals were analysed using the ASI Resolution 193 nm excimer laser that splits the ablated material in two. One stream goes to the Thermo ICAPTQ triple quadrupole ICP–MS for the U–Pb ages whereas the other is directed to a Thermo ICAPQ quadrupole ICP–MS where rare earth and selected trace elements were analysed.

The minerals were sampled in a He atmosphere with the laser operating at a repetition rate of 10 Hz and a 25 µm spot size. The laser energy used for zircon and titanite was approximately 4 Jcm^{-2}. Each analysis began with 20–second measurement of the gas background, followed by 15 seconds with the laser switched on. The ablated material was split into two equal amounts using a Y junction placed just downstream the ablation cell. The ablated material fed the ICPMS torches for the U–Pb ages and trace elements determinations. The length of the tubing carrying the ablated material from the Y junction to the two ICP–MS torches was the same. This guaranteed the same raise time of the signal on both mass spectrometers and avoided decoupled U–Pb ages and trace element information.

For the U–Pb ages, the following masses were analysed: ^{202}Hg, ^{204}Pb, ^{206}Pb, ^{207}Pb, ^{208}Pb, ^{232}Th, and ^{238}U. Dwell time for ^{202}Hg, ^{204}Pb was 30 ms, for ^{206}Pb 40 ms, for ^{207}Pb 70 ms, for ^{208}Pb 20 ms and for ^{232}Th and ^{238}U 10 ms. For the trace elements and some major elements, different masses were analysed depending on the mineral. For zircon ^{29}Si, ^{47}Ti, ^{49}Ti, ^{89}Y, ^{91}Zr, ^{93}Nb, ^{139}La, ^{140}Ce, ^{141}Pr, ^{146}Nd, ^{147}Sm, ^{153}Eu, ^{157}Gd, ^{159}Tb, ^{163}Dy, ^{165}Ho, ^{166}Er, ^{169}Tm, ^{172}Yb, ^{175}Lu, ^{181}Ta. For titanite, ^{29}Si, ^{44}Ca, ^{88}Sr, ^{89}Y, ^{91}Zr, ^{93}Nb, ^{139}La, ^{140}Ce, ^{141}Pr, ^{146}Nd, ^{147}Sm, ^{153}Eu, ^{157}Gd, ^{159}Tb, ^{163}Dy, ^{165}Ho, ^{166}Er, ^{169}Tm, ^{172}Yb, ^{175}Lu, ^{177}Hf, ^{178}Hf, ^{181}Ta. For monazite ^{31}P, ^{43}Ca, ^{88}Sr, ^{89}Y, ^{91}Zr, ^{93}Nb, ^{139}La, ^{140}Ce, ^{141}Pr, ^{146}Nd, ^{147}Sm, ^{153}Eu, ^{157}Gd, ^{159}Tb, ^{163}Dy, ^{165}Ho, ^{166}Er, ^{169}Tm, ^{172}Yb, ^{175}Lu, ^{181}Ta.

For the U–Pb component, instrumental mass bias, drift, and downhole fractionation were taken into account by analysing every half hour throughout the analytical session different standard material. For zircon the Plešovice standard (Slama *et al.* 2008) was used as the primary calibration standard, and GJ–1 zircon (Jackson *et al.,* 2004) and Temora 1 zircon (Blacke *et al.,* 2003) were analysed as unknowns, or secondary standard, for quality control purposes.

In the case of titanite BLR–1 titanite (Aleinikoff et al., 2007) was used as the primary standard and OLT–1 titanite (Kennedy et al., 2010) as a secondary standard. For monazite, the MAdel monazite (Payne et al., 2008) was used as the primary standard and the 44069 monazite (Aleinikoff et al., 2006) as a secondary standard.

For the trace elements component, the raw data was reduced using the Iolite 3.6 software (Paton *et al.* 2010, Paton *et al.* 2011) and quantitative results were obtained using the NIST610 glass as the primary external standard and using the stoichiometric content of Si in Zircon and titanite, and Ca in monazite for internal standardisation. The NIST612 glass, USGS standard BHVO 2G and BCR 2G were analysed throughout the analytical session to check for precision and accuracy and the results. Around 1% of the analysis were discarded during data reduction due to blurred or unclear ICP–MS signal or large error bars. Therefore some dates are not coupled with trace elements, and vice–versa.

3.2 Common lead corrections for titanite

Since titanite grains generally exhibit a low radiogenic–Pb/common–Pb ratio, the data were plotted in a Tera–Wasserburg diagram, in which the variable ^{206}Pb/^{207}Pb ratios define a Discordia line with a lower intercept that is defined as *corrected ^{207}Pb/^{206}Pb* date. The initial ^{206}Pb/^{207}Pb ratio of 0.86 was used to anchor the Discordia based on the model evolution of Stacey (1975) for c. 470–440 Ma. Also, individual points were corrected by anchoring them and taking the lower intercept as the corrected *^{207}Pb/^{206}Pb* date.

3.3 Whole–rock geochemistry

Samples were selected for geochemical analysis in order to characterise the nature of the Ca–rich siliciclastic metasedimentary rocks and to provide a basis to infer the metamorphic evolution through metamorphic thermodynamic modelling. These samples were milled using a tungsten–carbide grinder. Major element analyses were conducted at the Australian Research Council Centre of Excellence in Ore Deposits (CODES), University of Tasmania, Australia, on a Panalytical Axios Advanced 4.0 kW X–ray Fluorescence (XRF) Spectrometer. Trace element analyses were obtained at Monash University, Victoria, Australia, using dissolution ICP–MS.

3.4 Mineral geochemistry

In order to constrain P–T conditions in the metamorphic thermodynamic modelling, mineral chemistry was used. The mineral analysis was conducted at the University of Melbourne by means of electron microprobe (EMP) using a Cameca SX50 electron microprobe with four vertical wavelength dispersive spectrometers (WDS). The electron beam used an accelerating voltage of 15 kV, beam current of 35 nA, and a spot size of 10 µms to minimise migration of volatile elements. Counting times for all elements were 20 seconds peak and 10 seconds on two backgrounds on either side of the peak position. Polished thin sections were carbon–coated by carbon vacuum evaporation to 250 Angstroms. The data reduction software used was SAMx with an integrated matrix correction software program PAP (Pouchou and Pichoir, 1991). Mineral structural formula calculations were based on Deer (1992).

3.5 Thermodynamic modelling

In order to determine peak P–T conditions for the migmatites in the Agua del Sapo complex, we constructed P–T pseudosection based on the whole rock geochemistry of one migmatite sample and refined with its mineral composition obtained from the garnet and biotite microprobe analysis. The software used for calculating the phase diagrams was THERMOCALC 3.33 (Powell et al., 1998, 2009 upgrade) and the internally consistent thermodynamic data set 5.5 (Holland and Powell, 1998, 2003 update). The pseudosections were calculated in the system MnO–Na2O-CaO–K2O–FeO–MgO–Al2O3–SiO2–H2O–TiO2–O (NCKFMASH–TO).

The amount of water in the modelling was the amount required the saturate the solidus. For O, we assumed all O derived from iron Fe2+. It is expected iron to be mostly Fe2+ but there should be a small amount of Fe3+, so some O was added into the bulk composition to reflect that (we added 0.2 Fe2O3 into the bulk composition). That is a conservative estimate of how much Fe2O3 would typically be in a pelitic rock. The Fe3+/Fe2+ in these rocks is usually 0.05 or below (Dyar et al., 2002).

The activity–composition models used were as follows: melt from White et al. (2007), cordierite and staurolite from a combination of Mahar et al. (1997) and Holland and Powell (1998), garnet, ilmenite and biotite from White et al. (2005), orthopyroxene from White et al. (2002), muscovite from Coggon and Holland (2002), and plagioclase and K–feldspar from Holland and Powell (2003).

Isopleth notations used are: Almandine (Alm) = Fe/(Ca+Fe+Mg+Mn), Grossular (Grs) = Ca/(Ca+Fe+Mg+Mn), Spessartine (Sps) = Mn/(Ca+Fe+Mg+Mn), Pyrope (Prp)= Mg/(Ca+Fe+Mg+Mn), X_{Fe}= Fe/(Fe+Mg), Ca(Pl) = Ca/(Ca+Na+K). Mineral abbreviations are after Kretz (1983).

4 Results

In order to fill the gap of geochronological information and critically asses the response of the different geochronometers to the metamorphic conditions in the Agua del Sapo complex, we dated zircon and monazite from Al–rich siliciclastic rocks and zircon and titanite from Ca–rich siliciclastic rocks. As explained in the method section, the LASS–ICP–MS technique allowed us to combine radiometric dates with mineral chemistry and, in the case of in–situ titanite dating, we could further integrate the geochemical and geochronological results with the petrography. We start this section with a petrographic description of the samples analysed followed by the metamorphic thermodynamic modelling of a migmatite sample, and continue with the geochronology and mineral geochemistry results. Table 2 lists the samples, their key features, and the mineral(s) dated. We investigated eleven samples, four from the Al–rich siliciclastic package and seven from the Ca–rich siliciclastic group. We also report the monazite U–Pb age results of Finch (2017) for completion. The location of the samples and the geochronometers used are depicted in (Fig. 2).

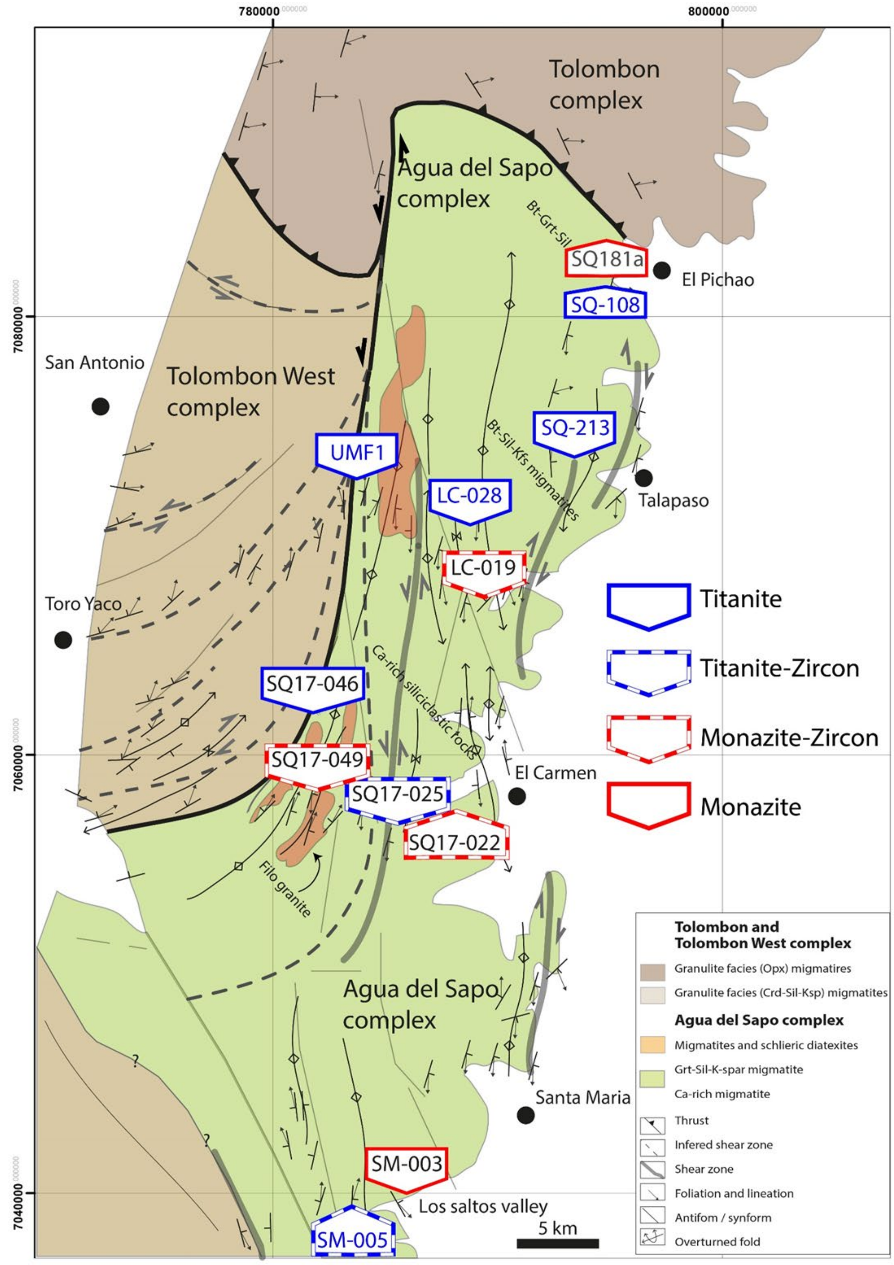

Figure 2– The Sierra de Quilmes simplified geological map with location and type of sampling

4.1 Petrography

Four samples from the Al–rich siliciclastic rocks were used to analyse zircon and/or monazite. We added one sample from Finch (2017) for completion. Also, seven samples from the Ca–rich siliciclastic rocks were used for zircon and/or titanite analysis. The mineral paragenesis with the most important features and analytical method of all samples are summarized in Table 2. For petrographic details see Appendix 3.

The Al–siliciclastic group is represented by one schist (SQ–181a) (Finch et al., 2017), two metatexite migmatites (SM–003, LC–019), a leucosome (SQ17–022), and a schlieric granite (SQ17–049). The schist SQ–181a is a Grt–Ms schist located some 5 km from the Pichao shear zone. It contains Qtz+Ms+Bt+Kfs+Pl+Grt and Tur+Ap+Mnz+Zrn as accessory phases. Zircon is typically included in biotite. Garnet porphyroblasts are partially retrogressed to Bt+Chl at their edges, and Bt is partially retrogressed to Chl. The schist is sheared (Fig. 3a). The metatexites are composed of Qtz+Bt+Pl+Kfs+Ms+Sil+Grt with Tur+Mnz+Ap+Zrn as accessory phases. Kfs forms large 0.5–1 cm poikiloblasts with rounded inclusions of Qtz and Bt, and fibrolite typically forms c. 1 cm “nests” that outline small crenulations (Fig. 3b). The schlieric granite is part of an array of igneous bodies that crop out along the western flank of the complex. This granite is elongated north–south, extending for at least 5 km (Fig. 2). It is composed by Qtz+Pl+Kfs+Bt+Grt+Ms, with Mnz+Ap+Zrn as accessory phases.

The Ca–rich siliciclastic group is represented by two Ca–rich schist (SQ–108 and SQ–213) hosted in the Al–rich siliciclastic package, in the north part of the complex (Fig. 2), three Ca–rich metatexites (SQ17–025, LC–028, SM–005), one ortho–amphibolite (SQ17–046c), and one mylonite (UMF) from the Filo shear zone. All these rocks are characterised by a mineral paragenesis of Qtz+Hbl+Bt+Kfs+Pl+Ms+Ep±Cal with Ap+Ttn+Aln+Ilm as accessory phases (Fig. 3c). The difference is that meionite (Ca–rich scapolite) is present in SM–005 as isolated subhedral grains, and Cpx in sample LC–028, typically in contact with Hbl and calcite. Titanite in SQ17–025 has Ilm cores (Fig. 3d). Allanite, LREE–rich epidote and epidote form core–mantle–rim respectively in all rocks (Fig. 3e), and zircon is typically in biotite or quartz (Fig. 3f).

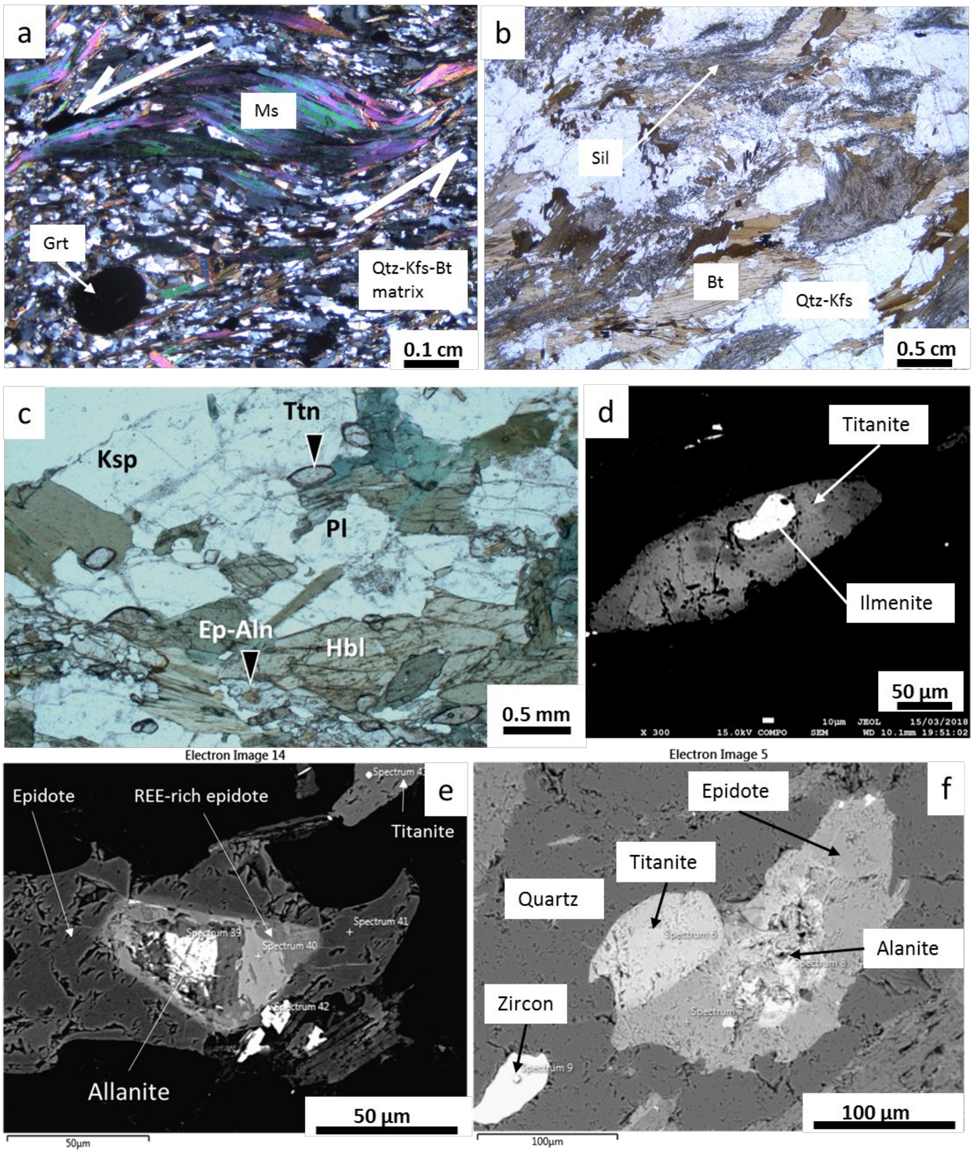

Figure 3– Photomicrographs of Al–rich siliciclastic rocks (a–b), and Ca–rich siliciclastic rocks (c–d). a) Cross polarized light (XPL) of Grt–Ms schist SQ–181a. b) Plane polarized light (PPL) representing metatexites with abundant Sil. c) Ca–rich siliciclastic sample showing texture and mineral paragenesis (PPL). D to f are SEM images. d) Titanite with ilmenite core. e) Allanite core, LREE–rich epidote mantle, and epidote rim texture. f) Same as (e), but lacking LREE–rich epidote mantle. Note zircon grain included in quartz.

Table 2– Summary of samples. Sample SQ181a from Finch (2017) is summarized here for completion (LA stands for LA–ICP–MS, LASS for LASS–ICP–MS). Coordinates are in UTM zone 19.

Sample	*Rock group*	*Rock type*	*Notes*	*Mineral paragenesis*	*Zircon*	*Monazite*	*Titanite*	*In–situ or mounted grains (M)*
SM–003 *E785028* *N7038928*	Al–rich	Grt–Sil metatexite	Weak shearing	Qtz–Bt–Pl–Kfs–Sil–Grt		LA		M
LC–019 *E789541* *N7066524*	Al–rich	Nebulitic metatexite	In lithon	Qtz–Bt–Pl–Kfs–Grt–Sil–Ms–Tur	LA	LA		M
SQ17–022 *E787387* *N7057776*	Al–rich	In–source leucosome	In lithon	Qtz–Bt–Pl–Kfs–Ms	LASS	LASS		M
SQ17–049 *E781540* *N7056763*	Al–rich	Schlieric granite	Hosted in Ca–rich rocks	Qtz–Bt–Grt–Pl–Kfs–Sil–Ms	LASS	LASS		M
SQ181a *E796885* *N7077289*	Al–rich	Grt–Ms Schist	Footwall of PSZ No Sil	Qtz–Bt–Pl–Kfs–Grt–Ms		*SHRIMP*		M
UMF *E780400* *N7050032*	Ca–rich	Mylonite	Fine–grained mylonite	Qtz–Pl–Bt–Kfs–Hbl– Ep–Aln–Ttn			LASS	In situ
SQ17–025 *E786461* *N7057063*	Ca–rich	Ca–rich metatexite	Sheared	Qtz–Pl–Bt–Kfs–Hbl– Ep–Aln–Ap–Ttn	LASS		LASS	M
SQ–213 *E794870* *N7072826*	Ca–rich	Ca–rich schist	Sheared	Qtz–Pl–Bt–Kfs–Hbl– Ep–Aln–Ap–Ttn			LASS	In situ
SQ–108 *E779004* *N7090438*	Ca–rich	Ca–rich schist	Footwall of PSZ	Qtz–Pl–Bt–Kfs–Hbl– Ep–Aln–Ap–Ttn			LASS	In situ
SQ17–046c *E780632* *N7057375*	Ca–rich	Ortho–amphibolite	Sheared FSZ	Qtz–Pl–Kfs–Hbl–Ap–Ttn			LASS	M
LC–028 *E787767* *N7069006*	Ca–rich	Ca–rich metatexite	Weak shearing	Qtz–Pl–Bt–Kfs–Hbl– **Cpx**–Ep–Aln–Ap–Ttn			LASS	In situ
SM–005 *E784026* *N7039176*	Ca–rich	Ca–rich metatexite	In–situ melting	Qtz–Pl–Bt–Kfs–Hbl– **Scp**–Ep–Aln–Ap–Ttn	LASS		LASS	In situ

4.2 Metamorphic thermodynamic modelling

A metamorphic pseudosection was calculated based on the bulk geochemistry and mineral composition of a Grt–Sil–Kfs migmatite (Sample SQ17–034b) (Fig. 4). This sample was chosen as it represents the core of the high grade migmatites in the Agua del Sapo complex. The results show that the metamorphic peak mineral paragenesis Bt+Grt+Kfs+Sil+Pl+Ilm+Liq is stable across a wide range of temperatures (c. 675 – 775 °C), and pressures (4 – >7.5 kbar). Isopleth thermobarometry better constrains these mineral equilibration conditions. The Fe/(Fe+Mg) isopleth for biotite narrows the temperature range between 710–740 °C, and garnet rim composition constrained the pressure between 5.5–6 kbar. The garnet is zoned with grossular (Ca–Al garnet) and almandine (Fe garnet) components increasing from core to rim, and pyrope (Mg garnet) and spessartine (Mn garnet) decreasing from core to rim. This pattern suggests that the core most likely equilibrated at a greater temperature than the rim (Powell and J. B. Holland, 1994; Winter, 2001). Mineral geochemistry details in Table 1 in Appendix 3.

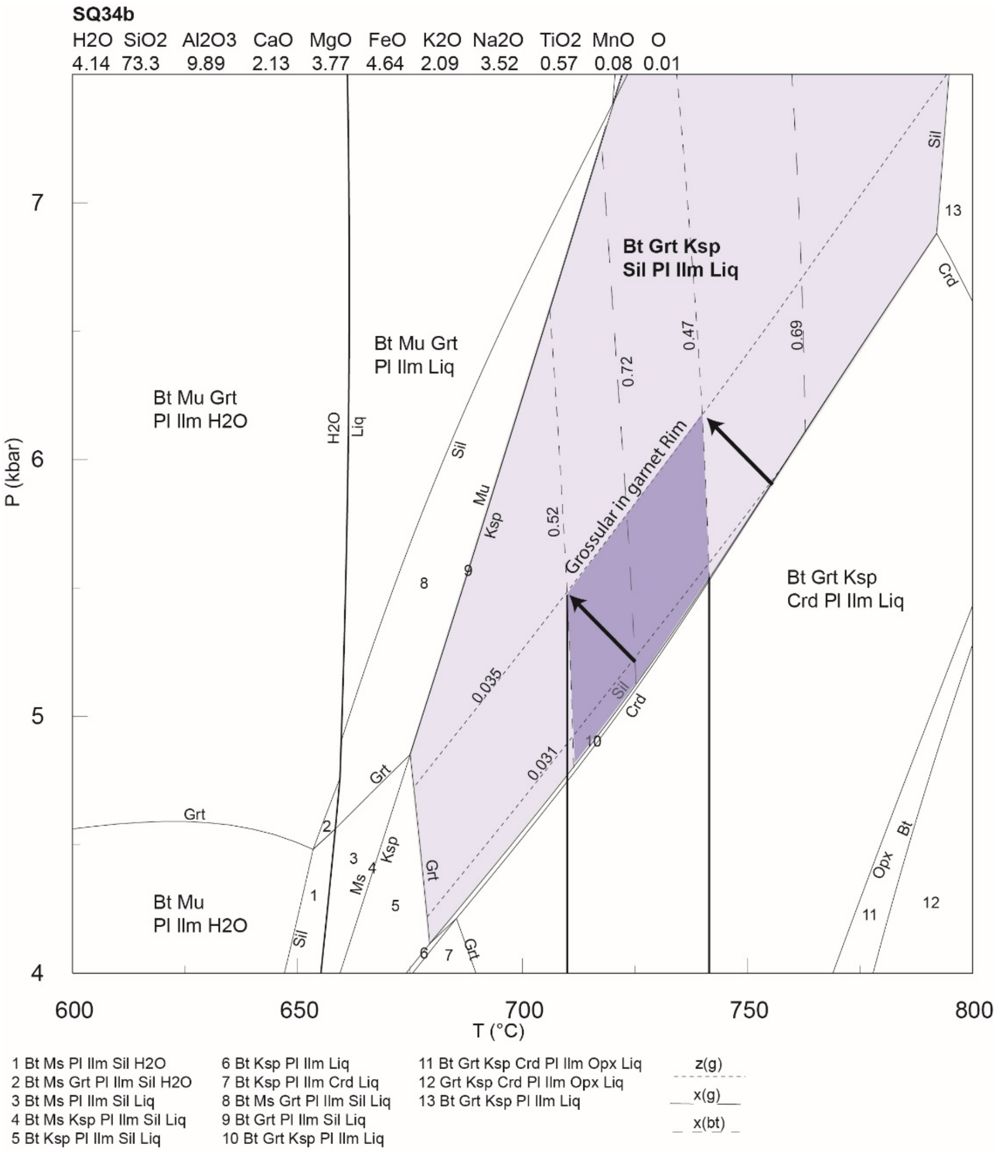

*Figure 4– MnO–Na2O–CaO–K2O–FeO–MgO–Al2O3–SiO2–H2O–TiO2–O (MnNCKFMASHTO) pressure–temperature pseudosection for sample SQ34B. The stable paragenesis is Bt–Grt–Ksp–Sil–Pl–Ilm+Liq (light blue zone). Isopleths constrain the temperature to 710–740 ºC, and pressure between c. 5.5–6 kbar. For biotite, x(bt)= Fe/(Fe+Mg), values are between 0.47–0.52. For grossular, z(g)= Ca/(Fe+Mg+Ca+Mn)*100, the maximum value in the garnet rim is 3.5 % (0.035) z (g) isopleth, black arrows represent the trend from grossular values in the mantle to the rim. Mineral abbreviations after Kretz (1983).*

4.3 Geochronology and mineral geochemistry

We start this section by presenting the geochronological results and mineral chemistry of zircon, followed by monazite and finally titanite. Sample location is shown in Fig. 2 and all geochronological and mineral geochemistry data are presented in Appendix 2.

4.3.1 Zircon

Zircon grains from five samples were investigated (Table 2). They include one schlieric granite (SQ17–049), two migmatite samples from the Al–rich siliciclastic group (SQ17–022 and LC–019) and two migmatite samples from the Ca–rich siliciclastic group (SQ17–025 and SM–005). Most of the zircon grains have detrital zircon (DZ) cores (Fig. 5). These are rounded or anhedral and with younger rims of variable thickness, morphology and cathodoluminiscence (CL) texture. The interface between DZ cores and their rims typically have a thin bright CL fringe and signs of resorption (Fig. 5). CL images of the rims are usually featureless, but can also have 'ghost zoning' with remnants of original oscillatory textures, or fuzzy sector zoning (Fig. 5b), characteristic of metamorphic zircon (Hoskin and Black, 2000; Hoskin and Schaltegger, 2003; Taylor et al., 2016).

The DZ cores in all four migmatite samples are older than the Cambrian Pampean magmatism, and the rims are of Famatinian age. The granite sample SQ17–049 is different in that it has substantial Pampean ages in both cores and rims, with some rims of Famatinian ages. We first present the DZ ages of the migmatites to elucidate maximum depositional ages, before presenting results for zircon rims. We then present ages from the granite sample SQ17–049, and finish with the geochemistry of zircon.

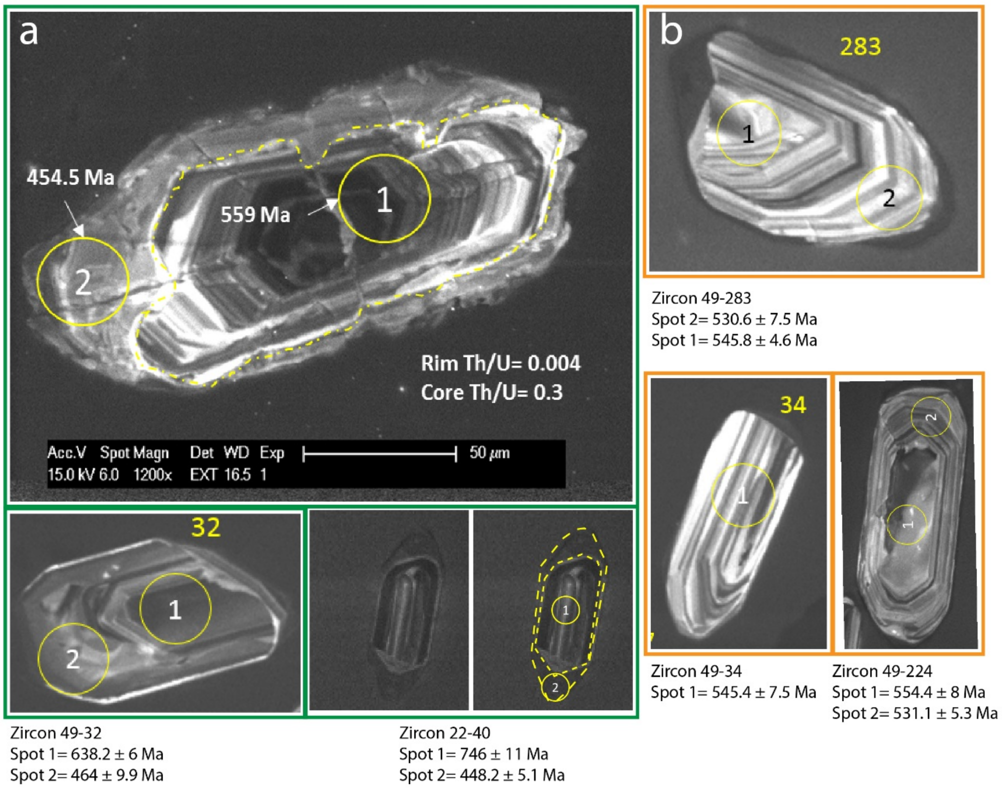

Figure 5– (a) Typical CL image of core–rim texture in zircon. The dissolution front of the detrital zircon is marked by a bright CL line a few µm wide marked by the discontinuous yellow line that truncates the internal zonation. The metamorphic rim has a diffuse featureless zonation and very low Th/U ratios compared to the core. Below a) other examples of featureless zircon rims on detrital zircon (DZ). (b) Oscillatory textures in igneous zircon from Filo granite sample SQ17–049.

4.3.1.1 Detrital zircon (DZ) ages in migmatites

Detrital zircon dates are clustered in two groups: a broad one ranging from 550 to 690 Ma, and the other from 920 to 1000 Ma (Fig. 6). The migmatites lack Pampean age zircons (c. 540–510 Ma) and have instead conspicuous age peaks between c. 700–800 Ma, that for samples LC–022 and SQ17–025 are comparable in magnitude with the 550 to 600 Ma group (Fig. 6). The maximum depositional age (MDA) (Gehrels, 2014) given by the youngest detrital zircons in the migmatites of Agua del Sapo is >550 Ma.

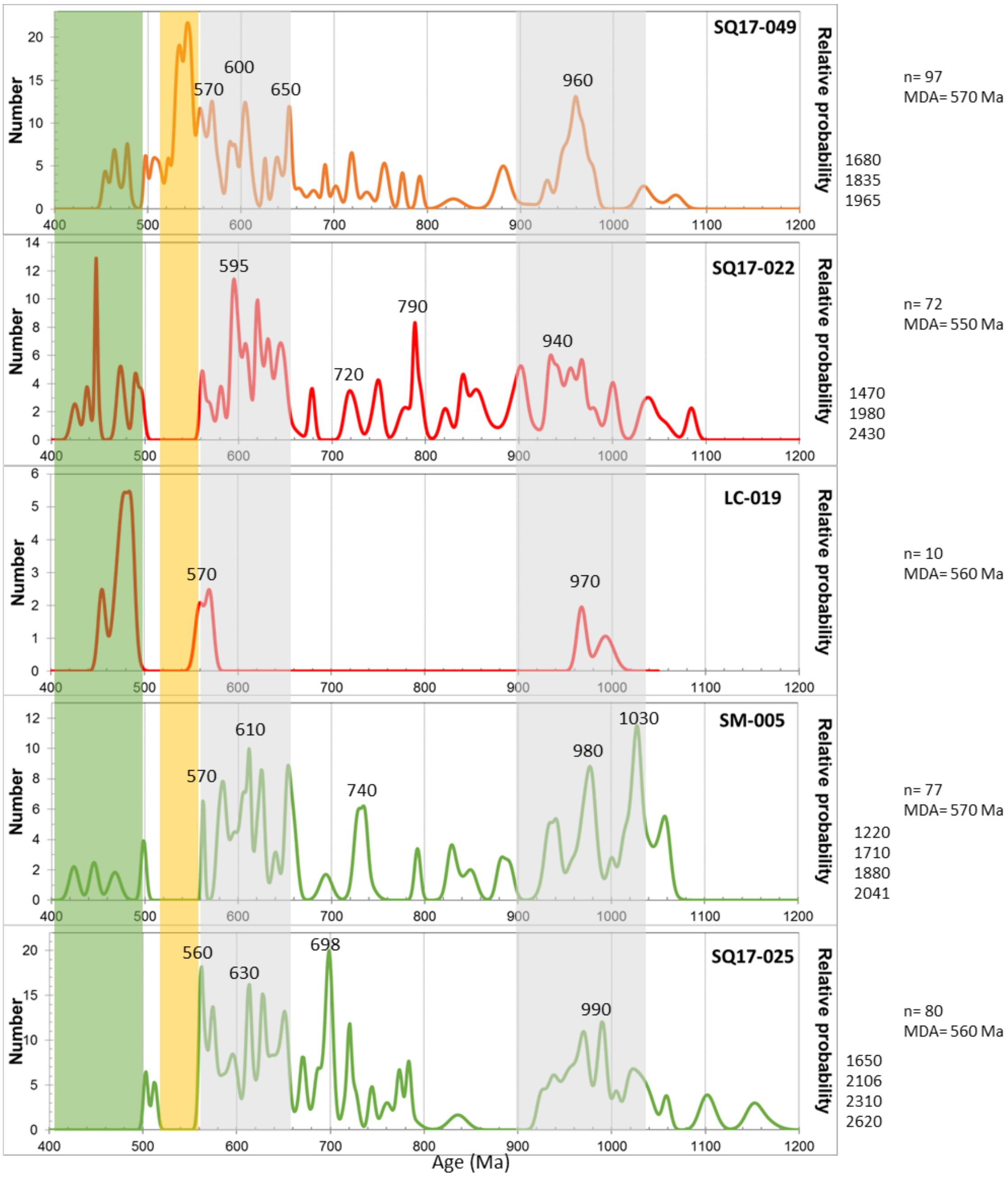

Figure 6– Probability plots of detrital zircon age. In orange is the schlieric granite, red the Al–rich siliciclastic rocks and green the Ca–rich siliciclastic rocks. Green vertical strip indicates the duration of Famatinian orogeny, yellow strip the Pampean orogeny, and grey strips indicate the typical ages of the Puncoviscana formation detrital zircons. The period from 515 to 500 Ma is the transition (magmatic lull) between the orogenies (Weinberg et al., 2018b). Ages <550 Ma are magmatic-metamorphic.

4.3.1.2 Migmatites: Famatinian–age zircon rims

We have only obtained a small number of Famatinian ages in zircon rims from three out of four migmatite samples (LC–019, SQ17–022 and SM–005). Sample SQ17–025 did not have rims wide enough for placing an analytical laser spot. The Famatinian ages in all samples are scattered between 498 and 424 Ma with most frequent ages around 470 Ma (Fig. 7). These ages are typically found in zircon rims and occasionally in zircon cores (LC–019). The zircon rims are not considered metamictic, as the CL texture does not indicate radiation damage, and their U content is less than 1000 ppm (Table 1 in appendix).

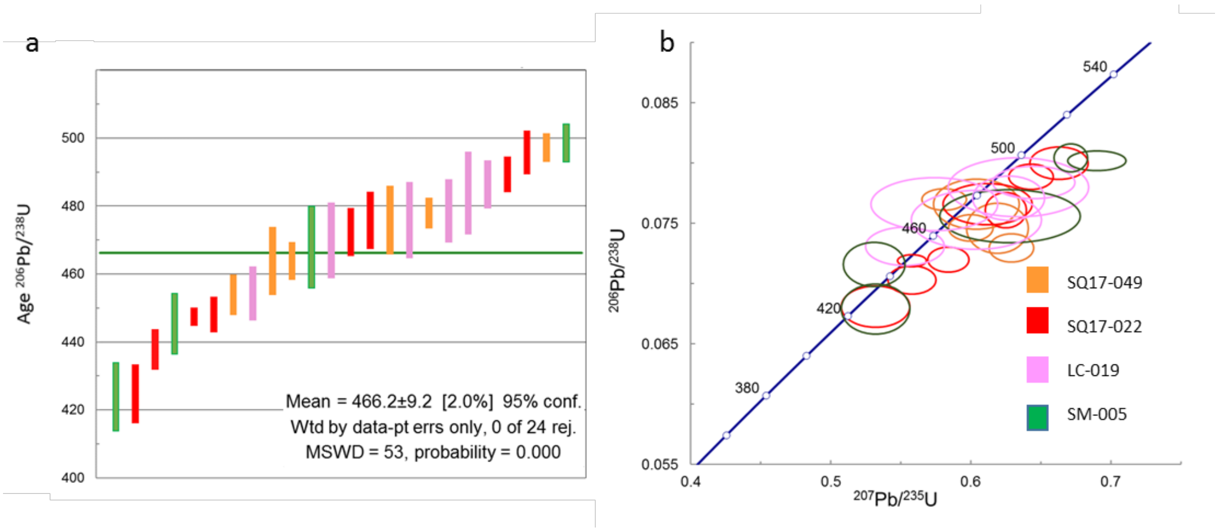

Figure 7– (a) Weighted average of all Famatinian ages combined. The weighted average of 466.2 ± 9.2 Ma with MSWD of 53 is meaningless, however, there is a small concentration of ages at c. 470Ma. (b) Concordia diagram of the same points from (a). The odd trend in the Concordia diagram reflects a common Pb trend.

4.3.1.3 Filo granite: Schlieric granite of Pampean age

The Filo granite is elongated in the north–south direction, weakly foliated and concordant with the country–rock foliation. It has have a low–magnetic signature in the aeromagnetic images; however, they have a wide range of magnetic susceptibility values measured in–situ, between 10 and 200, but typically 20. The high magnetic values are associated with biotite–magnetite–rich clots of restitic material. The mineralogy is simple and characterised by quartz, plagioclase, K–feldspar, garnet, biotite, sillimanite and muscovite, with accessory zircon, monazite, and rare apatite. This granite have aligned biotite–garnet–rich schlieren and sometimes 1 cm–long phenocrysts of K–feldspar with abundant inclusions of biotite and rounded quartz, similar to those in the migmatites.

Unlike the migmatites above, Filo granite represented by sample SQ17–049 has Pampean–age zircon, both in cores and rims and only a small number of Famatinian rim ages. The zircon grains are usually euhedral to subhedral, and with a 1:2 to 1:4 aspect ratio. The CL texture of Pampean–age zircons is characterised by an oscillatory pattern and their rare Famatinian–age rims have featureless or sector zoning textures (Fig. 5). The relative probability graph in (Fig. 8) shows a major peak between c. 550 and 520 Ma, coinciding with Pampean magmatism (Rapela et al., 1998a; Schwartz et al., 2008a), and outliers between 550–570 Ma and between 504–510 Ma with sector zoning texture (Fig. 8a–b).

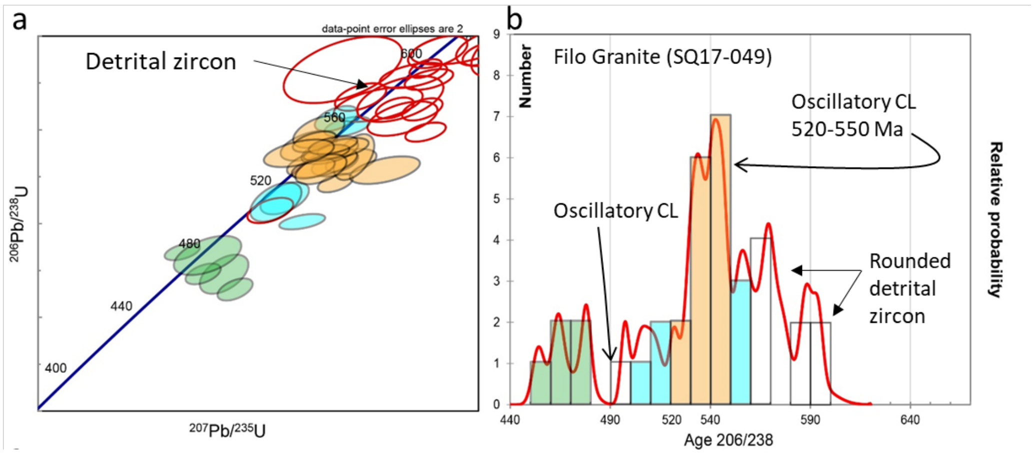

Figure 8– Zircon U–Pb age in a Concordia diagram (a) and in a probability graph (b) showing how they relate to CL textures. In green metamorphic Famatinian rims, light–blue Pampean zircon with featureless CL texture, orange Pampean oscillatory CL texture. The odd trend of Pampean and Famatinian ages reflect a common Pb issue.

4.3.1.4 Zircon chemistry

Th/U ratio in zircon

Most of the Famatinian–age rims have a Th–U ratio < 0.1, which is typical of metamorphic zircons (Rubatto, 2002; Yakymchuk et al., 2018). The Pampean age zircon grains of sample SQ17–049 have Th/U ratio > 0.1 (Fig. 9).

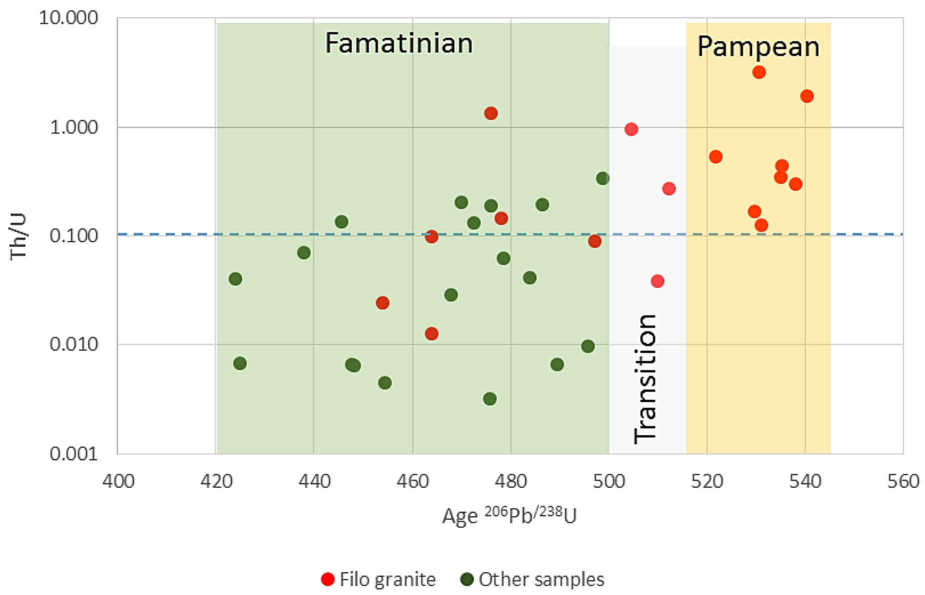

Figure 9– Th/U of zircons from all samples. Note that Pampean age zircon (orange band) from Filo granite SQ17–049 has only Th/U > 0.1, whereas most of the Famatinian zircon (green band) most analyses are < 0.1.

Ti–in–Zircon temperature

Temperature estimations were obtained using the Ti–in–zircon method with calibrations of Watson (2006) with an estimated uncertainty of ± 10 ºC. This method was calibrated for rocks with Ti–bearing mineral phases (titanite, ilmenite or rutile), which are used to estimate the titanium activity *a*Ti. Ilmenite is present in all our samples indicating $a\mathrm{TiO_2}$ >0.8 (Chambers and Kohn, 2012; Schwartz et al., 2008b). The shortcoming of this technique is that the innate incompatibility of Ti in zircon under most common temperature for zircon formation results in low Ti content (c. 0.3–50 ppm). Because of this, LASS–ICP–MS analyses resulted in c. 50% of the spots having values of Ti below detection limits or with low accuracy.

Results for migmatite SQ17–022 yielded an average of 670 ± 10 °C, and for migmatite SM–005 only one value at 720 ± 10 °C was obtained (Table 3). The schlieric granite sample SQ17–049 show differences in the Ti–in–zircon temperatures between Pampean and Famatinian spots (Fig. 10). Pampean age zircon spots resulted in higher temperatures if compared with the Famatinan rims. The former with an average temperature of c. 770 °C and maximum of c. 800 ± 10 °C, and the latter with an average of c. 690 °C and maximum temperature of 710 ± 10 °C.

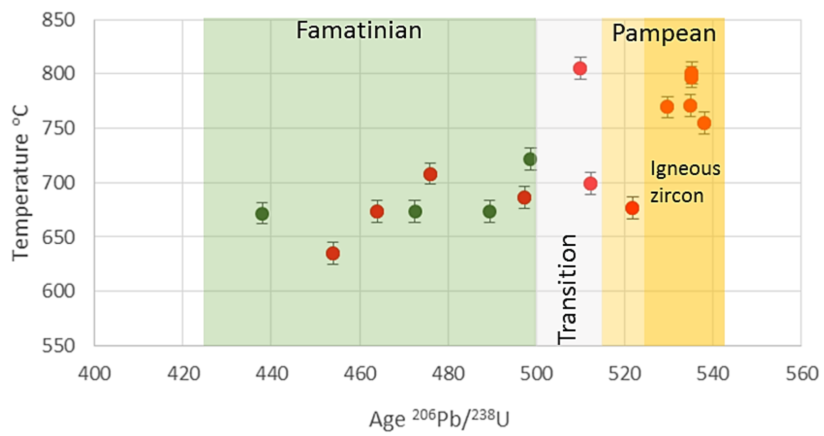

Figure 10– Ti–in–zircon temperature versus age of analyzed spot. Red spots for Filo granite, and green for the rest. Note that the Pampean igneous zircon with oscillatory CL texture records temperatures > 750 °C, while the Famatinian zircon rims are mostly below 700 °C.

Table 3– Ti–in–zircon temperature.

Sample	Spot	$^{206}Pb/^{238}U$	±	Ti-in-zircon temperature (± 10 °C)
SQ17-049 Famatinian	49-180-2	454	5.8	635
	49-183-2	464	5.4	674
	49-222-2	476	10	708
	49-69-2	497.3	4	687
SQ17-049 Pampean	49-38a-1	510	10	805
	49-5-2	512.3	8.1	699
	49-35-1	521.8	4.7	677
	49-58-1	529.7	7	769
	49-78-1	534.9	7.4	771
	49-30-1	535.1	6.9	797
	49-40-2	535.2	5.2	801
	49-60-1	538	12	755
SQ17-022	22-31-1	438	5.8	672
	22-48-22a	472.5	6.9	674
	22-35-2	489.4	5.1	674
SM-005	005-11-1	498.7	5.6	722

Zircon REE

Zircon REE was analysed to trace potential formation and or destruction of other mineral phases like garnet or monazite (Taylor et al., 2016, and references within). For example, the depletion of heavy rare earth elements (HREE) in zircon is usually associated with prograde growth of garnet (Rubatto, 2002; Whitehouse and Platt, 2003).

The REE chondrite–normalized diagram of Fig. 11 shows no differences in REE values among Famatinian–age zircon rims between granite SQ17–049 and migmatite SQ17–022. They have a Lu_n/Sm_n c. 150, with a negative Eu anomaly and a positive Ce anomaly with a substantial dispersion of LREE values, due to their low concentrations in zircons.

Figure 12 compares the REE values of Pampean and Famatinian–age spots from the granite SQ17–049. All analyses have a similarly steep REE pattern (Lu_n/Sm_n c. 150). The oscillatory zoning in Pampean zircon is responsible, at least in part, for the larger compositional variations among grains.

The Famatinian rims lack such zonation, and as a result, they have smaller compositional variations. There is a difference in the middle rare earth elements (MREE) content (Gd, Tb, and Dy) where the Famatinian–age zircon rims have lower values compared with the Pampean–age spots.

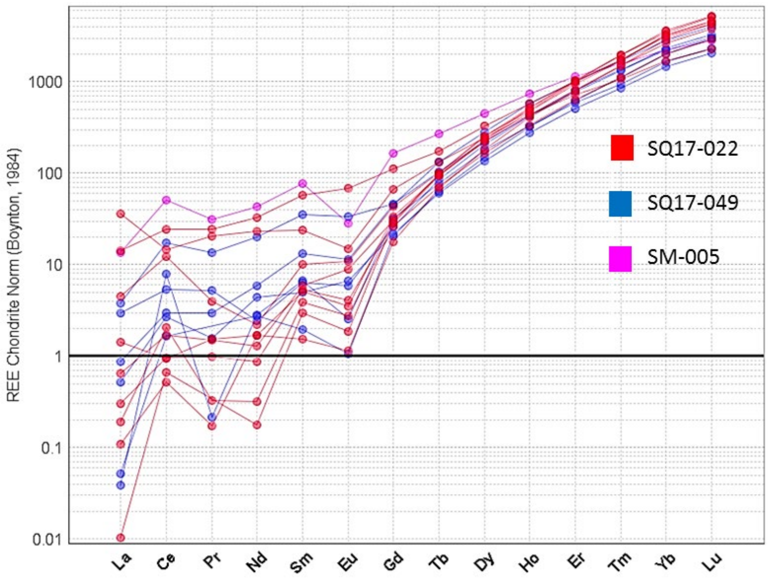

Figure 11– Chondrite normalized REE diagram for Famatinian zircon rims. REE pattern is typical of zircon (Rubatto, 2002).

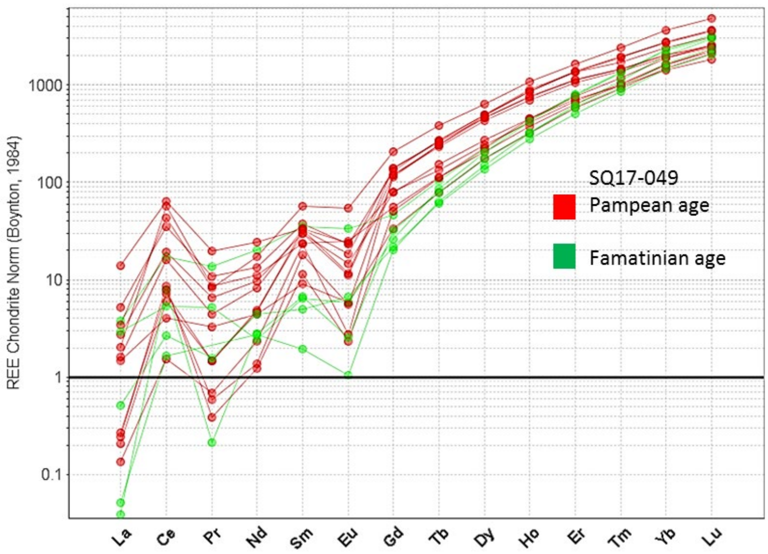

Figure 12– Chondrite normalized REE diagram with values from granite SQ17–049. In red Pampean age and in green Famatinian zircon age spot. Note that Famatinian zircon has low MREE values, typically associated with metamorphic zircon.

In summary, the four migmatites and the schlieric granite yielded: 1) detrital zircon cores with typical age peaks of the Puncoviscana sediments with the youngest DZ age at c. 550 Ma, 2) All samples have Famatinian–age zircon scattered among c. 440–490 Ma, usually as thin rims with Th/U < 0.1 and CL textures characteristic of metamorphic zircon. 3) The granite sample records a population of Pampean ages, that is lacking in all four migmatite samples, and is associated with oscillatory CL texture and Th/U > 0.1, both typical of igneous zircon. 4) The Ti–in–zircon temperatures calculated from the Pampean zircon at 770 to 800 °C are higher than the Famatinian zircon rims at 650–700 °C.

4.3.2 Monazite

A total of four samples were selected for monazite dating. Samples SQ17–049 and SQ17–022 were dated by means of LASS–ICP–MS and samples SM–003 and LC–019 by LA–ICP–MS (Table 2). All of these samples, except SM–003, had their zircon age described in the previous section. Monazite grains were hand–picked and separated based on colours, shape, and size. Most of the monazites are light amber colours, roughly rounded and 100–150 µm in diameter. The BSE images show no internal zonation, however most grains where more than one spot was analysed, yielded variable U–Pb ages.

4.3.2.1 Age range

Monazite $^{206}Pb/^{238}U$ dates were calculated. In order to discriminate between different age populations, the Unmix function of Isoplot (Ludwig, 2003b) was used. This function detects multiple populations and estimates the most likely age in each group, based on the mixture modelling approach originally designed to disentangle zircon U–Pb ages (Sambridge and Compston, 1994). Results are presented in Appendix 2.

Sixty–nine monazite grains were dated for sample SQ17–022, with a total of 72 analyses. Thirty–eight out of the total analysis are 100% concordant, and the rest is < 5 % discordant (Fig. 13). The ages range between 444 and 465 Ma. The weighted average of all analysis yields a mean age of 456.9 ± 0.86 Ma with a [MSWD] = 8.1, and a probability of fit [*p*]=0.00.

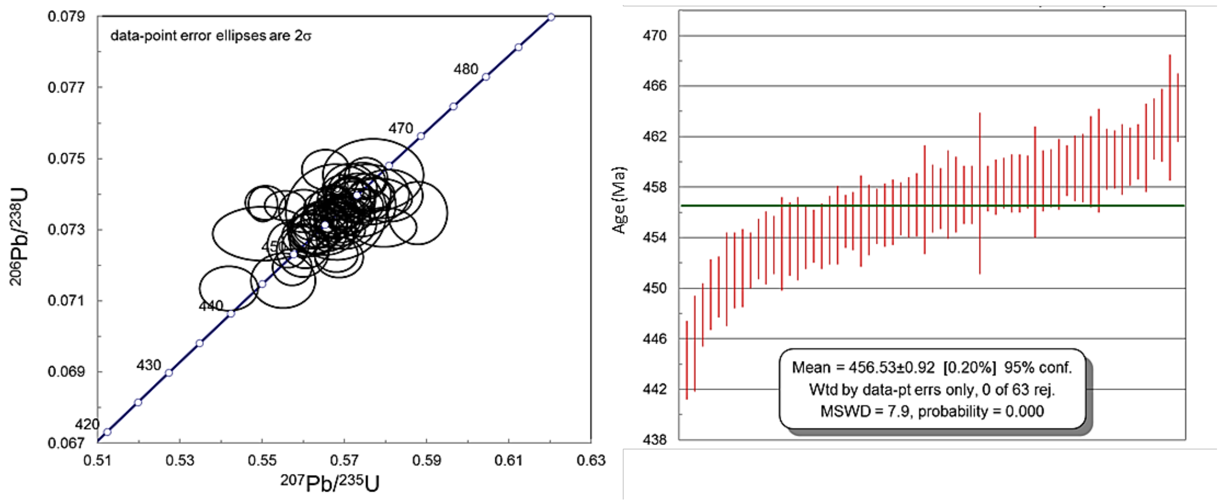

Figure 13– Concordia diagram (left) and weighted average diagram (right) for monazite U–Pb ages in sample SQ17–022, note the large MSWD of the mean value. All error ellipses and bars are in 2σ.

Twelve monazite grains with a total of 20 spots were analysed for sample LC–019. The analyses are all < 3 % discordant (Fig. 14). The ages range between 442 and 492 Ma. The weighted average is not meaningful due to the large and semi–continuous age spread. The Unmix function of Isoplot return these two peaks at 470.11 ± 1.1 Ma (65 % of all analysis), and 449.97 ± 1.4 Ma (35 % of all values), with a relative misfit of 0.368.

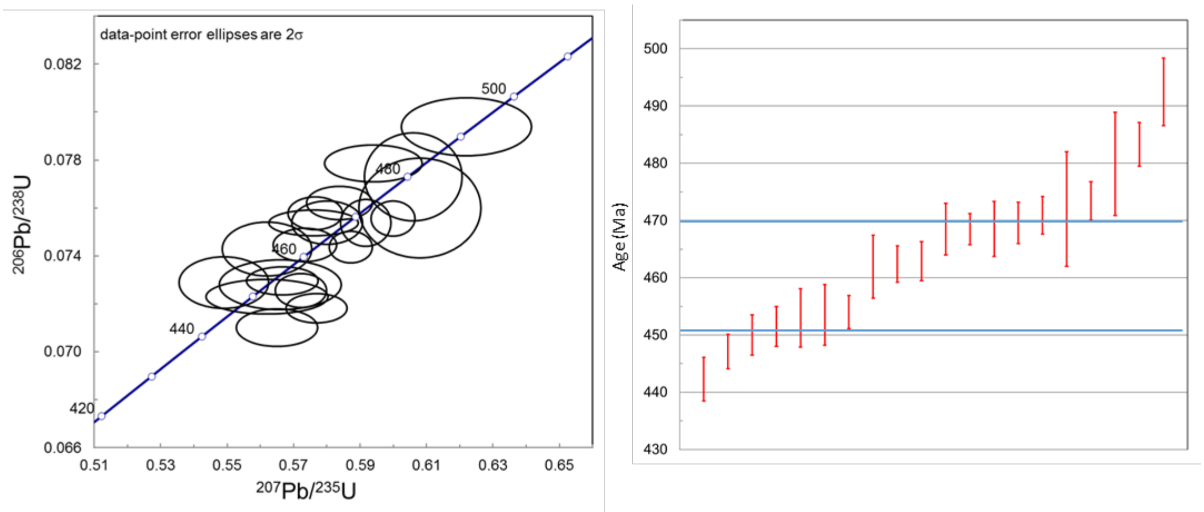

Figure 14– Concordia diagram (left) and weighted average diagram (right) for monazite U–Pb ages in sample LC–019, with blue lines showing the two UnMix age peaks. All error ellipses and bars are in 2σ.

Eighty–six monazite grains were dated for the schlieric granite sample SQ17–049, and a total of 89 spots analysed. All analysis are < 5 % discordant. There is a spread of ages between 447 and 467 Ma with a mean age of 457.95 ± 0.84 Ma with a large [MSWD] = 10.6, and [*p*]=0.00.

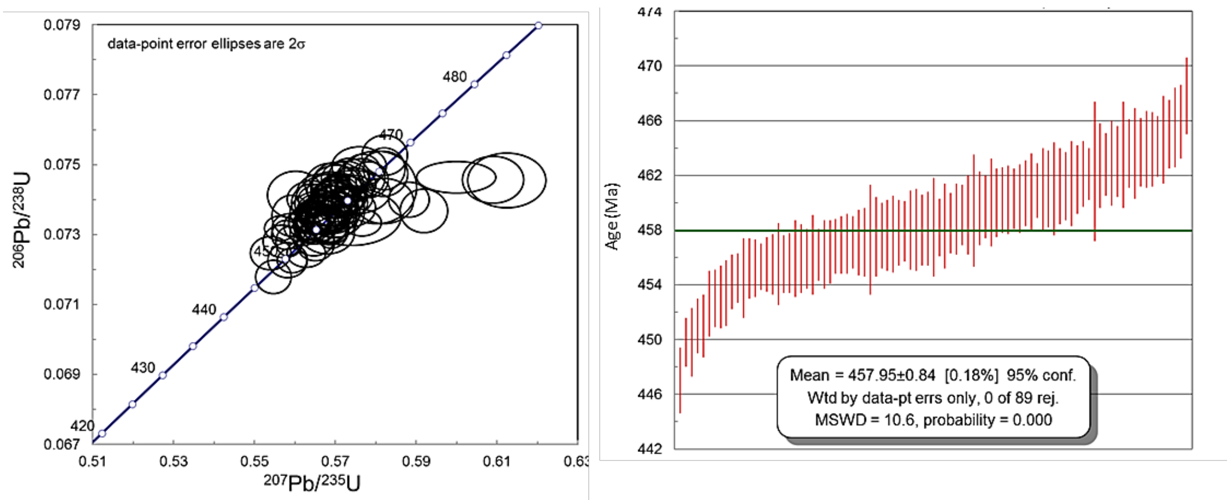

Figure 15– Concordia diagram (left) and weighted average diagram (right) for monazite U–Pb ages in sample SQ17–049. All error ellipses and bars are in 2σ.

Twenty–nine monazite grains in sample SM–003 were analysed with a total of 45 spots. The ages range between 417 and 471 Ma, and a mean age of 453.5 ± 3.3 with a MSWD of 28 and [*p*]=0.00.

The probability graph shows multiple peaks younger than the mean age. The Unmix function of Isoplot return two peaks at 456.54 ± 0.64 Ma (87 % of all analysis), and 426.16 ± 1.9 Ma (13 % of all values), with a relative misfit of 0.387.

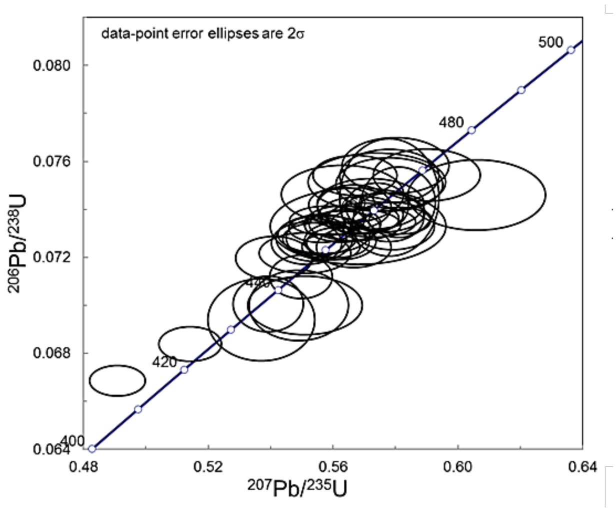

Figure 16– Concordia diagram for monazite U–Pb ages in sample SM–003. Note smearing of ages towards < 440 Ma ages. All error ellipses and bars are in 2σ.

4.3.2.2 Summary of ages

The probability plots (Fig. 17) show a wide sprad of ages with large MSWD values and probability of fit [*p*]=0.00, which highlights the lack of coherence between the uncertainty of the samples and the intrasample variation, suggesting multiple age populations within the dataset (Ludwig, 2003a; Schoene et al., 2013). The granite Filo (SQ17–049) and migmatite leucosome SQ17–022 have the narrowest distribution with ages varying between c. 445 and c. 465 Ma, spanning c. 20 Myr. The metatexites LC–019 and SM–003 have a wider spread of ages, covering the duration of the entire Famatinian orogeny, and in the case of SM–003 with some ages < 440 Ma. Most of the probability curves are skewed towards younger ages. Interestingly, the monazite ages in all samples overlap with those of its Famatinian metamorphic zircon rims.

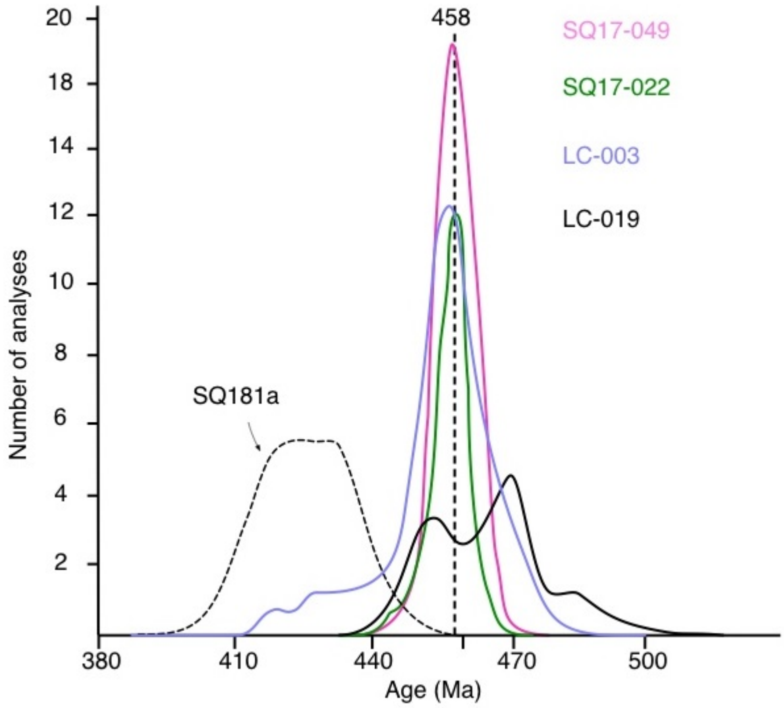

Figure 17– Probability plot of all samples showing a wide spread around a central age at c. 458 Ma. Samples SQ181a (Finch et al., 2017) and SM–003 have ages < 440 Ma.

4.3.2.3 Monazite REE

The monazite REE distribution for samples SQ17–022, SQ17–049, and SM–003 (Fig. 18) shows a typical monazite steep REE pattern (Sm_n /Lu_n c. 200), and negative Eu anomaly. Although similar REE patterns, there are some differences in the LREE and Eu content. Monazites from migmatite SQ17–022 have higher LREE content followed by the schlieric granite SQ17–049 and the Bt–Grt schist SM–003 with the smaller values. In terms of Eu, monazite from granite SQ17–049 and leucosome SQ17–022 has the largest Eu anomaly, followed by those of metatexite SM–003 and schist SQ–181a with the smallest Eu value (Fig. 18b).

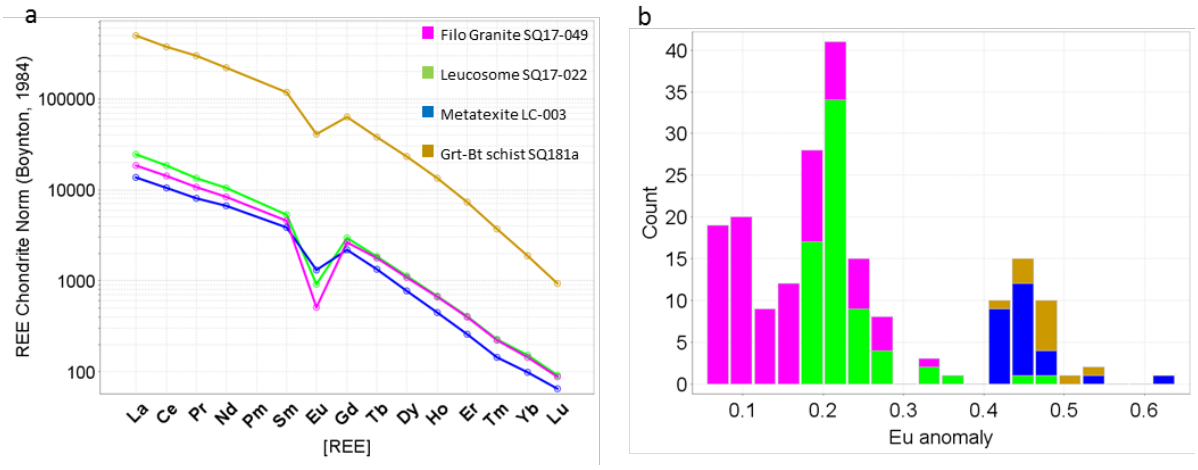

Figure 18– (a) Chondrite normalized REE diagram (mean value) for monazite of samples SQ17–022 (leucosome), SQ17–049 (Filo granite), SM–003 (Grt–Sil metatexite), and SQ181a (Bt–Grt schist) from Finch (2017). (b) Eu anomaly of all monazites. Note that the granite and leucosome have a larger Eu anomaly (smaller values), compared with the metatexite and schist.

4.3.3 Titanite

LASS–ICP–MS spot analysis was conducted for titanites from seven different Ca–rich siliciclastic rocks, some in–situ and some from mounted separates (Table 2). Out of these, samples SQ17–025 and SM–005 had their zircon analysed (section 4.3.1). Most of the grains are 100–150 µm in size, euhedral to subhedral with aspect ratios between 1 and 4. The back–scattered electron images show zoning defined by dark and bright, angular, and irregular zones of different size with sharp edges (Fig. 22).

4.3.3.1 Age range and distribution

The corrected $^{207}Pb/^{206}Pb$ date of every spot was defined as the lower intercept of the anchored Discordia line with the Concordia in a Tera–Wasserburg diagram (Fig. 19). The Discordia is anchored to a $^{207}Pb/^{206}Pb$ value of 0.86 based on the model evolution of Stacey (1975) for c. 470–440 Ma (for details see section 3.2). These corrected $^{207}Pb/^{206}Pb$ dates were plotted in a probability graph to visualise the age distribution (Fig. 20).

There are two titanite U–Pb date populations across the complex (Fig. 20a). Samples (SQ17–025, UMF, SQ17–046C) define a unimodal age distribution centred on 460 Ma [500–440 Ma] with few spots younger than 440 Ma. In contrast, samples (SM–005, SQ17–028) record a broad peak of younger ages ranging between 440 and 380 Ma with fewer spots older than 440 Ma. The remaining two samples SQ–213 and SQ–108 have a mix of those age groups and in the case of SQ–108, some spots older than 480 Ma (Fig. 20b).

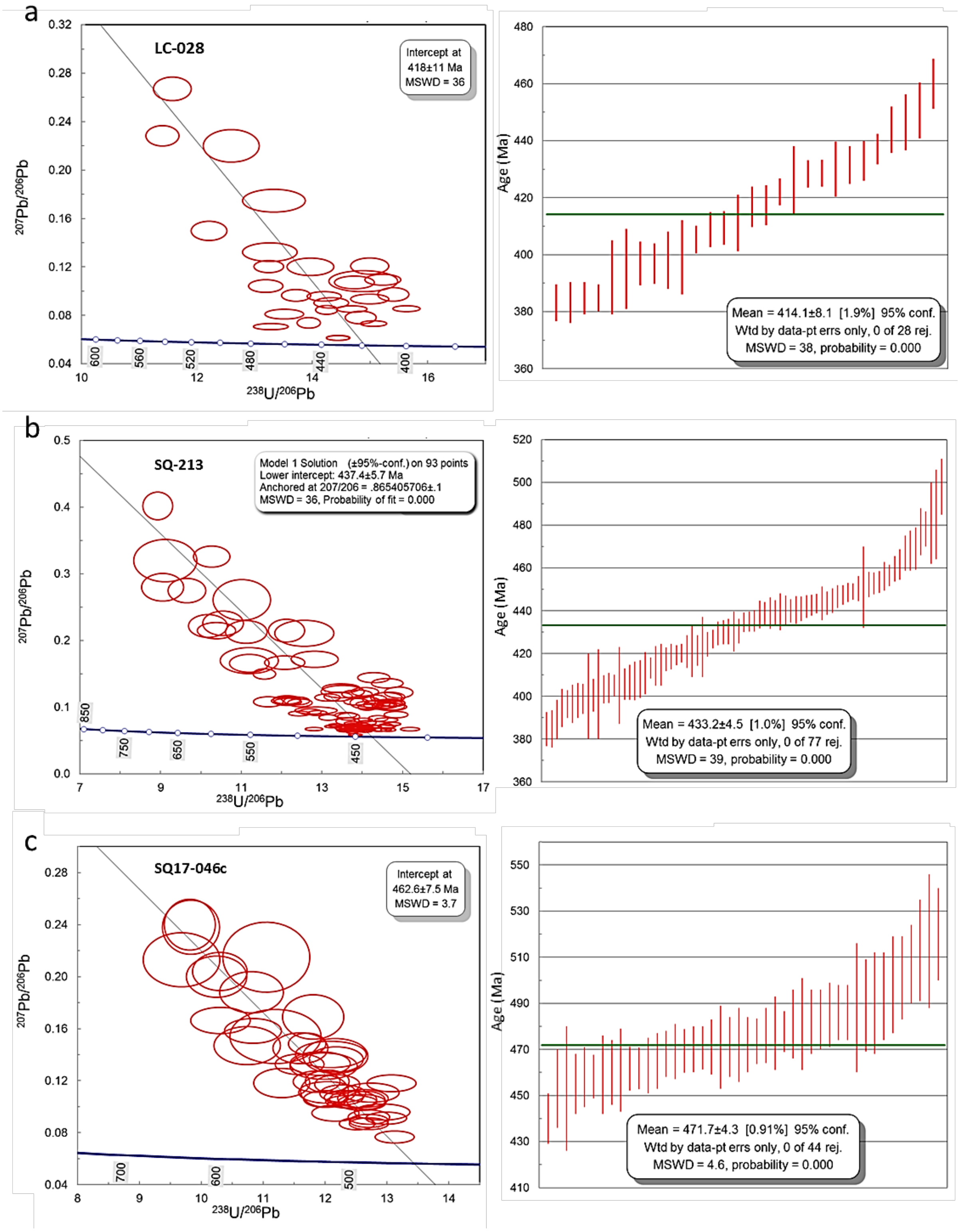
a
LC-028
Intercept at 418±11 Ma MSWD = 36
$^{207}Pb/^{206}Pb$
$^{238}U/^{206}Pb$
Age (Ma)
Mean = 414.1±8.1 [1.9%] 95% conf.
Wtd by data-pt errs only, 0 of 28 rej.
MSWD = 38, probability = 0.000
b
SQ-213
Model 1 Solution (±95%-conf.) on 93 points
Lower intercept: 437.4±5.7 Ma
Anchored at 207/206 = .865405706±.1
MSWD = 36, Probability of fit = 0.000
Mean = 433.2±4.5 [1.0%] 95% conf.
Wtd by data-pt errs only, 0 of 77 rej.
MSWD = 39, probability = 0.000
c
SQ17-046c
Intercept at 462.6±7.5 Ma MSWD = 3.7
Mean = 471.7±4.3 [0.91%] 95% conf.
Wtd by data-pt errs only, 0 of 44 rej.
MSWD = 4.6, probability = 0.000

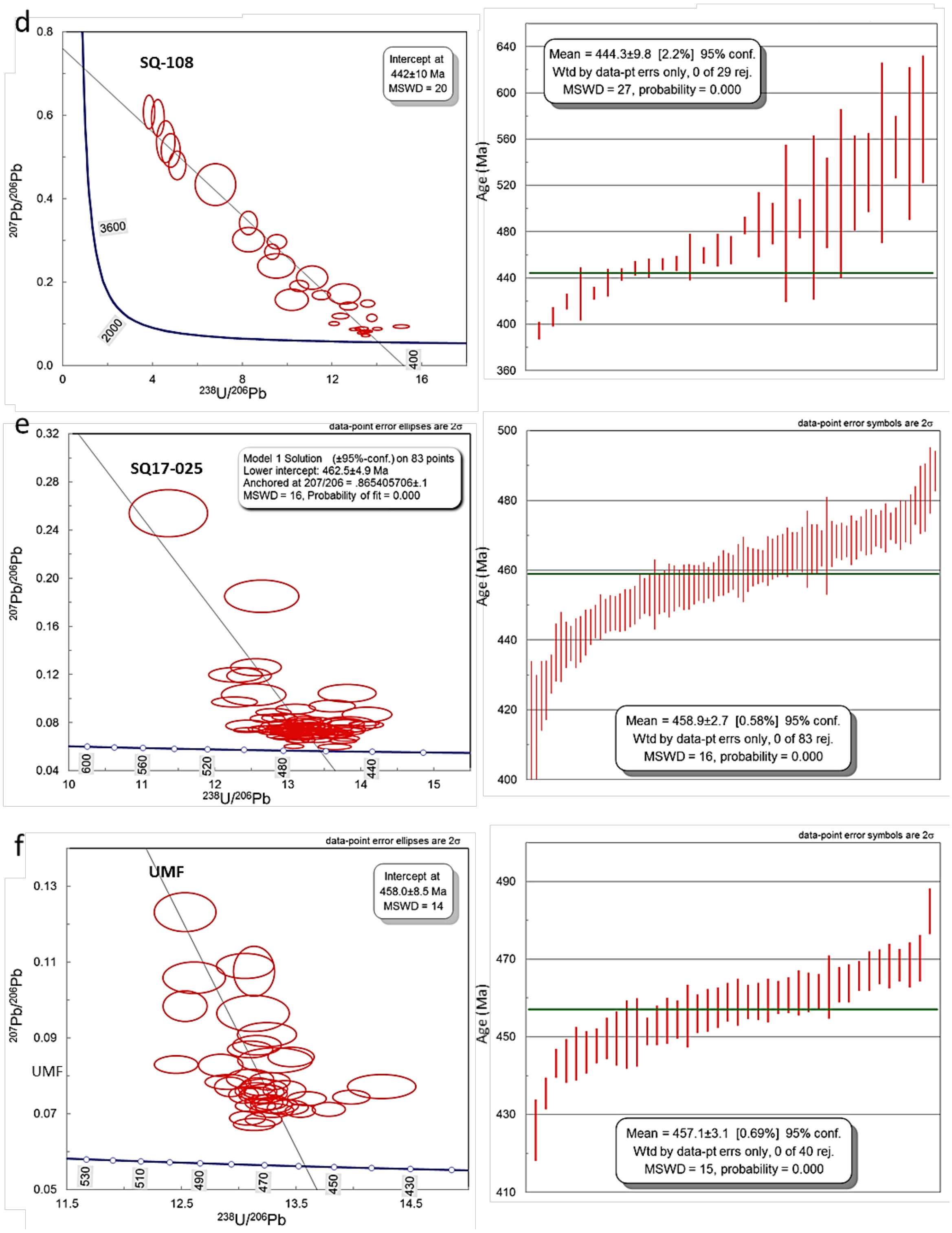

Figure 19– Tera–Wasserburg diagram with anchored age (left), and weighted average plot (right) of all titanite samples. All error ellipses and bars are in 2σ.

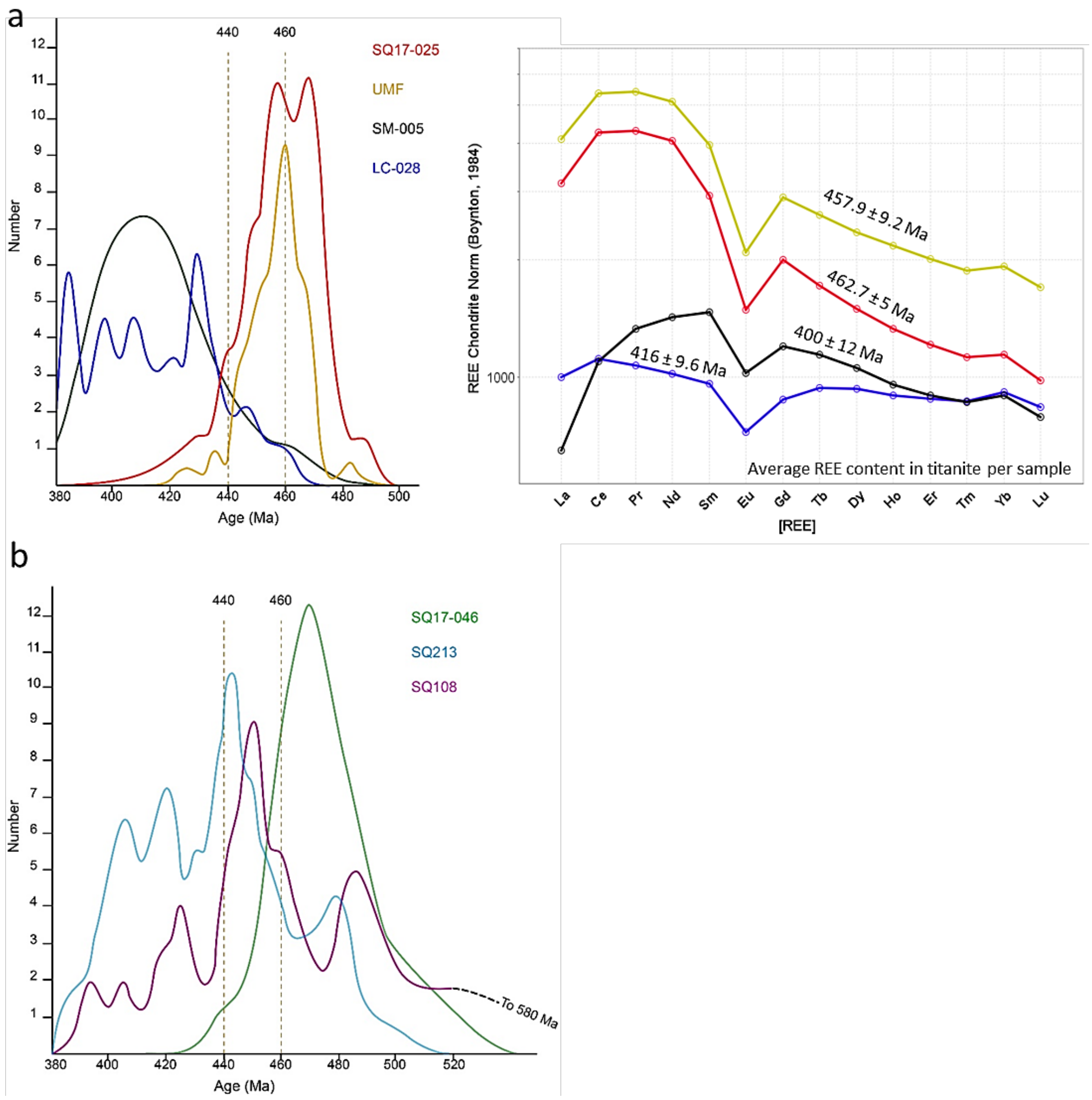

Figure 20– (a) Probability graph of U–Pb ages (left), and chondrite normalized average REE for titanites in same samples (right). Note the direct correlation between age and composition. Titanites > 440 Ma have higher REE and titanites younger than 440 Ma lower REE and particularly lower LREE. (b) Same as a) for samples SQ–213 and SQ–108. Samples are split in (a) and (b) for emphasize differences.

4.3.3.2 Titanite REE

Figure 21 and 22 show that there is a systematic change in the LREE content with time. The older spots have higher total REE contents (Fig. 21), recording a positive correlation between LREE composition and age. This pattern was also obtained for individual grains. Most of the titanites have bright and dark zones in BSE images. Bright zones, usually but not always in the core are older, and have higher LREE and higher La/Lu than the dark rim zones (Fig. 22).

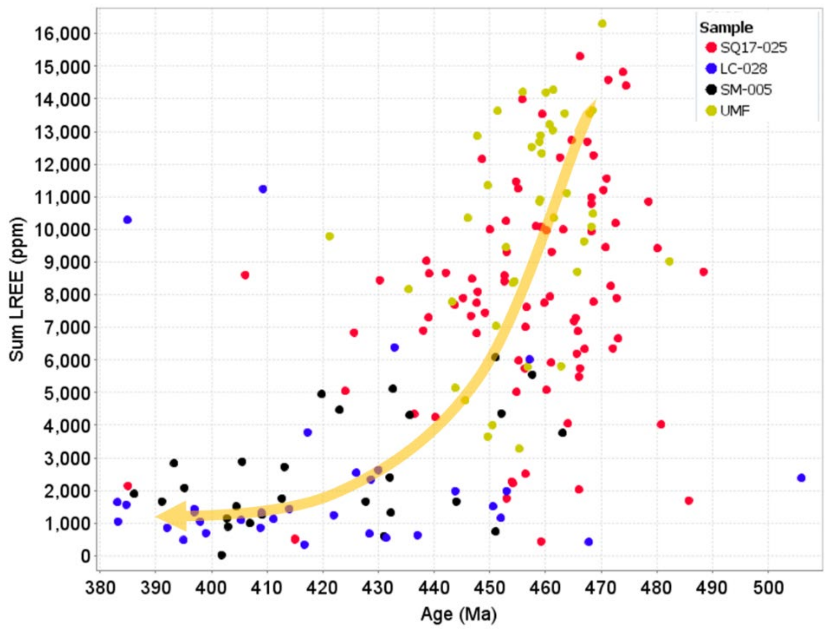

Figure 21– Total LREE content in monazite as a function of age.

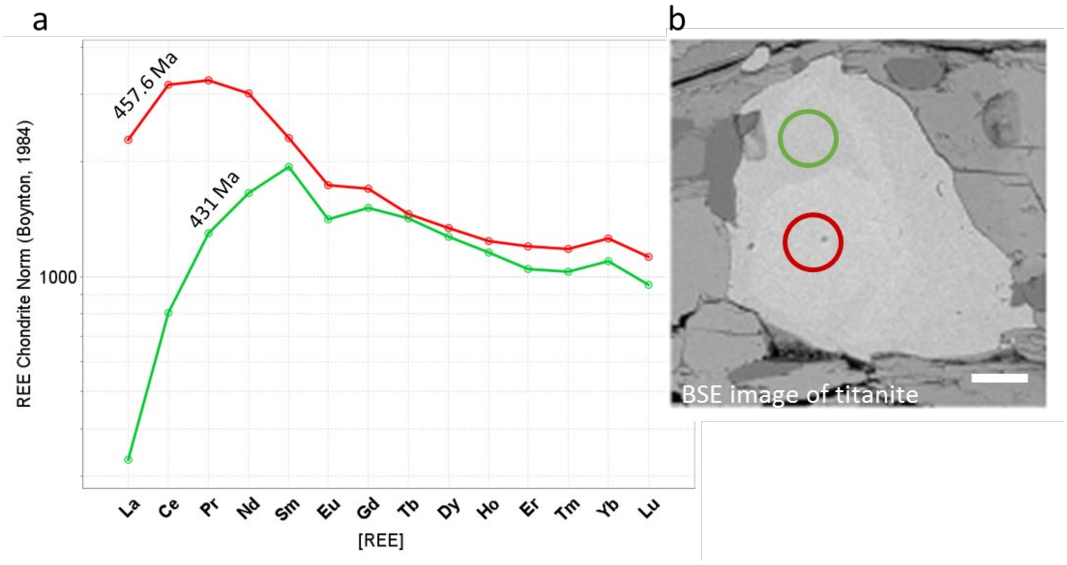

Figure 22– Zoned titanite grain from sample SQ–213. (a) REE diagram from two spots in the grain. (b) BSE image. Bright zone with older age and higher LREE (red spot analysis) in the core of a younger dark zone with lower LREE values (green spot analysis). Scale in BSE image is 25 µm.

Given the curved nature of the REE chondrite–normalised diagrams patterns, we used the polynomials defined by λ coefficients ("REE shape coefficients") defined in O'Neill (2016). Particularly useful is the λ_1 versus λ_2 diagrams where the λ_1 coefficient described the slope of the REE pattern (LREE–enriched analysis have a positive λ_1), and λ_2 describes the quadratic curvature. In our case, both change as a function of the age of the spot analysis, with λ_1 trend clearer than λ_2 (Fig. 23). The depletion of LREE with respect to the HREE in the younger titanite spots compared to the older ones is indicated by decreasing λ values. Figure 23 shows a relatively constant λ_1 for the from 480 to 440 Ma at which point it starts to decrease, reaching negative λ_1 values at around 400 Ma.

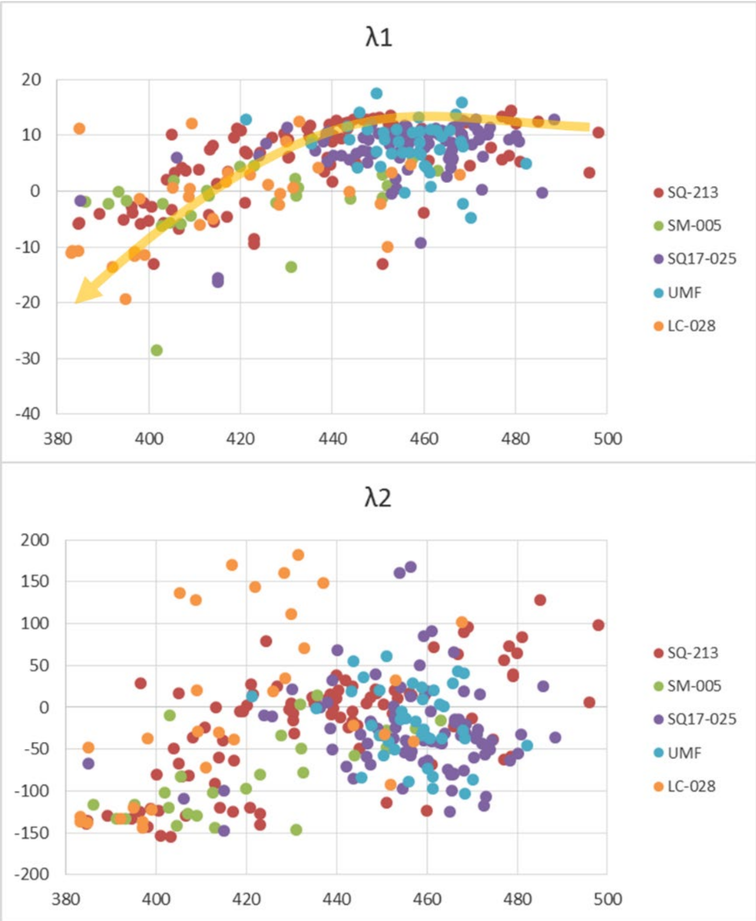

Figure 23– λ_1 and λ_2 versus time. λ_1: relatively constant values of 0–10 between 480 to 440 Ma decreases towards negative values after 440 Ma. This pattern is for both individual samples (e.g. SQ213 in red) and all samples combined. λ_2 trend is similar to λ_1, but values (e.g. LC–028) are more scattered.

4.3.3.3 Zr–in–titanite geothermometer

In order to assess (re) crystallisation temperatures in titanite, we use the Zr –in–titanite method using Hayden (2008) calibration. Analytical uncertainties on Zr measurements are from 5–10 % (2σ) which gives temperature uncertainties of 5–10 °C. Pressure and activity uncertainties result in even larger temperature uncertainties. From the original experiments Hayden (2008) determined $a\mathrm{TiO_2}$ to be 1 in samples with rutile, and c. 0.5 in samples with titanite and no other Ti–bearing face. Our samples lack rutile and have abundant ilmenite. Samples with ilmenite have $a\mathrm{TiO_2} > 0.8$ (Chambers and Kohn, 2012; Kapp et al., 2009; Kohn, 2017; Schwartz et al., 2008b), the value assumed here. Pressure estimates for the surrounding migmatitic complexes (Tolombon and Tolombon West complexes) are in the range of 6–5 kbar (Büttner et al., 2005; Finch et al., 2017). We assume a value of 5.5 kbar for the titanite–bearing migmatites, as suggested by the metamorphic thermodynamic modelling in Fig 4 and mineral paragenesis of neighbouring Al–rich migmatites. In an attempt to reflect the uncertainties, we assume a minimum 2σ uncertainty of 25 °C for each datum.

Temperature estimates increase with time from c. 520 Ma to c. 460 Ma reaching maxima in excess of 750 °C and then decreases steadily to c. 700 °C at 380 Ma (Fig. 24). Samples SQ17–25 and UMF, which have most of their titanites in the c. 460 Ma age group have a weighted average temperature of 745 ± 4 °C and 755 ± 6 °C respectively. Samples SM–005 and LC–028 that have titanites in the range of 380–440 Ma have weighted average temperatures of 715 ± 8 °C and 730 ± 9 °C, respectively. These and the rest of the temperatures calculated from Zr–in–titanite are listed in Appendix 2 and summarised in Table 4.

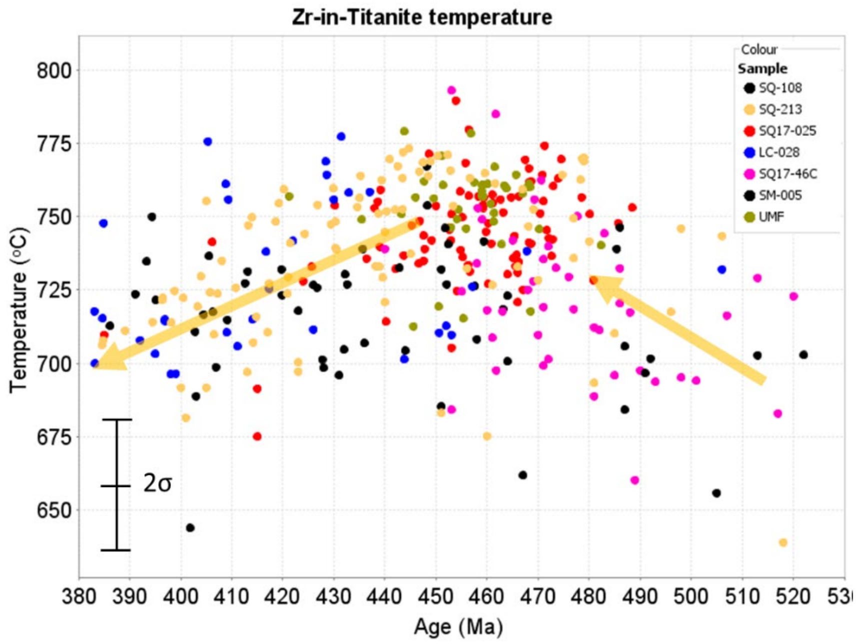

Figure 24– Zr–in–titanite temperature through time in all samples. Arrows indicate prograde and retrograde evolution.

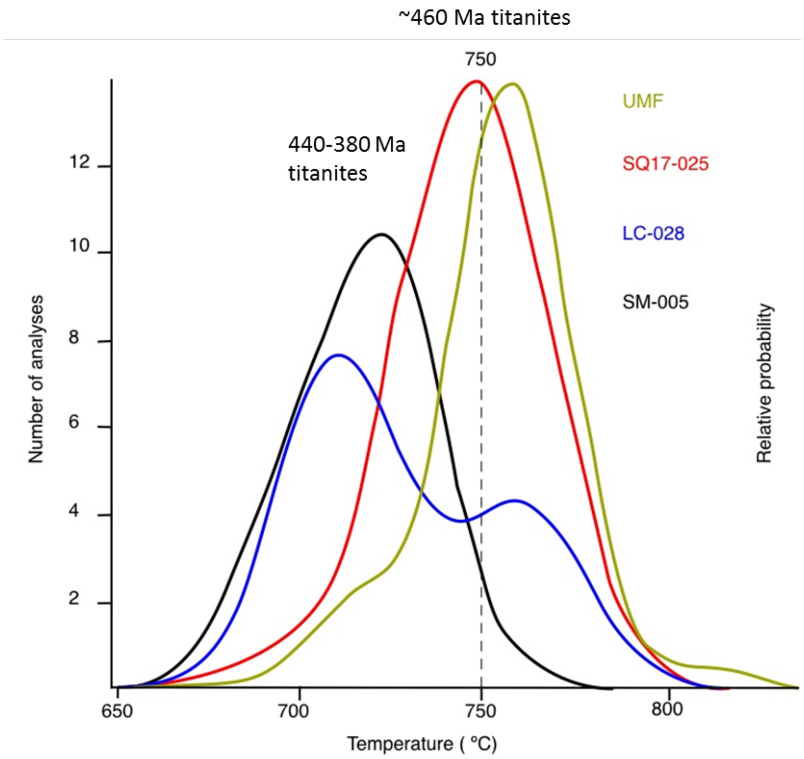

Figure 25– Relative probability diagram for Zr–in–titanite temperatures from four samples.

Table 4. Weighted average of Zr–in–titanite temperatures per sample

Sample	*Zr–in–titanite temperature Weighted average [°C]*	*Age group [Ma]*	*Comment*
SQ17–046c	722 ± 8	480–440	Sheared ortho–amphibolite near Filo shear zone
UMF	755 ± 6	480–440	Mylonite at the Filo SZ
SQ17–025	745 ± 4	480–440	Sheared migmatite
LC–028	730 ± 9	<440	Migmatite, weakly sheared
SM–005	715 ± 8	<440	Migmatite, weakly sheared

In summary, titanites show that there are two groups of ages with different REE compositions, represented in different samples across the Agua del Sapo complex. The c. 480–440 Ma group is represented by samples SQ17–025, UMF, SQ17–046C with higher LREE content and higher Zr–in–titanite temperatures compared to the younger 440–380 Ma group found in samples SM–005 and SQ17–028 (Fig. 25).

5 Discussion

5.1 Maximum depositional age of sedimentary sequence

The meta–turbidites in this complex have detrital zircon (DZ) ages that match those of the Puncoviscana formation. In this formation they fall into two groups: a late Mesoproterozoic–early Neoproterozoic (1200–900 Ma) and a Neoproterozoic–Early Cambrian (670–545 Ma) (Miller et al., 2011) and occasionally minor Paleo– to Mesoproterozoic peaks are present (Adams et al., 2011; Escayola et al., 2011; Hauser et al., 2011; Miller et al., 2011; Schwartz and Gromet, 2004). However, the two main age groups of the Puncoviscana formation are variable in range and relative probability depending on the sample location. For example, Adams (2011) extended the younger peak all the way to 520 Ma indicating that the sediments of the Puncoviscana formation were sourced, at least in part, from the already established c. 550–520 Ma Pampean arc (Adams et al., 2011; Hauser et al., 2011; Rapela et al., 2015; Sims et al., 1998). Weinberg et al. (2018) discussed how the Puncoviscana sequence includes what is effectively two formations, an earlier one, deposited before the onset of the subduction and growth of the Pampean Arc, and a late Puncoviscana sequence that formed in the fore–arc of the Pampean Orogen. Adams (2011; Sola et al., 2013) reported Puncoviscana DZ ages from samples collected c. 100 km north of the Sierra de Quilmes where the 1150–850 Ma and 650–520 Ma age–groups are present together with minor peaks in between. However, as we have seen above, the absence of Pampean age zircons in the Agua del Sapo complex suggest that the parental sediments of the migmatites were deposited before the onset of the Pampean magmatic arc.

5.2 Filo granite: A Pampean intrusion?

Sample SQ17–049 of the Filo granite is the only one with Pampean–age zircons. We consider two possibilities: a) that this is the crystallisation age of the granite, and that the younger zircon rims and monazites represent the overprinting Famatinian high–grade metamorphism; or b) that the Pampean ages are inherited from the source and the Famatinian zircon rims represent the granite crystallisation age. Alternative (a) is favoured because: 1) the Pampean–age zircons have igneous features such as grain morphology (euhedral and with 1:2 to 1:4 aspect ratios), oscillatory zoning, and high Th/U typically > 0.1 (Fig. 5) (Hoskin and Schaltegger, 2003; Rubatto, 2002; Taylor et al., 2016). This contrasts with the Famatinian zircon rims that have metamorphic features such as ill–defined zonation, and Th/U <0.1; 2) the host migmatites surrounding the Filo granite lack Pampean age zircon or monazite, suggesting that the local protolith in the Sierra de Quilmes lacked Pampean detrital zircons.

The further implication of this finding is that the Pampean–age metamorphism at this crustal level was not sufficiently hot to trigger zircon or monazite growth. This is the case for the entire Sierra de Quilmes where the record of Pampean high–grade metamorphism is absent (Büttner et al., 2005; Lucassen et al., 2011; Lucassen et al., 2000). We conclude that the peraluminous, schlieric, two–mica Filo granite is a Pampean intrusion that crystallized between 550-520 Ma (Fig. 8) that intruded Puncoviscana low–grade meta–sedimentary rocks. This hypothesis is solely based on geochronology, and further work is needed to evaluate the nature of the contact between tha Filo granite and the host migmatites.

This granite is located c. 100 km east of the main Pampean magmatic arc, where contemporaneous metaluminous magmatism was taking place (e.g., the 533 ± 4 Ma Guasayán pluton, (Dahlquist et al., 2016). The Pampean fore–arc is unusual because in some places it underwent Pampean–age high–grade metamorphism and anatexis. This is the case in a region some 50 km west of the Sierra de Quilmes, in what is known as the Western Eruptive Belt of the Puna (Coira et al., 2009). Our results suggest that meta–sedimentary rocks underwent anatexis during the Pampean cycle to form the Filo granite and that they do not crop out defining a lower–grade Pampean–age corridor going through the Sierra de Quilmes between the magmatic arc and the Western Eruptive Belt.

5.3 Famatinian U–Pb ages in zircon, monazite, and titanite

Famatinian dates in migmatite samples and the schlieric Filo granite sample are typically recorded in rims and range between c. 500 and 440 Ma. Unlike zircons from the hotter Tolombon Complex where entire zircons yielded common Famatinian dates, zircons from the Agua del Sapo Complex samples are dominated by detrital zircons, and only a few Famatinian rims were wide enough to place an analytical spot. Out of 278 analyses for all our samples, only 24 yielded Famatinian dates, and all were in rims, none in cores. In spite of the relatively small number of analysis, when combined, the dates are centred at around c. 465 Ma, coinciding with the peak of the Famatinian arc magmatism and metamorphism (Bellos et al., 2015; Ducea et al., 2017; Ducea et al., 2010; Mulcahy et al., 2014; Pankhurst et al., 1998).

Monazite from the same samples also resulted in wide spread of dates that span the same range between c. 500 and 440 Ma, peaking at around c. 460 Ma. The large MSWD values of all samples suggest multiple populations within the dataset (Ludwig, 2003a; Schoene et al., 2013); however, it is hard to differentiate age groups with confidence. The probability plot (Fig. 17) shows that samples SQ17–022 and SQ17–049 have the narrowest monazite date distribution between c. 470–440 Ma with a unimodal distribution centred at c. 458 Ma and slightly skewed towards the younger side of the spectrum. Samples LC–019 and SM–003 have a wider distribution. LC–019 records dates between c. 500 and 440 Ma with a bimodal distribution of ages and peaks at c. 455 and c. 470 Ma. Sample SM–003 records a peak at c. 458 Ma strongly skewed toward dates younger than 440 Ma. These young dates were also found for sample SQ181a in the footwall of the Pichao shear zone (Finch et al., 2017). This sample yield dates in the range of 440–410 Ma, with two peaks at 435.2 ± 1.9 and 420.8 ± 1.8 Ma (Fig. 17).

Titanite date distributions are different. It yields two broad groups: one between 500 and 440 Ma, coincident with both monazite and zircon dates, the other between c. 440 and 380 Ma. The latter seems to strengthen the ill–defined young dates obtained from monazite. The two titanite date groups have different REE composition (Fig. 20). This indicates that titanite were either recrystallised, or newly grown after 440 Ma.

In summary, all three accessory phases record Famatinian U–Pb dates widely spread between c. 500–440 Ma, with a distribution centred at c. 460 Ma. Both monazite and titanite yield a younger age group between 440–380 Ma, recording a total spread across c. 120 Ma, lasting beyond the inferred 440 Ma end of the Famatinian orogeny. The younger group suggest continued high temperatures beyond 440 Ma, but these dates are regionally atypical (Bellos et al., 2015; Castro et al., 2014; Ducea et al., 2017; Ducea et al., 2010; Finch et al., 2015; Mulcahy et al., 2014; Pankhurst et al., 1998), as most of the published zircon, monazite and titanite geochronology indicate dates between 500–440 Ma (Büttner et al., 2005; Finch et al., 2017; Lucassen and Becchio, 2003; Weinberg et al., 2018b; Wolfram et al., 2019). These results raise some questions: Why are these dates so widely spread? And what is the meaning of the < 440 Ma monazite and titanite dates? Before addressing these questions, we need to discuss the closure temperature of these accessory minerals, and the record of temperatures experienced by the Agua del Sapo complex during the Famatinian Orogen.

5.3.1 U–Pb closure temperature in zircon, monazite, and titanite

The U–Pb date of every geochronometer is associated with a particular closure temperature (T_c) or blocking temperature. For a specific isotope, T_c refers to the temperature at which a mineral has cooled so that it blocks significant diffusion of the isotope (Braun et al., 2006; Rollinson, 1995; Turekian and Holland, 2013). For any mineral, the closure temperature of an element depends on factors such as diffusivity (D), effective diffusion radius and grain radius which are not always the same, as different crystallographic faces may have different diffusion rates, and cooling rate (Dodson, 1973). In general, the closure temperature will be higher in larger grains and at fast cooling rates.

The T_c for the diffusion of Pb in zircon is typically in excess of 900 °C for a typical 100–μm–long zircon grain and a cooling rate of 10 °C/Ma (Cherniak and Watson, 2001; Lee et al., 1997). Under a faster cooling rate of 100 °C/Ma, a 100–μm–long zircon would close for Pb diffusion at 950 °C (Cherniak and Watson, 2001). Under temperatures common in the continental crust, the radiogenic–Pb loss is only possible in metamict zircon. However, zircon that remains above 600–650 °C will be continuously annealed and lattice damage will not accumulate (Cherniak, 2010; Cherniak and Watson, 2001; Mezger and Krogstad, 1997), hence preventing Pb loss. Based on our thermodynamic modelling (section 3.5), mineral paragenesis, and Zr–in–titanite temperatures (see below section 4.3.3.3), the Agua del Sapo complex remained above 700 °C from c. 500–380 Ma excluding the possibility of Pb loss driven by metamictization. Also, zircon that experienced significant Pb loss typically shows discordant ages in Concordia diagrams, which is not the case for our results, which are usually <10 % discordant. Thus, we argue that Pb loss is not likely to have played a significant role, and the ages reflect new zircon rim growth below T_c, over partially dissolved detrital zircon. A similar case is reported in the migmatites around the anatectic Cooma granodiorite in the Lachlan Fold Belt in southwestern Australia (Williams, 2001), and in other high-grade terranes (Högdahl et al., 2012; McFarlane et al., 2006; Rubatto et al., 2013).

For monazite, prolonged periods of temperatures > 900 °C are necessary for diffusion rates to operate and alter the trace element composition, for example, a 10 µm monazite grain would have Pb T_c in excess of 900 °C under a cooling rate of 10 °C/Ma (Cherniak and Pyle, 2008; Cherniak et al., 2004). Later Gardés (2007) confirmed the values of Pb diffusivity, concluding that Pb diffusion is too slow at typical metamorphic temperatures to alter U–Th–Pb ages in monazite. Seydoux-Guillaume (2003) and Foster (2002) suggested that monazite anneals rapidly and therefore does not lose Pb. However, coupled dissolution–precipitation can give rise to new monazite with perturbed ages due to incomplete radiogenic Pb dissolution (Seydoux-Guillaume et al., 2019). Otherwise, its closure temperature is similar to that of the zircon, and therefore U–Pb ages from rocks of the Agua del Sapo complex should record monazite growth, rather than cooling through closure temperature.

For titanite there has been a long–lasting debate about its Pb closure temperature (T_c), with values that range from 450–500 °C (Mattinson, 1978) to over 825 °C (Gao et al., 2012) for relatively small grains of c. 100 µm cooled at typical orogenic gradients (c. 10 °C/Ma). Recent studies of naturally occurring titanite tend to set higher closure temperatures. Most of these studies agree that the T_c of titanite is typically above 660 °C (Cherniak, 1993; Scott and St-Onge, 1995; Zhang and Schärer, 1996), possibly above 800 °C (Gao et al., 2012; Kohn, 2017; Kohn and Corrie, 2011). The high closure temperature in titanite indicates that its U–Pb age in most metamorphic rocks reflects titanite growth, rather than closure temperature. Interestingly, titanite is very reactive during metamorphism (Scott and St-Onge, 1995) which implies that its U–Pb systematics is likely to be reset during retrogression by the growth of new titanite, rather than by diffusion (Frost et al., 2001).

In summary, all three geochronometers have relatively high T_c, so that if they are all in the same rock package, they should start their radiometric clock roughly at a similar time. This in part, explains their similar dates (500–440 Ma). However, their response in terms of growth, coupled dissolution–precipitation and reaction with other minerals during the protracted high temperatures varies. In the rocks investigated here, zircon was the least reactive of the three geochronometers, with only new thin layers of new zircon grown over detrital ones, while monazite and titanite were more reactive. Monazite may have experienced coupled dissolution–precipitation that perturbed its U-Pb systematics (Foster et al., 2002; Seydoux-Guillaume et al., 2003), and titanite reacted during retrogression that led to new grains during the extended 440–380 Ma period.

5.3.2 Thermal evolution from zircon and titanite thermometers, and metamorphic modelling

One of the advantages of the LASS–ICP–MS technique is that we can extract U–Pb dates and trace element composition from the same analytical spot. By calculating temperatures based on Ti–in–zircon and Zr–in–titanite we can explore the thermal evolution of the rocks during and after peak metamorphism. The Ti–in–zircon method is unaffected by Ti loss because extremely low diffusion prevents its escape even when radiogenic ages are lost (Cherniak and Watson, 2007). However, this method is known to yield lower temperatures than peak temperatures derived from metamorphic thermodynamic modelling because zircon crystallisation does not always coincide with the thermal maximum (Baldwin et al., 2007; Ewing et al., 2013; Kohn et al., 2015; Korhonen et al., 2014). Using the calibration by Watson (2006), the Ti–in–zircon temperatures from spots that yielded Famatinian ages range between 670 and >700 ± 10 °C with an ill–defined cooling trend from 500 to 440 Ma (Fig. 10).

The larger dataset from titanite (Fig. 24) allows us to explore the temporal evolution of temperature. The Zr–in–titanite temperature (Hayden et al., 2008) varies as a function of age (Fig. 26), starting with temperatures of c. 700 °C for the older spots and progressively increasing to values in excess of 750 °C by 460 Ma and then decreasing gradually to c. 700 °C from 440 to 380 Ma. This trend defines slow heating during a prograde path to a maximum at c. 460 Ma followed by very slow cooling at a rate of c. 1 °C/Ma for the next 80 Ma. The older temperature estimations (~480-500 Ma) indicate that the rocks were partial melt-bearing by then. This is reinforced by studies in the Tolombon complex were the older zircon are c. 505 Ma, suggesting that the rocks started to melt around that time.

The temperatures calculated from titanite and zircon of similar age do not coincide. Zr–in–titanite record in Fig. 26 shows that temperatures were above 700 °C for c. 120 Ma. Ti–in–zircon temperatures are c. 50 °C lower than Zr–in–titanite temperatures, a difference larger than the uncertainty of the methodologies (2σ of ± 10 °C for zircon and ± 25 °C for titanite). Temperature estimations from titanite are supported by P–T calculations in pseudosection (Fig. 4), which show that the mineral paragenesis of the Al–rich siliciclastic migmatite equilibrated between 740–710 °C.

Another constraint on peak temperature comes from monazite. Kelsey (2008) modelled the thermodynamic behaviour of monazite during melting of Al–rich siliciclastic rocks similar to ours.

They found that monazite should completely dissolve in the melt at temperatures over 700–750 °C, in rocks with LREE content of 170–200 ppm, like our case (Appendix 1). The lack of monazite with ages older than Famatinian suggests that our migmatites reached those temperatures. However, studies like Yakymchuk (2019) have found that monazite can survive to higher temperatures, in which case our T estimations for the Famatinian could have been underestimated.

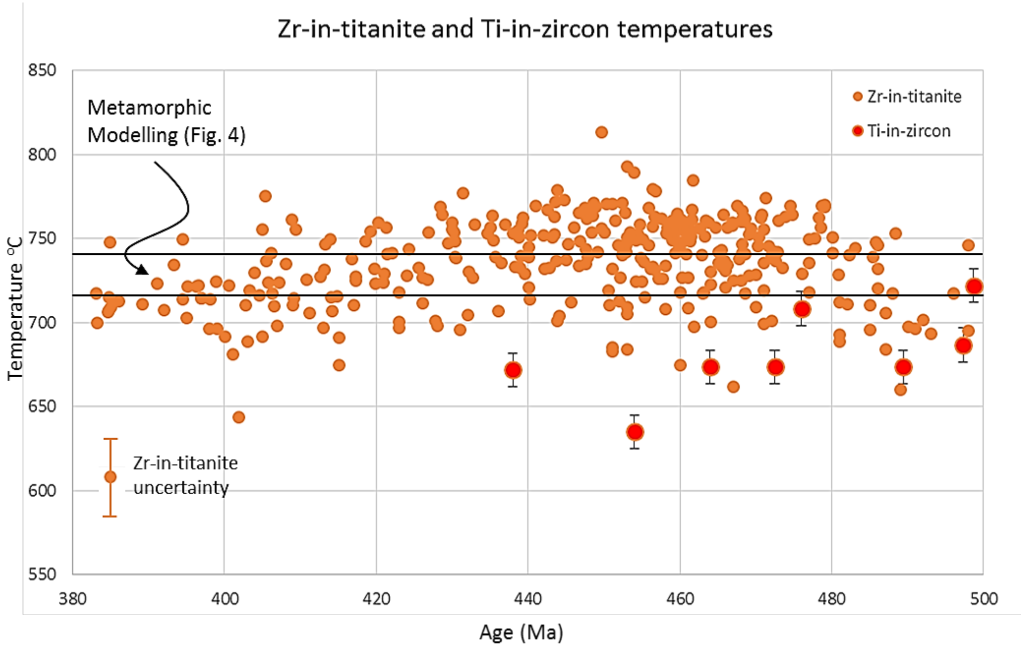

Figure 26– Temperature estimates from Zr–in–titanite (samples SQ17–025, LC–028, UMF, SM–005), Ti–in–zircon (red circles with uncertainty whiskers), plotted as a function of time. The two continuous lines indicate the range of temperature from Fig. 4. Only a few Famatinian zircon analyses are available.

5.3.3 Why the spread of dates?

A spread of U–Pb dates has been reported in numerous cases for zircon (Cavalcante et al., 2018; Davis et al., 2003; Howard et al., 2015; Keay et al., 2001; Paquette et al., 2004; Paquette et al., 2003; Rossi et al., 2006; Smithies et al., 2011; Taylor et al., 2016), for monazite (Goncalves, 2002; Howard et al., 2015; Kirkland et al., 2016a; Parrish, 1990; Taylor et al., 2016; Williams et al., 2011), and for titanite (Kohn, 2017; Lucassen and Becchio, 2003; Schwartz et al., 2016; Scibiorski et al., 2019a).

There are numerous processes that can give rise to this, such as: a) deformation–induced Pb mobility that creates faster pathways for Pb to move (Kovaleva et al., 2017; Reddy et al., 2006); b) thermally–induced Pb mobility, or volume diffusion controlled by temperature (Taylor et al., 2016); c) crystal–state Pb mobility as a result of radiation damage – only active in metamictic grains (Cherniak, 2010; Cherniak and Watson, 2001); and d) fluid–induced Pb mobility (Cherniak et al., 2004; Harlov and Hetherington, 2010; Schoene, 2014; Taylor et al., 2016). There are more mechanisms that can explain the protracted ages, and they will be discussed in the next chapters, when we compare the behaviour of the three accessory minerals in the different complexes. In this section, we summarise the findings from the neighbouring Tolombon complex (Finch et al., 2017; Wolfram et al., 2019), and whether they apply to our results.

Zircon and monazite

Wolfram (2019) reported a similar range of zircon and monazite dates in the Tolombon complex. Entirely new zircon grains defined up to five age peaks spread across the 500–440 Ma with a recurrence time of 10–15 Myr. Monazite from the same samples yielded a wide spread of dates defining a single broad peak between 500–440 Ma, centred at c. 470–460 Ma (Wolfram et al. (in review). They concluded that the wide spread of zircon dates was due to the long–lasting (c. 60 Myr) high temperatures that peaked above the solidus every 10–15 Myr, triggering several anatectic events (Wolfram et al., 2019). Old zircon that survived new melting events were likely disconnected from the newly formed melt network. Wolfram, (submitted) argued that monazites from the Tolombon complex remained stable during the c. 60 Myr anatectic event. This was because apatite saturated the peraluminous melt in LREE stabilising monazite (Wolf and London, 1995). The spread of monazite dates was explained by coupled dissolution–precipitation mechanisms (Catlos et al., 2010; Harlov and Hetherington, 2010; Hetherington et al., 2010; Seydoux-Guillaume et al., 2003; Teufel and Heinrich, 1997; Williams et al., 2011). During this process radiogenic Pb from original monazite remains in the grain during dissolution–precipitation, causing micro–domains enriched in radiogenic Pb, not resolvable by larger laser spots, that yield older ages with no geological significance (Seydoux-Guillaume et al., 2019; Seydoux-Guillaume et al., 2003).

The Agua del Sapo complex underwent a protracted high–temperature event giving rise to zircon rims and monazite dates ranging between c. 500–440 Ma. Any possible thermal peaks recorded by zircon from the Tolombon complex cannot be resolved by zircon in the Agua del Sapo complex because of the reduced number of analysis. The wide spread of dates in each of our monazite samples can be a result of coupled dissolution–precipitation resulting from a semi–continuous prolonged thermal event or by a late event towards the end of the Famatinian Orogeny affecting early formed monazites. This late event can be as young as c. 420 Ma, the younger monazite date in the complex (Fig. 17). We favour the first scenario and argue that in the Agua del Sapo complex, monazite grains started forming at c. 500 Ma, early in the Famatinian orogeny, coeval with zircon growth in the same rocks. Subsequent events of coupled dissolution–precipitation during the protracted high–temperatures of the Famatinian Orogen would have given rise to new grains that inherited radiogenic Pb, that yield geologically meaningless mixed dates. We also contemplate the possibility that the protracted high-grade metamorphism caused protracted mineral growtt before and after metamorphic peak. It is known that these accessor minerals can grow during the prograde and retrograde paths paths (Kelsey et al., 2008; Kohn, 2017; Kohn et al., 2018; Taylor et al., 2016; Yakymchuk and Brown, 2014).

Titanite

The spread of ages in titanite (Fig. 20) can represent either continuous growth or be a product of Pb diffusion (Mattinson, 1978; Mezger et al., 1993; Schärer et al., 1994), or U dissusion (Kirkland et al., 2016b). However, some authors argue that the diffusion of Pb and other trace elements in titanites is limited (Gao et al., 2012; Kohn, 2017; Kohn and Corrie, 2011). Further to that, Kirkland (2016b) argues taht the smallest analysed titanites in their study need > 695-725 °C in 6.5-8.5 kbar to reset its U-Pb systematics. In the Sierra de Quilmes, we have evidence for negligible Pb–diffusion. This is indicated by the date distribution of in–situ analysis of titanite in samples that have both age groups, such as sample SQ–213 (in Fig. 19). Most of the titanite grains are c. 100 µm in size with few as large as 400 µm. As shown in Fig. 27, there is no systematic variation of date with either grain size or position of the spot within the grain. The smallest titanite grains, that can be as small as 50 µm, preserve the entire range from older to younger (500–440 Ma) and they are demonstrably not included in other resistant minerals. Similarly, the oldest dates are recorded in titanite rims of larger grains. If diffusion was active, these older ages would be reset in small titanites or in the rims of larger grains. In counterbalance, we note that the youngest ages are all found within 20 µm from the edge of the grain (Fig. 27). This could indicate either new growth, coupled dissolution–precipitation at the margins, or diffusion. We are unable to discern between them. On balance, we consider that diffusion did not significantly reset U–Pb titanite dates, and interpret the younger titanite group (440–380 Ma), to have grown at conditions below its closure temperature during the protracted cooling of the complex (Fig. 26).

Kirkland et al. 2016 argue that older titanite ages are artefacts of younger thermal events that triggered U-loss. It is also argued that grain size has a strong effect on the preservation or resetting of metamorphic U-Pb ages. They found that the smaller titanites need > 695-725 °C to reset its U-Pb systematic. In the titanites in the Agua del Sapo complex we found no correlation between common-Pb-corrected dates and U content. Further to that, and more importantly, we found no clear correlation between grain-size and age (Fig. 27), or with microstructural features in the thin section.

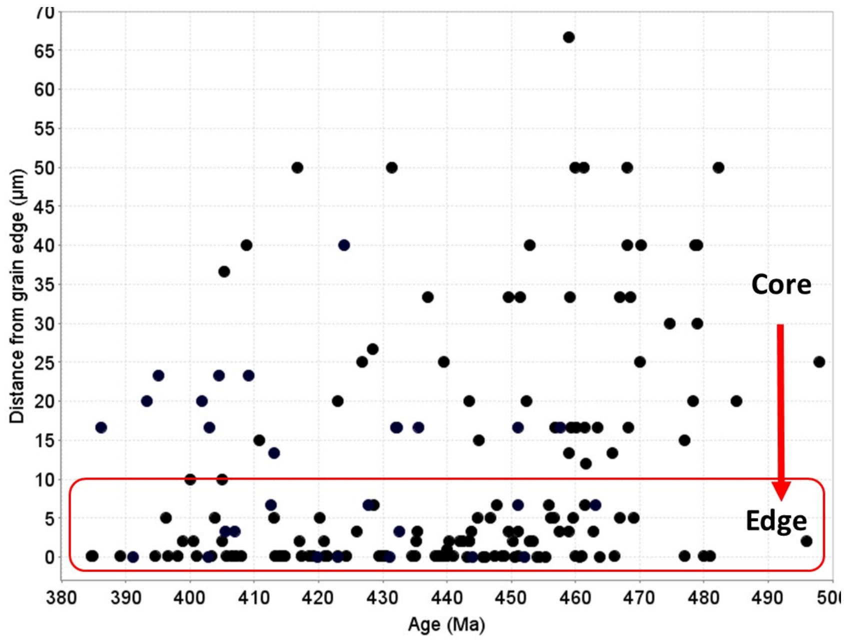

Figure 27– Distance from edge of the grain versus age, all in–situ analyses from samples SQ–213, SM–005, LC–028, and UMF. While ages in the core tend to be older and those within 20 µm from the edge yield the youngest ages, the relationship between position in the grain and age is weak, suggesting negligible effects of diffusion. The spots at the edge of the grains (marked by the box) record the entire 100 Ma age range. The larger distance from the grain edge implies larger grains, menaing that there is not correlation between grainsize and age.

5.4 Meaning of the <440 Ma ages in monazite and titanite

A significant aspect of this work is the finding of date peaks between 440 and 380 Ma in monazite and titanite, not previously recorded in association with the Famatinian Orogen. This marks the time gap between the Famatinian and the Achalian/Chanic orogen (Weinberg et al., 2018b), thought to have started possibly as early as 400–390Ma (Aceñolaza and Toselli, 1981; De Luchi et al., 2007; Drobe et al., 2010; Drobe et al., 2009; Ramos et al., 1986; Rapela et al., 1998a; Siegesmund et al., 2009; Sims et al., 1998; Steenken et al., 2006; Stuart-Smith et al., 1999).

Monazite

Monazite samples SM–003 and SQ108a record these young U–Pb dates (Fig. 17). Finch (2017) argued that such dates (their sample SQ108a, shown in Fig. 17) are the product of delayed peak metamorphism in the footwall of the Pichao shear zone thrust. However, the c. 30 Myr time gap between the hanging wall and footwall monazite dates seems excessive considering that the younger sample is c. 5 km away (in map view) from the base of the thrust. The typical delay in thrust zones is in the order of 5–10 Myr (Crowley and Parrish, 1999; Kohn et al., 2001; Mottram et al., 2014). An alternative could be late monazite hydrothermal recrystallization (Hecht and Cuney, 2000; Kelly et al., 2012; Poitrasson et al., 1996; Poitrasson et al., 2000; Rolland et al., 2003; Rubatto et al., 2013), but Finch (2017) found no systematic covariations between monazite composition and U–Pb dates that would support this. The same is true for our sample SM–003. Therefore, it seems that the renewed growth of monazite took place locally after 440 Ma. The delayed and sustained metamorphism in the footwall proposed by Finch (2017) is supported by new data from titanite that indicates protracted high–temperature (> 700 ºC) in the complex from 440–380 Ma. We argue that these long–lasting high–temperatures triggered some monazite growth after 440 Ma.

In addition to high–temperatures, features like rock fabric, grain–size, and texture could also impact in the monazite formation. Kelsey (2008) and Yakymchuk (2014) modelled pelitic metasedimentary rocks similar to ours, and found that temperature and LREE content of the rock are the most critical factors controlling the formation or dissolution of monazite during metamorphism. Kelsey (2008) defined the concept of “effective LREE content” as the fraction of the bulk LREE content of the rock that interacts with monazite. This effective LREE is controlled mainly by the breakdown of LREE–bearing minerals.

The bulk LREE content of three of our monazite samples has similar values. Metatexite SM–003, leucosome SQ17–022 and Filo granite SQ17–049 have a total of 187, 156 and 170 ppm LREE, respectively (Appendix 1). If we assume that the temperatures were similar in all these rocks, we should expect similar monazite behaviour, including similar date distribution. However, the weakly deformed and coarse–grained granite and leucosome samples have a much narrower date range (c. 20 Myr) compared with the c. 60 Myr and younger than 440 Ma of the metatexite (Fig. 14–16). This variable spread of ages could reflect a mechanism that modulates the "effective LREE" interacting with monazite, and possibly related to the internal fabric of the rock.

There is also the possibility not only temperature caused the formation of new monazite, but that shearing could have also triggered new monazite after 440 Ma (Mahan et al., 2006; Rolland et al., 2003; Wawrzenitz et al., 2015; Wawrzenitz et al., 2012; Williams et al., 2007). Wawrzenitz (2012) argues that different deformation mechanisns (e.g., dissolution-reprecipitation creep (DCP), or dislocation creep) will result in new monazite with a composition that reflect such mechanisnms. For example, if DPC is the dominant mechanis, the chemical composition of the new monazite will record the dissolution of the partially dissolved feldspar by a less pronounced negative Eu anomaly compared to the old pre-kinematic monazite. We found no clear differences in the Eu -anomaly in the monazites that could reflect such mechanisms.

Titanite

We found no petrological, chemical, or structural differences between titanite–bearing samples that yield the older dates with samples hosting younger titanite. All samples have the same mineral paragenesis, bulk geochemistry, and structural make–up. The cause of titanite growth in specific samples after 440 Ma remains inconclusive.

Angiboust (2017) by means of experimental petrography found that Ca–rich rocks with c. 3 wt % CaO, such as our Ca–rich siliciclastic sequence (CaO > 2 wt. %, Appendix 1), at pressure below 7 kbar, form titanite that rims ilmenite, and REE–enriched epidote that rims allanite cores (both common in our samples, Fig. 3). They found that the REE released during the dissolution of allanite during prograde reactions are partially incorporated by the newly forming titanite. Similarly Papapavlou (2017) suggested that the low LREE content in titanite could be a result of contemporaneous growth of allanite in the rock, which has a larger equilibrium partition coefficient than titanite (Garber et al., 2017; Regis et al., 2012), and therefore it would sequester the available LREE. These studies reinforce the intimate relation between allanite and titanite in Ca–rich rocks and explain why the young titanite has low REE (Fig. 21).

The Zr–in–titanite thermometer indicates cooling from a steady temperature of c. 750 °C at 440 Ma to 700 °C at 380 Ma (Fig. 26) was accompanied by a progressive and steady decrease of LREE in titanite (Fig. 21). We argue that this is due to the preferential partitioning of LREE into allanite plus epidote that increased in modal content as temperature decreased. This means that the younger titanite age group is dating the gradual retrogression of the rock leading to increased allanite–epidote modal content (Fig. 28).

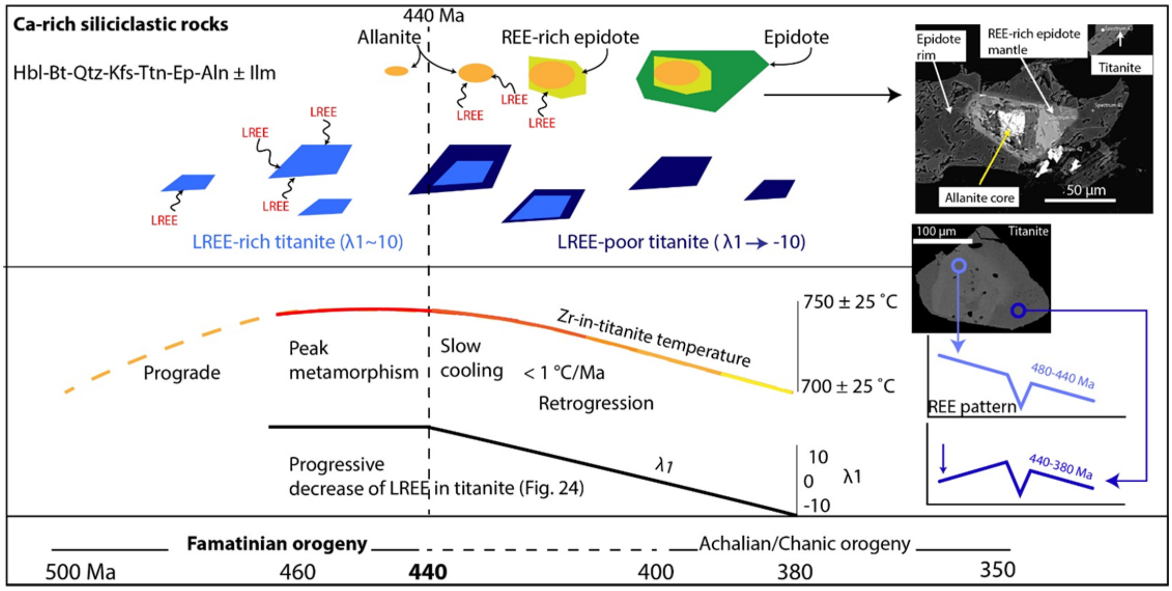

Figure 28– 120 Myr evolution tracked by titanite. During peak metamorphic conditions, titanite (light blue) takes in the available LREE in the rock. After 440 Ma, the temperature drops below 750 °C, stabilising allanite that is the preferred sink for LREE. New titanite (dark blue) is depleted in LREE. The growth of allanite followed by REE–rich epidote and epidote forming core–mantle–rim (SEM image in the top right side of figure), indicates the progressive depletion of REE during retrogression.

5.5 The Sierra de Quilmes record in the Famatinian back–arc

In areas outside the Sierra de Quilmes, in the Famatinian back–arc, the anatexis was sustained from c. 505 to 440 Ma (Table 1 in (Bahlburg and Berndt, 2016) indicating the persistence of high–temperature during the orogenic cycle. In some other areas of the orogen, the high–temperature record is extended for longer. For example, in the southern Puna (Lucassen and Becchio, 2003) reported long–standing high–temperatures (600–750 °C) and low pressure c. 5–7 kb that dominated during the Famatinian for 50 Myr from 470–420 Ma. Also in the southern Sierras Pampeanas, near the contact between the MARA terrane and the Famatinian arc (Mulcahy et al., 2014) found that the temperature remained over the solidus for c. 30 Myr after peak metamorphism at c. 461 ± 1.7 Ma. This was followed by cooling in a nearly isobaric path from c. 850 °C at c. 465 Ma, to c. 650 °C at c. 407 Ma (c. 4 °C/Ma), similar to the estimations of Gallien (2010) and (Cristofolini et al., 2014) of 3–6

°C/Ma. Based on the above we argue that, like in the Sierra de Quilmes, the high–temperature was maintained over a long period across different areas of the Famatinian orogen, supporting the idea that the Famatinian orogen was indeed a hot and long–lived orogen.

6 Summary and conclusions

As summarised in figure 30, detrital zircon in the migmatites of the Agua del Sapo complex indicates that they derive from the turbidites of the Puncoviscana sequence. The lack of Pampean age detrital zircon (550–520 Ma) suggests that this sequence was deposited just before the onset of the Pampean magmatic arc. During the magmatic climax of the Pampean orogenic cycle, the Filo granite intruded the Puncoviscana sequence. The lack of Pampean age zircon or monazite suggests that these metaturbidites reached only low–grade of metamorphism. The onset of the Famatinian orogenic cycle and its associated high–grade HT–LP metamorphism is marked by zircon, monazite and titanite ages ranging between 500–440 Ma roughly centred at c. 470–460 Ma. However, some monazite and titanite samples yielded dates in the range of 440–380 Ma, extending the high – temperature record for another c. 60 Myr, hence a total of c. 120 Ma. The combined use of metamorphic modelling, Ti–in–zircon and Zr–in titanite geothermometers allowed to better constrain the thermal evolution of this long–lived complex. Temperatures reached maximum values of c. 750 °C at c. 460 Ma and were sustained until 440 Ma when they start dropping with a cooling rate of c. 1 °C/Ma, getting to 700 °C at 380 Ma. During that time, the geochronometers reacted in different ways. Zircon formed metamorphic rims on partially dissolved detrital zircon cores. Monazite was affected by coupled dissolution–precipitation, and the different date range may respond to differences in the host rock fabric, as fine–grained foliated rocks were more fertile for monazite formation after peak temperature. Titanite–bearing rocks show no differences in composition, fabric, or mineral paragenesis; however, they yield different dates. The cause of such variation remains inconclusive. We also found that Pb diffusion in titanite is unlikely to account for the younger titanite, suggesting new titanite growth below the closure temperature. This is further supported by changes in titanite chemistry with young titanite recording increased modality of allanite+epidote.

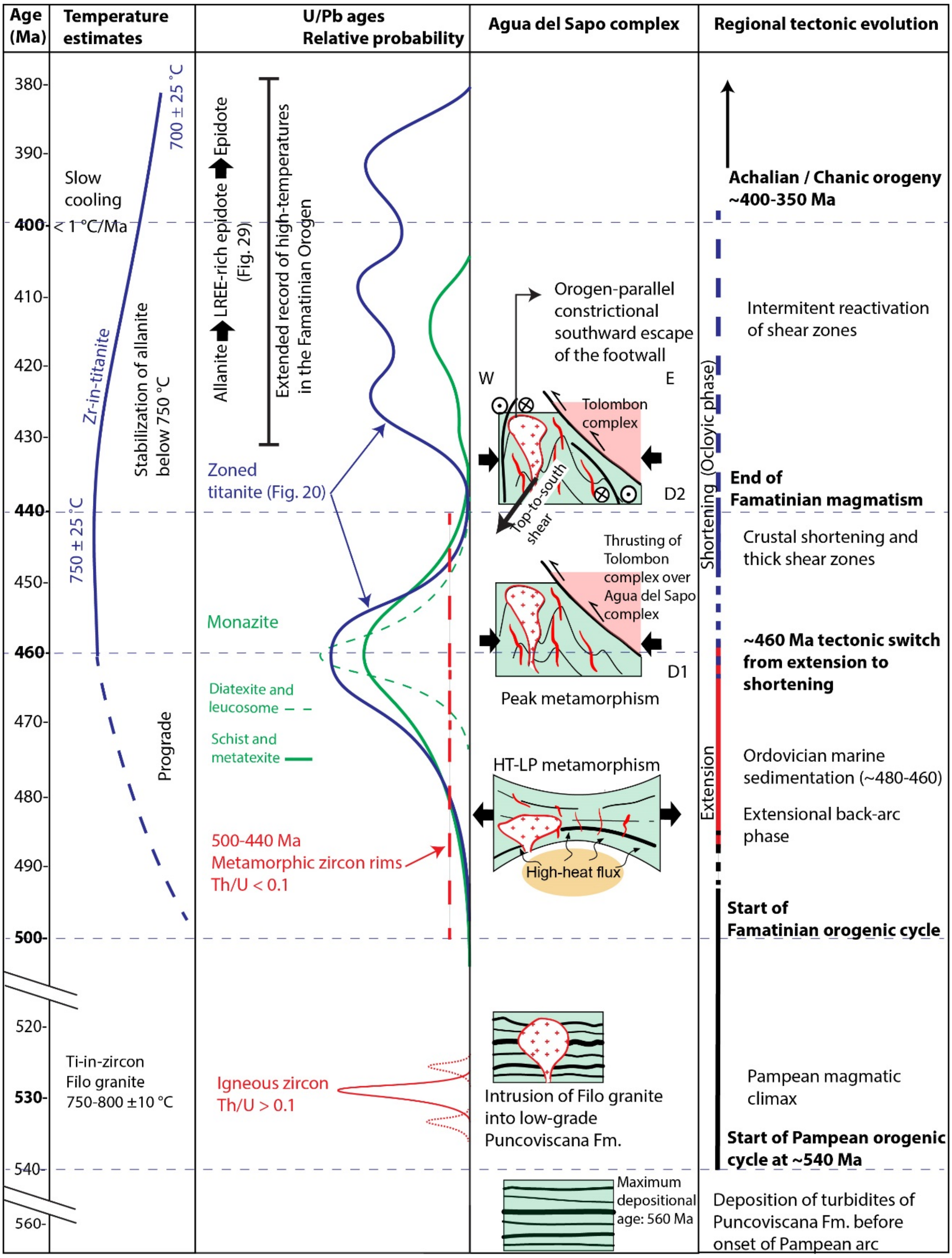

Figure 29– Summary of temperature estimations and geochronological results for the Agua del Sapo complex and comparison with its structural evolution and regional tectonic settings.

The use of U-Pb age coupled with trace elements composition from three different geochronometers allowed us to unravel the protracted tectono–thermal evolution of the Agua del Sapo complex, and the dating of several samples of apparently similar features allowed us to get a better geochronological picture, as they yield different ages. This highlights that some mechanisms are still not fully understood.

We argue that the thrusting of the high–grade Tolombon complex over the Agua del Sapo complex served to maintain the prolonged cooling of the complex after 440 Ma (Fig. 29). This thrusting event resulted in the cooling of the hanging wall Tolombon complex and closure of its zircon and monazite U/Pb systematics by 440 Ma (Wolfram et al., 2019), and the slow cooling of c. 1 ºC/Ma and retrogression of the footwall complex that is well recorded in titanite. Furthermore, from previous work (Chapter 2), we speculated that this thrusting (D1) triggered the constrictional shearing of the footwall Agua del Sapo complex (D2), which strongly overprinted the anatectic structures. Now we know that the peak metamorphism and related anatexis in the Agua del Sapo complex occurred at c. 460 Ma; therefore, we can argue that D2 was active well after 460 Ma.

References

Aceñolaza, F., and Toselli, A., 1981, Geología del Noroeste Argentino: Publicación Especial de la Facultad de Ciencias Naturales, Universidad Nacional de Tucumán., p. 1-212.

Aceñolaza, F. G., Miller, H., and Toselli, A. J., 2002, Proterozoic - Early Paleozoic evolution in western South America - A discussion: Tectonophysics, v. 354, p. 121-137.

Aceñolaza, F. G., and Toselli, A., 2009, Chapter 6 The Pampean Orogen: Ediacaran-Lower Cambrian Evolutionary History of Central and Northwest Region of Argentina, Developments in Precambrian Geology, 16, p. 239-254.

Adams, C. J., Miller, H., Aceñolaza, F. G., Toselli, A. J., and Griffin, W. L., 2011, The Pacific Gondwana margin in the late Neoproterozoic–early Paleozoic: Detrital zircon U–Pb ages from metasediments in northwest Argentina reveal their maximum age, provenance and tectonic setting: Gondwana Research, v. 19, p. 71-83.

Aleinikoff, J. N., Schenck, W. S., Plank, M. O., Srogi, L. A., Fanning, C. M., Kamo, S. L., and Bosbyshell, H., 2006, Deciphering igneous and metamorphic events in high-grade rocks of the Wilmington complex, Delaware: Morphology, cathodoluminescence and backscattered electron zoning, and SHRIMP U-Pb geochronology of zircon and monazite: Bulletin of the Geological Society of America, v. 118, p. 39-64.

Aleinikoff, J. N., Wintsch, R. P., Tollo, R. P., Unruh, D. M., Fanning, C. M., and Schmitz, M. D., 2007, Ages and origins of rocks of the Killingworth dome, south-central Connecticut: Implications for the tectonic evolution of southern New England: American Journal of Science, v. 307, p. 63-118.

Angiboust, S., and Harlov, D., 2017, Ilmenite breakdown and rutile-titanite stability in metagranitoids: Natural observations and experimental results: American Mineralogist, v. 102, p. 1696-1708.

Astini, R. A., 1998, Stratigraphical evidence supporting the rifting, drifting and collision of the Laurentian Precordillera terrane of western Argentina.: The Geological Society.

Astini, R. A., Benedetto, J. L., and Vaccari, N. E., 1995, The early Paleozoic evolution of the Argentine Precordillera as a Laurentian rifted, drifted, and collided terrane: A geodynamic model: Geological Society of America Bulletin, v. 107, p. 253-273.

Astini, R. A., and Dávila, F. M., 2004, Ordovician back arc foreland and Ocloyic thrust belt development on the western Gondwana margin as a response to Precordillera terrane accretion: Tectonics, v. 23, p. TC4008 1-19.

Bahlburg, H., and Berndt, J., 2016, Provenance from zircon U-Pb age distributions in crustally contaminated granitoids: Sedimentary Geology, v. 336, p. 161-170.

Bahlburg, H., Berndt, J., and Gerdes, A., 2016, The ages and tectonic setting of the Faja Eruptiva de la Puna Oriental, Ordovician, NW Argentina: Lithos, v. 256-257, p. 41-54.

Bahlburg, H., and Hervé, F., 1997, Geodynamic evolution and tectonostratigraphic terranes of northwestern Argentina and northern Chile: Bulletin of the Geological Society of America, v. 109, p. 869-884.

Baldwin, J. A., Brown, M., and Schmitz, M. D., 2007, First application of titanium-in-zircon thermometry to ultrahigh-temperature metamorphism: Geology, v. 35, p. 295-298.

Bellos, L. I., Castro, A., Díaz-Alvarado, J., and Toselli, A., 2015, Multi-pulse cotectic evolution and in-situ fractionation of calc-alkaline tonalite-granodiorite rocks, Sierra de Velasco batholith, Famatinian belt, Argentina: Gondwana Research, v. 27, p. 258-280.

Braun, J., Van Der Beek, P., and Batt, G., 2006, Quantitative thermochronology: Numerical methods for the interpretation of thermochronological data, 1-258 p.

Büttner, S. H., 2009, The Ordovician Sierras Pampeanas–Puna basin connection: Basement thinning and basin formation in the Proto-Andean back-arc: Tectonophysics, v. 477, p. 278-291.
Büttner, S. H., Glodny, J., Lucassen, F., Wemmer, K., Erdmann, S., Handler, R., and Franz, G., 2005, Ordovician metamorphism and plutonism in the Sierra de Quilmes metamorphic complex: Implications for the tectonic setting of the northern Sierras Pampeanas (NW Argentina): Lithos, v. 83, p. 143-181.
Castro, A., Díaz-Alvarado, J., and Fernández, C., 2014, Fractionation and incipient self-granulitization during deep-crust emplacement of Lower Ordovician Valle Fértil batholith at the Gondwana active margin of South America: Gondwana Research, v. 25, p. 685-706.
Catlos, E. J., Baker, C., Sorensen, S. S., Çemen, I., and Hançer, M., 2010, Geochemistry, geochronology, and cathodoluminescence imagery of the Salihli and Turgutlu granites (central Menderes Massif, western Turkey): Implications for Aegean tectonics: Tectonophysics, v. 488, p. 110-130.
Cavalcante, C., Hollanda, M. H., Vauchez, A., and Kawata, M., 2018, How long can the middle crust remain partially molten during orogeny?: Geology, v. 46, p. 839-842.
Cawood, P. A., 2005, Terra Australis Orogen: Rodinia breakup and development of the Pacific and Iapetus margins of Gondwana during the Neoproterozoic and Paleozoic: Earth-Science Reviews, v. 69, p. 249-279.
Chambers, J. A., and Kohn, M. J., 2012, Titanium in muscovite, biotite, and hornblende: Modeling, thermometry, and rutile activities of metapelites and amphibolites: American Mineralogist, v. 97, p. 543-555.
Cherniak, D. J., 1993, Lead diffusion in titanite and preliminary results on the effects of radiation damage on Pb transport: Chemical Geology, v. 110, p. 177-194.
Cherniak, D. J., 2010, Diffusion in accessory minerals: Zircon, titanite, apatite, monazite and xenotime, Reviews in Mineralogy and Geochemistry, 72, p. 827-869.
Cherniak, D. J., and Pyle, J. M., 2008, Th diffusion in monazite: Chemical Geology, v. 256, p. 52-61.
Cherniak, D. J., and Watson, E. B., 2001, Pb diffusion in zircon: Chemical Geology, v. 172, p. 5-24.
Cherniak, D. J., and Watson, E. B., 2007, Ti diffusion in zircon: Chemical Geology, v. 242, p. 473-486.
Cherniak, D. J., Watson, E. B., Grove, M., and Harrison, T. M., 2004, Pb diffusion in monazite: A combined RBS/SIMS study: Geochimica et Cosmochimica Acta, v. 68, p. 829-840.
Coira, B., Koukharsky, M., Guevara, S. R., and Cisterna, C. E., 2009, Puna (Argentina) and northern Chile Ordovician basic magmatism: A contribution to the tectonic setting: Journal of South American Earth Sciences, v. 27, p. 24-35.
Cristofolini, E. A., Otamendi, J. E., Walker, B. A., Tibaldi, A. M., Armas, P., Bergantz, G. W., and Martino, R. D., 2014, A Middle Paleozoic shear zone in the Sierra de Valle Fértil, Argentina: Records of a continent-arc collision in the Famatinian margin of Gondwana: Journal of South American Earth Sciences, v. 56, p. 170-185.
Crowley, J. L., and Parrish, R. R., 1999, U-Pb isotopic constraints on diachronous metamorphism in the northern Monashee complex, southern Canadian Cordillera: Journal of Metamorphic Geology, v. 17, p. 483-502.
Dahlquist, J., Verdecchia, S. O., Baldo, E., Basei, M., Alasino, P., Rapela, C. W., Campos Neto, M. d. C., Zandomeni, P., and Uran, G., 2016, Early Cambrian U-Pb zircon age and Hf-isotope data from the Guasayán pluton, Sierras Pampeanas, Argentina: implications for the northwestern boundary of the Pampean arc: Andean Geology, v. 1, p. 137-150.
Davila, F. M., Astini, R. A., and Schmidt, C. J., 2003, Unraveling 470 m.y. of shortening in the Central Andes and documentation of Type O superposed folding: Geology, v. 31, p. 275-278.
Davis, W. J., Canil, D., MacKenzie, J. M., and Carbno, G. B., 2003, Petrology and U–Pb geochronology of lower crustal xenoliths and the development of a craton, Slave Province, Canada: Lithos, v. 71, p. 541-573.

De Luchi, M. G. L., Siegesmund, S., Wemmer, K., Steenken, A., and Naumann, R., 2007, Geochemical constraints on the petrogenesis of the Paleozoic granitoids of the Sierra de San Luis, Sierras Pampeanas, Argentina: Journal of South American Earth Sciences, v. 24, p. 138-166.

Deer, W. A., Howie, R. A., and Zussman, J., 1992, An introduction to the rock-forming minerals. Second edition: An introduction to the rock-forming minerals. Second edition.

Dodson, M. H., 1973, Closure temperature in cooling geochronological and petrological systems: Contributions to Mineralogy and Petrology, v. 40, p. 259-274.

Drobe, M., de Luchi, M. L., Steenken, A., Wemmer, K., Naumann, R., Frei, R., and Siegesmund, S., 2010, Geodynamic evolution of the Eastern Sierras Pampeanas (Central Argentina) based on geochemical, Sm–Nd, Pb–Pb and SHRIMP data: International Journal of Earth Sciences, v. 100, p. 631-657.

Drobe, M., López de Luchi, M. G., Steenken, A., Frei, R., Naumann, R., Siegesmund, S., and Wemmer, K., 2009, Provenance of the late Proterozoic to early Cambrian metaclastic sediments of the Sierra de San Luis (Eastern Sierras Pampeanas) and Cordillera Oriental, Argentina: Journal of South American Earth Sciences, v. 28, p. 239-262.

Ducea, M. N., Bergantz, G. W., Crowley, J. L., and Otamendi, J., 2017, Ultrafast magmatic buildup and diversification to produce continental crust during subduction: Geology, v. 45, p. 235-238.

Ducea, M. N., Otamendi, J. E., Bergantz, G., Stair, K. M., Valencia, V. A., and Gehrels, G. E., 2010, Timing constraints on building an intermediate plutonic arc crustal section: U- Pb zircon geochronology of the Sierra Valle Fértil-La Huerta, Famatinian arc, Argentina: Tectonics, v. 29, p. n/a-n/a.

Dyar, M., Lowe, E., Guidotti, C., and Delaney, J., 2002, Fe3+ and Fe2+ partitioning among silicates in metapelites: A synchrotron micro-XANES study: American Mineralogist, v. 87.

Escayola, M. P., van Staal, C. R., and Davis, W. J., 2011, The age and tectonic setting of the Puncoviscana Formation in northwestern Argentina: An accretionary complex related to Early Cambrian closure of the Puncoviscana Ocean and accretion of the Arequipa-Antofalla block: Journal of South American Earth Sciences, v. 32, p. 438-459.

Ewing, T. A., Hermann, J., and Rubatto, D., 2013, The robustness of the Zr-in-rutile and Ti-in-zircon thermometers during high-temperature metamorphism (Ivrea-Verbano Zone, northern Italy): Contributions to Mineralogy and Petrology, v. 165, p. 757-779.

Finch, M. A., Weinberg, R. F., Fuentes, M. G., Hasalová, P., and Becchio, R., 2015, One kilometre-thick ultramylonite, Sierra de Quilmes, Sierras Pampeanas, NW Argentina: Journal of Structural Geology, v. 72, p. 33-54.

Finch, M. A., Weinberg, R. F., Hasalová, P., Becchio, R., Fuentes, M. G., and Kennedy, A., 2017, Tectono-metamorphic evolution of a convergent back-arc: The Famatinian orogen, Sierra de Quilmes, Sierras Pampeanas, NW Argentina: Bulletin of the Geological Society of America, v. 129, p. 1602–1621.

Finch, M. A., Weinberg, R. F., and Hunter, N. J. R., 2016, Water loss and the origin of thick ultramylonites: Geology, v. 44, p. 599-602.

Foster, G., Gibson, H. D., Parrish, R., Horstwood, M., Fraser, J., and Tindle, A., 2002, Textural, chemical and isotopic insights into the nature and behaviour of metamorphic monazite: Chemical Geology, v. 191, p. 183-207.

Frost, B. R., Chamberlain, K. R., and Schumacher, J. C., 2001, Sphene (titanite): Phase relations and role as a geochronometer: Chemical Geology, v. 172, p. 131-148.

Gallien, F., Mogessie, A., Bjerg, E., Delpino, S., de Machuca, B. C., Thöni, M., and Klötzli, U., 2010, Timing and rate of granulite facies metamorphism and cooling from multi-mineral chronology on migmatitic gneisses, Sierras de La Huerta and Valle Fértil, NW Argentina: Lithos, v. 114, p. 229-252.

Gao, X. Y., Zheng, Y. F., Chen, Y. X., and Guo, J., 2012, Geochemical and U-Pb age constraints on the occurrence of polygenetic titanites in UHP metagranite in the Dabie orogen: Lithos, v. 136-139, p. 93-108.
Garber, J. M., Hacker, B. R., Kylander-Clark, A. R. C., Stearns, M., and Seward, G., 2017, Controls on Trace Element Uptake in Metamorphic Titanite: Implications for Petrochronology: Journal of Petrology, v. 58, p. 1031-1057.
Gardés, E., Montel, J. M., Seydoux-Guillaume, A. M., and Wirth, R., 2007, Pb diffusion in monazite: New constraints from the experimental study of Pb2 + ⇔ Ca2 + interdiffusion: Geochimica et Cosmochimica Acta, v. 71, p. 4036-4043.
Gehrels, G., 2014, Detrital zircon U-Pb geochronology applied to tectonics, Annual Review of Earth and Planetary Sciences, 42, p. 127-149.
Goncalves, P., 2002, Pétrologie et géochronologie des granulites de ultra-hautes températures de l'unité basique d'Andriamena (centre-nord Madagascar) : apport de la géochronologie in-situ U-Th-Pb à l'interprétation des trajets P-T.
Harlov, D. E., and Hetherington, C. J., 2010, Partial high-grade alteration of monazite using alkali-bearing fluids: Experiment and nature: American Mineralogist, v. 95, p. 1105-1108.
Hauser, N., Matteini, M., Omarini, R. H., and Pimentel, M. M., 2011, Combined U–Pb and Lu–Hf isotope data on turbidites of the Paleozoic basement of NW Argentina and petrology of associated igneous rocks: Implications for the tectonic evolution of western Gondwana between 560 and 460Ma: Gondwana Research, v. 19, p. 100-127.
Hayden, L. A., Watson, E. B., and Wark, D. A., 2008, A thermobarometer for sphene (titanite): Contributions to Mineralogy and Petrology, v. 155, p. 529-540.
Hecht, L., and Cuney, M., 2000, Hydrothermal alternation of monazite in the Precambrian crystalline basement of the Athabasca Basin (Saskatchewan, Canada): Implications for the formation of unconformity-related uranium deposits: Mineralium Deposita, v. 35, p. 791-795.
Hetherington, C. J., Harlov, D. E., and Budzyń, B., 2010, Experimental metasomatism of monazite and xenotime: Mineral stability, REE mobility and fluid composition: Mineralogy and Petrology, v. 99, p. 165-184.
Högdahl, K., Majka, J., Sjöström, H., Nilsson, K. P., Claesson, S., and Konečný, P., 2012, Reactive monazite and robust zircon growth in diatexites and leucogranites from a hot, slowly cooled orogen: Implications for the Palaeoproterozoic tectonic evolution of the central Fennoscandian Shield, Sweden: Contributions to Mineralogy and Petrology, v. 163, p. 167-188.
Hoskin, P. W. O., and Black, L. P., 2000, Metamorphic zircon formation by solid-state recrystallization of protolith igneous zircon: Journal of Metamorphic Geology, v. 18, p. 423-439.
Hoskin, P. W. O., and Schaltegger, U., 2003, The composition of zircon and igneous and metamorphic petrogenesis, Reviews in Mineralogy and Geochemistry, 53.
Howard, H. M., Smithies, R. H., Kirkland, C. L., Kelsey, D. E., Aitken, A., Wingate, M. T. D., Quentin de Gromard, R., Spaggiari, C. V., and Maier, W. D., 2015, The burning heart - The Proterozoic geology and geological evolution of the west Musgrave Region, central Australia: Gondwana Research, v. 27, p. 64-94.
Kapp, P., Manning, C. E., and Tropper, P., 2009, Phase-equilibrium constraints on titanite and rutile activities in mafic epidote amphibolites and geobarometry using titanite-rutile equilibria: Journal of Metamorphic Geology, v. 27, p. 509-521.
Keay, S., Lister, G., and Buick, I., 2001, The timing of partial melting, Barrovian metamorphism and granite intrusion in the Naxos metamorphic core complex, Cyclades, Aegean Sea, Greece: Tectonophysics, v. 342, p. 275-312.

Kelly, N. M., Harley, S. L., and Möller, A., 2012, Complexity in the behavior and recrystallization of monazite during high-T metamorphism and fluid infiltration: Chemical Geology, v. 322-323, p. 192-208.
Kelsey, D. E., Clark, C., and Hand, M., 2008, Thermobarometric modelling of zircon and monazite growth in melt-bearing systems: Examples using model metapelitic and metapsammitic granulites: Journal of Metamorphic Geology, v. 26, p. 199-212.
Kennedy, A. K., Kamo, S. L., Nasdala, L., and Timms, N. E., 2010, Grenville skarn titanite: Potential reference material for sims U-Th-Pb analysis: Canadian Mineralogist, v. 48, p. 1423-1443.
Kirkland, C. L., Erickson, T. M., Johnson, T. E., Danišík, M., Evans, N. J., Bourdet, J., and McDonald, B. J., 2016a, Discriminating prolonged, episodic or disturbed monazite age spectra: An example from the Kalak Nappe Complex, Arctic Norway: Chemical Geology, v. 424, p. 96-110.
Kirkland, C. L., Hollis, J., Danišík, M., Petersen, J., Evans, N. J., and McDonald, B. J., 2017, Apatite and titanite from the Karrat Group, Greenland; implications for charting the thermal evolution of crust from the U-Pb geochronology of common Pb bearing phases: Precambrian Research, v. 300, p. 107-120.
Kirkland, C. L., Spaggiari, C. V., Johnson, T. E., Smithies, R. H., Danišík, M., Evans, N., Wingate, M. T. D., Clark, C., Spencer, C., Mikucki, E., and McDonald, B. J., 2016b, Grain size matters: Implications for element and isotopic mobility in titanite: Precambrian Research, v. 278, p. 283-302.
Kohn, M. J., 2017, Titanite Petrochronology: Reviews in Mineralogy and Geochemistry, v. 83, p. 419-441.
Kohn, M. J., Catlos, E. J., Ryerson, F. J., and Harrison, T. M., 2001, Pressure-temperature-time path discontinuity in the Main Central thrust zone, central Nepal: Geology, v. 29, p. 571-574.
Kohn, M. J., and Corrie, S. L., 2011, Preserved Zr-temperatures and U-Pb ages in high-grade metamorphic titanite: Evidence for a static hot channel in the Himalayan orogen: Earth and Planetary Science Letters, v. 311, p. 136-143.
Kohn, M. J., Corrie, S. L., and Markley, C., 2015, The fall and rise of metamorphic zircon: American Mineralogist, v. 100, p. 897-908.
Kohn, M. J., Engi, M., and Lanari, P., 2018, Petrochronology: Methods and Applications, 1-575 p.
Korhonen, F. J., Clark, C., Brown, M., and Taylor, R. J. M., 2014, Taking the temperature of Earth's hottest crust: Earth and Planetary Science Letters, v. 408, p. 341-354.
Kovaleva, E., Klötzli, U., Habler, G., Huet, B., Guan, Y., and Rhede, D., 2017, The effect of crystal-plastic deformation on isotope and trace element distribution in zircon: Combined BSE, CL, EBSD, FEG-EMPA and NanoSIMS study: Chemical Geology, v. 450, p. 183-198.
Kretz, R., 1983, Symbols for rock-forming minerals: American Mineralogist, v. 68, p. 277-279.
Larrovere, M. A., Alasino, P. H., and Baldo, E. G., 2016, The double-vergent ductile shear zone of northwestern sierra de Velasco: Deformation of the middle crust during the Famatinian orogeny: Revista de la Asociacion Geologica Argentina, v. 73, p. 117-133.
Lee, J. K. W., Williams, I. S., and Ellis, D. J., 1997, Pb, U and Th diffusion in natural zircon: Nature, v. 390, p. 159-162.
Lucassen, F., and Becchio, R., 2003, Timing of high-grade metamorphism: Early Palaeozoic U-Pb formation ages of titanite indicate long-standing high-T conditions at the western margin of Gondwana (Argentina, 26-29°S): Journal of Metamorphic Geology, v. 21, p. 649-662.
Lucassen, F., Becchio, R., and Franz, G., 2010, The Early Palaeozoic high-grade metamorphism at the active continental margin of West Gondwana in the Andes (NW Argentina/N Chile): International Journal of Earth Sciences, v. 100, p. 445-463.
Lucassen, F., Becchio, R., and Franz, G., 2011, The early Palaeozoic high-grade metamorphism at the active continental margin of West Gondwana in the Andes (NW Argentina/N Chile): International Journal of Earth Sciences, v. 100, p. 445-463.

Lucassen, F., Becchio, R., Wilke, H. G., Franz, G., Thirlwall, M. F., Viramonte, J., and Wemmer, K., 2000, Proterozoic-Paleozoic development of the basement of the Central Andes (18-26°S) - A mobile belt of the South American craton: Journal of South American Earth Sciences, v. 13, p. 697-715.

Ludwig, K. R., 2003a, Mathematical-statistical treatment of data and errors for230Th/U geochronology, Reviews in Mineralogy and Geochemistry, 52.

Ludwig, K. R., 2003b, User's Manual for Isoplot/Ex rev. 3.00: A Geochronological Toolkit for Microsoft Excel.

Mahan, K. H., Goncalves, P., Williams, M. L., and Jercinovic, M. J., 2006, Dating metamorphic reactions and fluid flow: Application to exhumation of high-P granulites in a crustal-scale shear zone, western Canadian Shield: Journal of Metamorphic Geology, v. 24, p. 193-217.

Martino, R. D., 2003, Ductile deformation shear belts at Pampean Ranges near Córdoba, Central Argentina: A review: Revista de la Asociacion Geologica Argentina, v. 58, p. 549-571.

Mattinson, J. M., 1978, Age, origin, and thermal histories of some plutonic rocks from the Salinian block of California: Contributions to Mineralogy and Petrology, v. 67, p. 233-245.

McFarlane, C., Connelly, J., and Carlson, W., 2006, Contrasting response of monazite and zircon to a high-T thermal overprint: Lithos, v. 88, p. 135-149.

Mezger, K., Essene, E. J., van der Pluijm, B. A., and Halliday, A. N., 1993, U-Pb geochronology of the Grenville Orogen of Ontario and New York: constraints on ancient crustal tectonics: Contributions to Mineralogy and Petrology, v. 114, p. 13-26.

Mezger, K., and Krogstad, E. J., 1997, Interpretation of discordant U-Pb zircon ages: An evaluation: Journal of Metamorphic Geology, v. 15, p. 127-140.

Miller, H., Adams, C., Aceñolaza, F. G., and Toselli, A. J., 2011, Evolution of exhumation and erosion in western West Gondwanaland as recorded by detrital zircons of late Neoproterozoic and Cambrian sedimentary rocks of NW and Central Argentina: International Journal of Earth Sciences, v. 100, p. 619-629.

Mottram, C. M., Warren, C. J., Regis, D., Roberts, N. M. W., Harris, N. B. W., Argles, T. W., and Parrish, R. R., 2014, Developing an inverted barrovian sequence; insights from monazite petrochronology: Earth and Planetary Science Letters, v. 403, p. 418-431.

Mulcahy, S. R., Roeske, S. M., McClelland, W. C., Ellis, J. R., Jourdan, F., Renne, P. R., Vervoort, J. D., and Vujovich, G. I., 2014, Multiple migmatite events and cooling from granulite facies metamorphism within the Famatina arc margin of northwest Argentina: Tectonics, v. 33, p. 1-25.

O'Neill, H. S. C., 2016, The smoothness and shapes of chondrite-normalized rare earth element patterns in basalts: Journal of Petrology, v. 57, p. 1463-1508.

Omarini, R. H., Sureda, R. J., Götze, H. J., Seilacher, A., and Pflüger, F., 1999, Puncoviscana folded belt in northwestern Argentina: Testimony of Late Proterozoic Rodinia fragmentation and pre-Gondwana collisional episodes: International Journal of Earth Sciences, v. 88, p. 76-97.

Otamendi, J. E., Castellarini, P. A., Fagiano, M. R., Demichelis, A. H., and Tibaldi, A. M., 2004, Cambrian to Devonian Geologic Evolution of the Sierra de Comechingones, Eastern Sierras Pampeanas, Argentina: Evidence for the Development and Exhumation of Continental Crust on the Proto-Pacific Margin of Gondwana: Gondwana Research, v. 7, p. 1143-1155.

Pankhurst, R. J., Rapela, C. W., and Fanning, C. M., 2000, Age and origin of coeval TTG, I- and S-type granites in the Famatinian belt of NW Argentina, Special Paper of the Geological Society of America, 350, p. 151-168.

Pankhurst, R. J., Rapela, C. W., Saavedra, J., Baldo, E., Dahlquist, J., Pascua, I., and Fanning, C. M., 1998, The Famatinian magmatic arc in the central Sierras Pampeanas: an Early to Mid-Ordovician continental arc on the Gondwana margin: Geological Society, London, Special Publications, v. 142, p. 343-367.

Papapavlou, K., Darling, J. R., Storey, C. D., Lightfoot, P. C., Moser, D. E., and Lasalle, S., 2017, Dating shear zones with plastically deformed titanite: New insights into the orogenic evolution of the Sudbury impact structure (Ontario, Canada): Precambrian Research, v. 291, p. 220-235.
Paquette, J.-L., Goncalves, P., Devouard, B., and Nicollet, C., 2004, Micro-drilling ID-TIMS U-Pb dating of single monazites: A new method to unravel complex poly-metamorphic evolutions. Application to the UHT granulites of Andriamena (North-Central Madagascar): Contributions to Mineralogy and Petrology, v. 147, p. 110-122.
Paquette, J.-L., Ménot, R.-P., Pin, C., and Orsini, J.-B., 2003, Episodic and short-lived granitic pulses in a post-collisional setting: evidence from precise U–Pb zircon dating through a crustal cross-section in Corsica: Chemical Geology, v. 198, p. 1-20.
Parrish, R. R., 1990, U-Pb dating of monazite and its application to geological problems: Canadian Journal of Earth Sciences, v. 27, p. 1431-1450.
Payne, J. L., Hand, M., Barovich, K. M., and Wade, B. P., 2008, Temporal constraints on the timing of high-grade metamorphism in the northern Gawler Craton: Implications for assembly of the Australian Proterozoic: Australian Journal of Earth Sciences, v. 55, p. 623-640.
Poitrasson, F., Chenery, S., and Bland, D. J., 1996, Contrasted monazite hydrothermal alteration mechanisms and their geochemical implications: Earth and Planetary Science Letters, v. 145, p. 79-96.
Poitrasson, F., Chenery, S., and Shepherd, T. J., 2000, Electron microprobe and LA-ICP-MS study of monazite hydrothermal alteration: Implications for U-Th-Pb geochronology and nuclear ceramics: Geochimica et Cosmochimica Acta, v. 64, p. 3283-3297.
Pouchou, J.-L., and Pichoir, F., 1991, Quantitative Analysis of Homogeneous or Stratified Microvolumes Applying the Model "PAP", *in* Heinrich, K. F. J., and Newbury, D. E., eds., Electron Probe Quantitation: Boston, MA, Springer US, p. 31-75.
Powell, R., and J. B. Holland, T., 1994, Optimal geothermometry and geobarometry, 120-133 p.
Ramos, V. A., 2004, Cuyania, an exotic block to Gondwana: Review of a historical success and the present problems: Gondwana Research, v. 7, p. 1009-1026.
Ramos, V. A., 2008, The basement of the Central Andes: The arequipa and related terranes, *in* Jeanloz, R., Albee, A. L., Burke, K. C., and Freeman, K. H., eds., Annual Review of Earth and Planetary Sciences, 36, p. 289-324.
Ramos, V. A., Dallmeyer, R. D., and Vujovich, G., 1998, Time constraints on the Early Palaeozoic docking of the Precordillera, central Argentina, Geological Society Special Publication, 142, p. 143-158.
Ramos, V. A., Escayola, M., Mutti, D. I., and Vujovich, G. I., 2000, Proterozoic-early Paleozoic ophiolites of the Andean basement of southern South America, Special Paper of the Geological Society of America, 349, p. 331-349.
Ramos, V. A., Jordan, T. E., Allmendinger, R. W., Mpodozis, C., Kay, S. M., Cortés, J. M., and Palma, M., 1986, Paleozoic terranes of the central Argentine-Chilean Andes: Tectonics, v. 5, p. 855-880.
Ramos, V. A., Vujovich, G., Martino, R., and Otamendi, J., 2010, Pampia: A large cratonic block missing in the Rodinia supercontinent: Journal of Geodynamics, v. 50, p. 243-255.
Rapela, C., Pankhurst, R., Casquet, C., A. Dahlquist, J., Mark Fanning, C., G. Baldo, E., Galindo, C., Alasino, P., Ramacciotti, C., Verdecchia, S., Murra, J., and Basei, M., 2018, A review of the Famatinian Ordovician magmatism in southern South America: Evidence of lithosphere reworking and continental subduction in the early proto-Andean margin of Gondwana.
Rapela, C. W., 1976a, El Basamento Metamorfico de la Region de Cafayate, Provincia de Salta. Aspectos Petrologicos y Geoquimicos: Revista de la Asociacion Geologica Argentina, v. 3, p. 203-222.

Rapela, C. W., 1976b, Las Rocas Granitoides de la Region de Cafayate, Provincia de Salta. Aspectos Petrologicos y Geoquimicos: Revista de la Asociacion Geologica Argentina, v. 4, p. 260-278.
Rapela, C. W., Pankhurst, R. J., Casquet, C., Baldo, E., Saavedra, J., and Galindo, C., 1998a, Early evolution of the Proto-Andean margin of South America: Geology, v. 26, p. 707.
Rapela, C. W., Pankhurst, R. J., Casquet, C., Baldo, E., Saavedra, J., Galindo, C., and Fanning, C. M., 1998b, The Pampean Orogeny of the southern proto-Andes: Cambrian continental collision in the Sierras de Cordoba: Geological Society, London, Special Publications, v. 142, p. 181-217.
Rapela, C. W., Pankhurst, R. J., Saavedra, J., and Galindo, C., 1998c, Early evolution of the proto-andean margin of South America: Geology, v. 26, p. 707-710.
Rapela, C. W., Verdecchia, S. O., Casquet, C., Pankhurst, R. J., Baldo, E. G., Galindo, C., Murra, J. A., Dahlquist, J. A., and Fanning, C. M., 2015, Identifying Laurentian and SW Gondwana sources in the Neoproterozoic to Early Paleozoic metasedimentary rocks of the Sierras Pampeanas: Paleogeographic and tectonic implications: Gondwana Research.
Reddy, S., E. Timms, N., Kinny, P., Buchan, C., Trimby, P., and Blake, K., 2006, Crystal-plastic deformation of zircon: A defect in the assumption of chemical robustness, 257-260 p.
Regis, D., Cenki-Tok, B., Darling, J., and Engi, M., 2012, Redistribution of REE, Y, Th, and U at high pressure: Allanite-forming reactions in impure meta-quartzites (Sesia Zone, Western Italian Alps): American Mineralogist, v. 97, p. 315-328.
Rolland, Y., Cox, S., Boullier, A. M., Pennacchioni, G., and Mancktelow, N., 2003, Rare earth and trace element mobility in mid-crustal shear zones: Insights from the Mont Blanc Massif (Western Alps): Earth and Planetary Science Letters, v. 214, p. 203-219.
Rollinson, H., 1995, Using Geochemical Data: Evolution, Presentation, Interpretation.
Rossi, J., and Toselli, A., 1976, Migmatization y Metamorfismo en el basamento de la Sierra de Quilmes, al Oeste de Colalao del Valle, Tucuman: Revista de la Asociacion Geologica Argentina, v. 2, p. 83-94.
Rossi, P., Cocherie, A., Fanning, C. M., and Deloule, É., 2006, Variscan to eo-Alpine events recorded in European lower-crust zircons sampled from the French Massif Central and Corsica, France: Lithos, v. 87, p. 235-260.
Rubatto, D., 2002, Zircon trace element geochemistry: Partitioning with garnet and the link between U-Pb ages and metamorphism: Chemical Geology, v. 184, p. 123-138.
Rubatto, D., Chakraborty, S., and Dasgupta, S., 2013, Timescales of crustal melting in the Higher Himalayan Crystallines (Sikkim, Eastern Himalaya) inferred from trace element-constrained monazite and zircon chronology: Contributions to Mineralogy and Petrology, v. 165, p. 349-372.
Sambridge, M. S., and Compston, W., 1994, Mixture modeling of multi-component data sets with application to ion-probe zircon ages: Earth and Planetary Science Letters, v. 128, p. 373-390.
Schärer, U., Lian-Sheng, Z., and Tapponnier, P., 1994, Duration of strike-slip movements in large shear zones: The Red River belt, China: Earth and Planetary Science Letters, v. 126, p. 379-397.
Schoene, B., 2014, 4.10 - U–Th–Pb Geochronology, *in* Holland, H. D., and Turekian, K. K., eds., Treatise on Geochemistry (Second Edition): Oxford, Elsevier, p. 341-378.
Schoene, B., Condon, D. J., Morgan, L., and McLean, N., 2013, Precision and accuracy in geochronology: Elements, v. 9, p. 19-24.
Schwartz, J. J., and Gromet, L. P., 2004, Provenance of a late Proterozoic–early Cambrian basin, Sierras de Córdoba, Argentina: Precambrian Research, v. 129, p. 1-21.
Schwartz, J. J., Gromet, L. P., and Miro, R., 2008a, Timing and Duration of the Calc‐Alkaline Arc of the Pampean Orogeny: Implications for the Late Neoproterozoic to Cambrian Evolution of Western Gondwana: The Journal of Geology, v. 116, p. 39-61.

Schwartz, J. J., Gromet, L. P., and Miró, R., 2008b, Timing and duration of the calc-alkaline arc of the pampean orogeny: Implications for the late neoproterozoic to cambrian evolution of Western Gondwana: Journal of Geology, v. 116, p. 39-61.
Schwartz, J. J., Stowell, H. H., Klepeis, K. A., Tulloch, A. J., Kylander-Clark, A. R. C., Hacker, B. R., and Coble, M. A., 2016, Thermochronology of extensional orogenic collapse in the deep crust of Zealandia: Geosphere, v. 12, p. 647-677.
Scibiorski, E., Kirkland, C., Kemp, A. I. S., Tohver, E., and Evans, N. J., 2019a, Trace elements in titanite: A potential tool to constrain polygenetic growth processes and timing.
Scibiorski, E., Kirkland, C. L., Kemp, A. I. S., Tohver, E., and Evans, N. J., 2019b, Trace elements in titanite: A potential tool to constrain polygenetic growth processes and timing: Chemical Geology.
Scott, D. J., and St-Onge, M. R., 1995, Constraints on Pb closure temperature in titanite based on rocks from the Ungava orogen, Canada: implications for U-Pb geochronology and P-T-t path determinations: Geology, v. 23, p. 1123-1126.
Semenov, I., and Weinberg, R. F., 2017, A major mid-crustal decollement of the Paleozoic convergent margin of western Gondwana: The Guacha Corral shear zone, Argentina: Journal of Structural Geology, v. 103, p. 75-99.
Seydoux-Guillaume, A.-M., Fougerouse, D., Laurent, A. T., Gardés, E., Reddy, S., and Saxey, D., 2019, Nanoscale resetting of the Th/Pb system in an isotopically-closed monazite grain: A combined atom probe and transmission electron microscopy study, 65-76 p.
Seydoux-Guillaume, A.-M., Goncalves, P., Wirth, R., and Deutsch, A., 2003, Transmission electron microscope study of polyphase and discordant monazites: Site-specific specimen preparation using the focused ion beam technique: Geology, v. 31, p. 973-976.
Siegesmund, S., Steenken, A., Martino, R. D., Wemmer, K., López de Luchi, M. G., Frei, R., Presnyakov, S., and Guereschi, A., 2009, Time constraints on the tectonic evolution of the Eastern Sierras Pampeanas (Central Argentina): International Journal of Earth Sciences, v. 99, p. 1199-1226.
Sims, J. P., Ireland, T. R., Camacho, A., Lyons, P., Pieters, P. E., Skirrow, R. G., Stuart-Smith, P. G., and Miró, R., 1998, U-Pb, Th-Pb and Ar-Ar geochronology from the southern Sierras Pampeanas, Argentina: implications for the Palaeozoic tectonic evolution of the western Gondwana margin, Geological Society Special Publication, 142, p. 259-281.
Smithies, R. H., Howard, H. M., Evins, P. M., Kirkland, C. L., Kelsey, D. E., Hand, M., Wingate, M. T. D., Collins, A. S., and Belousova, E., 2011, High-Temperature Granite Magmatism, Crust–Mantle Interaction and the Mesoproterozoic Intracontinental Evolution of the Musgrave Province, Central Australia: Journal of Petrology, v. 52, p. 931-958.
Sola, A. M., Becchio, R. A., and Pimentel, M. M., 2013, Petrogenesis of migmatites and leucogranites from Sierra de Molinos, Salta, Northwest Argentina: A petrologic and geochemical study: Lithos, v. 177, p. 470-491.
Sola, A. M., Hasalová, P., Weinberg, R. F., Suzaño, N. O., Becchio, R. A., Hongn, F. D., and Botelho, N., 2017, Low-P melting of metapelitic rocks and the role of H2O: Insights from phase equilibria modelling: Journal of Metamorphic Geology, v. 35, p. 1131-1159.
Stacey, J. S., and Kramers, J., 1975, Approximation of Terrestrial Lead Isotope Evolution by a 2-Stage Model, 207-221 p.
Steenken, A., Siegesmund, S., López de Luchi, M., Frei, R., and Wemmer, K., 2006, Neoproterozoic to Early Palaeozoic events in the Sierra de San Luis: Implications for the Famatinian geodynamics in the Eastern Sierras Pampeanas (Argentina), 965-982 p.
Stuart-Smith, P. G., Camacho, A., Sims, J. P., Skirrow, R. G., Lyons, P., Pieters, P. E., Black, L. P., and Miró, R., 1999, Uranium-lead dating of felsic magmatic cycles in the southern Sierras

Pampeanas, Argentina: Implications for the tectonic development of the proto-Andean Gondwana margin, Special Paper of the Geological Society of America, 336, p. 87-114.
Taylor, R. J. M., Kirkland, C. L., and Clark, C., 2016, Accessories after the facts: Constraining the timing, duration and conditions of high-temperature metamorphic processes: Lithos, v. 264, p. 239-257.
Teufel, S., and Heinrich, W., 1997, Partial resetting of the U-Pb isotope system in monazite through hydrothermal experiments: An SEM and U-Pb isotope study: Chemical Geology, v. 137, p. 273-281.
Thomas, W. A., and Astini, R. A., 2003, Ordovician accretion of the Argentine Precordillera terrane to Gondwana: A review: Journal of South American Earth Sciences, v. 16, p. 67-79.
Toselli, A., Rossi, J., and Rapela, C. W., 1978, El Basamento Metamorfico de la Sierra de Quilmes, Republica Argentina: Revista de la Asociacion Geologica Argentina, v. 33, p. 105-121.
Turekian, K. K., and Holland, H. D., 2013, Treatise on Geochemistry: Second Edition, 1-80 p.
Turner, J. C. M., 1975, Geología del sector oriental de los Departamentos de Santa Victoria e Iruya, Provincia de Salta. República Argentina: Boletín de la Academia Nacional de Ciencias: Boletín de la Academia Nacional de Ciencias, v. 51, p. 11-24.
Vaughan, A. P. M., and Pankhurst, R. J., 2008, Tectonic overview of the West Gondwana margin: Gondwana Research, v. 13, p. 150-162.
Watson, E. B., Wark, D. A., and Thomas, J. B., 2006, Crystallization thermometers for zircon and rutile: Contributions to Mineralogy and Petrology, v. 151, p. 413-433.
Wawrzenitz, N., Krohe, A., Baziotis, I., Mposkos, E., Kylander-Clark, A., and Romer, R., 2015, LASS U-Th-Pb monazite and rutile geochronology of felsic high-pressure granulites (Rhodope, N Greece): Effects of fluid, deformation and metamorphic reactions in local subsystems: Lithos, v. 232, p. 266-285.
Wawrzenitz, N., Krohe, A., Rhede, D., and Romer, R., 2012, Dating rock deformation with monazite: The impact of dissolution precipitation creep: Lithos, v. 134-135, p. 52-74.
Weinberg, R. F., Becchio, R., Farias, P., Suzaño, N., and Sola, A., 2018a, Early Paleozoic accretionary orogenies in NW Argentina: Growth of West Gondwana: Earth-Science Reviews, v. 187, p. 219-247.
Weinberg, R. F., Becchio, R., Farias, P., Suzaño, N., and Sola, A., 2018b, Early paleozoic accretionary orogenies in NW Argentina: Growth of West Gondwana: Earth-Science Reviews.
Weinberg, R. F., and Geordie, M., 2008, Magma migration, folding, and disaggregation of migmatites in the Karakoram Shear Zone, Ladakh, NW India: Bulletin of the Geological Society of America, v. 120, p. 994-1009.
Whitehouse, M. J., and Platt, J. P., 2003, Dating high-grade metamorphism—constraints from rare-earth elements in zircon and garnet: Contributions to Mineralogy and Petrology, v. 145, p. 61-74.
Whitmeyer, S. J., and Simpson, C., 2003, High strain-rate deformation fabrics characterize a kilometers-thick Paleozoic fault zone in the Eastern Sierras Pampeanas, central Argentina: Journal of Structural Geology, v. 25, p. 909-922.
Williams, I. S., 2001, Response of detrital and zircon and monazite, and their U-Pb isotopic systems, to regional metamorphism and host-rock partial melting, Cooma Complex, Southeastern Australia: Australian Journal of Earth Sciences, v. 48, p. 557-580.
Williams, M. L., Jercinovic, M. J., Harlov, D. E., Budzyń, B., and Hetherington, C. J., 2011, Resetting monazite ages during fluid-related alteration: Chemical Geology, v. 283, p. 218-225.
Williams, M. L., Jercinovic, M. J., and Hetherington, C. J., 2007, Microprobe monazite geochronology: Understanding geologic processes by integrating composition and chronology, *in* Jeanloz, R., Albee, A. L., Burke, K. C., and Freeman, K. H., eds., Annual Review of Earth and Planetary Sciences, 35, p. 137-175.

Winter, J., 2001, An Introduction to Igneous and Metamorphic Petrology.
Wolf, M. B., and London, D., 1995, Incongruent dissolution of REE- and Sr-rich apatite in peraluminous granitic liquids: differential apatite, monazite, and xenotime solubilities during anatexis: American Mineralogist, v. 80, p. 765-775.
Wolfram, L. C., Weinberg, R. F., Hasalová, P., and Becchio, R., 2017, How melt segregation affects granite chemistry: Migmatites from the Sierra de Quilmes, NW Argentina: Journal of Petrology, v. 58, p. 2339-2364.
Wolfram, L. C., Weinberg, R. F., Nebel, O., Hamza, K., Hasalová, P., Míková, J., and Becchio, R., 2019, A 60-Myr record of continental back-arc differentiation through cyclic melting: Nature Geoscience, v. 12, p. 215-219.
Yakymchuk, C., and Brown, M., 2014, Behaviour of zircon and monazite during crustal melting: Journal of the Geological Society, v. 171, p. 465-479.
Yakymchuk, C., and Brown, M., 2019, Divergent behaviour of Th and U during anatexis: Implications for the thermal evolution of orogenic crust: Journal of Metamorphic Geology, v. 37, p. 899-916.
Yakymchuk, C., Kirkland, C. L., and Clark, C., 2018, Th/U ratios in metamorphic zircon: Journal of Metamorphic Geology, v. 36, p. 715-737.
Zhang, L. S., and Schärer, U., 1996, Inherited Pb components in magmatic titanite and their consequence for the interpretation of U-Pb ages: Earth and Planetary Science Letters, v. 138, p. 57-65.

Chapter 4

Behaviour of zircon, monazite, and titanite in protracted HT–LP conditions: unravelling 120 Ma of orogeny

Abstract

Zircon, monazite, and titanite are used to understand the thermal and magmatic history of long–lived migmatitic terranes. This chapter used their different records and varied responses to determine the key features of the prolonged high–temperature and low–pressure (HT–LP) event in the back–arc of the Ordovician Famatinian Orogen exposed in the Sierra de Quilmes, NW Argentina. Zircons from this area have previously defined a 60 Myr hot period with possibly five discrete melting events with a recurrence of 10–15 Myr, while monazite from the same samples yields a single wide distribution of dates centered at around 460–470 Ma. We investigated U–Pb geochronology of zircon, monazite, and titanite from a metamorphic complex in the footwall of the ones previously dated. We found that behaviors are varied. Combined, the results of three different geochronometers, indicate sustained temperatures above 700 °C for over 120 Myr, c. 60 Myr longer than expected. Comparison of the different behaviours of the accessory minerals in the different complexes, after slightly different teconothermal histories indicate that: a) in the hotter hanging wall, where temperatures reached 800 °C, zircon grew several times as entirely new grains, while at 750 °C in the footwall complex, very similar rocks only generated narrow zircon rims, b) monazite ages reflect the entire duration of Famatinian peak metamorphism, except for one sample, not different from the others except for being sheared, that yielded an unexpected younger peak at 407 Ma, suggesting that either late shearing or hydrothermal alteration reset monazite at ≥ 700 °C (as recorded by titanite), and c) titanite grew continually without much Pb diffusion, first during the prograde path and then during slow cooling responding to allanite growth, and recording a total of 120 Myr. Not only do minerals change behaviour with temperature and shearing conditions, but they are also not homogenized in either a single sample or in the same complex, even when submitted to similar histories. Therefore, analyses of several accessory phases from a number of samples are the most efficient way to obtain the complete overview of the evolution of a terrane.

1 Introduction

There are a limited number of studies where the tectono–thermal evolution of high–grade metamorphic terranes is investigated using multiple geothermometers, and even fewer studies that compare the behaviour of accessory phases geochronometers such as zircon, monazite, and titanite from the same rock and across metamorphic complexes of the same orogeny exposed to slightly different PT evolutions. Because of different behaviours of the accessory phases during metamorphism, such as different closure temperatures or susceptibility to dissolve and reprecipitate in melts and fluids, they yield different U-Pb dates. Combining these dates with the mineral composition of the accessory phases, we can better understand the record and constrain the tectono–thermal evolution of orogens. In this chapter, we apply this approach to migmatites from the Sierra de Quilmes in NW Argentina, where the mid–crustal section of the long–lived Ordovician Famatinian orogen is currently being uplifted by the Andean Orogeny. The Sierra de Quilmes is composed by metamorphic complexes derived from a single turbiditic package that were metamorphosed to high–temperature and low–pressure (HT–LP) conditions that triggered extensive anatexis for over 60 Myr in the back–arc of the orogen (Wolfram et al., 2019). The rocks were strained and juxtaposed by unusually wide shear zones (Finch et al., 2015; Finch et al., 2017). The protracted history of high–temperature and structural complexity make the Sierra de Quilmes an excellent study case for understanding the behaviour of zircon, monazite, and titanite.

The U–Th–Pb isotopic system is commonly used to date events that occurred at high–temperature (>600 °C). This is a popular isotopic system due to the abundance of U–rich stable minerals like zircon, monazite, and titanite in a large variety of rock–types (Schoene, 2014) and references therein). Each geochronometer has a particular closure temperature (T_c) for U and Pb diffusion. Zircon with the highest closure temperature is followed by monazite and titanite (Cherniak and Watson, 2001; Flowers et al., 2005; Gao et al., 2012; Kohn, 2017; Kohn and Corrie, 2011; Rollinson, 1995; Schwartz et al., 2016; Turekian and Holland, 2013). The closure temperature is the temperature at which the mineral has cooled, so the diffusion of radiogenic Pb becomes insignificant, precluding its escape from the mineral, which in turn starts working as geochronometer. Traditionally, zircon U-Pb is used for constraining the crystallization age of igneous rocks including magmas in migmatites (Schaltegger et al., 1999; Yakymchuk and Brown, 2014), or in the case of detrital zircon, as a source tracer of sediments (Gehrels, 2014). Monazite U-Pb age is typically associated to pre and post peak metamorphic ages in high–grade rocks (Collins et al., 2014), and when linked to mineral chemistry has been used to trace and date the formation of other mineral phases in the rock during both, the prograde and retrograde paths (Kohn et al., 2005; Rubatto et al., 2013). Titanite U-Pb age has been traditionally associated with cooling ages of high–grade rocks (Mattinson, 1978; Schoene, 2014). However, T_c depends mainly on factors like diffusivity, grain shape and size, and cooling rate (Dodson, 1973). Also, once the mineral is below its T_c, other factors can disturb the U-Pb ratio, leading to radiogenic Pb loss or redistribution and partially or completely reset the dates. These factors can be deformation (Kohn, 2017; Kovaleva et al., 2017), metamictization (Cherniak and Watson, 2001; Cherniak et al., 2004), fluid–mineral interaction (Cherniak et al., 2004; Williams et al., 2011), coupled dissolution–precipitation (Catlos et al., 2010; Harlov and Hetherington, 2010; Hetherington et al., 2010; Seydoux-Guillaume et al., 2019; Seydoux-Guillaume et al., 2002; Williams et al., 2011), or a later thermal event that reopens the system and resets the mineral U-Pb systematics. All these factors are likely to affect the geochronometer, particularly during long–lived tectono–thermal events (Korhonen et al., 2013; Reno et al., 2012; Walsh et al., 2015).

Recent work in the north of the Sierra de Quilmes established the existence of thermal cyclicity in the back–arc of the Famatinian Orogeny, usually reported in Cordilleran magmatic arcs (Decelles et al., 2009). This cyclicity is represented by five U-Pb zircon age groups, interpreted to represent discrete melting events with a recurrence of 10–15 Myr that together span the c. 60 Myr of the orogeny (Wolfram et al., 2019). The same rocks that were analysed for zircon have monazite grains that yield a single wide age group that spans the entire 60 Myr of orogeny with no indication of the discrete subdivisions in age peaks (Wolfram et al., 2019). This demonstrates how different geochronometers, in the same rock, record a similar process differently. Similarly, in the Agua del Sapo complex (Chapter 3), we found that titanite, and some monazite continued growing after 440 Ma, when temperatures dropped below 750 °C during the slow cooling and retrogression of the rocks, while zircon and most of the monazite had its U-Pb isotopic system closed, making titanite the best at recording the duration of retrogression at temperatures between 750 and 700 °C.

In this work we compare the results in the literature with our new results for three metamorphic complexes of the Sierra de Quilmes: the Tolombon (Finch et al., 2017; Wolfram et al., 2017; Wolfram et al., 2019), Agua del Sapo (Chapter 3) and the Tolombon West complex (new data here), each having undergone slightly different metamorphic evolutions. The results fine–tune the thermal evolution and the >120 Ma duration of high–temperature metamorphism in the region, while also providing a better understanding of how zircon, monazite, and titanite behave during such protracted orogeny. The chapter starts with a brief geological background followed by an overview of the geochronology results available in the literature and previous chapter. Then new geochronology data is presented for the Tolombon West complex before discussing the results and comparing the behaviour of geochronometers.

2 Geological background

The Sierra de Quilmes is part of the Sierras Pampeanas in NW Argentina (Fig. 1). The Sierras Pampeanas are a series of north–south trending ranges currently being uplifted in the Andean foreland. These rocks represent the mid–crustal sections of a long–lived accretionary margin that was once part of the Western Gondwana supercontinent, and the Terra Australis orogen (Cawood, 2005). The Sierras Pampeanas are mainly composed of metasedimentary rocks that underwent Palaeozoic metamorphism and arc magmatism during the Pampean (c. 540–520 Ma), Famatinian (c. 500–440 Ma) and Achalian (c. 400–350 Ma) orogenic cycles (Rapela et al., 1998a; Weinberg et al., 2018). These orogenies were driven by subduction of the proto–Pacific oceanic crust in the western margin of Gondwana and each ended after the accretion of a Laurentian–derived terrane (Aceñolaza et al., 2002; Aceñolaza and Toselli, 2009; Astini, 1998; Escayola et al., 2011; Omarini et al., 1999; Ramos, 2004, 2008; Ramos et al., 1998; Ramos et al., 2000; Ramos et al., 1986; Ramos et al., 2010; Rapela et al., 1998c; Rapela et al., 2015; Vaughan and Pankhurst, 2008). The rocks in Sierra de Quilmes record metamorphism and anatexis that occurred in the back–arc of the Famatinian orogenic cycle.

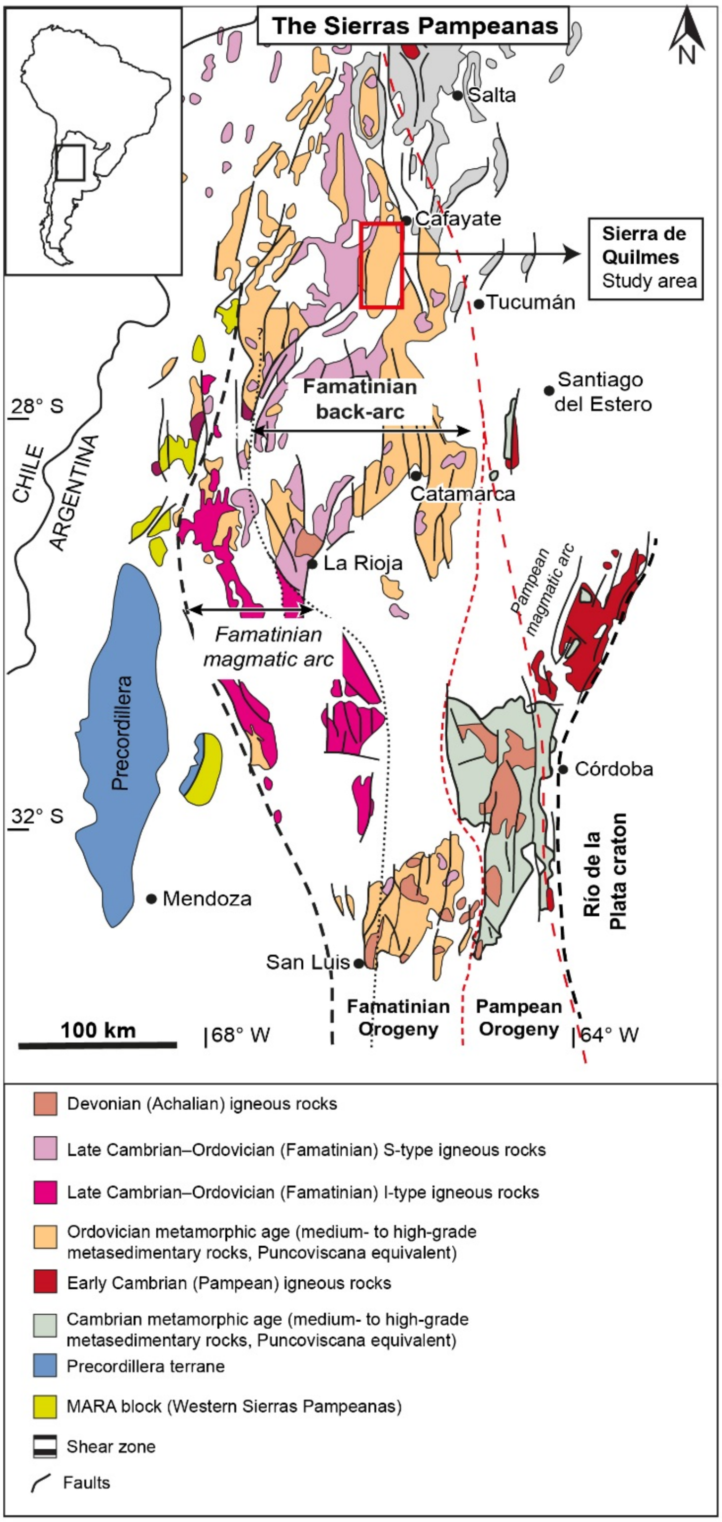

Figure 1– Sierras Pampeanas and study area location. Outline of Pampean and Famatinian orogen. The Sierra de Quilmes is located in the Famatinian back–arc.

2.1 Famatinian orogenic cycle

The Famatinian orogenic cycle was a subduction–related Andean–type continental orogeny. The present–day expression of its metaluminous magmatic arc and back–arc with peraluminous magmatism is depicted in Fig. 1. The orogenic cycle initiated at c. 505–500 Ma, as indicated by zircon U-Pb ages in peraluminous magmatic rocks of the Famatinian back–arc (Bahlburg et al., 2016; Wolfram et al., 2017). The back–arc was first dominated by an extensional tectonic regime as suggested by the sedimentary basins formed between c. 485–470 Ma (Astini, 2008; Bahlburg and Breitkreuz, 1991; Bahlburg and Hervé, 1997b; Büttner, 2009; Moya, 2015; Rapela et al., 2018). This switched into a shortening tectonic event known as the Oclóyic phase (Turner, 1975). This event was triggered by the arrival and docking of a Laurentian–derived terrane to the western margin of Gondwana and marked by regional unconformities formed during the inversion of the basins (Astini and Dávila, 2004; Bahlburg and Hervé, 1997a; Davila et al., 2003; Ramos, 2008; Thomas and Astini, 2003). Several wide shear zones formed in this mid–crustal levels (Finch et al., 2015; Larrovere et al., 2016; Larrovere et al., 2011; Rapela et al., 1998b; Semenov and Weinberg, 2017). The Famatinian orogenic cycle finished at around 440–435 Ma when magmatism waned (2009; Bahlburg et al., 2016; Büttner et al., 2005; Mulcahy et al., 2014; Wolfram et al., 2017).

2.2 The Sierra de Quilmes geology

The Sierra de Quilmes represents mid–crustal sections of the Famatinian back–arc (Büttner et al., 2005; Finch et al., 2015; Lucassen and Becchio, 2003; Lucassen et al., 2011; Pankhurst et al., 2000; Wolfram et al., 2017). The protolith of the Sierra de Quilmes is the extensive turbidite sequence of the Puncoviscana Formation (Rapela, 1976a, b; Toselli et al., 1978) deposited between > 600 and 520 Ma (Drobe et al., 2009; Omarini et al., 1999; Rapela et al., 1998b; Schwartz and Gromet, 2004; Sims et al., 1998). Regionally, this sequence was affected first by the Pampean orogenic cycle that caused high–temperature metamorphism to the west and east of Sierra de Quilmes, but little evidence in between (Collo et al., 2009; Rapela et al., 2015; Weinberg et al., 2018). In Chapter 3, we have demonstrated that the Pampean–age Filo granite intruded the turbidites of the Agua del Sapo complex that do not record Pampean high–temperature metamorphism. The sequence was later strongly overprinted by the Famatinian orogenic cycle that shaped the currently exposed migmatitic terranes of the Sierra de Quilmes.

2.2.1 Metamorphic complexes

The three metamorphic complexes that make up the central part of the Sierra de Quilmes, the Tolombon, Tolombon West, and Agua del Sapo complexes, are separated by thick shear zones (Fig. 2). The Tolombon complex is composed by metasedimentary rocks that range from greenschist facies in the north–east, to migmatites in the garnet–cordierite–sillimanite zone, and to orthopyroxene granulite facies in the south–west. The latter is sheared by the complex–bounding Pichao shear zone (Büttner et al., 2005; Finch et al., 2015; Finch et al., 2017). The peak metamorphic conditions were constrained to c. 6 kbar and 800 °C, and its mineral paragenesis indicates high–temperature low–pressure (HT–LP) conditions followed by isobaric cooling (Büttner et al., 2005; Finch et al., 2017). The prevailing high temperatures led to extensive partial melting and formation of diatexites and S–type leucogranitic plutons (Wolfram et al., 2017).

The Agua del Sapo complex is in the footwall of the Tolombon complex, below the Pichao shear zone. It has been detailed in chapters 2 and 3, and here we only provide a brief summary. The complex is composed of metasedimentary rocks that are similar to the ones of the Tolombon complex, but with less voluminous evidence for anatexis (e.g. less voluminous leucosomes in migmatites), but with more intense deformation (Chapter 2). The lithology and metamorphic grade vary from north to south, from Bt–Grt schists and gneisses grading to Grt–Sil–Kfs migmatites. These are stromatic metatexites resembling those of the Tolombon complex. The difference is that these rocks never reach the Opx–stability field. The bulk composition and mineralogy of the metasedimentary sequence also changes from north to south. The typical Al–rich metaturbidite sequence, rich in Ms+Crd+Sil, transitionally changes to a Ca–rich sequence that is comprised of Qtz+Pl+Bt+Hbl+Kfs+Ep+Cpx+Scp±Grt±Ms with accessory allanite, apatite, titanite, and ilmenite. In effect, the whole rock geochemistry and mineralogy of these Ca–rich rocks is similar to a metaluminous granodiorite (Fig. 6 and Table 1, Chapter 2). Results from thermodynamic modelling of the Al–rich migmatite (Chapter 3) shows that the metamorphic peak mineral paragenesis Grt+Pl+Kfs+Sil±Ilm was stabilized at 725 ± 25 °C and 5.5 ± 0.5 kbar. These conditions are cooler than those reached in the Tolombon complex.

The Tolombon West complex is separated from the two other complexes by the western continuation of the Pichao shear zone, and by the north–south trending Filo shear zone (Fig. 2). It is composed of similar Al–rich turbidite sequences, also metamorphosed into migmatites in the garnet–cordierite–sillimanite zone. Cordierite–bearing metatexites and scattered peraluminous igneous bodies reaching a few kilometres in length are common in the west side of the complex, and garnet–bearing metatexites with large volumes of diatexites are prevalent in the eastern side of the complex, flanking the complex–bounding Filo shear zone (Fig. 2). This complex was not previously investigated in the literature and details of its petrology and metamorphic mineral paragenesis will be given here.

2.2.2 *Shear zones and deformational events*

The two shear zones that separate the three complexes form the Pichao–Filo thrust system. This thrust system juxtaposes, the Tolombon over the Tolombon West complex, which in turn are thrusted over the Agua del Sapo complex, forming thrust–bound duplex system (see Chapter 2, Fig.

15). Therefore the Tolombon and Tolombon West complexes together form the hanging wall and the Agua del Sapo complex the footwall of the thrust system. This thrusting event is characterized by a top–to–west tectonic transport that is associated with the D1 tectono–metamorphic crustal thickening event (Chapter 2). The southern part of the Tolombon West complex and the entire footwall Agua del Sapo complex record a second event dominated by upright, N or S plunging folds, and pervasive top–to–south constrictional shearing. This second event (D2) is interpreted to record the stretching, parallel to the orogen, of the thermally–weakened footwall complex in response to the D1 crustal thickening event (Chapter 2).

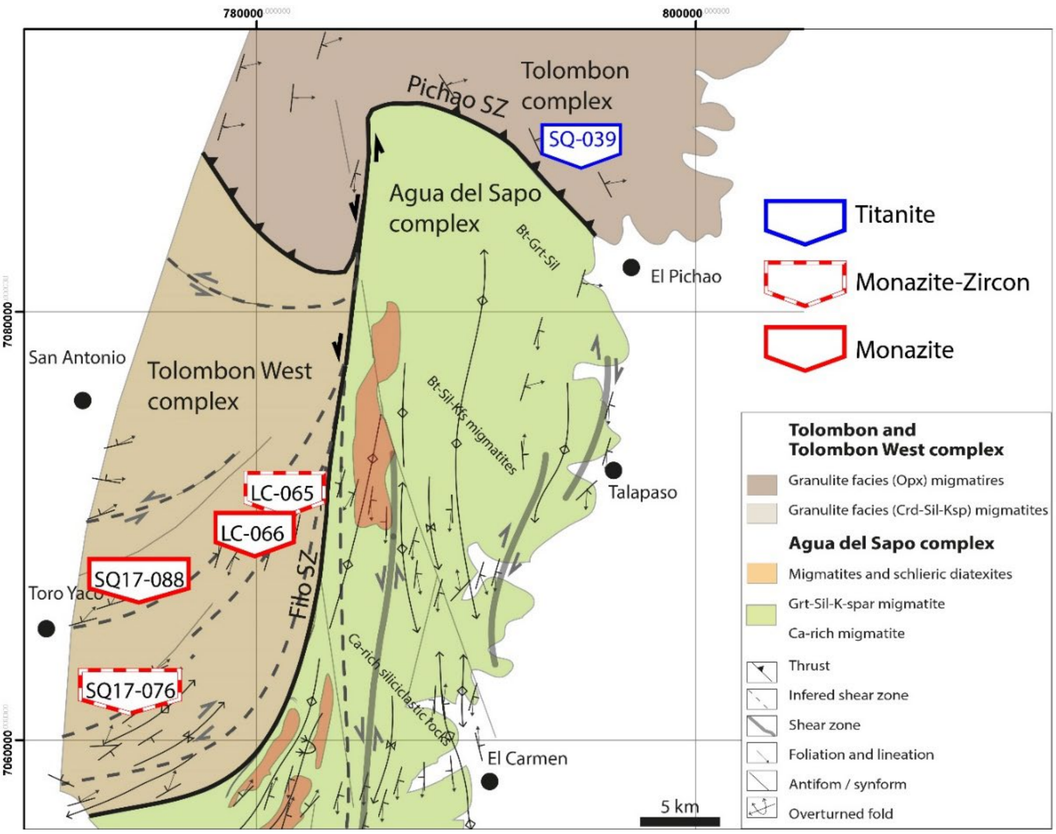

Figure 2– Simplified map of central Sierra de Quilmes with sample location and type of geochronometer used in this study.

2.3 Geochronology

Previous geochronological studies focused mostly on the hanging wall Tolombon complex (Büttner et al., 2005; Finch et al., 2017; Lucassen et al., 2000; Wolfram et al., 2017) with only a published monazite dating study in the footwall Agua del Sapo complex (Finch et al., 2017)(Table 1). In the western part of the Tolombon complex, Wolfram (2019) obtained melt crystallization ages of diatexites and leucocratic granites by means of LA – ICP – MS U-Pb ages in zircon. The results show different zircon–growing events that span the entire Famatinian orogeny with a recurrence of c. 10–15 Myr, between 505 and 440 Ma, suggesting protracted high–temperature conditions and multiple anatectic events. Büttner (2005) estimated the age of metamorphism to be 477 ± 11 Ma based on a garnet aplite whole–rock Sm/Nd isochron. Monazite in the Tolombon complex yielded dates that span the entire Famatinian orogenic cycle (Wolfram et al., 2019). Büttner (2005) obtained U-Pb TIMS monazite ages of c. 470 Ma. However, the total grain dissolution technique used could potentially mix different ages. Finch (2017) reported monazite U-Pb SHRIMP dates from sheared migmatites. These dates form ill–defined peaks across the 500–440 Ma range similar to the results of Weinberg (2020). The latter author found that monazite in the Tolombon complex was compositionally zoned but with no old–core, young–rim systematics and argued that the decoupling between mineral composition and date was a result of coupled dissolution–precipitation (Seydoux-Guillaume et al., 2003; Seydoux-Guillaume et al., 2002). In terms of cooling ages, ^{40}Ar–^{39}Ar age of muscovite from pegmatites in the Tolombon complex yielded ages of 442 ± 11 Ma, and muscovite in small shear zones yielded 408 ± 7 Ma (Büttner et al., 2005).

In the Agua del Sapo complex Finch (2017) reported monazite U-Pb dates from a sample collected at the immediate footwall of the Pichao shear zone. This sample is a mylonitic Grt–schist with no evidence of retrogression and yielded dates between 450 and 490 Ma, which are comparable with the monazite dates of the hanging wall Tolombon complex. A Bt–Ms–Grt schist sampled c. 1 km south of the previous sample, records younger monazite dates between 435–420 Ma. This rock contains Bt+Qtz+Kfs+Pl+Ms+Grt+Tur, where garnet is partially retrogressed to Bt–Chl, and biotite is partially replaced by chlorite. Finch (2017) argued that the younger dates are the result of heating of the amphibolite–facies rocks in the footwall after the thrusting of the hot granulite–facies Tolombon complex. Büttner (2005) reported a single U-Pb age of 459 ± 2 Ma from titanite in this complex. Finally, In Chapter 3 we reported zircon, monazite and titanite ages from the Agua del Sapo complex. A summary of the ages is provided in Table 1.

Table 1– Summary of geochronological data from previous studies in the Sierra de Quilmes.

	*Zircon (U-Pb) (Ma)**	*Monazite (U-Pb)(Ma)**	*Titanite (U-Pb)(Ma)**	*Muscovite (Ar–Ar)(Ma)**	*Sm/Nd (Ma)**	*Rb/Sr (Ma)**
Tolombon Complex	c. 505[a] c. 490[a] c. **475–465**[a] c. 460[a] c. 450–445[a]	c. 470[b] c. 460[c] 473 ± 4[d] 468 ± 2[d] 484.8 ± 2.3[g] 470.7 ± 2.2[g]	459–468[d]	442 ± 11[e] 408 ± 7[f]	442 ± 9[j] 477 ± 11[K]	450 ± 7[l] 416 6[m]
Agua del Sapo Complex	c. 500–440[n] 533.6 ± 2.7[o]	463.6 ± 2.2[h] 484.6 ± 2.6[h] 420.8 ± 1.8[i] 435.2 ± 1.9[i] c. (500–440)[p]	459 ± 2[r] c. 460[q] c. 440–380[q]			

**All uncertainties are 2σ*

[a] Five different age peaks were determined between c. 500 and c. 445 Ma with the most intense peaks at 474 ± 1.8 Ma and 459 ± 1.3 Ma (LA–ICP–MS)(Wolfram et al., 2019)
[b] Schlieren diatexite. Monazite dates between 450–490 Ma with a central age at c. 470 Ma (LASS–ICP–MS) (Wolfram et al., 2017)
[c] Pink leucogranite. Monazite dates between 440–480 Ma with a central age at c. 460 Ma (LASS–ICP–MS) (Wolfram et al., 2017)
[d] Bt–Grt–Crd migmatite (TIMS whole–grain dissolution) (Büttner et al., 2005)
[e] Large muscovite grains (Büttner et al., 2005)
[f] Small muscovite grains in shear zone (Büttner et al., 2005)
[g] Pichao shear zone (SHRIMP) (Finch et al., 2017)
[h] Schist at base of Pichao shear zone (SHRIMP) (Finch et al., 2017)
[I] Schist at the immediate footwall of the Pichao shear zone (SHRIMP) (Finch et al., 2017)
[j] Isochron (Grt–Pl–WR) in calc–silicate rock at granulite facies (Lucassen et al., 2000)
[k] Isochron (Grt–Ap–WR) in garnet aplite (Büttner et al., 2005)
[l] Retrograde muscovite from migmatite (Büttner et al., 2005)
[m] Fine–grained syn–kinematic muscovite. Maximum age of deformation (Büttner et al., 2005)
[n] Large spread of metamorphic zircon dates centred at c. 465 Ma (LASS–ICP–MS) Chapter 3
[o] Pampean granite (LASS–ICP–MS) Chapter 3
[p] Monazite ages between 500–440 Ma with a central age at c. 460 Ma (LASS–ICP–MS) Chapter 3
[q] Titanite ages from Ca–rich migmatites (Chapter 3). Two age group: an older with ages between 500–440 Ma centred at c. 460 Ma and a younger group between 440–380 Ma. The two age groups have different titanite composition (LASS–ICP–MS) Chapter 3.
[r] Qtz–Pl–Grt–Ttn migmatite (TIMS whole–grain dissolution) (Büttner et al., 2005)

3 Dating Method

3.1 LA–ICP–MS and LASS–ICP–MS

After mineral separation and sample preparation (details in Chapter 3), backscattered electron images (BSE) and energy–dispersive X–ray spectroscopy (EDS) analysis were done at the Monash

University Centre for Electron Microscopy, MCEM, using a JEOL 7001F scanning electron microscope coupled with an Oxford X–Max 80 EDS detector. Zircon was imaged using cathode–luminescence (CL) on the Philips (FEI) XL30 ESEM TMP electron microscope with a Gatan CL detector at the scanning electron microscope facility at Melbourne University.

Zircon, monazite and titanite dating was done at the School of Earth, Atmosphere, and Environment, Monash University by means of Laser Ablation Inductively Coupled Plasma Mass Spectrometry (LA–ICP–MS) and Laser Ablation Split Stream Inductively Coupled Plasma Mass Spectrometry (LASS–ICP–MS). In the LASS–ICP–MS system, the ablated material is split between two ICP–MS instruments, allowing U-Pb age and trace elements to be measured simultaneously from a single ablation site. All minerals were analysed using a Thermo ICAPTQ triple quadrupole ICP–MS for the U-Pb ages whereas rare earth and selected trace elements were analysed using a Thermo ICAPQ quadrupole ICP–MS. The mass spectrometers were coupled with an ASI Resolution 193 nm excimer laser equipped with a dual volume Laurin Technic S155 ablation cell.

Spot–size of 25 μm was used in both LA–ICP–MS and LASS–ICP–MS for zircon and titanite, U-Pb ages and composition. For monazite from samples LC–066 and LC–065, LA–ICP–MS was used with 11 μm spot–size for U-Pb analysis and 30 μm for trace element analysis. The 11 μm spots allowed analysing different spots across a single grain.

4 Results

In order to complete the picture for the evolution of Sierra de Quilmes and better understand how the geochronometers behave in the different complexes, zircon and monazite were analysed for samples from the Tolombon West complex and titanite from the granulite facies rocks of the

Tolombon complex. Before detailing these results, this section first details the petrology and metamorphic conditions inferred for the Tolombon West complex.

4.1 Rocks of the Tolombon West complex

4.1.1 Tolombon West migmatites and metamorphic conditions

The lithology of the Tolombon West complex is similar to the Tolombon complex dominated by migmatitic Al–rich metaturbidites of the Puncoviscana sequence. The difference is the lack of low–grade metamorphic zones and lack of Opx–granulite facies. This complex is dominated by a HT–LP mineral assemblage with Crd+Sil+Kfs paragenesis common in the west side, and Grt+Sil+Kfs common in the east side of the complex (Fig. 2).

The Crd–Sil–Kfs zone is dominated by coarse–grained stromatic metatexites with minor scattered km–scale schlieric diatexites. In the metatexites, the leucosome stroma comprises up to 30 % of the rock and contain Qtz+Pl+Bt+Kfs+Sil+Crd±Ms. The melanosome contains similar mineralogy but with a paragenesis dominated by biotite (c. 30 %), quartz, plagioclase, and K–feldspar (c. 20 % each) and sillimanite (<10 %) with minor cordierite, plagioclase, muscovite and magnetite. Biotite forms symplectities with quartz (Fig. 3a) and cordierite has larger Bt–Sil rims than in the leucosomes (Fig. 3b). Magnetite can reach up to c. 5 % in axial planar foliation and in cm–scale shear zones. Furthermore, the Crd–Sil–Kfs zone is characterized by high magnetic susceptibility values of over 2000, indicating high magnetite content. Field measurements are in agreement with aeromagnetic signature (Chapter 2).

The Grt–Sil–Kfs zone in the eastern half of the complex is characterized by larger volumes of diatexite and more intense shearing. Cordierite is not preserved, but there are Bt–Sil–Ms nodules in the rock that could represent retrogressed cordierite. There is a gradational change in the fabric of the diatexites: coarse–grained leucocratic diatexites with schollen or rafts of source rock tend to become more homogeneous and include flow–induced schlieren when approaching the eastern boundary of the complex close to the Filo shear zone. Garnet is poikiloblasitic and when in melanosomes, it is almost exclusively located in the core of large 1–5 mm Bt–Sill elongated nodules.

4.1.1.1 Schlieric granite samples

Schlieric granite samples SQ17–076 and SQ17–088 were collected for dating on the western side of the complex. They have similar bulk mineralogy but differences in the deformation intensity and magnetite content. Granite SQ17–076 is weakly sheared and magnetite modal content is higher when compared with SQ17–088. They are both composed of Qtz+Kfs+Pl+Bt+Ms+Sil+Grt with accessory Ap+Mnz+Zrc+Mag and hosted in the Crd–Sil–Kfs migmatites of the western zone. Qtz and Kfs are abundant and represent c. 70 % (area) of the rock. Kfs phenocrysts are up to 1 cm, and some of them are poikiloblasitic with Bt–Qtz rounded inclusions (Fig. 3c). Plagioclase is rare and forms euhedral crystals, sometimes with blurred zonation. Biotite and muscovite are 0.5 cm long and rarely with zircon inclusions. Fibrolite sillimanite is either in quartz triple–junctions or forming aggregates with biotite.

Schlieric diatexites samples LC–065 and LC–066 are from within Grt–Sil–Kfs migmatite of the eastern edge of the complex. Their mineralogy is similar to that of the western schlieric granites. However, the modal content of biotite is larger, up to 20%. Sample LC–065, from closer to the Filo shear zone, is strongly sheared.

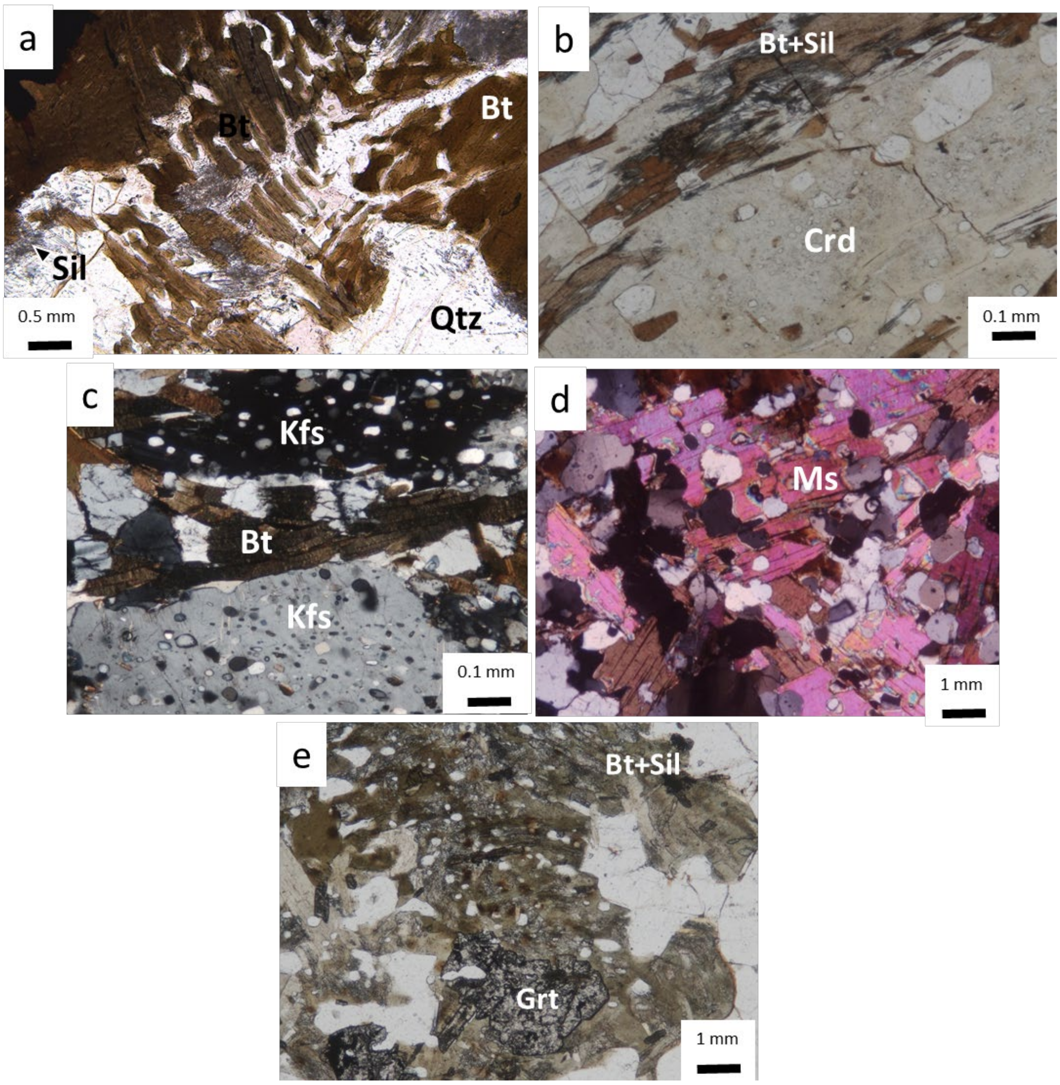

Figure 3– Photomicrographs from diatexites in Tolombon West complex. (a) and (b), are in PPL, and (c) and (d) in XPL). a) Corroded biotite, nearly skeletal. b) Cordierite partially replaced by Bt+Sil. c) Poikiloblastic Kfs. d) Retrograde decussate muscovite. e) Garnet partially replaced by biotite and sillimanite.

4.1.1.2 Metamorphic conditions

Peak metamorphic conditions can be estimated from the mineral paragenesis in the Tolombon West complex, which is the same as the Grt–Crd–Sil zone reported for the Tolombon complex by Büttner (2005). They argued that dehydration melting reaction of biotite with sillimanite to form cordierite and/or garnet and K–feldspar plus melt occurred in excess of 700–750 °C and 5 kbar. In the migmatites of the Tolombon West complex symplectites of Bt–Qtz–Kfs attests to biotite dehydration melting (Turlin et al., 2018) (Fig. 3a), and the absence of prograde muscovite suggest that muscovite dehydration reaction went to completion. Therefore, the metamorphic facies of the Tolombon West complex must have reached 700–750 °C and 5 kbar. Retrogression of the migmatite paragenesis in this complex is evidenced by: 1) cordierite and garnet partially replaced by biotite–sillimanite (Fig. 3e), and b) sillimanite and K–feldspar replaced by muscovite. The retrograde muscovite typically forms mica fish in narrow shear zones or have a decussate texture in undeformed migmatites (Fig. 3d).

4.2 New geochronology and mineral composition

In this section, we present new zircon and monazite geochronology coupled with mineral composition from samples of the Tolombon West complex, and new titanite U-Pb dates and composition from the granulite facies of the Tolombon complex (Table 2). All analysis have U-Pb dates coupled with mineral composition (LASS–ICP–MS), except for zircon from diatexite LC–065 that has only U-Pb dates (LA–ICP–MS). All the U–Pb isotopic and mineral chemistry data are listed in Appendix 2.

Table 2. Details of sample mineralogy, calculated temperature and dating methods used. LASS stands for LASS–ICP–MS and LA for LA–ICP–MS.

Sample	*Complex*	*Rock type*	*Notes*	*Mineral paragenesis*	*Zr–in–titanite (±25 ∫C)*	*Ti–in–zircon (±10 ∫C)*	*Zircon*	*Monazite*	*Titanite*
SQ17–076	Tolombon West	Diatexite	From Crd–Sil zone. Weak shearing	Qtz+Bt+Kfs–Pl+Ms+Sil		735	✓LASS	✓LASS	
SQ17–88		Diatexite	Magnetite–rich diatexite from Crd–Sil zone	Qtz+Bt+Kfs–Pl+Ms+Sil				✓LASS	
LC–065		Schlieric diatexite	Sheared diatexite	Qtz+Bt+Pl+Kfs+Mc+Sil±Ms			✓LA	✓LA	
LC–066		Schlieric diatexite	Non–sheared diatexite	Qtz+Bt+Pl+Kfs+Sil+Mc±Ms				✓LA	
SQ–039	Tolombon	Calc–silicate	Opx–zone	Qtz–Pl–Bt–Kfs–Hbl– Ep–Aln–Ap–Ttn	810				✓LASS

4.2.1 Zircon $^{238}U/^{206}Pb$ dates

Zircon grains were separated from the diatexite samples near the Filo shear zone (LC–065) and the western half of the Tolombon West complex (SQ17–076) (Table 2). Most of the grains in both samples have inherited detrital zircon (DZ) cores. Famatinian dates are mostly found in rims around the DZ and as completely new zircon grains.

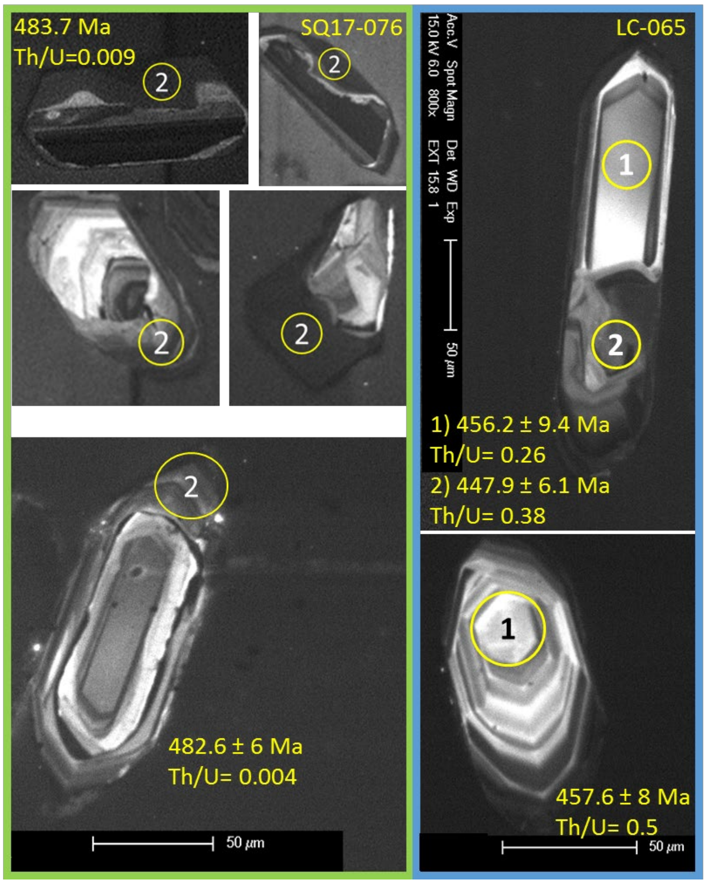

Figure 4– CL images of zircon grains from SQ17–076 (left green box) and from LC–065 (right blue box). In SQ17–076 the Famatinian dates are in featureless zircon rims with low Th/U values. The partially dissolved zircon cores are detrital. In LC–065 the Famatinian dates are in newly formed zircon grains with oscillatory CL texture and rarely in zircon rims. Spot size is 25 µm.

In sample SQ17–076 only eight out of the sixty–nine analysed spots are Famatinian in age and less than 5 % discordant. These Famatinian dates are from rims with featureless or sector zoning CL textures (Fig. 4). Most of these have Th/U ratios < 0.1 but three have values close to one and are both some of the oldest and youngest in the population (Fig. 5b). The dates are scattered in the range 500–440 Ma, with a large mean square of weighted deviates (MSWD) of 3.3 and probability of fit of 0.003 (Fig. 5a).

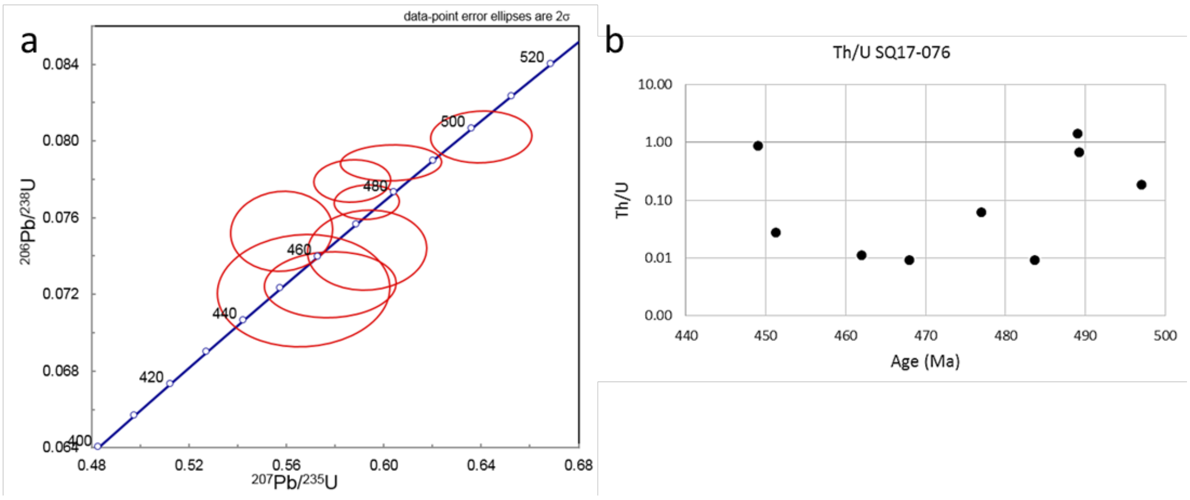

Figure 5– a) Concordia diagram for Famatinian zircon rim dates in sample SQ17–076 (<5% discordant). b) Famatinian zircon rim dates versus Th/U.

For diatexite sample LC–065, sixteen analysis are Famatinian in age, of which thirteen are < 5% discordant. Unlike sample SQ17–076, the Famatinian spots are found in cores and rims. The majority of them have oscillatory CL textures and Th/U ratios > 0.1 (Fig. 6b). The only two spots with Th/U < 0.1 are from rims with featureless CL textures. As with the other diatexite sample, the dates are spread between 500–440 Ma. In order to discriminate between different populations, the *Unmix* function of Isoplot (Ludwig, 2003b) was used. This function detects multiple populations and estimates the most likely age in each group, based on the mixture modelling approach originally designed for disentangling zircon U-Pb dates (Sambridge and Compston, 1994). The *Unmix* function defined one group at 450.4 ± 2.7 Ma and the other at 480.1 ± 2.7 Ma (Fig. 6a).

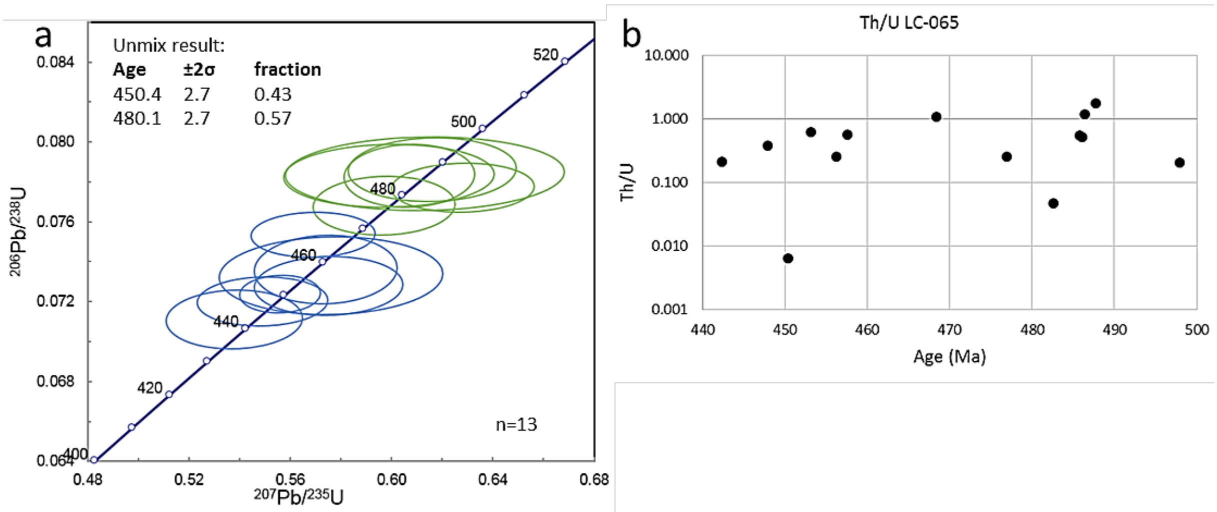

Figure 6– a) Concordia diagram of Famatinian zircon dates from sample LC–065. The ellipse colours highlight two groups calculated by Unmix function. b) Famatinian zircon rim dates versus Th/U.

4.2.2 Zircon composition

The rare–earth elements (REE) chondrite–normalized diagram for sample SQ17–076 shows a typical zircon pattern (Rubatto, 2002) with higher heavy–rare–earth elements (HREE) and lower light–rare–earth elements (LREE), defining a Lu_n/Sm_n c. 150, and also a negative Eu and positive Ce anomalies (Fig. 7). The more dispersed values in LREE in comparison with the HREE reflects low concentrations as LREE are naturally incompatible in zircon (Rubatto, 2002).

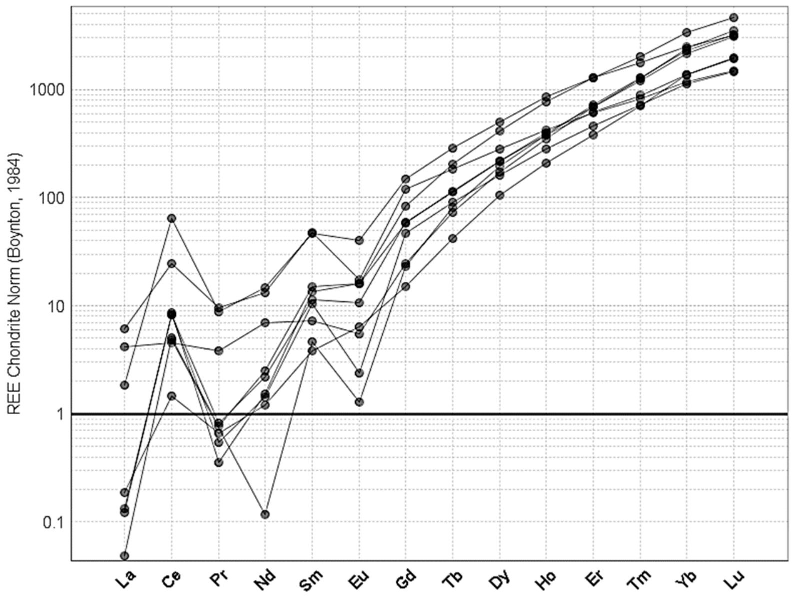

Figure 7– REE diagram for zircon spot analyses from sample SQ17–076

4.2.2.1 Ti–in–zircon temperature

Temperatures of zircon formation were calculated using the Ti content from LASS–ICP–MS analyses for sample SQ17–076 and the calibration equation of Watson (2006). Details of the technique, uncertainties and limitations are detailed in Chapter 3. Temperature values vary between a maximum of 820 ± 10 °C and a minimum of 655 ± 10 °C (Fig. 8).

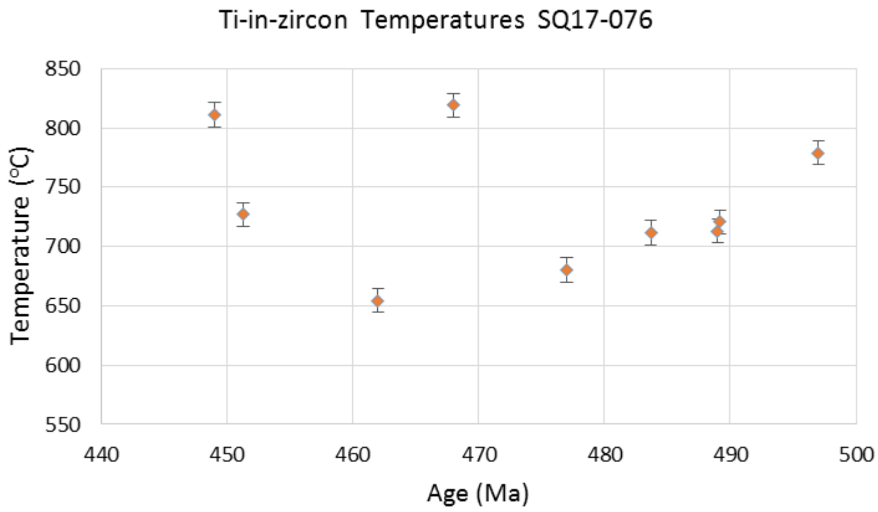

Figure 8– Ti–in–zircon temperature for sample SQ17–076

4.2.3 Monazite

Monazite grains were separated from all four samples in Table 2: two diatexites (LC–066 and LC–065) and two schlieric granites (SQ17–076 and SQ17–088). The monazite grains from all samples are amber to light–green in colour, rounded and variable in size, ranging between 50–200 µm. They are unzoned (Fig. 9a), except for a group of grains from LC–065 that are greener than the rest in natural light, and obvious zoning in BSE images (Fig. 9b). These monazites typically present sector zoning and less common concentric zoning (Williams et al., 2007) in BSE images. The zoning in monazite is attributed to variable REE content (Williams et al., 2007; Wolfram et al., 2019), where bright zones have relatively higher LREE than the dark zones (see below). Reported monazite dates are all < 5 % discordant, and none were excluded.

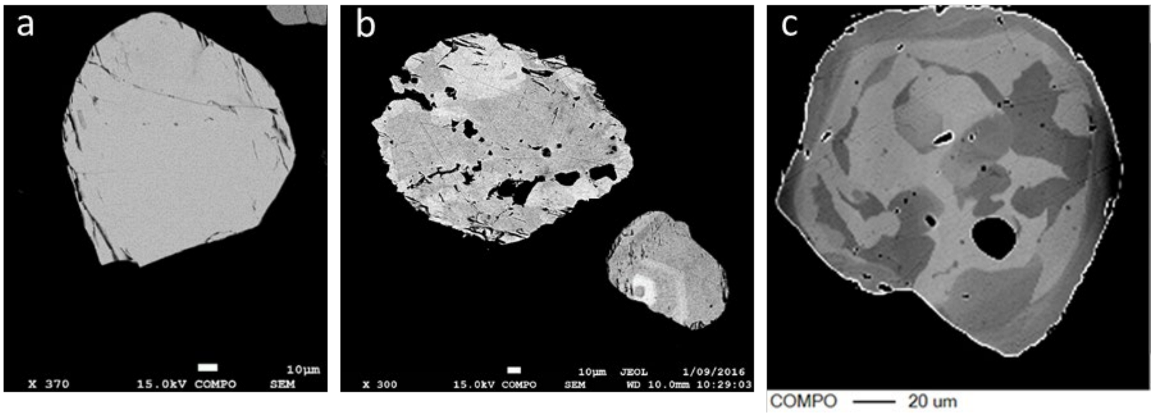

Figure 9– BSE images of monazite grains of different groups. a) Unzoned monazite representing the typical monazite in Tolombon West, and Agua del Sapo complex (Chapter 3). b) Zoned monazite from sheared diatexite LC–065. Larger grain with sector zoning and smaller grain with concentric zoning. c) Zoned monazite grain from Tolombon complex for comparison. Scale size for (a) and (b) are within the image.

4.2.3.1 Monazite $^{238}U/^{206}Pb$ dates

Forty monazite grains were dated in sample LC–065, with a total of 88 spots (Fig. 10a). Some grains were large enough to fit several spots. The dates range between 399 and 495 Ma. They can be grouped into two (Fig. 10b). One group (64 % of all values) older than 440 Ma with a mean of 462.2 ± 3 and a MSWD of 30, and a group younger than 440 Ma (36% of all values) with a mean of 407.5 ± 2.3 and a MSWD of 10.4, both groups with a probability of fit [*p*]=0.00. Fifty–five monazite grains from sample LC–066 were analysed with a total of 96 spots (Fig. 10b). Despite the lack of BSE zoning, monazite grains record variable dates. Most of them within analytical error. The dates range between 435 to 498 Ma and show a near–continuous variation with no clear plateaus. The weighted average gives a mean age of 460.6 ± 2.4 Ma with a MSWD= 38, and the probability of fit [*p*]=0.00. Fifty–two monazite grains were analysed in sample SQ17–076 with one spot per grain (Fig. 10c). The dates range between 457 and 475 Ma, with a mean value of 465.5 ± 1.1 Ma and MSWD of 10.1. The Concordia diagram shows monazite dates very close to concordant (typically < 1% discordancy) but widely spread. Fifty–one monazite grains were analysed in sample SQ17–088 with one spot per grain

(Fig. 10d). The dates define a more compact range between 456 and 469 Ma with a unimodal distribution. The weighted average of all ages is 462.03 ± 0.84 Ma with an MSWD of 5.3 and [*p*]=0.00. In the Concordia diagram the monazite dates are concordant (typically < 1% discordancy) but widely spread.

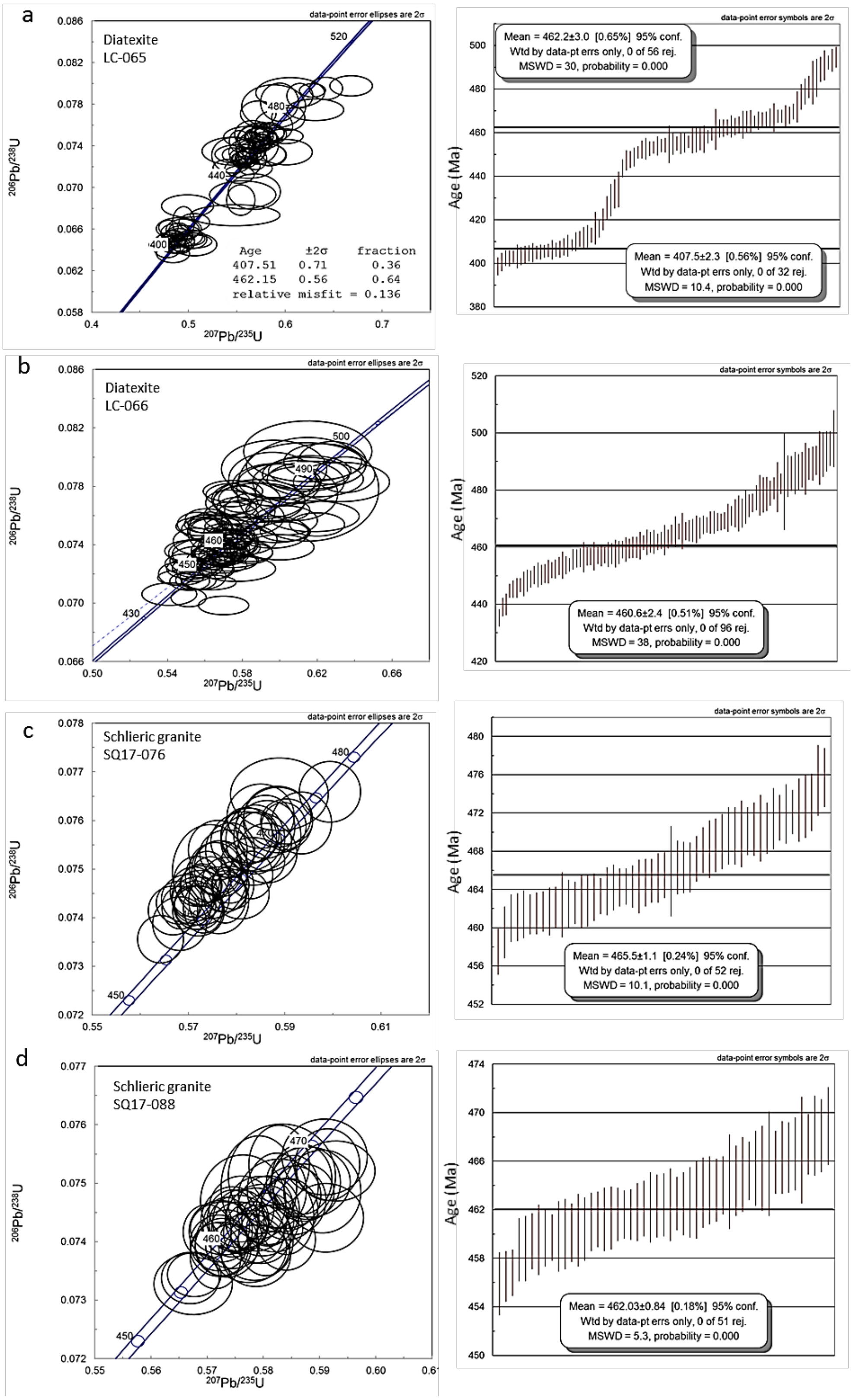

Figure 10– Dating results for all monazite samples. Concordia diagram (left), with weighted average diagram with mean value (right). For LC–065 (a) the Concordia diagram with Unmix data age groups.

Weighted average diagrams in sample LC–066, SQ17–076 and SQ17–088 show a near–continuous variation of dates with no plateaus. None of the values were removed. All error ellipses and bars are in 2σ.

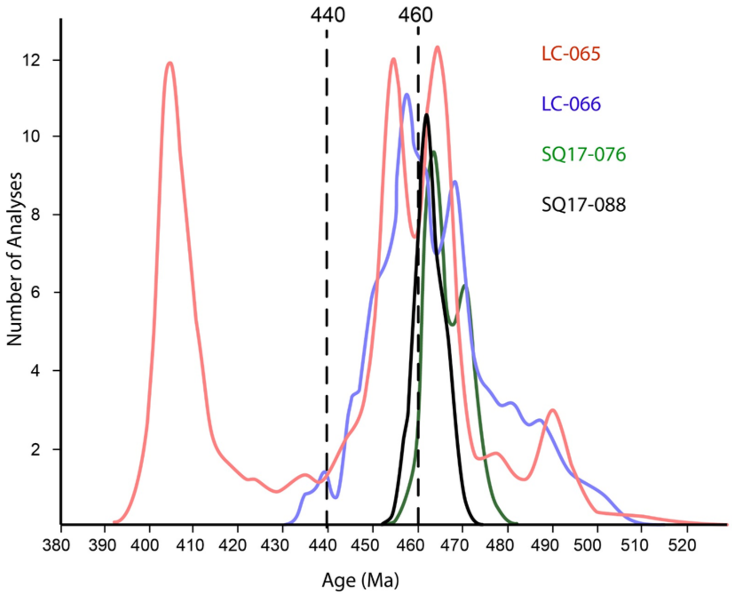

Figure 11– Monazite dates in a probability diagram combining all samples. Note the younger c. 407 Ma group for the zoned monazites in sample LC–065 that stands out from the rest.

In summary, the monazite dates in the schlieric diatexites near the Filo shear zone (samples LC–065 and LC–066) have widely dispersed values in the range of c. 440–500 Ma. Sample LC–065 that is sheared have monazite grains with a discrete younger group of c. 407 Ma that contrasts with the rest of the samples (Figs. 10 and 11). These younger monazites are the only ones in the entire complex that have a clear BSE zoning (Fig. 9b) and, as we will detail in the next section, different REE composition. The other two diatexites in the west of the complex (SQ17–076 and SQ17–088), have a narrower dispersion of dates in the range c. 455–480 Ma. Regardless, all diatexites in the complex yield values centred on c. 460 Ma, and the distribution of dates in all samples have large MSWD values and probability of fit [*p*]=0.00, which highlights the lack of coherence between the uncertainty of the samples and the intra–sample variation (Ludwig, 2003a; Schoene et al., 2013), suggesting either multiple age populations within the dataset or a perturbation of the system by, for example, coupled dissolution – precipitation, or long-lived high-grade metamorphism.

4.2.3.2 Monazite composition

Trace elements were measured by LA–ICP–MS in monazites from LC–066 and LC–065 and by LASS–ICP–MS in the case of SQ17–076 and SQ17–088. The monazite REE pattern from all samples is typical of monazites with enriched LREE composition in comparison to HREE (La_n/Lu_n c. 200) and with a negative Eu anomaly (Stepanov et al., 2012) (Fig. 12). There is a group of monazites from sample LC–065 that stands out from the rest, as they have higher REE content (Fig. 13). They are the zoned younger (407 Ma) grains.

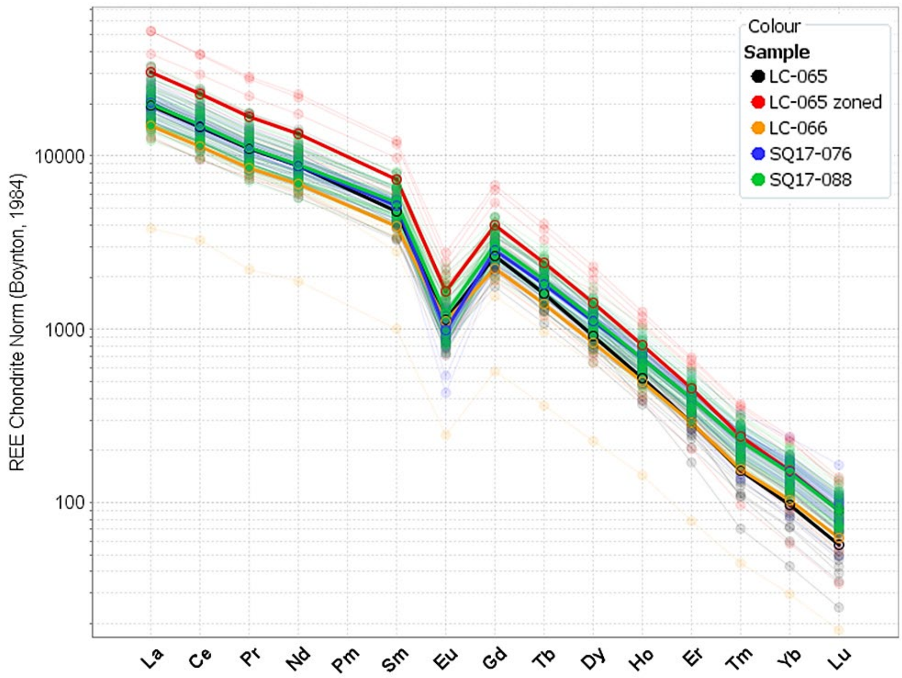

Figure 12– REE chondrite normalized graph of monazite in all diatexites. The solid lines are the mean value.

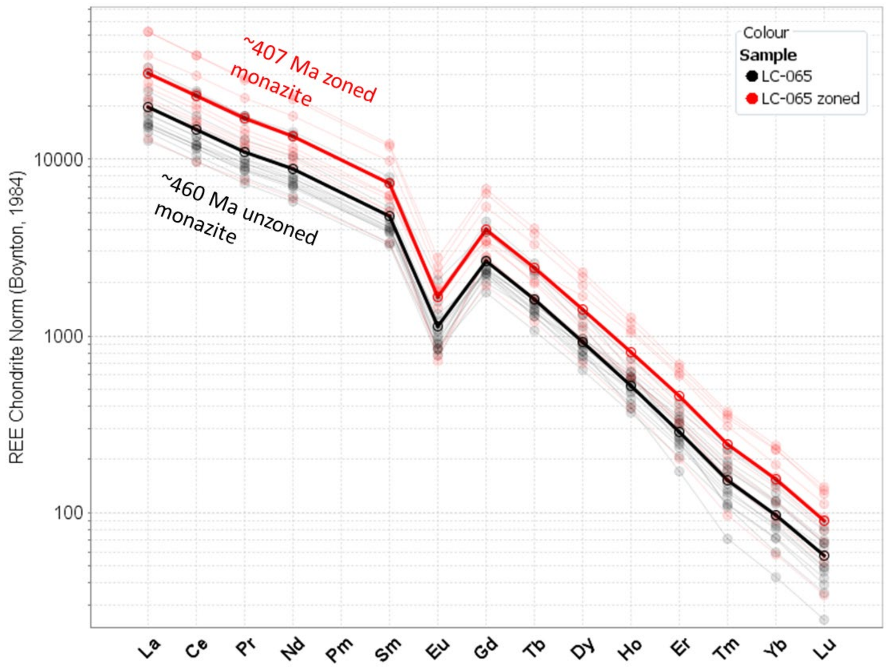

Figure 13– REE chondrite normalized graph of monazites in sample LC–065. The solid line represents the mean value of each group. Samples with higher REE content are from zoned monazites.

4.2.4 Titanite. Tolombon complex

In Chapter 3 we presented results from titanite from the Agua del Sapo complex. In this section, we add results from in–situ titanite grains from a calc–silicate rock (SQ–039) from within the granulite facies migmatites (Opx–zone) of the Tolombon complex, for completion. No such titanite–bearing samples are available from the Tolombon West complex. Titanite was analysed using LASS–ICP–MS. The rock is composed by Qtz+Pl+Cpx+Ep+Ttn with apatite, ilmenite, and magnetite as accessory phases. The microscopic texture of the rock is granoblastic and equigranular with a 200–500 µm grain–size. Plagioclase (c. 40%), quartz (c. 30%) and clinopyroxene (diopside)(c. 30 %) form the bulk of the rock. Titanite is typically 100–150 µm long, euhedral, with aspect ratios between 1 and 4, and with anhedral ilmenite cores. The SEM images showed no zoning.

4.2.4.1 Titanite $^{206}Pb/^{207}Pb$ dates

Since titanite grains generally exhibit variable radiogenic–Pb/common–Pb ratio, the data were plotted in a Tera–Wasserburg diagram. The initial $^{206}Pb/^{207}Pb$ ratio of 0.86 was calculated with the model evolution of Stacey (1975) assuming that titanite formed between 500–440 Ma. This ratio was used to anchor the Discordia and calculate the lower intercept in the Concordia (Fig. 16a). The Tera–Wasserburg diagram shows a lower intercept at 457.3 ± 1.9 Ma with a MSWD of 4.9. Also, every date was corrected individually by anchoring it to 0.86 and obtaining the corrected $^{206}Pb/^{207}Pb$ date as the lower intercept in the Concordia. These corrected $^{206}Pb/^{207}Pb$ dates were plotted in a probability diagram (Fig. 16b), which shows that individual dates are scattered in the range 445–475 Ma.

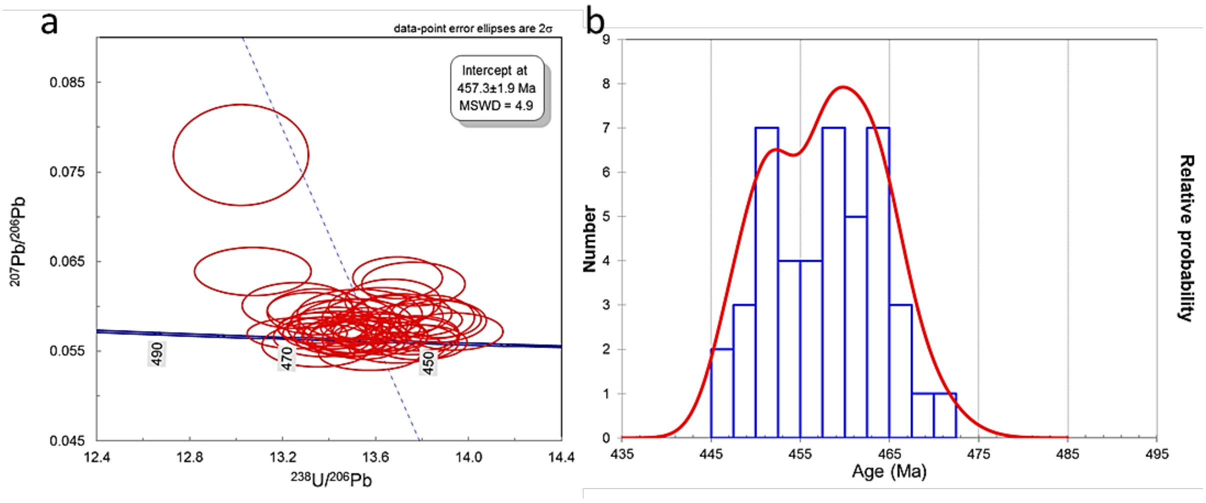

Figure 14– U-Pb dates of in–situ titanite, sample SQ–039. a) Tera–Wasserburg diagram. b) Probability plot of individual corrected $^{206}Pb/^{207}Pb$ dates showing a dispersion of c. 30 Myr between 445–475 Ma.

4.2.4.1 Titanite composition

Titanite was analysed for trace elements, including Zr, Sr, Y, Nb, and REE (Appendix 2). The REE pattern from SQ–039 is typical of titanite with enriched LREE composition in comparison to HREE (La_n/Lu_n c. 5) and with a negative Eu anomaly (Fig. 15) (Kohn, 2017; Scibiorski et al., 2019). We found no variations in the REE fractionation with time, which is usually associated with garnet formation (Kohn, 2017; Scibiorski et al., 2019; Stearns et al., 2015), or LREE with allanite growth as we demonstrated in Chapter 3. In Chapter 3 we used λ1 (O'Neill, 2016) to measure the variability of LREE with time. λ1 remains stable across the c. 30 Myr for sample SQ–039 (Fig. 15b). The same invariability was noticed for Sr or Th/U ratio (Fig. 15b).

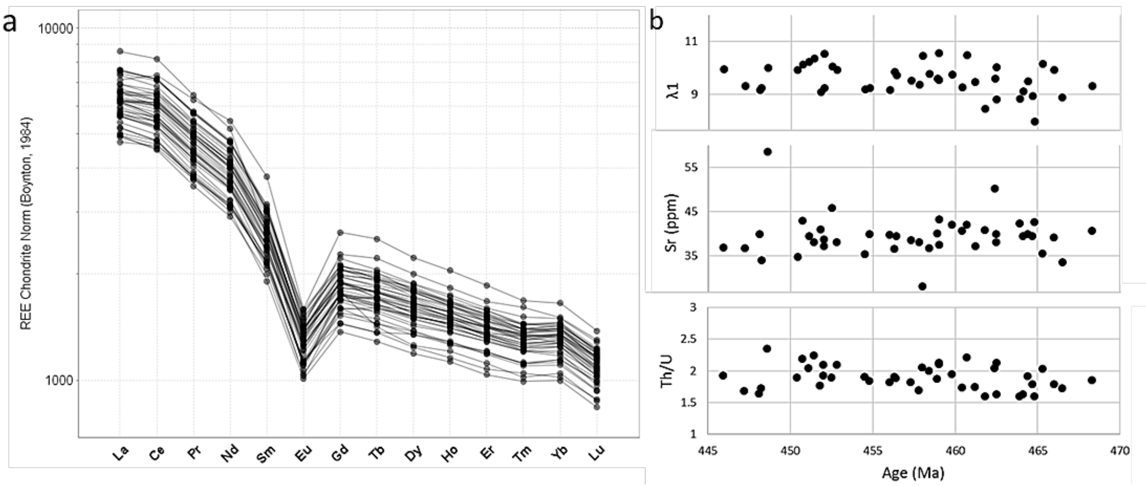

Figure 15– (a) REE diagram for SQ–039 titanites. (b) λ1, Sr, and Th/U values in titanite. There is no trend with time.

4.2.4.2 Zr–in–titanite thermometry

The details of the Zr–in–titanite geothermometer technique (Hayden et al., 2008), its limitations and uncertainties are given in Chapter 3. Using the same methodology, we calculated the Zr–in–titanite temperatures for every spot analysed. Titanite from the Opx–granulite facies of the Tolombon complex records a weighted average temperature of 809.4 ± 3.7 °C (Fig. 16), which is in accordance with the estimated peak metamorphic conditions (Büttner et al., 2005) and considerably higher than Zr–in–titanite temperature in the Agua del Sapo complex (see Fig. 24 in Chapter 3).

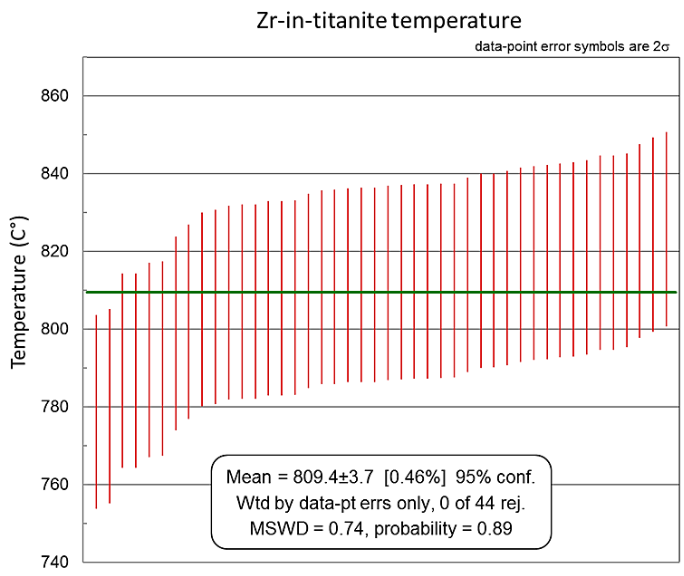

Figure 16– Zr–in–titanite temperature (°C). Weighted average diagram. Every datum has an uncertainty of ± 25 °C associated with the method.

5 Discussion

In order to understand the behavior of the geochronometers in the different complexes, we need to constrain their metamorphic conditions. Table 3 summarizes the findings for all three complexes (Büttner et al., 2005; Finch et al., 2017; Wolfram et al., 2017; Wolfram et al., 2019). This is followed by a brief discussion of the stability and closure temperature of the different accessory phases in high–grade rocks. With this background, we compare the behavior of the three accessory phases and their implication for the tectono–thermal evolution of the complex.

5.1 Metamorphic conditions in the Sierra de Quilmes

As we mentioned in section 2.2.1, the three metamorphic complexes in the Sierra de Quilmes derive from the same metaturbidites (Puncoviscana sequence), and even though they all underwent anatexis, they record slightly different metamorphic conditions. The highest grade was reached in the Tolombon complex where the temperature was higher than 800 °C (e.g., Fig. 19) and pressure c. 6 kbar in the Opx–granulite, and associated with a large volume of peraluminous magmatism (Büttner et al., 2005; Wolfram et al., 2017; Wolfram et al., 2019)(Table 3). The Tolombon West and Agua del Sapo complexes, record peak temperatures of 700–750 °C and 5 kbar (see section 4.1.1.2). In the former, those conditions triggered a larger volume of diatexite than in the latter. Also, the footwall Agua del Sapo complex was strongly sheared (Chapter 2) and remained hot (> 700 °C) for c. 60 Myr longer than the other complexes (Fig. 30 in Chapter 3).

Table 3– Summary of metamorphic conditions and duration from different methods, for the different complexes.

	Tolombon	*Tolombon West*	*Agua del Sapo*
Mineral paragenesis	Opx–granulite facies and Bt dehydration melting. 800 °C and c. 6 kbar (Büttner et al., 2005)	Grt–Crd–Sil. Beginning of Bt dehydration melting. 700–750 °C and 5 kbar	Bt–Grt–Sil granulite facies 700–750 °C and 5 kbar
Ti–in–zircon temperature (±10 °C)		650–819 °C	635–720 °C (Fig. 10 Chapter 3)
Zr–in–titanite temperature (±25 °C)	Titanite from Opx–granulite 810 °C (Fig. 19)	N/A	c. 750 °C to 440 Ma dropping to 700 °C by 380 Ma
Thermodynamic model			725 ± 25 °C 5.5 ± 0.5 kbar
High–temperature period (U-Pb ages)	500–440 Ma (zircon and monazite) (Wolfram et al., 2019)	500–440 Ma (zircon and monazite, this study) One sample with peak at 407.5 ± 2.3 Ma	500–380 Ma (zircon, monazite and titanite, Chapter 3)

5.2 Stability of geochronometers in migmatites

How did zircon, monazite, and titanite react to the long metamorphic and deformation history? The stability of these accessory phases in migmatites depends mainly on temperature and the bulk composition of the rock. During prograde metamorphism, and once the temperature crosses the solidus, detrital zircon and monazite will start dissolving and will reprecipitate when the rock cools down (Kelsey et al., 2008; Yakymchuk and Brown, 2014). The rate of zircon and monazite dissolution–reprecipitation depends on the available Zr or LREE in the melt with which they interact (Fraser et al., 1997; Kelsey et al., 2008; Rapp et al., 1987; Rapp and Watson, 1986; Watson, 1996; Watson and Harrison, 1983; Wolf and London, 1995; Yakymchuk and Brown, 2014). This available Zr or LREE is referred in Kelsey (2008) to as “effective Zr or LREE content” respectively, which is usually less than the total Zr or LREE content in the rock.

According to the thermodynamic model of Kelsey (2008), a rock with c. 170–200 ppm Zr, like our diatexites (Appendix 1), that experience a maximum temperature of 800 °C, will result in partial zircon dissolution. Its complete dissolution in the model would occur only be between 850–900 °C. Hence this thermodynamic model matches our rocks with partially dissolved detrital zircon with metamorphic rims.

Unlike zircon, monazite is expected to be completely dissolved at those conditions. The thermodynamic models of Kelsey (2008) and Yakymchuk (2014), based on a rock with less than 170 ppm LREE, like our rocks, that experiences peak temperatures between 700–800 °C will result in complete monazite dissolution. This would lead to resetting all pre–Famatinian monazites. However, there are several cases where monazite has remained stable during such high temperatures. For example, there are cases where monazite is protected from reactive melt or fluids in stable peritectic garnet and feldspar (Collins et al., 2014; Taylor et al., 2016; Turlin et al., 2018), or cases where the gradual release of LREE from the break–up of other minerals like apatite, allanite, and xenotime modulates the effective LREE content (Johnson et al., 2015; Korhonen et al., 2013; Rossi et al., 2006; Weinberg et al., 2020). In the Tolombon complex of the Sierra de Quilmes, it has been postulated that monazite remained stable for c. 60 Myr time in the HT–LP migmatites and peraluminous granites (Weinberg et al., 2020). These authors argued that the preferential dissolution of apatite during anatexis maintained a high budget of LREE in melts and kept monazite saturated (Johnson et al., 2015; Wolf and London, 1995) and limited its dissolution, even under temperatures at which monazite is expected to be dissolved (Kelsey et al., 2008; Yakymchuk and Brown, 2014). In a recent work Yakymchuk (2019) postulated that monazite can remain stable in granulites, as the dissolution kinematics is far slower than previously thought, hence monazite would survive high-temperature metamorphism and melting for longer.

The stability of titanite depends on temperature, pressure and the CaO and Ti content of the rock (Carswell et al., 1996; Corfu et al., 1994; Dasgupta, 1993; Enami et al., 1993; Frost et al., 2001; Kohn, 2017; Mezger et al., 1993; Santos Zalduegui et al., 1996). High Ca and Ti tend to stabilize titanite in high–grade rocks (Kohn, 2017). In metamorphic rocks with felsic–intermediate compositions (e.g, a metadacite with 2.5–4 % CaO (Spencer et al., 2013), titanite is stable in intermediate P–T conditions (c. 500–800 °C, and 5–15 kbar), between rutile that is stable in higher pressure and ilmenite stable at lower pressures (Fig. 7a, in (Kohn, 2017). In calc–silicates with 20–25 % CaO (Cottle et al., 2011) titanite is stable well into granulite facies (Kohn, 2017). Our titanite–bearing rocks have c. 3–5 % CaO and 11 % CaO for the amphibolite (Appendix 1), which is in between the mentioned models, but closer to the first one. Therefore we should expect titanite stable at peak metamorphic conditions. In summary, all three accessory phases have the potential to remain stable during the peak metamorphic conditions detailed above.

As mentioned before, closure temperature (T_c) or blocking temperature for a specific isotope, refers to the temperature at which a mineral has cooled so that diffusion of the isotope becomes negligible in a particular mineral (Braun et al., 2006; Rollinson, 1995; Turekian and Holland, 2013). However, as Cherniak (1993) stated: “closing temperature calculated by laboratory experiments apply over a narrowly defined range of conditions, usually under dry conditions.” As we discussed in Chapter 3, the effect of factors like mineral strain (Gasser et al., 2015; Kovaleva et al., 2017; Reddy et al., 2006), radiation damage and metamictization (Cherniak, 2010; Cherniak and Watson, 2001), or fluid–mineral interaction (Cherniak et al., 2004; Harlov and Hetherington, 2010; Schoene, 2014; Taylor et al., 2016), is that T_c covers a range of temperatures rather than a single value. In Chapter 3, we concluded that all three geothermometers have T_c higher than the peak metamorphic temperature, indicating that their U-Pb age reflects the time of mineral growth rather than the cooling ages.

5.3 Different behaviors of geochronometers during the long–lived Famatinian event

As mentioned in section 2.3, the geochronological results from the Tolombon (Finch et al., 2017; Wolfram et al., 2017; Wolfram et al., 2019) and Agua del Sapo complex (Chapter 3) suggest that the Famatinian high–temperatures extended from c. 500 Ma to 440 Ma, continuing for another 60 Myr in the footwall Agua del Sapo complex, as it started cooling after 440 Ma at a rate of c. 1 °C/Ma. In this chapter we found that titanite from the Tolombon complex also formed during peak metamorphism, between 475–445 Ma (lower intercept at 457.3 ± 1.9 Ma), and that the Tolombon West complex, have zircon (Fig. 5 and 6) and monazite (Fig. 11) that yields the same 500–440 Ma ages as the other complexes, except for the one sheared sample the also yielded a peak at c. 407 Ma (Fig. 11). With this background summarized in Fig. 17, we can now compare and discuss the variable behaviour of the geochronometers in the different metamorphic complexes.

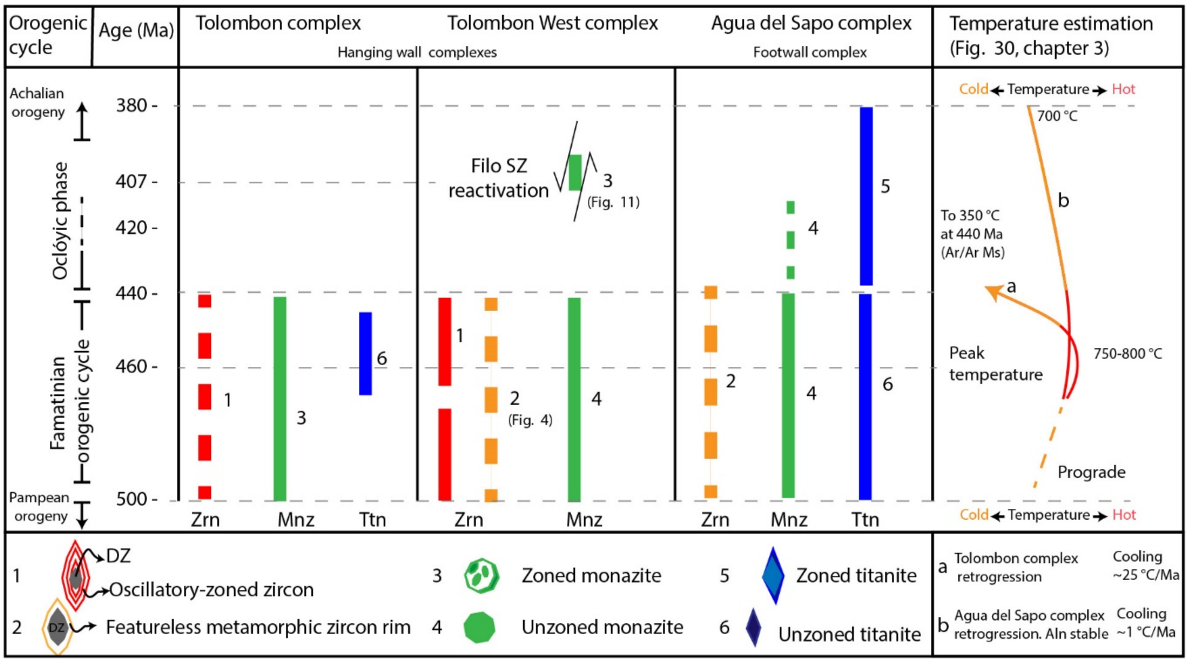

Figure 17– Zircon, monazite, and titanite age ranges. In the Tolombon complex, zircon yield up to five peak ages, that in total span the entire Famatinian orogeny (Wolfram et al., 2019). Zoned monazite yield a continuum of ages in the same age range as zircon. In the Tolombon West oscillatory–zoned zircon are common in the sheared diatexite (LC–065), while metamorphic rims are typical in all other diatexites. Zoned, high–REE c. 407 Ma monazite is found in the sheared diatexite LC–065. In the Agua del Sapo complex the record of ages extends to 380 Ma in titanite, and until c. 420 Ma in some monazite sample (Chapter 3). The temperature estimates and cooling rate for the hanging wall Tolombon complex are from descriptions of metamorphism and Ar–Ar ages of muscovite (Büttner et al., 2005). The slow cooling of the footwall Agua del Sapo complex after 440 Ma is from Zr–in–titanite (Chapter 3).

Zircon

Zircon from the granulite–facies Tolombon complex yielded Famatinian U-Pb ages represented by new euhedral grains with dominantly oscillatory–zoned textures in both core and rims (Wolfram et al., 2019). The Famatinian zircon ages range from 505 to 440 Ma with up to five discrete peaks every 10–15 Myr. In the Tolombon West complex, zircon presents a similar age range but with different internal textures (Fig. 4). In the western diatexites, Famatinian dates are found in featureless metamorphic rims around detrital cores, while in the sheared diatexite near the Filo shear zone

Famatinian dates are mainly associated with oscillatory–zoned textures and Th/U ratios > 0.1 commonly associated with igneous zircon (Rubatto, 2002; Taylor et al., 2016; Yakymchuk et al., 2018). In the migmatites of the Agua del Sapo complex, Famatinian zircon dates are from thin, featureless metamorphic rims cored by detrital zircon.

The multiple zircon age groups identified in the Tolombon complex were not resolved in the other complexes as the lower temperatures there were insufficient to partially dissolve detrital zircon and reprecipitate as metamorphic rims. It is possible that they do not record multiple date groups because of the lower temperature and lower zircon reactivity with small melt volumes formed only narrow rims, that were either not dated or mixed together. The entirely new oscillatory–zoned Famatinian zircon on the sheared diatexite (LC–065) suggest that this area either went through higher temperatures, as the Zr content is similar to the diatexites with metamorphic zircon rims, or the dissolution–reprecipitation process was assisted by shearing.

Monazite

In the Tolombon complex, the monazite yields the same age range than zircon (c. 500–440 Ma) (Weinberg et al., 2020). The monazite is compositionally zoned (Fig. 9c), but those zones are unrelated to age zones. Weinberg (2020) argued that monazite was formed at c. 500–490 Ma early in the orogenic cycle and remained stable during peak metamorphic conditions, as dissolution of apatite in the melt (Johnson et al., 2015; Wolf and London, 1995) kept the rock saturated in LREE. In a recent work Yakymchuk (2019) concludes that monazite can survive in residual granulites, at higher temperatures than previously calculated when assisted by percolating upward melt. Monazite went through one or several coupled dissolution–reprecipitation events (Kirkland et al., 2016; Seydoux-Guillaume et al., 2003; Seydoux-Guillaume et al., 2002; Weinberg et al., 2020) that could be as young as c. 440 Ma, and gave rise to new monazite that inherited radiogenic Pb from the pre–

existing grains, thus yielding dates older than 440 Ma with no geological significance. The dissolution-precipitation occurred above, or close to the solidus as it needs interaction with the melt (Weinberg et al., 2020). We assume that the same mechanism acted over monazite in the other complexes, and the mixing of Pb–rich zones resulted in the spread of dates.

The spread of dates varies in different rocks. In the Tolombon West, in the western diatexites, monazite dates spread between c. 455–475 Ma (c. 20 Myr). The monazite from the sheared diatexites near the Filo shear zone has a much wider date distribution (c. 440–500 Ma) with ill–defined peaks (Fig. 10a), and with a distinctive population of zoned monazite grains that yield a much younger date (c. 407 Ma). In the Agua del Sapo complex, all monazite dates are concentrated around c. 460 Ma, but their range is variable (Chapter 3). For example, monazite from two of the samples (a diatexite and a leucosome) yielded dates in the range of c. 440–470 Ma (c. 30 Myr), and the other two migmatites (metatexites) yielded a broader distribution of c. 60 Myr. In Chapter 3 (section 4.4) we argued that this difference can be attributed to the rock fabric, as the finer–grained and more foliated rock was more fertile for monazite formation across the entire thermal event than the coarse–grained rock where monazite has increased likelihood to be locked within larger grains of quartz or feldspar (Turlin et al., 2018). The same concept can be applied to the monazite in diatexites of the Tolombon West complex, as sheared and foliated diatexite samples LC–065 and LC–066 yield wider date ranges than the non–foliated samples SQ17–076 and SQ17–088 (Fig. 19a).

Some samples have ill–defined multiple peaks (LC–065, LC–066, LC–019, SM–003) while the monazite samples in the Tolombon complex, have a unimodal distribution of dates (Fig. 19a). We suggest that the difference is due to the size of the Pb–rich domains. Recently Seydoux-Guillaume (2019) found that in a protracted HT environment, the radiogenic Pb of monazite is clustered within the grain at the nano–scale, resulting in 50–150 nm Pb–rich clusters hosted in the monazite matrix that remains open, feeding the clusters, until the monazite cools below c. 700 °C. Regardless of this internal reorganization of the radiogenic Pb, the grain remains a closed system during the entire HT event (Fig. 18). In monazite of the Sierra de Quilmes, we should expect to mix age zones as the analytical spot is larger than such Pb–rich micro–domains. Therefore the difference between the unimodal distribution of ages in monazites from the Tolombon complex and the polymodal and ill–defined age peaks of the monazites from the Tolombon West could be because of a difference in the size of these Pb–rich micro–domains or their heterogeneous distribution. Figure 20b depicts the concept. The monazites in the granulite–facies Tolombon complex could have smaller age domains than in the other complexes and therefore increased chances that the analytical spot mixes different domains, resulting in a single average value. An alternative explanation for the multiple age peaks is that drainage melt could have percolated in different pulses that could trigger monazite crystallization events (Yakymchuk and Brown, 2019).

Regardless of the ill-defined peaks and differences in age range between samples, they all represent a significant spread of dates that most likely reflect the protracted Famatinian metamorphism. As explained in Chapter 3, this spread of dates could reflect the monazite formation during the prograde and retrograde paths. We envisage the old prograde monazite being locked from the reactive protracted HT environment in garnet of feldspar, but further petrochronology study is required to establish this.

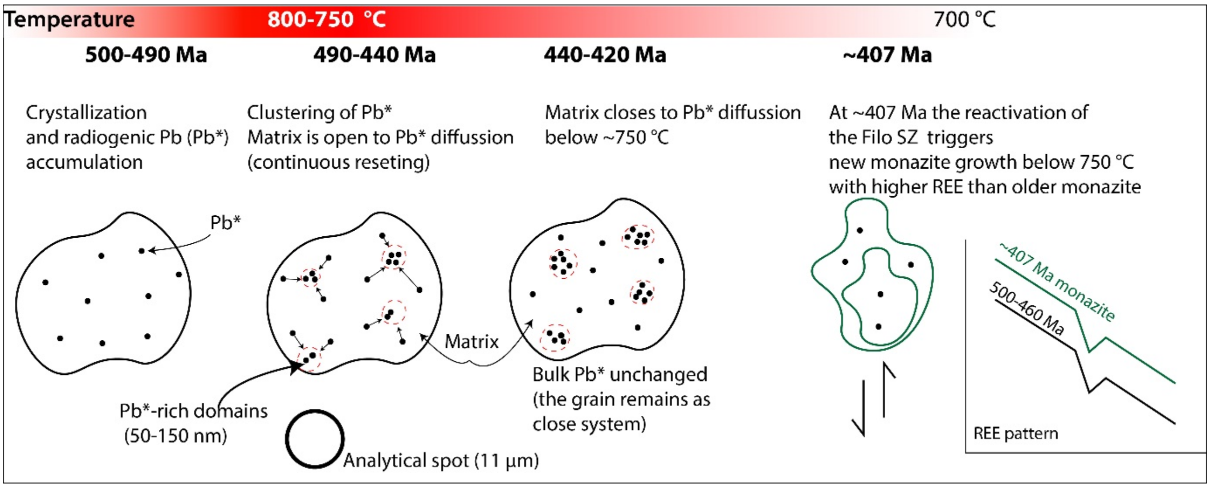

Figure 18– Modified from Seydoux-Guillaume (2019). Illustration of the possible evolution of Pb clusters in monazite during 100 Myr of high–temperatures in Sierra de Quilmes. Mixed ages are expected as the analytical spot is larger than the Pb–rich microdomains.

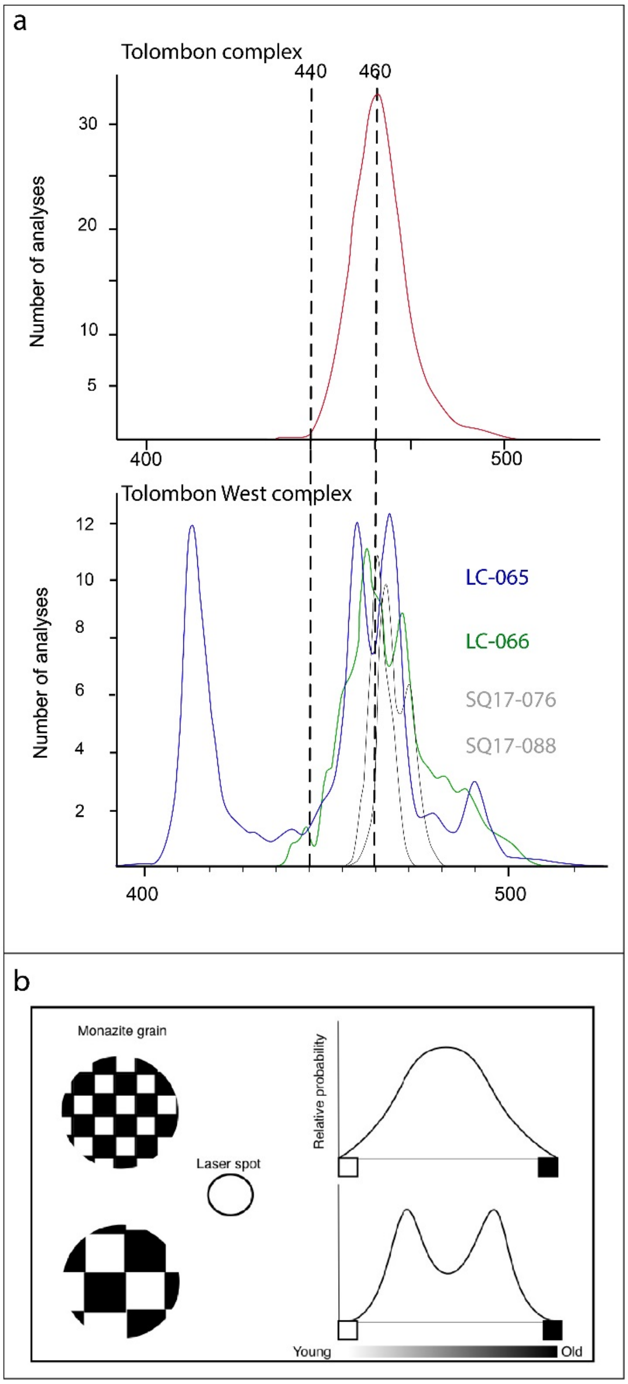

Figure 19– a) Probability diagram of monazite ages from sample SQ231a in Tolombon complex (Weinberg et al., 2020), and from Tolombon West complex. They all yield ages ranging 500–440 Ma (except for the c. 407 Ma peak), but Tolombon West monazites have multiple ill–defined peaks. The difference could be the size of the age domains in monazite in (b), for a fixed size of laser spot. The LA–ICP–MS spot size used in samples of the Tolombon and Tolombon West is similar (10 and 11 µm, respectively)

The younger monazite date (c. 407 Ma) is from zoned high–REE monazite in the sheared diatexite LC–065, near the Filo shear zone. This diatexite sample have also unzoned monazite in the range 500–440 Ma, similar to the other samples in the Tolombon West complex. This suggests that shearing played a role in the formation of these young monazite grains, but it was not enough to reset the entire monazite population in the sample. From microstructural analysis of the Filo shear zone (Chapter 2), we concluded that it was a long–lived structure, active in the temperature range of 700–500 °C and reactivated or continuous shearing during metamorphic retrogression as indicated by the sheared epidote–allanite, and late muscovite.

Zircon and most of the monazite stopped forming at 440 Ma in sample LC–065, suggesting a temperature drop. Also, the nearby Agua del Sapo complex was over 700 °C until 380 Ma. Therefore we can assume that LC–065 diatexite was probably sheared in amphibolite to greenschist facies at that time. Mid–crustal shearing is commonly associated with fluids (Fossen and Cavalcante, 2017), that can redistribute elements, including LREE (Rolland et al., 2003). This shearing could have triggered the formation of new monazite grains in specific areas within the sample, or reset the pre–existing grains. Fluid–related coupled dissolution–reprecipitation can completely reset the U-Pb age of monazite below its closure temperature (Williams et al., 2011) resulting in complexly zoned monazites (Harlov and Hetherington, 2010; Taylor et al., 2014) like in our case (Fig. 10). We conclude that: a) the Filo shear zone was reactivated at c. 407 Ma at amphibolite facies, and b) monazite in HT–LP terranes, can be reset in active shear zones at amphibolite facies.

Titanite

In the Tolombon complex, the unzoned titanite yield dates between 480–440 Ma, with a lower intercept at 457.3 ± 1.9 Ma (Fig. 14). Titanite, like monazite and zircon, was closed after 440 Ma, possibly due to cooling related to thrusting (Chapter 2). Unlike the Tolombon complex, the footwall

Agua del Sapo complex remained hot for longer allowing continued growth of titanite after 440 Ma for another 60 Myr, during the slow cooling of the rocks, and recording the formation of allanite. The protracted high–temperature and slow cooling from 750 to 700 °C, combined with the post–anatectic top–to–south shearing (Chapter 2) triggered the growth of titanite below its closure temperature during that time. There are similar cases of shear–assisted titanite formation. Gasser (2015) reported protracted titanite formation assisted by retrograde shearing in the Kalal Nappe Complex, in Norway. Also, Lucassen (2003) reported a similar case in the Western Sierras Pampeanas, in a Famatinian migmatitic terrane, where deformation–enhanced recrystallization of titanite at temperature > 650 °C resulted in a semi–continuous titanite formation between 470–420 Ma. In conclusion, our study shows that titanite can continuously form if the temperature is sustained over 650–700 °C, and most likely assisted by deformation.

6 Conclusion

The new geochronological data in combination with previous work in the Sierra de Quilmes gave us a better understanding of the tectono–thermal evolution of the terrane. We found that the geochronometers reacted differently to the protracted HT–LP Famatinian orogeny. Entirely new zircon grains grew in the Tolombon complex where temperatures were above 800 °C. They record multiple ages peaks between 500–440 Ma associated with discrete melting events with a recurrence of 10–15 Myr (Wolfram et al., 2019). Similarly, in the sheared diatexite of the Tolombon West complex, new zircon grains grew with CL oscillatory textures and Th/U > 0.1 typical of igneous zircons. In all other locations, where the temperature reached a maximum of 750 °C, only metamorphic rims grew over partially dissolved detrital zircon.

Monazite in the Tolombon complex is zoned, and the zones are decoupled from the U-Pb dates. The dates range between c. 60–30 Myr in all complexes because of coupled dissolution–precipitation that perturbed the U-Pb systematics during the long–lived high–temperatures. In the Tolombon West and Agua del Sapo complexes monazite is unzoned, and the different date ranges seem to reflect differences in the rock fabric. Typically narrower age ranges are associated with unfoliated coarse–grained leucosomes and granite. Also, monazite in the Tolombon complex may have smaller or more homogeneously distributed radiogenic Pb–rich microdomains than in the lower temperature complexes. We found that amphibolite facies shearing in the Filo shear zone triggered the formation of new high–REE and zoned monazite grains in some parts of the sample or partially reset pre–existing ones at c. 407 Ma.

Titanite formed during peak metamorphism between c. 480–440 Ma, and continued forming new grains for another c. 60 Myr during the protracted retrogression and cooling of the footwall Agua del Sapo complex down to 700 °C. This was probably assisted by protracted retrograde shearing. This suggests that titanite can continuously grow below its closure temperature in structurally active terranes if the temperature is maintained over >700 °C, well after monazite and zircon become inactive.

This work combined the results of three different geochronometers that indicate sustained temperatures above 700 °C for over 120 Mys in the mid–crustal sections of the back–arc of the Famatinian Orogen. We argue that the geochronometers changed their behaviour and the nature of their time record, mostly due to differences in temperature. However, each rock sample preserves a wide and unpredictable time record. This reflects mechanisms beyond temperature, such as rock fabric and deformation, as well as the distribution of grains. Thus, analyses of various phases from different samples are the most efficient way to obtain the broadest most accurate record of the evolution of a terrane.

References

Aceñolaza, F. G., Miller, H., and Toselli, A. J., 2002, Proterozoic - Early Paleozoic evolution in western South America - A discussion: Tectonophysics, v. 354, p. 121-137.

Aceñolaza, F. G., and Toselli, A., 2009, Chapter 6 The Pampean Orogen: Ediacaran-Lower Cambrian Evolutionary History of Central and Northwest Region of Argentina, Developments in Precambrian Geology, 16, p. 239-254.

Astini, R., 2008, Sedimentación, facies, discordancias y evolución paleoambiental durante el Cambro-Ordovícico, Revista de la Asociacion Geologica Argentina, 50-73 p.

Astini, R. A., 1998, Stratigraphical evidence supporting the rifting, drifting and collision of the Laurentian Precordillera terrane of western Argentina.: The Geological Society.

Astini, R. A., and Dávila, F. M., 2004, Ordovician back arc foreland and Ocloyic thrust belt development on the western Gondwana margin as a response to Precordillera terrane accretion: Tectonics, v. 23, p. TC4008 1-19.

Bahlburg, H., Berndt, J., and Gerdes, A., 2016, The ages and tectonic setting of the Faja Eruptiva de la Puna Oriental, Ordovician, NW Argentina: Lithos, v. 256-257, p. 41-54.

Bahlburg, H., and Breitkreuz, C., 1991, Paleozoic evolution of active margin basins in the southern Central Andes (northwestern Argentina and northern Chile): Journal of South American Earth Sciences, v. 4, p. 171-188.

Bahlburg, H., and Hervé, F., 1997a, Geodynamic evolution and tectonostratigraphic terranes of northwestern Argentina and northern Chile: Bulletin of the Geological Society of America, v. 109, p. 869-884.

Bahlburg, H., and Hervé, F., 1997b, Geodynamic evolution and tectonostratigraphic terranes of northwestern Argentina and northern Chile: Geological Society of America Bulletin, v. 109, p. 869-884.

Braun, J., Van Der Beek, P., and Batt, G., 2006, Quantitative thermochronology: Numerical methods for the interpretation of thermochronological data, 1-258 p.

Büttner, S. H., 2009, The Ordovician Sierras Pampeanas–Puna basin connection: Basement thinning and basin formation in the Proto-Andean back-arc: Tectonophysics, v. 477, p. 278-291.

Büttner, S. H., Glodny, J., Lucassen, F., Wemmer, K., Erdmann, S., Handler, R., and Franz, G., 2005, Ordovician metamorphism and plutonism in the Sierra de Quilmes metamorphic complex: Implications for the tectonic setting of the northern Sierras Pampeanas (NW Argentina): Lithos, v. 83, p. 143-181.

Carswell, D. A., Wilson, R. N., and Zhai, M., 1996, Ultra-high pressure aluminous titanites in carbonate-bearing eclogites at Shuanghe in Dabieshan, central China: Mineralogical Magazine, v. 60, p. 461-471.

Catlos, E. J., Baker, C., Sorensen, S. S., Çemen, I., and Hançer, M., 2010, Geochemistry, geochronology, and cathodoluminescence imagery of the Salihli and Turgutlu granites (central Menderes Massif, western Turkey): Implications for Aegean tectonics: Tectonophysics, v. 488, p. 110-130.

Cawood, P. A., 2005, Terra Australis Orogen: Rodinia breakup and development of the Pacific and Iapetus margins of Gondwana during the Neoproterozoic and Paleozoic: Earth-Science Reviews, v. 69, p. 249-279.

Cherniak, D. J., 1993, Lead diffusion in titanite and preliminary results on the effects of radiation damage on Pb transport: Chemical Geology, v. 110, p. 177-194.

Cherniak, D. J., 2010, Diffusion in accessory minerals: Zircon, titanite, apatite, monazite and xenotime, Reviews in Mineralogy and Geochemistry, 72, p. 827-869.

Cherniak, D. J., and Watson, E. B., 2001, Pb diffusion in zircon: Chemical Geology, v. 172, p. 5-24.
Cherniak, D. J., Watson, E. B., Grove, M., and Harrison, T. M., 2004, Pb diffusion in monazite: A combined RBS/SIMS study: Geochimica et Cosmochimica Acta, v. 68, p. 829-840.
Collins, A. S., Clark, C., and Plavsa, D., 2014, Peninsular India in Gondwana: The tectonothermal evolution of the Southern Granulite Terrain and its Gondwanan counterparts: Gondwana Research, v. 25, p. 190-203.
Collo, G., Astini, R. A., Cawood, P. A., Buchan, C., and Pimentel, M., 2009, U-Pb detrital zircon ages and Sm-Nd isotopic features in low-grade metasedimentary rocks of the Famatina belt: implications for late Neoproterozoic-early Palaeozoic evolution of the proto-Andean margin of Gondwana: Journal of the Geological Society, v. 166, p. 303-319.
Corfu, F., Heaman, L. M., and Rogers, G., 1994, Polymetamorphic evolution of the Lewisian complex, NW Scotland, as recorded by U-Pb isotopic compositions of zircon, titanite and rutile: Contributions to Mineralogy and Petrology, v. 117, p. 215-228.
Cottle, J. M., Waters, D. J., Riley, D., Beyssac, O., and Jessup, M. J., 2011, Metamorphic history of the South Tibetan Detachment System, Mt. Everest region, revealed by RSCM thermometry and phase equilibria modelling: Journal of Metamorphic Geology, v. 29, p. 561-582.
Dasgupta, S., 1993, Contrasting mineral parageneses in high‐temperature calc‐silicate granulites: examples from the Eastern Ghats, India: Journal of Metamorphic Geology, v. 11, p. 193-202.
Davila, F. M., Astini, R. A., and Schmidt, C. J., 2003, Unraveling 470 m.y. of shortening in the Central Andes and documentation of Type O superposed folding: Geology, v. 31, p. 275-278.
Decelles, P. G., Ducea, M. N., Kapp, P., and Zandt, G., 2009, Cyclicity in Cordilleran orogenic systems: Nature Geoscience, v. 2, p. 251-257.
Dodson, M. H., 1973, Closure temperature in cooling geochronological and petrological systems: Contributions to Mineralogy and Petrology, v. 40, p. 259-274.
Drobe, M., López de Luchi, M. G., Steenken, A., Frei, R., Naumann, R., Siegesmund, S., and Wemmer, K., 2009, Provenance of the late Proterozoic to early Cambrian metaclastic sediments of the Sierra de San Luis (Eastern Sierras Pampeanas) and Cordillera Oriental, Argentina: Journal of South American Earth Sciences, v. 28, p. 239-262.
Enami, M., Suzuki, K., Liou, J. G., and Bird, D. K., 1993, Al-Fe3+ and F-OH substitutions in titanite and constraints on their P-T dependence: European Journal of Mineralogy, v. 5, p. 219-231.
Escayola, M. P., van Staal, C. R., and Davis, W. J., 2011, The age and tectonic setting of the Puncoviscana Formation in northwestern Argentina: An accretionary complex related to Early Cambrian closure of the Puncoviscana Ocean and accretion of the Arequipa-Antofalla block: Journal of South American Earth Sciences, v. 32, p. 438-459.
Finch, M. A., Weinberg, R. F., Fuentes, M. G., Hasalová, P., and Becchio, R., 2015, One kilometre-thick ultramylonite, Sierra de Quilmes, Sierras Pampeanas, NW Argentina: Journal of Structural Geology, v. 72, p. 33-54.
Finch, M. A., Weinberg, R. F., Hasalová, P., Becchio, R., Fuentes, M. G., and Kennedy, A., 2017, Tectono-metamorphic evolution of a convergent back-arc: The Famatinian orogen, Sierra de Quilmes, Sierras Pampeanas, NW Argentina: Bulletin of the Geological Society of America, v. 129, p. 1602–1621.
Flowers, R. M., Bowring, S. A., Tulloch, A. J., and Klepeis, K. A., 2005, Tempo of burial and exhumation within the deep roots of a magmatic arc, Fiordland, New Zealand: Geology, v. 33, p. 17-20.
Fossen, H., and Cavalcante, G. C. G., 2017, Shear zones – A review: Earth-Science Reviews, v. 171, p. 434-455.
Fraser, G., Ellis, D., and Eggins, S., 1997, Zirconium abundance in granulite-facies minerals, with implications for zircon geochronology in high-grade rocks, 607-610 p.

Frost, B. R., Chamberlain, K. R., and Schumacher, J. C., 2001, Sphene (titanite): Phase relations and role as a geochronometer: Chemical Geology, v. 172, p. 131-148.

Gao, X. Y., Zheng, Y. F., Chen, Y. X., and Guo, J., 2012, Geochemical and U-Pb age constraints on the occurrence of polygenetic titanites in UHP metagranite in the Dabie orogen: Lithos, v. 136-139, p. 93-108.

Gasser, D., Jeřábek, P., Faber, C., Stünitz, H., Menegon, L., Corfu, F., Erambert, M., and Whitehouse, M. J., 2015, Behaviour of geochronometers and timing of metamorphic reactions during deformation at lower crustal conditions: Phase equilibrium modelling and U-Pb dating of zircon, monazite, rutile and titanite from the Kalak Nappe Complex, northern Norway: Journal of Metamorphic Geology, v. 33, p. 513-534.

Gehrels, G., 2014, Detrital zircon U-Pb geochronology applied to tectonics, Annual Review of Earth and Planetary Sciences, 42, p. 127-149.

Harlov, D. E., and Hetherington, C. J., 2010, Partial high-grade alteration of monazite using alkali-bearing fluids: Experiment and nature: American Mineralogist, v. 95, p. 1105-1108.

Hayden, L. A., Watson, E. B., and Wark, D. A., 2008, A thermobarometer for sphene (titanite): Contributions to Mineralogy and Petrology, v. 155, p. 529-540.

Hetherington, C. J., Harlov, D. E., and Budzyń, B., 2010, Experimental metasomatism of monazite and xenotime: Mineral stability, REE mobility and fluid composition: Mineralogy and Petrology, v. 99, p. 165-184.

Johnson, T. E., Clark, C., Taylor, R. J. M., Santosh, M., and Collins, A. S., 2015, Prograde and retrograde growth of monazite in migmatites: An example from the Nagercoil Block, southern India: Geoscience Frontiers, v. 6, p. 373-387.

Kelsey, D. E., Clark, C., and Hand, M., 2008, Thermobarometric modelling of zircon and monazite growth in melt-bearing systems: Examples using model metapelitic and metapsammitic granulites: Journal of Metamorphic Geology, v. 26, p. 199-212.

Kirkland, C. L., Erickson, T. M., Johnson, T. E., Danišík, M., Evans, N. J., Bourdet, J., and McDonald, B. J., 2016, Discriminating prolonged, episodic or disturbed monazite age spectra: An example from the Kalak Nappe Complex, Arctic Norway: Chemical Geology, v. 424, p. 96-110.

Kohn, M. J., 2017, Titanite Petrochronology: Reviews in Mineralogy and Geochemistry, v. 83, p. 419-441.

Kohn, M. J., and Corrie, S. L., 2011, Preserved Zr-temperatures and U-Pb ages in high-grade metamorphic titanite: Evidence for a static hot channel in the Himalayan orogen: Earth and Planetary Science Letters, v. 311, p. 136-143.

Kohn, M. J., Wieland, M. S., Parkinson, C. D., and Upreti, B. N., 2005, Five generations of monazite in Langtang gneisses: Implications for chronology of the Himalayan metamorphic core: Journal of Metamorphic Geology, v. 23, p. 399-406.

Korhonen, F. J., Clark, C., Brown, M., Bhattacharya, S., and Taylor, R., 2013, How long-lived is ultrahigh temperature (UHT) metamorphism? Constraints from zircon and monazite geochronology in the Eastern Ghats orogenic belt, India: Precambrian Research, v. 234, p. 322-350.

Kovaleva, E., Klötzli, U., Habler, G., Huet, B., Guan, Y., and Rhede, D., 2017, The effect of crystal-plastic deformation on isotope and trace element distribution in zircon: Combined BSE, CL, EBSD, FEG-EMPA and NanoSIMS study: Chemical Geology, v. 450, p. 183-198.

Larrovere, M. A., Alasino, P. H., and Baldo, E. G., 2016, The double-vergent ductile shear zone of northwestern sierra de Velasco: Deformation of the middle crust during the Famatinian orogeny: Revista de la Asociacion Geologica Argentina, v. 73, p. 117-133.

Larrovere, M. A., de los Hoyos, C. R., Toselli, A. J., Rossi, J. N., Basei, M. A. S., and Belmar, M. E., 2011, High T/P evolution and metamorphic ages of the migmatitic basement of northern

Sierras Pampeanas, Argentina: Characterization of a mid-crustal segment of the Famatinian belt: Journal of South American Earth Sciences, v. 31, p. 279-297.
Lucassen, F., and Becchio, R., 2003, Timing of high-grade metamorphism: Early Palaeozoic U-Pb formation ages of titanite indicate long-standing high-T conditions at the western margin of Gondwana (Argentina, 26-29°S): Journal of Metamorphic Geology, v. 21, p. 649-662.
Lucassen, F., Becchio, R., and Franz, G., 2011, The early Palaeozoic high-grade metamorphism at the active continental margin of West Gondwana in the Andes (NW Argentina/N Chile): International Journal of Earth Sciences, v. 100, p. 445-463.
Lucassen, F., Becchio, R., Wilke, H. G., Franz, G., Thirlwall, M. F., Viramonte, J., and Wemmer, K., 2000, Proterozoic-Paleozoic development of the basement of the Central Andes (18-26°S) - A mobile belt of the South American craton: Journal of South American Earth Sciences, v. 13, p. 697-715.
Ludwig, K. R., 2003a, Mathematical-statistical treatment of data and errors for230Th/U geochronology, Reviews in Mineralogy and Geochemistry, 52.
Ludwig, K. R., 2003b, User's Manual for Isoplot/Ex rev. 3.00: A Geochronological Toolkit for Microsoft Excel.
Mattinson, J. M., 1978, Age, origin, and thermal histories of some plutonic rocks from the Salinian block of California: Contributions to Mineralogy and Petrology, v. 67, p. 233-245.
Mezger, K., Essene, E. J., van der Pluijm, B. A., and Halliday, A. N., 1993, U-Pb geochronology of the Grenville Orogen of Ontario and New York: constraints on ancient crustal tectonics: Contributions to Mineralogy and Petrology, v. 114, p. 13-26.
Moya, M., 2015, La Fase Ocloyica (Ordovicico Superior) en el noroeste argentino. Interpretacion historica y evidencias en contrario: Serie Correlacion Geologica, v. 3, p. 73-110.
Mulcahy, S. R., Roeske, S. M., McClelland, W. C., Ellis, J. R., Jourdan, F., Renne, P. R., Vervoort, J. D., and Vujovich, G. I., 2014, Multiple migmatite events and cooling from granulite facies metamorphism within the Famatina arc margin of northwest Argentina: Tectonics, v. 33, p. 1-25.
O'Neill, H. S. C., 2016, The smoothness and shapes of chondrite-normalized rare earth element patterns in basalts: Journal of Petrology, v. 57, p. 1463-1508.
Omarini, R. H., Sureda, R. J., Götze, H. J., Seilacher, A., and Pflüger, F., 1999, Puncoviscana folded belt in northwestern Argentina: Testimony of Late Proterozoic Rodinia fragmentation and pre-Gondwana collisional episodes: International Journal of Earth Sciences, v. 88, p. 76-97.
Pankhurst, R. J., Rapela, C. W., and Fanning, C. M., 2000, Age and origin of coeval TTG, I- and S-type granites in the Famatinian belt of NW Argentina, Special Paper of the Geological Society of America, 350, p. 151-168.
Ramos, V. A., 2004, Cuyania, an exotic block to Gondwana: Review of a historical success and the present problems: Gondwana Research, v. 7, p. 1009-1026.
Ramos, V. A., 2008, The basement of the Central Andes: The arequipa and related terranes, *in* Jeanloz, R., Albee, A. L., Burke, K. C., and Freeman, K. H., eds., Annual Review of Earth and Planetary Sciences, 36, p. 289-324.
Ramos, V. A., Dallmeyer, R. D., and Vujovich, G., 1998, Time constraints on the Early Palaeozoic docking of the Precordillera, central Argentina, Geological Society Special Publication, 142, p. 143-158.
Ramos, V. A., Escayola, M., Mutti, D. I., and Vujovich, G. I., 2000, Proterozoic-early Paleozoic ophiolites of the Andean basement of southern South America, Special Paper of the Geological Society of America, 349, p. 331-349.
Ramos, V. A., Jordan, T. E., Allmendinger, R. W., Mpodozis, C., Kay, S. M., Cortés, J. M., and Palma, M., 1986, Paleozoic terranes of the central Argentine-Chilean Andes: Tectonics, v. 5, p. 855-880.

Ramos, V. A., Vujovich, G., Martino, R., and Otamendi, J., 2010, Pampia: A large cratonic block missing in the Rodinia supercontinent: Journal of Geodynamics, v. 50, p. 243-255.
Rapela, C., Pankhurst, R., Casquet, C., A. Dahlquist, J., Mark Fanning, C., G. Baldo, E., Galindo, C., Alasino, P., Ramacciotti, C., Verdecchia, S., Murra, J., and Basei, M., 2018, A review of the Famatinian Ordovician magmatism in southern South America: Evidence of lithosphere reworking and continental subduction in the early proto-Andean margin of Gondwana.
Rapela, C. W., 1976a, El Basamento Metamorfico de la Region de Cafayate, Provincia de Salta. Aspectos Petrologicos y Geoquimicos: Revista de la Asociacion Geologica Argentina, v. 3, p. 203-222.
Rapela, C. W., 1976b, Las Rocas Granitoides de la Region de Cafayate, Provincia de Salta. Aspectos Petrologicos y Geoquimicos: Revista de la Asociacion Geologica Argentina, v. 4, p. 260-278.
Rapela, C. W., Pankhurst, R. J., Casquet, C., Baldo, E., Saavedra, J., and Galindo, C., 1998a, Early evolution of the Proto-Andean margin of South America: Geology, v. 26, p. 707.
Rapela, C. W., Pankhurst, R. J., Casquet, C., Baldo, E., Saavedra, J., Galindo, C., and Fanning, C. M., 1998b, The Pampean Orogeny of the southern proto-Andes: Cambrian continental collision in the Sierras de Cordoba: Geological Society, London, Special Publications, v. 142, p. 181-217.
Rapela, C. W., Pankhurst, R. J., Saavedra, J., and Galindo, C., 1998c, Early evolution of the proto-andean margin of South America: Geology, v. 26, p. 707-710.
Rapela, C. W., Verdecchia, S. O., Casquet, C., Pankhurst, R. J., Baldo, E. G., Galindo, C., Murra, J. A., Dahlquist, J. A., and Fanning, C. M., 2015, Identifying Laurentian and SW Gondwana sources in the Neoproterozoic to Early Paleozoic metasedimentary rocks of the Sierras Pampeanas: Paleogeographic and tectonic implications: Gondwana Research.
Rapp, R. P., Ryerson, F. J., and Miller, C. F., 1987, Experimental evidence bearing on the stability of monazite during crustal anaatexis: Geophysical Research Letters, v. 14, p. 307-310.
Rapp, R. P., and Watson, E. B., 1986, Monazite solubility and dissolution kinetics: implications for the thorium and light rare earth chemistry of felsic magmas: Contributions to Mineralogy and Petrology, v. 94, p. 304-316.
Reddy, S., E. Timms, N., Kinny, P., Buchan, C., Trimby, P., and Blake, K., 2006, Crystal-plastic deformation of zircon: A defect in the assumption of chemical robustness, 257-260 p.
Reno, B. L., Piccoli, P. M., Brown, M., and Trouw, R. A. J., 2012, In situ monazite (U-Th)-Pb ages from the Southern Brasília Belt, Brazil: Constraints on the high-temperature retrograde evolution of HP granulites: Journal of Metamorphic Geology, v. 30, p. 81-112.
Rolland, Y., Cox, S., Boullier, A. M., Pennacchioni, G., and Mancktelow, N., 2003, Rare earth and trace element mobility in mid-crustal shear zones: Insights from the Mont Blanc Massif (Western Alps): Earth and Planetary Science Letters, v. 214, p. 203-219.
Rollinson, H., 1995, Using Geochemical Data: Evolution, Presentation, Interpretation.
Rossi, P., Cocherie, A., Fanning, C. M., and Deloule, É., 2006, Variscan to eo-Alpine events recorded in European lower-crust zircons sampled from the French Massif Central and Corsica, France: Lithos, v. 87, p. 235-260.
Rubatto, D., 2002, Zircon trace element geochemistry: Partitioning with garnet and the link between U-Pb ages and metamorphism: Chemical Geology, v. 184, p. 123-138.
Rubatto, D., Chakraborty, S., and Dasgupta, S., 2013, Timescales of crustal melting in the Higher Himalayan Crystallines (Sikkim, Eastern Himalaya) inferred from trace element-constrained monazite and zircon chronology: Contributions to Mineralogy and Petrology, v. 165, p. 349-372.
Sambridge, M. S., and Compston, W., 1994, Mixture modeling of multi-component data sets with application to ion-probe zircon ages: Earth and Planetary Science Letters, v. 128, p. 373-390.

Santos Zalduegui, J. F., Schärer, U., Gil Ibarguchi, J. I., and Girardeau, J., 1996, Origin and evolution of the Paleozoic Cabo Ortegal ultramafic-mafic complex (NW Spain): U-Pb, Rb-Sr and Pb-Pb isotope data: Chemical Geology, v. 129, p. 281-304.
Schaltegger, U., Fanning, C. M., Günther, D., Maurin, J. C., Schulmann, K., and Gebauer, D., 1999, Growth, annealing and recrystallization of zircon and preservation of monazite in high-grade metamorphism: Conventional and in-situ U-Pb isotope, cathodoluminescence and microchemical evidence: Contributions to Mineralogy and Petrology, v. 134, p. 186-201.
Schoene, B., 2014, 4.10 - U–Th–Pb Geochronology, *in* Holland, H. D., and Turekian, K. K., eds., Treatise on Geochemistry (Second Edition): Oxford, Elsevier, p. 341-378.
Schoene, B., Condon, D. J., Morgan, L., and McLean, N., 2013, Precision and accuracy in geochronology: Elements, v. 9, p. 19-24.
Schwartz, J. J., and Gromet, L. P., 2004, Provenance of a late Proterozoic–early Cambrian basin, Sierras de Córdoba, Argentina: Precambrian Research, v. 129, p. 1-21.
Schwartz, J. J., Stowell, H. H., Klepeis, K. A., Tulloch, A. J., Kylander-Clark, A. R. C., Hacker, B. R., and Coble, M. A., 2016, Thermochronology of extensional orogenic collapse in the deep crust of Zealandia: Geosphere, v. 12, p. 647-677.
Scibiorski, E., Kirkland, C., Kemp, A. I. S., Tohver, E., and Evans, N. J., 2019, Trace elements in titanite: A potential tool to constrain polygenetic growth processes and timing.
Semenov, I., and Weinberg, R. F., 2017, A major mid-crustal decollement of the Paleozoic convergent margin of western Gondwana: The Guacha Corral shear zone, Argentina: Journal of Structural Geology, v. 103, p. 75-99.
Seydoux-Guillaume, A.-M., Fougerouse, D., Laurent, A. T., Gardés, E., Reddy, S., and Saxey, D., 2019, Nanoscale resetting of the Th/Pb system in an isotopically-closed monazite grain: A combined atom probe and transmission electron microscopy study, 65-76 p.
Seydoux-Guillaume, A.-M., Goncalves, P., Wirth, R., and Deutsch, A., 2003, Transmission electron microscope study of polyphase and discordant monazites: Site-specific specimen preparation using the focused ion beam technique: Geology, v. 31, p. 973-976.
Seydoux-Guillaume, A. M., Paquette, J. L., Wiedenbeck, M., Montel, J. M., and Heinrich, W., 2002, Experimental resetting of the U-Th-Pb systems in monazite: Chemical Geology, v. 191, p. 165-181.
Sims, J. P., Ireland, T. R., Camacho, A., Lyons, P., Pieters, P. E., Skirrow, R. G., Stuart-Smith, P. G., and Miró, R., 1998, U-Pb, Th-Pb and Ar-Ar geochronology from the southern Sierras Pampeanas, Argentina: implications for the Palaeozoic tectonic evolution of the western Gondwana margin, Geological Society Special Publication, 142, p. 259-281.
Spencer, K. J., Hacker, B. R., Kylander-Clark, A. R. C., Andersen, T. B., Cottle, J. M., Stearns, M. A., Poletti, J. E., and Seward, G. G. E., 2013, Campaign-style titanite U-Pb dating by laser-ablation ICP: Implications for crustal flow, phase transformations and titanite closure: Chemical Geology, v. 341, p. 84-101.
Stacey, J. S., and Kramers, J., 1975, Approximation of Terrestrial Lead Isotope Evolution by a 2-Stage Model, 207-221 p.
Stearns, M., Hacker, B., Ratschbacher, L., Rutte, D., and Kylander-Clark, A., 2015, Titanite petrochronology of the Pamir gneiss domes: Implications for middle to deep crust exhumation and titanite closure to Pb and Zr diffusion: TITANITE RECORD FROM THE PAMIR MID CRUST.
Stepanov, A. S., Hermann, J., Rubatto, D., and Rapp, R. P., 2012, Experimental study of monazite/melt partitioning with implications for the REE, Th and U geochemistry of crustal rocks: Chemical Geology, v. 300-301, p. 200-220.
Taylor, R. J. M., Clark, C., Fitzsimons, I. C. W., Santosh, M., Hand, M., Evans, N., and McDonald, B., 2014, Post-peak, fluid-mediated modification of granulite facies zircon and monazite in the

Trivandrum Block, southern India: Contributions to Mineralogy and Petrology, v. 168, p. 1-17.
Taylor, R. J. M., Kirkland, C. L., and Clark, C., 2016, Accessories after the facts: Constraining the timing, duration and conditions of high-temperature metamorphic processes: Lithos, v. 264, p. 239-257.
Thomas, W. A., and Astini, R. A., 2003, Ordovician accretion of the Argentine Precordillera terrane to Gondwana: A review: Journal of South American Earth Sciences, v. 16, p. 67-79.
Toselli, A., Rossi, J., and Rapela, C. W., 1978, El Basamento Metamorfico de la Sierra de Quilmes, Republica Argentina: Revista de la Asociacion Geologica Argentina, v. 33, p. 105-121.
Turekian, K. K., and Holland, H. D., 2013, Treatise on Geochemistry: Second Edition, 1-80 p.
Turlin, F., Deruy, C., Eglinger, A., Vanderhaeghe, O., André-Mayer, A. S., Poujol, M., Moukhsil, A., and Solgadi, F., 2018, A 70 Ma record of suprasolidus conditions in the large, hot, long-duration Grenville Orogen: Terra Nova, v. 30, p. 233-243.
Turner, J. C. M., 1975, Geología del sector oriental de los Departamentos de Santa Victoria e Iruya, Provincia de Salta. República Argentina: Boletín de la Academia Nacional de Ciencias: Boletín de la Academia Nacional de Ciencias, v. 51, p. 11-24.
Vaughan, A. P. M., and Pankhurst, R. J., 2008, Tectonic overview of the West Gondwana margin: Gondwana Research, v. 13, p. 150-162.
Walsh, A. K., Kelsey, D. E., Kirkland, C. L., Hand, M., Smithies, R. H., Clark, C., and Howard, H. M., 2015, P-T-t evolution of a large, long-lived, ultrahigh-temperature Grenvillian belt in central Australia: Gondwana Research, v. 28, p. 531-564.
Watson, E., 1996, Dissolution, growth and survival of zircons during crustal fusion: Kinetic principles, geological models and implications for isotopic inheritance, 43-56 p.
Watson, E. B., and Harrison, T. M., 1983, Zircon saturation revisited: temperature and composition effects in a variety of crustal magma types: Earth and Planetary Science Letters, v. 64, p. 295-304.
Watson, E. B., Wark, D. A., and Thomas, J. B., 2006, Crystallization thermometers for zircon and rutile: Contributions to Mineralogy and Petrology, v. 151, p. 413-433.
Weinberg, R. F., Becchio, R., Farias, P., Suzaño, N., and Sola, A., 2018, Early paleozoic accretionary orogenies in NW Argentina: Growth of West Gondwana: Earth-Science Reviews.
Weinberg, R. F., Wolfram, L. C., Nebel, O., Hasalová, P., Závada, P., Kylander-Clark, A. R. C., and Becchio, R., 2020, Decoupled U-Pb date and chemical zonation of monazite in migmatites: The case for disturbance of isotopic systematics by coupled dissolution-reprecipitation: Geochimica et Cosmochimica Acta, v. 269, p. 398-412.
Williams, M. L., Jercinovic, M. J., Harlov, D. E., Budzyń, B., and Hetherington, C. J., 2011, Resetting monazite ages during fluid-related alteration: Chemical Geology, v. 283, p. 218-225.
Williams, M. L., Jercinovic, M. J., and Hetherington, C. J., 2007, Microprobe monazite geochronology: Understanding geologic processes by integrating composition and chronology, *in* Jeanloz, R., Albee, A. L., Burke, K. C., and Freeman, K. H., eds., Annual Review of Earth and Planetary Sciences, 35, p. 137-175.
Wolf, M. B., and London, D., 1995, Incongruent dissolution of REE- and Sr-rich apatite in peraluminous granitic liquids: differential apatite, monazite, and xenotime solubilities during anatexis: American Mineralogist, v. 80, p. 765-775.
Wolfram, L. C., Weinberg, R. F., Hasalová, P., and Becchio, R., 2017, How melt segregation affects granite chemistry: Migmatites from the Sierra de Quilmes, NW Argentina: Journal of Petrology, v. 58, p. 2339-2364.
Wolfram, L. C., Weinberg, R. F., Nebel, O., Hamza, K., Hasalová, P., Míková, J., and Becchio, R., 2019, A 60-Myr record of continental back-arc differentiation through cyclic melting: Nature Geoscience, v. 12, p. 215-219.

Yakymchuk, C., and Brown, M., 2014, Behaviour of zircon and monazite during crustal melting: Journal of the Geological Society, v. 171, p. 465-479.
Yakymchuk, C., and Brown, M., 2019, Divergent behaviour of Th and U during anatexis: Implications for the thermal evolution of orogenic crust: Journal of Metamorphic Geology, v. 37, p. 899-916.
Yakymchuk, C., Kirkland, C. L., and Clark, C., 2018, Th/U ratios in metamorphic zircon: Journal of Metamorphic Geology, v. 36, p. 715-737.

Chapter 5

Summary, discussion and conclusion

1– Introduction

This thesis investigated the tectono–thermal evolution of the southern part of the Sierra de Quilmes, complementing the work done in the northern part by other authors. The aims were to characterise the structural evolution of the area and to constrain the time of high–grade metamorphism, in order to understand the tectono–thermal evolution of the Ordovician Famatinian orogen. For that, we used geological mapping, supported by geophysics, petrology, geochemistry, and geochronology. This lead to a thesis divided into two major blocks. The first focuses on the structural evolution of the Sierra de Quilmes (Chapter 2), and the second comprises results of geochronology and mineral composition of zircon, monazite, and titanite (Chapters 3 and 4). In this chapter, we bring together the implications of the structural and geochronological results that constrain the evolution of this long–lived, hot, accretionary orogen. The results also demonstrated the variable behaviour of zircon, monazite, and titanite in such terranes. Here we also discuss unresolved topics and possible further research and directions.

2– Implications of the structural results

2.1 Famatinian Orogen: a failed large–hot orogen in Western Gondwana

The Oclóyic shortening phase of the Famatinian cycle resulted in crustal thickening and orogenesis (see Chapter 1, section 5.3). In Chapter 2, we found that this thickening, associated with thrusting and folding, was counter–balanced by an orogen–parallel escape and decoupling of the thermally weakened footwall complex from the cooler hanging wall. This lateral displacement of material was the result of the inability of the orogen to keep thickening, inhibiting the formation of a thick crust and potentially high topography, in other words, failing to grow.

The Famatinian orogen shares characteristics with large–hot orogens (Jamieson and Beaumont, 2013) (Beaumont et al., 2010). These amalgamated and reworked terranes (Condie, 2007) that after crustal thickening and thermal incubation develop long–lived partially molten weak viscous regions in the crust associated with partial melting (Vanderhaeghe, 2012). They have the potential to develop gravitationally driven channel flow (Beaumont et al., 2010; Beaumont et al., 2002; Bird, 1991; Royden, 1996; Royden et al., 1997; Shen et al., 2001; Vanderhaeghe, 2012; Vanderhaeghe and Teyssier, 2001; Westaway, 1995) or post–convergent gravitationally–driven lateral spread (Cruden et al., 2006b; Franke, 2014; Ratschbacher et al., 1991). The presence of partially molten rocks in the mid–crustal sections of these orogens plays an important role in the structural response to tectonic forces and gravity (Vanderhaeghe, 2009; Vanderhaeghe and Teyssier, 2001), especially after reaching melt–interconnectivity values when rock strength decreases significantly (Ellis et al., 1998; Rosenberg and Handy, 2005; Sawyer, 2008).

The Famatinian hot and weak orogen and the thrusts that drove the crustal thickening are associated with HT–LP metamorphism (Buchan series metamorphism) (Larrovere et al., 2008; Otamendi et al., 2004; Weinberg et al., 2018a), suggesting that they were relatively shallow, precluding the formation of high–pressure mineralogy. Unlike other large–hot orogens like the Altiplano–Puna (Allmendinger et al., 1997; Chmielowski et al., 1999; Yuan et al., 2000; Zandt et al., 2003) or Grenvillian orogens (Turlin et al., 2018) (Table 1), the Famatinian orogen could not sustain high–topography, as it t was too weak, forcing the orogen to spread laterally (Beaumont et al., 2010; Cruden et al., 2006a; Franke, 2014; Ratschbacher et al., 1991).

Marine sedimentation was active during the Famatinian cycle, from c. 490 to 460–440 Ma (e.g., (Astini, 2008; Bahlburg and Breitkreuz, 1991; Büttner, 2009; Cisterna et al., 2017; Hauser et al., 2011) (see section 5.3 in Chapter 1). We found no evidence of such extension in the Sierra de Quilmes where syn–anatectic thrusting is associated with crustal thickening (Finch et al., 2017) (D1 in Chapter

2). Based on the monazite U/Pb age in the Tolombon complex (Finch et al., 2017) argued that anatexis peaked at c. 470–460 Ma together with thrusting. We can not discard the possibility that the thrusting in the Sierra de Quilmes overlapped at some point with the later stage of extension, or that there is a delay between the shortening in the mid–crustal section and the surface. In the Variscan orogeny, the time of orogenesis overlaps with marine sedimentation in the foreland and the internal parts of the orogen. This sedimentation occurred before and during the first stages of crustal thickening and magmatism, suggesting low topography and ruling out the possibility that this orogen represented Tibetan–style high plateaus during that time (Franke, 2014). Also, during the Variscan orogenic climax, intra–montane "mostly coal–bearing basins whose floras and faunas are not compatible with high and dry plateaus" were formed (Franke, 2014). It is proposed that topographic highs may only have occurred in narrow belts associated with crustal–scale shear zones. Weinberg (2018a) argues that a Famatinian dense lithosphere might have been a factor that contributed to maintaining low topography during the shortening Oclóyic phase.

We argue that the Famatinian orogen was similar to the Variscan orogeny (Franke, 2014; Guergouz et al., 2018; Karg et al., 2005), as both were large and thermally weakened orogens that failed to grow vertically, and instead spread laterally.

2.2 Wide and arc–verging shear zones

In the Sierra de Quilmes, as in most of the Famatinian back–arc, the shear zones are unusually wide and west verging, towards the magmatic arc. The fact that most of these shear zones are located in the back–arc is a well–known characteristic of accretionary orogens (Cawood et al., 2009). The high–heat flow and resulting rheological weakness of the back–arcs (regardless of their tectonic regime) (Curie and Hyndman, 2006; Hyndman et al., 2005) make them the most suitable site for focusing of deformation within the accretionary orogen systems (Cawood et al., 2009; Ellis et al., 1998). The

Famatinian shear zones are unusually thick (Finch et al., 2015; Larrovere et al., 2008; Semenov and Weinberg, 2017). This could be because these structures focused and reactivated older ones, like the fore–arc Pampean structures, resulting in a few long–lived structures that focused the strain during multiple orogenies, resulting in wide high–strain zones (Weinberg et al., 2018a). A good example of reactivated structures is in the current eastern Myanmar–western Thailand region (San–Thai block) that focuses deformation within inherited back–arc structures reactivated during the India–Asia collision (Morley, 2009). Finch (2015) found that hydrolytic weakening is an internal mechanism in the Pichao shear zone that could explain its widening through time. Hydrolytic weakening facilitates the strain localisation in the margins of a high–strain zone. A progressive water loss from the core of the high–strain zone results in a migration of strain from the dryer harder core towards the hydrated weaker margins, resulting in a widening of the shear zone with time.

Another unusual feature of the Famatinian back–arc structures is that they are west verging and record tectonic transport towards the arc. In an accretionary orogen, the largest structures formed in the back–arc are expected to have the opposite vergence with tectonic transport towards the foreland, away from the arc. In Weinberg (2018a) it is proposed that the cause of such vergence is that they are reactivated structures formed in the Pampean forearc. Similar to that, Mesozoic and Cenozoic structures from the Cretaceous rifting of NW Argentina and the Andean orogeny respectively, focused and reactivated Paleozoic structures (Hongn et al., 2010; Martino et al., 2012), suggesting that some of them may have been reactivated several times for more than 500 Ma.

3– Implications of the geochronology results

From Chapters 3 and 4 we found that the Sierra de Quilmes represents a long–lived terrane with evidence of Pampean magmatism, followed by extended Famatinian high–temperature metamorphism that lasted between c. 500–380 Ma. We also found that zircon, monazite, and titanite yield spread semi–continuous dates, and they responded differently to the Famatinian protracted HT–LP metamorphism, sensitive to peak thermal conditions.

The time constraint of a short–lived magmatic or metamorphic event is relatively simple, as it yields a statistically homogeneous age population (MSWD = 1) from concordant dates or from upper or lower Discordia lines intercept (Horstwood et al., 2016; Ludwig, 2003; Schoene, 2014; Schoene et al., 2013). In contrast, long–lived high–temperature events, like our case in the Sierra de Quilmes, are associated with dates spread over tens of millions of years (Table 1), sometimes composed of several continuous short–lived episodes events (Ague and Baxter, 2007; Clark et al., 2009; Clark et al., 2011; Davis et al., 2003; Grant et al., 2009; Harley, 2016; Hokada et al., 2004; Keay et al., 2001; Kelly and Harley, 2005; Kreissig et al., 2001; Love et al., 2004; Paquette et al., 2004; Paquette et al., 2003; Parrish, 1990; Rossi et al., 2006; Sal'nikova et al., 2007; Santosh et al., 2012; Taylor et al., 2016; Whitehouse and Platt, 2003; Wolfram et al., 2019). These protracted events allow minerals like zircon, monazite and titanite to record not only the U/Pb age, but also the variations in the mineral paragenesis of the host rock linked with the growth or destruction of other mineral phases (Kelsey and Powell, 2011; Rubatto et al., 2013; Taylor et al., 2016) that in a short–lived event, would be unresolvable. A classic example of this is zircon that can record the growth or destruction of garnet (Rubatto, 2002), or monazite that can record the formation of prograde feldspar (Rubatto et al., 2013). For titanite, we were able to recognise in its chemistry the gradual increase in modal content of allanite during the protracted retrogression of the Ca–rich siliciclastic rocks (Chapter 3).

3.1 Implications for the Sierra de Quilmes evolution and regional geology

The multiple and cyclical melting Famatinian events reported by Wolfram (2019) in the hanging wall Tolombon complex suggest prolonged anatectic conditions that lasted for c. 60 Myr from 505 to 440

Ma. In Chapter 3, we explored the footwall Agua del Sapo complex and found an even more extended geochronological record. The detrital zircon signature indicates that the protolith of the migmatites is part of the Puncoviscana sequence deposited before the onset of the Pampean arc (Adams et al., 2011; Weinberg et al., 2018a). During the Pampean orogeny, this package reached low metamorphic grade, and was intruded by a peraluminous Pampean granite at c. 530 Ma (the Filo granite). This was followed by Famatinian HT–LP metamorphism that triggered anatexis and peaked at c. 460–470 Ma, followed by a prolonged cooling that started at 440 Ma, when temperatures dropped from 750 °C to 700 °C at 380 Ma (c. 1 °C/Ma). This extended the Famatinian high–temperature record for another 60 Myr. This extended record overlaps the end of the Famatinian with the beginning of the Achalian orogenic cycle (c. 400–350 Ma).

If we compare the geochronology record of the three complexes with their structural record (Chapter 2), we can argue that the top-to-south shearing of the footwall Agua del Sapo complex continued after the metamorphic peak (c. 470–460 Ma). Unlike in the other complexes, in the Agua del Sapo complex, the anatectic structures are strongly overprinted by top–to–south shearing, suggesting that this event, exclusive of this complex, was active after anatexis.

3.2 On the behaviour of the geochronometers

All analysed accessory phases yield spread dates. The growth of zircon, monazite, and titanite is controlled by temperature, melt abundance and melt composition (see discussion in Chapter 4). The formation of these accessory phases can also occur during prograde and retrograde paths (Kelsey et al., 2008; Kohn, 2017; Kohn et al., 2018; Taylor et al., 2016; Yakymchuk and Brown, 2014). Zircon in migmatites forms mostly after the metamorphic peak, when melt crystallises, and thus yields minimum age of metamorphism and the onset of melt crystallisation (Collins et al., 2014; Taylor et al., 2016). However, there has been studies (Korhonen et al., 2013; Nemchin et al., 2001; Rossi et al.,

2006) that argue for zircon formation during the prograde part of the suprasolidus evolution. Monazite and titanite form during the prograde path, from the breakdown of LREE and Th–bearing minerals, like apatite, allanite, and xenotime, and Ti–bearing minerals such as ilmenite for titanite (Johnson et al., 2015; Korhonen et al., 2013; Rossi et al., 2006; Taylor et al., 2016). During melt crystallisation, these minerals will form progressively as the rock cools towards the solidus, and in the case of titanite, it can continue to grow until c. 500 °C (Kohn, 2017). In Chapter 4 we discussed how coupled dissolution–precipitation during the high–temperature event could have disturbed the internal organisation of radiogenic Pb and in turn, yield spread dates (Fig. 19 in Chapter 4). Also, the role of fluids in the amphibolite facies Filo shear zone that assisted the formation of new monazite grains with a different REE signature (Williams et al., 2011). In Chapter 4, we discussed the potential role of shearing combined with high–temperatures in the semi–continuous titanite formation. Therefore, protracted growth of the three geochronometers is expected as the rock cools from peak metamorphism, which in our case lasted more than 120 Myr.

There are other causes for this protracted record. Some of the early formed accessory phases can be preserved and armoured by stronger and larger minerals like peritectic garnet or K–feldspar (Turlin et al., 2018). Also early formed monazite, or titanite can be less reactive to fluids than later recrystallised ones (Collins et al., 2014; Taylor et al., 2016). In migmatites, some early–formed phases can be physically disconnected from new melt batches (Wolfram et al., 2019), or melt entrapment that isolates them from the main melt network (Harley and Nandakumar, 2014). At this stage, these mechanisms remain speculative as we cannot pinpoint them in our rocks.

We recorded different behaviour of the geochronometers across the complexes that evolved under relatively similar P–T conditions, varying in peak temperature within 50–100 °C, and derived from similar protolith. Also, their behaviour varies within the same complex, and sometimes within the same rock sample. This implies that the use of more than one mineral from the same rock, combined with their trace elements (e.g., REE) is the most efficient way to get a more accurate and broad record of the temporal evolution of a terrane than a single geochronometer (Kelsey et al., 2008; Kelsey and Hand, 2015). In our case, the more reactive monazite and titanite allowed identification of the reactivation of the Filo shear zone at 407 Ma, and the protracted high–temperature and slow cooling of the Agua del Sapo complex.

4– How can the middle–crust remain hot for so long?

The heat source responsible for high–temperature at mid-crustal levels (5-7 kbar) remains debated. Some of the invoked mechanisms include: (i) thickening of crust enriched in heat–producing elements (England and Bruce Thompson, 1986; Huerta et al., 1999; Jaupart et al., 2016; Sandiford and McLaren, 2002), (ii) frictional heating in fault and shear zones (Bird et al., 1975; Clark et al., 2011; England et al., 1992; Molnar and England, 1990), and (iii) heat transfer from the asthenosphere (Bird, 1978; De Yoreo et al., 1991) (Hyndman et al., 2005). All of these mechanisms may have been active during the Famatinian cycle (Weinberg et al., 2018a), and the combination of all contributed to the heat budget necessary to sustain high–temperatures during the Famatinian orogenic cycle. Expanding on the previous points, estimations of the heat from radiogenic decay from heat–producing elements (HPEs) from the protolith of most crystalline rocks, the Puncoviscana sequence, are c. 2 μWm^{-3}, c. 20 % more than the estimated for the upper continental crust (Alessio et al., 2018; Lucassen et al., 2001; Wolfram et al., 2017). The early extensional stage of the Famatinian back–arc resulted in a thin lithosphere and an upwelling hot asthenosphere (Clark et al., 2011; Curie and Hyndman, 2006; Hyndman et al., 2005; Tatsumi and Kimura, 1991; Ziegler et al., 1998), supported by evidence of mafic magmatism as the heat source during extension (Bial et al., 2015; Coira et al., 2009; Sims et al., 1998; Weinberg et al., 2018a). Also, the Famatinian back-arc had previously been part of the Pampean HT-LP forearc, therefore inheriting heat from an older orogeny. The Pampean forearc was relatively hot to judge from the titanite work of Lucassen (2011) and discussed in Weinberg (2018b). Collins (2002) invoked tectonic switching (shortening–extension) in the 700–km wide Lachlan orogen of eastern Australia as the leading mechanism that caused high–temperature metamorphism. They argued that the heat was inherited from short–lived extensional phases in between shortening stages modulated by the arrival of buoyant oceanic plateaus to the subduction zone. This switching of the tectonic regime induced closure of arcs and back–arcs, and localisation of strain into the ductile sections held between stiffer colder lithospheric blocks. The continuous trench–ward migration of these orogen–parallel hot zones resulted in the wider orogen. Similar mechanisms could have acted over the Famatinian orogeny. The extensional mode during the first stage of the Famatinian cycle later changed to shortening during the Oclóyic phase.

4.1 Other cases of long–lived high–temperature orogens

Examples of long–lived large–hot and ultra–high temperature (UHT) terranes are listed in Table 1. These orogens, as the Famatinian, typically record protracted high–temperature followed by slow isobaric cooling rates below 10 °C/Ma (Beaumont et al., 2010; Bial et al., 2015; Cavalcante et al., 2018; Guergouz et al., 2018; Högdahl et al., 2012; Jamieson and Beaumont, 2013; Nelson et al., 1996; Turlin et al., 2018).

In a review about heat sources in UHT terranes, Kelsey (2015) concluded that most of the long–lived UHT terranes require previous heating from extended crust before being thickened and heated, and also a subdued or negative topography that would prevent high erosion rates and fast vertical extrusion rates (Chardon et al., 2009). The concentrated HPEs then sustained the high–temperature, and the low extrusion rate would keep the hot rocks at constant depths for longer. Although the Famatinian orogeny did not reach UHT, the principles are still valid. The Famatinian back–arc most likely inherited the heat from previous Pampean orogenic cycle, amplified by mantle–sourced heat transfer during the early extensional period (c. 500–470 Ma), and maintained during the Oclóyic phase, as the structurally unfit orogen precluded high topography and low erosion rates aided to maintain a near–isobaric cooling. The near isobaric cooling in the Sierra de Quilmes is argued by Büttner (2009)and Büttner (2005). Also, by (Sola et al., 2013) in migmatites of the Famatinian back-arc.

An important point to discuss is that during orogenesis, rocks move through different thermal fields (Jamieson and Beaumont, 2013). When it comes to the timescale of a particular orogen–scale thermal event, we must consider that a hand–sized rock sample may not adequately record the complete cycle. The fraction of the event recorded by a particular rock sample will depend on the P–T–t path that the rock followed within the orogen (Kelsey and Hand, 2015). A rock exhumed rapidly will have fewer chances to record the real duration of the event than a rock that remains relatively stable within the orogen cooling in a near–isobaric path. This has implications in the understanding of how a thermal event can be recorded (or missed) in dynamic orogens.

Table 1. Examples of large–hot and long–lived orogens. Most of them Protherozoic, > 20 Myr of anatexis and slow cooling rates (<10 °C/Ma).

Orogen/complex	*Age*	*Anatexis duration (Myr)*	*Peak P–T (MPa/°C)*	*Cooling rate (°C/Ma)*	*Comments*	*Dated mineral*	*Study*
Araçuaí orogen	Late Proterozoic	c. 25	6/780	3	Channel flow		(Cavalcante et al., 2018)
Himalaya–Tibet	Current	c. 45	800–1000 (from 30–50 km depths)		Partially molten mid–crustal section beneath south Tibet	Monazite Zircon	(Hacker et al., 2000; Kind et al., 1996; Nelson et al., 1996)
Altiplano–Puna	Current	c. 25–10			Intracrustal low–velocity zone 10–20 km thick (partially molten rocks)		(Allmendinger et al., 1997; Chmielowski et al., 1999; Yuan et al., 2000; Zandt et al., 2003)
Variscan	420–290 Ma	c. 30	10–12/850–950	Rapid exhumation	Failed orogen	Zircon, monazite	(Franke, 2014; Karg et al., 2005)
Grenville	Mesoproterozoic	c. 60	9/ 850	2–6	HT after delamination of lithospheric mantle		(Turlin et al., 2018)
South Madagascar	Neoproterozoic–Cambrian	c. 65	9–12/800–850	?	Assembly of W – E Gondwana		(Horton et al., 2016)
Rogaland granulites, Norway	Neoproterozoic	c. 60	7/1000		UHT. Tectonic accretion followed by gravitational collapse	Zircon	(Drüppel et al., 2012)
Kalak complex, Norway	Neo–Proterozoic	c. 200	9/775	c. 1–3	Protracted Mnz growth (200 Myr)	Zircon, monazite, titanite	(Gasser et al., 2015)
Ghats orogenic belt, India	Late–Mesoproterozoic, Early–Neoproterozoic	>50 <200		c. 1	Zrn and Mnz growth post peak	Zircon, monazite	(Korhonen et al., 2013)
Southern Brasılian Belt	Late–Neoproterozoic	c. 70		c. 2		Monazite	(Reno et al., 2012)
Musgrave–Albany–Fraser orogen	Mid–late Mesoproterozoic	80–150	7–8/1000		UHT		(Walsh et al., 2015)
Namaquan orogeny	Mesoproterozoic	c. 250	5/800–900	c. 2	Heat transfer from mantle into thinned lithosphere in continental back–arc	Zircon, monazite	(Bial et al., 2015)

5– Extension versus shortening

Finch (2017) argued that crustal shortening in the Sierra de Quilmes was coeval with anatexis between c. 490–440 Ma. Büttner (2009) had a different view and proposed that crustal extension was established after metamorphic peak and anatexis in the Sierra de Quilmes at c. 480–470 Ma and lasted until 440 Ma. Most of the arguments in Büttner (2009) are based on stratigraphical studies done in sedimentary basins in NW Argentina (Bahlburg and Breitkreuz, 1991). Recent stratigraphical studies show that these basins record a more complex history (Astini, 2008; Moya, 2015). As we detailed in section 5.3 of Chapter 1, Famatinian age sedimentation started in an extensional back–arc setting during Early Ordovician and switched to foreland basins (structural basins that develop adjacent to mountain belts) at Mid–Late Ordovician times at c. 460 Ma (Astini and Dávila, 2004; Turner, 1975). These foreland basins have their depocenter in the western Puna region near the arc and recorded continuous sedimentation until the Late Ordovician (c. 440 Ma) when the Oclóyic phase uplifted the package (Bahlburg and Breitkreuz, 1991; Bahlburg and Furlong, 1996). To the east of these basins, in the Cordillera Oriental, closer to the Sierra de Quilmes, the sedimentary record finished earlier at c. 470 Ma, possibly due to the flexural bulge that caused the uplift and emergence of the Early Ordovician shelf (Astini and Dávila, 2004). This event is known as the Guandacol diastrophic phase (Aceñolaza et al., 2002; Astini, 2008; Astini et al., 2004; Bahlburg and Hervé, 1997; Collo and Astini, 2008; Moya, 2015). Based on the above, shortening was manifested in the surface at different times; at c. 470 Ma in the Cordillera Oriental, closer to the Sierra de Quilmes and c. 440 Ma in the Puna. This supports the idea of Finch (2017) and ours (Chapter 2), in that in the Sierra de Quilmes shortening (D1, in Chapter 2) was already active at c. 470–460 Ma.

In Chapter 3, we discuss that the footwall Agua del Sapo complex started to cool at 440 Ma when the other complexes were already below T_c of zircon, monazite, and titanite. At 440 Ma the western and deeper Ordovician basins are finally exhumed and partially eroded (Astini, 2008; Astini et al., 2004; Bahlburg and Hervé, 1997). The time at which the Agua del Sapo complex started cooling coincides with the regional exhumation event recorded in the sedimentary basins.

6– Conclusions

In this thesis, we investigated the structural behaviour of the mid–crustal section of the Famatinian back–arc, represented in the Sierra de Quilmes. We found that during the Oclóyic shortening phase of the orogenic cycle, the 470 ± 10 Ma crustal thickening event (D1), was counterbalanced by the stretching, parallel to the orogen (D2), of the thermally weakened footwall Agua del Sapo complex. This lateral flow was controlled by the balance between E–W horizontal tectonic and vertical gravitational forces and driven by variations in the crustal thickness. This escape happened after peak metamorphism and suggests that the orogen was unfit to support significant vertical thickening and failed to grow, similar to the large–hot Variscan orogen (Franke, 2014). The Famatinian large–hot orogen was also long–lived. The three metamorphic complexes were hot over a c. 60 Myr period, from c. 500–440 Ma. At c. 440 Ma, the hanging wall complexes were cooled below T_c of zircon, monazite, and titanite, while the footwall Agua del Sapo complex, started to cool slowly at c. 440 Ma from peak temperature of c. 750 °C to 700 °C at 380 Ma (c. 1 °C/Ma). The beginning of the cooling at 440 Ma coincides with the regional exhumation manifested in the surface, in the sedimentary basins. Zircon, monazite and titanite reacted differently in the complexes as the result of variable temperature and other factors like deformation and rock fabric. The different reactivity of zircon, monazite, and titanite was not only across complexes but also at the complex– and sample–scale. This implies that numerous variables are at play, and the use of more than one geochronometer from the same sample has the potential to provide more comprehensive insights into the temporal evolution of a terrane.

7– Open questions

7.1 What is the source of the Ca–rich siliciclastic rocks in Agua del Sapo complex?

The Al–rich metasedimentary rocks dominant in the Sierra de Quilmes have a bulk composition typical of turbidites derived from mature sediments, and the DZ record suggests that they were sourced in part by the c. 540–520 Ma Pampean magmatic arc. Unlike these, the Ca–rich metasedimentary rocks in the Agua del Sapo complex have a bulk composition typical of metaluminous or I–type igneous rocks, and their DZ record suggests that they were deposited before the onset of the Pampean magmatic arc (Chapter 3). López (2019) found similar rocks in the Cumbres Calchaquies, some 30 km east of the Sierra de Quilmes. They argued that they represent metamorphosed impure carbonates or marls ($CaCO_3$ between 35–65 %) (Pettijohn, 1957) that resulted in calc–silicate rocks. However, the Ca content of the Agua del Sapo rocks is lower than the calc–silicates.

Can these Ca–rich siliciclastic rocks derive from the erosion of a pre–Pampean calc–alkaline magmatic arc? In northeastern Brazil, Ep–bearing calc–alkaline high–K syn–kinematic magmas of 650–620 Ma and 590–560 Ma are associated with partial fusion of subducted oceanic basaltic crust (Sial and Ferreira, 2015). The petrographic texture of allanite–cored epidotes with titanite is similar to our Ca–rich migmatites. The problem with this is that these magmatic rocks are >2000 km away from the Sierra de Quilmes.

8– Further research

By using petrochronology, we can further understand the response of geochronometers (Kohn, 2017; Turlin et al., 2018), and link the geochronology with rock–forming processes and rock fabric. The response of these geochronometers to the HT–LP metamorphism and deformation is heterogeneous in many scales, and some of our arguments remain speculative. Petrochronology would help us better understand their behaviour and the particularities of every single grain in the context of the rock, specifically in deformed rocks. Also, detailed monazite studies at the nano–scale, such as in Seydoux-Guillaume (2019) and Seydoux-Guillaume (2003) would give us better constraint of the internal organisation radiogenic lead. This could add valuable information to how coupled dissolution–precipitation mechanisms acted in the monazite from the Sierra de Quilmes.

Dating allanite would reinforce the interpretation of titanite LREE signature (Chapter 3). We expect allanite forming after 440 Ma when the rock package started cooling below 750 ºC. Apatite and muscovite cooling ages from the different complexes would give us useful constraints into the thermal history of the Sierra de Quilmes.

References

Aceñolaza, F. G., Miller, H., and Toselli, A. J., 2002, Proterozoic - Early Paleozoic evolution in western South America - A discussion: Tectonophysics, v. 354, p. 121-137.

Adams, C. J., Miller, H., Aceñolaza, F. G., Toselli, A. J., and Griffin, W. L., 2011, The Pacific Gondwana margin in the late Neoproterozoic–early Paleozoic: Detrital zircon U–Pb ages from metasediments in northwest Argentina reveal their maximum age, provenance and tectonic setting: Gondwana Research, v. 19, p. 71-83.

Ague, J. J., and Baxter, E. F., 2007, Brief thermal pulses during mountain building recorded by Sr diffusion in apatite and multicomponent diffusion in garnet: Earth and Planetary Science Letters, v. 261, p. 500-516.

Alessio, K. L., Hand, M., Kelsey, D. E., Williams, M. A., Morrissey, L. J., and Barovich, K., 2018, Conservation of deep crustal heat production: Geology, v. 46, p. 335-338.

Allmendinger, R. W., Jordan, T. E., Kay, S. M., and Isacks, B. L., 1997, The evolution of the Altiplano-Puna plateau of the Central Andes, Annual Review of Earth and Planetary Sciences, 25, p. 139-174.

Astini, R., 2008, Sedimentación, facies, discordancias y evolución paleoambiental durante el Cambro-Ordovícico, Revista de la Asociacion Geologica Argentina, 50-73 p.

Astini, R. A., and Dávila, F. M., 2004, Ordovician back arc foreland and Ocloyic thrust belt development on the western Gondwana margin as a response to Precordillera terrane accretion: Tectonics, v. 23, p. TC4008 1-19.

Astini, R. A., Waisfeld, B. G., Toro, B. A., and Benedetto, J. L., 2004, Early and middle Paleozoic of the Los Colorados region in the western border of the Cordillera Oriental (Jujuy province): Revista de la Asociacion Geologica Argentina, v. 59, p. 243-260.

Bahlburg, H., and Breitkreuz, C., 1991, Paleozoic evolution of active margin basins in the southern Central Andes (northwestern Argentina and northern Chile): Journal of South American Earth Sciences, v. 4, p. 171-188.

Bahlburg, H., and Furlong, K. P., 1996, Lithospheric modeling of the Ordovician foreland basin in the Puna of northwestern Argentina: On the influence of arc loading on foreland basin formation: Tectonophysics, v. 259, p. 245-258.

Bahlburg, H., and Hervé, F., 1997, Geodynamic evolution and tectonostratigraphic terranes of northwestern Argentina and northern Chile: Bulletin of the Geological Society of America, v. 109, p. 869-884.

Beaumont, C., Jamieson, R., and Nguyen, M., 2010, Models of large, hot orogens containing a collage of reworked and accreted terranes: Canadian Journal of Earth Sciences, v. 47, p. 485-515.

Beaumont, C., Jamieson, R. A., Nguyen, M. H., and Lee, B., 2002, Himalayan tectonics explained by extrusion of a low-viscosity crustal channel coupled to focused surface denudation, 738-42 p.

Bial, J., Büttner, S. H., Schenk, V., and Appel, P., 2015, The long-term high-temperature history of the central Namaqua Metamorphic Complex: Evidence for a Mesoproterozoic continental back-arc in southern Africa: Precambrian Research, v. 268, p. 243-278.

Bird, P., 1978, Initiation of intracontinental subduction in Himalaya, 4975-4987 p.

Bird, P., 1991, Lateral extrusion of lower crust from under high topography in the isostatic limit: Journal of Geophysical Research: Solid Earth, v. 96, p. 10275-10286.

Bird, P., Nafi Toksöz, M., and Sleep, N., 1975, Thermal and Mechanical Models of Continent-Continent Convergence Zones, 4405-4416 p.

Büttner, S. H., 2009, The Ordovician Sierras Pampeanas–Puna basin connection: Basement thinning and basin formation in the Proto-Andean back-arc: Tectonophysics, v. 477, p. 278-291.
Büttner, S. H., Glodny, J., Lucassen, F., Wemmer, K., Erdmann, S., Handler, R., and Franz, G., 2005, Ordovician metamorphism and plutonism in the Sierra de Quilmes metamorphic complex: Implications for the tectonic setting of the northern Sierras Pampeanas (NW Argentina): Lithos, v. 83, p. 143-181.
Cavalcante, C., Hollanda, M. H., Vauchez, A., and Kawata, M., 2018, How long can the middle crust remain partially molten during orogeny?: Geology, v. 46, p. 839-842.
Cawood, P. A., Kröner, A., Collins, W. J., Kusky, T. M., Mooney, W. D., and Windley, B. F., 2009, Accretionary orogens through Earth history, Geological Society Special Publication, 318, p. 1-36.
Chardon, D., Gapais, D., and Cagnard, F., 2009, Flow of ultra-hot orogens: A view from the Precambrian, clues for the Phanerozoic: Tectonophysics, v. 477, p. 105-118.
Chmielowski, J., Zandt, G., and Haberland, C., 1999, The central Andean Altiplano-Puna magma body: Geophysical Research Letters, v. 26, p. 783-786.
Cisterna, C. E., Koukharsky, M., Coira, B., Günter, C., and Ulbrich, H. H., 2017, Arenigian tholeiitic basalts in the Famatina Ordovician basin, northwestern Argentina: emplacement conditions and their tectonic significance: Andean Geology, v. 44, p. 123-146.
Clark, C., Collins, A. S., Timms, N. E., Kinny, P. D., Chetty, T. R. K., and Santosh, M., 2009, SHRIMP U–Pb age constraints on magmatism and high-grade metamorphism in the Salem Block, southern India: Gondwana Research, v. 16, p. 27-36.
Clark, C., Fitzsimons, I., Healy, D., and Harley, S., 2011, How Does the Continental Crust Get Really Hot?, 235-240 p.
Coira, B., Koukharsky, M., Guevara, S. R., and Cisterna, C. E., 2009, Puna (Argentina) and northern Chile Ordovician basic magmatism: A contribution to the tectonic setting: Journal of South American Earth Sciences, v. 27, p. 24-35.
Collins, A. S., Clark, C., and Plavsa, D., 2014, Peninsular India in Gondwana: The tectonothermal evolution of the Southern Granulite Terrain and its Gondwanan counterparts: Gondwana Research, v. 25, p. 190-203.
Collins, W. J., 2002, Hot orogens, tectonic switching, and creation of continental crust: Geology, v. 30, p. 535-538.
Collo, G., and Astini, R. A., 2008, The Achavil Formation: A new low-grade metamorphic unit in the Upper Cambrian evolution of Famatina: Revista de la Asociacion Geologica Argentina, v. 63, p. 344-362.
Condie, K. C., 2007, Accretionary orogens in space and time, Memoir of the Geological Society of America, 200, p. 145-158.
Cruden, A. R., Nasseri, M. H. B., and Pysklywec, R., 2006a, Surface topography and internal strain variation in wide hot orogens from three-dimensional analogue and two-dimensional numerical vice models, Geological Society Special Publication, 253, p. 79-104.
Cruden, A. R., Nasseri, M. H. B., and Pysklywec, R., 2006b, Surface topography and internal strain variation in wide hot orogens from three-dimensional analogue and two-dimensional numerical vice models, Geological Society Special Publication, 253, p. 79-104.
Curie, C. A., and Hyndman, R. D., 2006, The thermal structure of subduction zone back arcs: Journal of Geophysical Research: Solid Earth, v. 111.
Davis, W. J., Canil, D., MacKenzie, J. M., and Carbno, G. B., 2003, Petrology and U–Pb geochronology of lower crustal xenoliths and the development of a craton, Slave Province, Canada: Lithos, v. 71, p. 541-573.
De Yoreo, J. J., Lux, D., and Guidotti, C. V., 1991, Thermal modeling in low-pressure/high-temperature metamorphic belts, 209-238 p.

Drüppel, K., Elsäßer, L., Brandt, S., and Gerdes, A., 2012, Sveconorwegian Mid-crustal Ultrahigh-temperature Metamorphism in Rogaland, Norway: U–Pb LA-ICP-MS Geochronology and Pseudosections of Sapphirine Granulites and Associated Paragneisses: Journal of Petrology, v. 54, p. 305-350.
Ellis, S., Beaumont, C., Jamieson, R. A., and Quinlan, G., 1998, Continental collision including a weak zone: The vise model and its application to the Newfoundland Appalachians: Canadian Journal of Earth Sciences, v. 35, p. 1323-1346.
England, P., and Bruce Thompson, A., 1986, Some thermal and tectonic models for crustal melting in continental collision zones, 83-94 p.
England, P., Le Fort, P., Molnar, P., and Pêcher, A., 1992, Heat sources for Tertiary metamorphism and anatexis in the Annapurna- Manaslu Region Central Nepal.
Finch, M. A., Weinberg, R. F., Fuentes, M. G., Hasalová, P., and Becchio, R., 2015, One kilometre-thick ultramylonite, Sierra de Quilmes, Sierras Pampeanas, NW Argentina: Journal of Structural Geology, v. 72, p. 33-54.
Finch, M. A., Weinberg, R. F., Hasalová, P., Becchio, R., Fuentes, M. G., and Kennedy, A., 2017, Tectono-metamorphic evolution of a convergent back-arc: The Famatinian orogen, Sierra de Quilmes, Sierras Pampeanas, NW Argentina: Bulletin of the Geological Society of America, v. 129, p. 1602–1621.
Franke, W., 2014, Topography of the Variscan orogen in Europe: Failed-not collapsed: International Journal of Earth Sciences, v. 103, p. 1471-1499.
Gasser, D., Jeřábek, P., Faber, C., Stünitz, H., Menegon, L., Corfu, F., Erambert, M., and Whitehouse, M. J., 2015, Behaviour of geochronometers and timing of metamorphic reactions during deformation at lower crustal conditions: Phase equilibrium modelling and U-Pb dating of zircon, monazite, rutile and titanite from the Kalak Nappe Complex, northern Norway: Journal of Metamorphic Geology, v. 33, p. 513-534.
Grant, M. L., Wilde, S. A., Wu, F., and Yang, J., 2009, The application of zircon cathodoluminescence imaging, Th–U–Pb chemistry and U–Pb ages in interpreting discrete magmatic and high-grade metamorphic events in the North China Craton at the Archean/Proterozoic boundary: Chemical Geology, v. 261, p. 155-171.
Guergouz, C., Martin, L., Vanderhaeghe, O., Thébaud, N., and Fiorentini, M., 2018, Zircon and monazite petrochronologic record of prolonged amphibolite to granulite facies metamorphism in the Ivrea-Verbano and Strona-Ceneri Zones, NW Italy: Lithos, v. 308-309, p. 1-18.
Hacker, B. R., Gnos, E., Ratschbacher, L., Grove, M., McWilliams, M., Sobolev, S. V., Wan, J., and Wu, Z., 2000, Hot and dry deep crustal xenoliths from Tibet: Science, v. 287, p. 2463-2466.
Harley, S. L., 2016, A matter of time: The importance of the duration of UHT metamorphism: Journal of Mineralogical and Petrological Sciences, v. 111, p. 50-72.
Harley, S. L., and Nandakumar, V., 2014, Accessory Mineral Behaviour in Granulite Migmatites: a Case Study from the Kerala Khondalite Belt, India: Journal of Petrology, v. 55, p. 1965-2002.
Hauser, N., Matteini, M., Omarini, R. H., and Pimentel, M. M., 2011, Combined U–Pb and Lu–Hf isotope data on turbidites of the Paleozoic basement of NW Argentina and petrology of associated igneous rocks: Implications for the tectonic evolution of western Gondwana between 560 and 460Ma: Gondwana Research, v. 19, p. 100-127.
Högdahl, K., Majka, J., Sjöström, H., Nilsson, K. P., Claesson, S., and Konečný, P., 2012, Reactive monazite and robust zircon growth in diatexites and leucogranites from a hot, slowly cooled orogen: Implications for the Palaeoproterozoic tectonic evolution of the central Fennoscandian Shield, Sweden: Contributions to Mineralogy and Petrology, v. 163, p. 167-188.

Hokada, T., Misawa, K., Yokoyama, K., Shiraishi, K., and Yamaguchi, A., 2004, SHRIMP and electron microprobe chronology of UHT metamorphism in the Napier Complex, East Antarctica: implications for zircon growth at >1,000 °C: Contributions to Mineralogy and Petrology, v. 147, p. 1-20.

Hongn, F., Mon, R., Petrinovic, I., del Papa, C., and Powell, J., 2010, Inversión y reactivación tectónicas cretácicocenozoicas en el Noroeste Argentino: influencia de las heterogeneidades del basamento neoproterozoico-paleozoico inferior, 38-53 p.

Horstwood, M. S. A., Košler, J., Gehrels, G., Jackson, S. E., McLean, N. M., Paton, C., Pearson, N. J., Sircombe, K., Sylvester, P., Vermeesch, P., Bowring, J. F., Condon, D. J., and Schoene, B., 2016, Community-Derived Standards for LA-ICP-MS U-(Th-)Pb Geochronology – Uncertainty Propagation, Age Interpretation and Data Reporting: Geostandards and Geoanalytical Research, v. 40, p. 311-332.

Horton, F., Hacker, B., Kylander-Clark, A., Holder, R., and Jöns, N., 2016, Focused radiogenic heating of middle crust caused ultrahigh temperatures in southern Madagascar: Tectonics, v. 35, p. 293-314.

Huerta, A., Royden, and Hodges, K., 1999, The effects of accretion, erosion and radiogenic heat on the metamorphic evolution of collisional orogens, 349-366 p.

Hyndman, R. D., Currie, C. A., and Mazzotti, S. P., 2005, Subduction zone backarcs, mobile belts, and orogenic heat: GSA Today, v. 15, p. 4-10.

Jamieson, R. A., and Beaumont, C., 2013, On the origin of orogens: Bulletin of the Geological Society of America, v. 125, p. 1671-1702.

Jaupart, C., Mareschal, J. C., and Iarotsky, L., 2016, Radiogenic heat production in the continental crust: Lithos, v. 262, p. 398-427.

Johnson, T. E., Clark, C., Taylor, R. J. M., Santosh, M., and Collins, A. S., 2015, Prograde and retrograde growth of monazite in migmatites: An example from the Nagercoil Block, southern India: Geoscience Frontiers, v. 6, p. 373-387.

Karg, H., Carter, A., Brix, M. R., and Littke, R., 2005, Late- and post-Variscan cooling and exhumation history of the northern Rhenish massif and the southern Ruhr Basin: New constraints from fission-track analysis: International Journal of Earth Sciences, v. 94, p. 180-192.

Keay, S., Lister, G., and Buick, I., 2001, The timing of partial melting, Barrovian metamorphism and granite intrusion in the Naxos metamorphic core complex, Cyclades, Aegean Sea, Greece: Tectonophysics, v. 342, p. 275-312.

Kelly, N. M., and Harley, S. L., 2005, An integrated microtextural and chemical approach to zircon geochronology: refining the Archaean history of the Napier Complex, east Antarctica: Contributions to Mineralogy and Petrology, v. 149, p. 57-84.

Kelsey, D. E., Clark, C., and Hand, M., 2008, Thermobarometric modelling of zircon and monazite growth in melt-bearing systems: Examples using model metapelitic and metapsammitic granulites: Journal of Metamorphic Geology, v. 26, p. 199-212.

Kelsey, D. E., and Hand, M., 2015, On ultrahigh temperature crustal metamorphism: Phase equilibria, trace element thermometry, bulk composition, heat sources, timescales and tectonic settings: Geoscience Frontiers, v. 6, p. 311-356.

Kelsey, D. E., and Powell, R., 2011, Progress in linking accessory mineral growth and breakdown to major mineral evolution in metamorphic rocks: a thermodynamic approach in the Na2O-CaO-K2O-FeO-MgO-Al2O3-SiO2-H2O-TiO2-ZrO2 system: Journal of Metamorphic Geology, v. 29, p. 151-166.

Kind, R., Ni, J., Zhao, W., Wu, J., Yuan, X., Zhao, L., Sandvol, E., Reese, C., Nabelek, J., and Hearn, T., 1996, Evidence from earthquake data for a partially molten crustal layer in southern Tibet: Science, v. 274, p. 1692-1694.

Kohn, M. J., 2017, Titanite Petrochronology: Reviews in Mineralogy and Geochemistry, v. 83, p. 419-441.

Kohn, M. J., Engi, M., and Lanari, P., 2018, Petrochronology: Methods and Applications, 1-575 p.

Korhonen, F. J., Clark, C., Brown, M., Bhattacharya, S., and Taylor, R., 2013, How long-lived is ultrahigh temperature (UHT) metamorphism? Constraints from zircon and monazite geochronology in the Eastern Ghats orogenic belt, India: Precambrian Research, v. 234, p. 322-350.

Kreissig, K., Holzer, L., Frei, R., Villa, I. M., Kramers, J. D., Kröner, A., Smit, C. A., and van Reenen, D. D., 2001, Geochronology of the Hout River Shear Zone and the metamorphism in the Southern Marginal Zone of the Limpopo Belt, Southern Africa: Precambrian Research, v. 109, p. 145-173.

Larrovere, M. A., Toselli, A., and Rossi De Toselli, J. N., 2008, Petrology and structure of La Chilca Shear Zone, Catamarca, 254-263 p.

López, J. P., Altenberger, U., Bellos, L. I., and Günter, C., 2019, The Cumbres Calchaquíes Range (NW-Argentina). Geochemical sedimentary provenance, tectonic setting and metamorphic evolution of a Neoproterozoic sedimentary basin: Journal of South American Earth Sciences.

Love, G. J., Kinny, P. D., and Friend, C. R. L., 2004, Timing of magmatism and metamorphism in the Gruinard Bay area of the Lewisian Gneiss Complex: comparisons with the Assynt Terrane and implications for terrane accretion: Contributions to Mineralogy and Petrology, v. 146, p. 620-636.

Lucassen, F., Becchio, R., and Franz, G., 2011, The early Palaeozoic high-grade metamorphism at the active continental margin of West Gondwana in the Andes (NW Argentina/N Chile): International Journal of Earth Sciences, v. 100, p. 445-463.

Lucassen, F., Becchio, R., Harmon, R., Kasemann, S., Franz, G., Trumbull, R., Wilke, H.-G., Romer, R. L., and Dulski, P., 2001, Composition and density model of the continental crust at an active continental margin—the Central Andes between 21° and 27°S: Tectonophysics, v. 341, p. 195-223.

Ludwig, K. R., 2003, User's Manual for Isoplot/Ex rev. 3.00: A Geochronological Toolkit for Microsoft Excel.

Martino, R., Guereschi, A. B., and Carignano, C., 2012, Influencia de la tectónica preandina sobre la tectónica andina: el caso de la falla de Sierra Chica, Sierras Pampeanas de Córdoba: Revista de la Asociacion Geologica Argentina, v. 69.

Molnar, P., and England, P., 1990, Temperatures, heat flux, and frictional stress near major thrust faults, 4833-4856 p.

Morley, C., 2009, Evolution from an oblique subduction back-arc mobile belt to a highly oblique collisional margin: The Cenozoic tectonic development of Thailand and eastern Myanmar, 373-403 p.

Moya, M., 2015, La Fase Ocloyica (Ordovicico Superior) en el noroeste argentino. Interpretacion historica y evidencias en contrario: Serie Correlacion Geologica, v. 3, p. 73-110.

Nelson, K. D., Zhao, W., Brown, L. D., Kuo, J., Che, J., Liu, X., Klemperer, S. L., Makovsky, Y., Meissner, R., Mechie, J., Kind, R., Wenzel, F., Ni, J., Nabelek, J., Chen, L., Tan, H., Wei, W., Jones, A. G., Booker, J., Unsworth, M., Kidd, W. S. F., Hauck, M., Alsdorf, D., Ross, A., Cogan, M., Wu, C., Sandvol, E., and Edwards, M., 1996, Partially molten middle crust beneath southern Tibet: Synthesis of project INDEPTH results: Science, v. 274, p. 1684-1685.

Nemchin, A. A., Giannini, L. M., Bodorkos, S., and Oliver, N. H. S., 2001, Ostwald ripening as a possible mechanism for zircon overgrowth formation during anatexis: theoretical constraints, a numerical model, and its application to pelitic migmatites of the Tickalara Metamorphics, northwestern Australia: Geochimica et Cosmochimica Acta, v. 65, p. 2771-2788.

Otamendi, J. E., Castellarini, P. A., Fagiano, M. R., Demichelis, A. H., and Tibaldi, A. M., 2004, Cambrian to Devonian Geologic Evolution of the Sierra de Comechingones, Eastern Sierras Pampeanas, Argentina: Evidence for the Development and Exhumation of Continental Crust on the Proto-Pacific Margin of Gondwana: Gondwana Research, v. 7, p. 1143-1155.

Paquette, J.-L., Goncalves, P., Devouard, B., and Nicollet, C., 2004, Micro-drilling ID-TIMS U-Pb dating of single monazites: A new method to unravel complex poly-metamorphic evolutions. Application to the UHT granulites of Andriamena (North-Central Madagascar): Contributions to Mineralogy and Petrology, v. 147, p. 110-122.

Paquette, J.-L., Ménot, R.-P., Pin, C., and Orsini, J.-B., 2003, Episodic and short-lived granitic pulses in a post-collisional setting: evidence from precise U–Pb zircon dating through a crustal cross-section in Corsica: Chemical Geology, v. 198, p. 1-20.

Parrish, R. R., 1990, U-Pb dating of monazite and its application to geological problems: Canadian Journal of Earth Sciences, v. 27, p. 1431-1450.

Pettijohn, F. J., 1957, Sedimentary rocks: New York, Harper.

Ratschbacher, L., Frisch, W., Linzer, H. G., and Merle, O., 1991, Lateral extrusion in the eastern Alps, PArt 2: Structural analysis: Tectonics, v. 10, p. 257-271.

Reno, B. L., Piccoli, P. M., Brown, M., and Trouw, R. A. J., 2012, In situ monazite (U-Th)-Pb ages from the Southern Brasília Belt, Brazil: Constraints on the high-temperature retrograde evolution of HP granulites: Journal of Metamorphic Geology, v. 30, p. 81-112.

Rosenberg, C. L., and Handy, M. R., 2005, Experimental deformation of partially melted granite revisited: Implications for the continental crust: Journal of Metamorphic Geology, v. 23, p. 19-28.

Rossi, P., Cocherie, A., Fanning, C. M., and Deloule, É., 2006, Variscan to eo-Alpine events recorded in European lower-crust zircons sampled from the French Massif Central and Corsica, France: Lithos, v. 87, p. 235-260.

Royden, L., 1996, Coupling and decoupling of crust and mantle in convergent orogens: Implications for strain partitioning in the crust, 17,679-17,705 p.

Royden, L., Burchfiel, B., King, R., Wang, E., Chen, Z. L., Shen, F., and Liu, Y. P., 1997, Surface Deformation and Lower Crustal Flow in Eastern Tibet, 788-90 p.

Rubatto, D., 2002, Zircon trace element geochemistry: Partitioning with garnet and the link between U-Pb ages and metamorphism: Chemical Geology, v. 184, p. 123-138.

Rubatto, D., Chakraborty, S., and Dasgupta, S., 2013, Timescales of crustal melting in the Higher Himalayan Crystallines (Sikkim, Eastern Himalaya) inferred from trace element-constrained monazite and zircon chronology: Contributions to Mineralogy and Petrology, v. 165, p. 349-372.

Sal'nikova, E. B., Kotov, A. B., Levitskii, V. I., Reznitskii, L. Z., Mel'nikov, A. I., Kozakov, I. K., Kovach, V. P., Barash, I. G., and Yakovleva, S. Z., 2007, Age constraints of high-temperature metamorphic events in crystalline complexes of the Irkut block, the Sharyzhalgai ledge of the Siberian platform basement: Results of the U-Pb single zircon dating: Stratigraphy and Geological Correlation, v. 15, p. 343-358.

Sandiford, M., and McLaren, S., 2002, Tectonic feedback and the ordering of heat producing elements within the continental lithosphere: Earth and Planetary Science Letters, v. 204, p. 133-150.

Santosh, M., Liu, S. J., Tsunogae, T., and Li, J. H., 2012, Paleoproterozoic ultrahigh-temperature granulites in the North China Craton: Implications for tectonic models on extreme crustal metamorphism: Precambrian Research, v. 222-223, p. 77-106.

Sawyer, E. W., 2008, Atlas of Migmatites, NRC Research Press and Mineralogical Association of Canada, 387 p.

Schoene, B., 2014, 4.10 - U–Th–Pb Geochronology, *in* Holland, H. D., and Turekian, K. K., eds., Treatise on Geochemistry (Second Edition): Oxford, Elsevier, p. 341-378.
Schoene, B., Condon, D. J., Morgan, L., and McLean, N., 2013, Precision and accuracy in geochronology: Elements, v. 9, p. 19-24.
Semenov, I., and Weinberg, R. F., 2017, A major mid-crustal decollement of the Paleozoic convergent margin of western Gondwana: The Guacha Corral shear zone, Argentina: Journal of Structural Geology, v. 103, p. 75-99.
Seydoux-Guillaume, A.-M., Fougerouse, D., Laurent, A. T., Gardés, E., Reddy, S., and Saxey, D., 2019, Nanoscale resetting of the Th/Pb system in an isotopically-closed monazite grain: A combined atom probe and transmission electron microscopy study, 65-76 p.
Seydoux-Guillaume, A.-M., Goncalves, P., Wirth, R., and Deutsch, A., 2003, Transmission electron microscope study of polyphase and discordant monazites: Site-specific specimen preparation using the focused ion beam technique: Geology, v. 31, p. 973-976.
Shen, F., Royden, L. H., and Burchfiel, B. C., 2001, Large-scale crustal deformation of the Tibetan Plateau: Journal of Geophysical Research: Solid Earth, v. 106, p. 6793-6816.
Sial, A. N., and Ferreira, V. P., 2015, Magma associations in Ediacaran granitoids of the Cachoeirinha–Salgueiro and Alto Pajeú terranes, northeastern Brazil: Forty years of studies: Journal of South American Earth Sciences, v. 68, p. 113-133.
Sims, J. P., Ireland, T. R., Camacho, A., Lyons, P., Pieters, P. E., Skirrow, R. G., Stuart-Smith, P. G., and Miró, R., 1998, U-Pb, Th-Pb and Ar-Ar geochronology from the southern Sierras Pampeanas, Argentina: implications for the Palaeozoic tectonic evolution of the western Gondwana margin, Geological Society Special Publication, 142, p. 259-281.
Sola, A. M., Becchio, R. A., and Pimentel, M. M., 2013, Petrogenesis of migmatites and leucogranites from Sierra de Molinos, Salta, Northwest Argentina: A petrologic and geochemical study: Lithos, v. 177, p. 470-491.
Tatsumi, Y., and Kimura, N., 1991, Backarc extension versus continental breakup: petrological aspects for active rifting, 127-137 p.
Taylor, R. J. M., Kirkland, C. L., and Clark, C., 2016, Accessories after the facts: Constraining the timing, duration and conditions of high-temperature metamorphic processes: Lithos, v. 264, p. 239-257.
Turlin, F., Deruy, C., Eglinger, A., Vanderhaeghe, O., André-Mayer, A. S., Poujol, M., Moukhsil, A., and Solgadi, F., 2018, A 70 Ma record of suprasolidus conditions in the large, hot, long-duration Grenville Orogen: Terra Nova, v. 30, p. 233-243.
Turner, J. C. M., 1975, Geología del sector oriental de los Departamentos de Santa Victoria e Iruya, Provincia de Salta. República Argentina: Boletín de la Academia Nacional de Ciencias: Boletín de la Academia Nacional de Ciencias, v. 51, p. 11-24.
Vanderhaeghe, O., 2009, Migmatites, granites and orogeny: Flow modes of partially-molten rocks and magmas associated with melt/solid segregation in orogenic belts: Tectonophysics, v. 477, p. 119-134.
Vanderhaeghe, O., 2012, The thermal-mechanical evolution of crustal orogenic belts at convergent plate boundaries: A reappraisal of the orogenic cycle, 124-145 p.
Vanderhaeghe, O., and Teyssier, C., 2001, Partial melting and flow of orogens: Tectonophysics, v. 342, p. 451-472.
Walsh, A. K., Kelsey, D. E., Kirkland, C. L., Hand, M., Smithies, R. H., Clark, C., and Howard, H. M., 2015, P-T-t evolution of a large, long-lived, ultrahigh-temperature Grenvillian belt in central Australia: Gondwana Research, v. 28, p. 531-564.
Weinberg, R. F., Becchio, R., Farias, P., Suzaño, N., and Sola, A., 2018a, Early paleozoic accretionary orogenies in NW Argentina: Growth of West Gondwana: Earth-Science Reviews.

Weinberg, R. F., Becchio, R., Farias, P., Suzaño, N., and Sola, A., 2018b, Early Paleozoic accretionary orogenies in NW Argentina: Growth of West Gondwana: Earth-Science Reviews, v. 187, p. 219-247.

Westaway, R., 1995, Crustal volume balance during the India-Eurasia collision and altitude of the Tibetan Plateau: A working hypothesis: Journal of Geophysical Research: Solid Earth, v. 100, p. 15173-15192.

Whitehouse, M. J., and Platt, J. P., 2003, Dating high-grade metamorphism—constraints from rare-earth elements in zircon and garnet: Contributions to Mineralogy and Petrology, v. 145, p. 61-74.

Williams, M. L., Jercinovic, M. J., Harlov, D. E., Budzyń, B., and Hetherington, C. J., 2011, Resetting monazite ages during fluid-related alteration: Chemical Geology, v. 283, p. 218-225.

Wolfram, L. C., Weinberg, R. F., Hasalová, P., and Becchio, R., 2017, How melt segregation affects granite chemistry: Migmatites from the Sierra de Quilmes, NW Argentina: Journal of Petrology, v. 58, p. 2339-2364.

Wolfram, L. C., Weinberg, R. F., Nebel, O., Hamza, K., Hasalová, P., Míková, J., and Becchio, R., 2019, A 60-Myr record of continental back-arc differentiation through cyclic melting: Nature Geoscience, v. 12, p. 215-219.

Yakymchuk, C., and Brown, M., 2014, Behaviour of zircon and monazite during crustal melting: Journal of the Geological Society, v. 171, p. 465-479.

Yuan, X., Sobolev, S. V., Kind, R., Oncken, O., Bock, G., Asch, G., Schurr, B., Graeber, F., Rudloff, A., Hanka, W., Wylegalla, K., Tibi, R., Haberland, C., Rietbrock, A., Giese, P., Wigger, P., Röwer, P., Zandt, G., Beck, S., Wallace, T., Pardo, M., and Comte, D., 2000, Subduction and collision processes in the Central Andes constrained by converted seismic phases: Nature, v. 408, p. 958-961.

Zandt, G., Leidig, M., Chmielowski, J., Baumont, D., and Yuan, X., 2003, Seismic detection and characterization of the Altiplano-Puna magma body, Central Andes: Pure and Applied Geophysics, v. 160, p. 789-807.

Ziegler, P. A., Van Wees, J., and Cloetingh, S., 1998, Ziegler, P. A., van Wees, J. D. & Cloetingh, S. Mechanical controls on collision-related compressional intraplate deformation. Tectonophysics 300, 103-129, 103-129 p.

Appendix 1

Whole-rock geochemistry

The file can be downloaded via the following link:

https://monash.figshare.com/s/4c1a8efec751f2b53533

Sample ID		SM-005_1	SM-005_2	SM-005_3	SQ17-25A	SQ17-46C	SQ17-015	SQ17-34B	SQ17-34A	SQ17-022	SQ17-049	SQ17-56	SM-003	SQ17-65B	SQ17-066	SQ17-076	SQ17-077	SQ17-88A	SQ17-88B	TY071	TY081	TY089	LC066	LC065
Complex		AdS	AdS	AdS	AdS	AdS	AdS	AdS	AdS	AdS	AdS	AdS	AdS	TW	TW	TW	TW	TW	TW	TW	TW	TW	TW	TW
Lithology		Ca-rich metatexite	Ca-rich metatexite	Ca-rich metatexite	Ca-rich metatexite	Amphibolite	Ca-rich metatexite	Meta-psammite	Metapeilte	Leucosome	Granite	Diatexite	Metatexite	Residual diatexite	Residual diatexite	Diatexite	Residual diatexite	Residual diatexite	Residual diatexite	Granite	Granite	Residual diatexite	Diatexite	Diatexite
SiO_2	%	59.13	67.93	72.36	70.37	57.41	62.52	66.44	58.75	67.56	70.78	69.64	60.78	63.04	62.39	71.76	68.08	62.15	64.39	69.78	62.96	61.90	67.21	71.10
TiO_2	%	0.79	0.82	0.61	0.63	1.14	0.78	0.69	0.24	0.69	0.51	0.54	0.90	0.75	0.76	0.50	0.69	0.82	0.79	0.57	0.55	0.81	0.69	0.47
Al_2O_3	%	14.83	12.61	12.72	12.04	13.52	14.23	15.20	23.07	14.80	13.65	14.53	16.86	16.77	16.99	13.48	15.78	17.71	16.40	14.00	17.03	17.83	15.09	14.09
Fe_2O_3	%	6.43	4.51	4.15	4.07	6.68	5.63	5.59	4.70	5.23	4.17	4.37	7.47	6.99	7.91	3.72	5.45	6.69	6.39	4.24	4.70	6.66	5.50	3.61
MnO	%	0.12	0.09	0.08	0.07	0.16	0.11	0.09	0.08	0.06	0.08	0.10	0.12	0.11	0.11	0.07	0.10	0.13	0.11	0.07	0.09	0.11	0.11	0.07
MgO	%	3.98	2.69	1.69	2.30	6.94	4.14	2.29	2.47	2.05	1.74	1.94	3.64	2.65	2.79	1.45	2.38	3.08	2.75	1.78	2.95	3.01	2.35	1.38
CaO	%	5.46	5.76	2.27	3.95	11.52	5.83	1.82	0.88	0.96	1.04	1.18	0.98	0.53	0.52	1.00	0.95	0.72	0.73	1.41	4.14	0.63	1.51	1.15
Na_2O	%	1.75	2.62	3.25	2.41	0.75	1.37	3.29	2.28	2.04	2.24	2.47	1.74	1.76	1.83	2.43	2.07	1.97	2.15	2.47	3.47	2.09	2.62	2.51
K_2O	%	6.14	1.33	2.18	2.75	0.29	3.74	2.97	6.34	4.46	3.94	3.30	4.83	5.54	5.06	4.01	3.26	5.00	4.43	3.89	2.30	5.20	3.40	4.13
P_2O_5	%	0.20	0.29	0.19	0.20	0.50	0.19	0.19	0.08	0.18	0.11	0.08	0.17	0.17	0.14	0.16	0.16	0.13	0.15	0.27	0.32	0.16	0.25	0.21
LOI	%	0.79	0.84	0.75	1.28	0.94	1.45	0.94	1.49	1.57	1.18	1.36	2.12	1.50	1.08	0.89	1.36	1.71	1.75	1.13	1.07	1.70	1.20	1.71
Li	ppm	26.76	23.34	58.95	31.91	16.74	60.04	44.88	60.54	96.37	59.93	70.78	134.96	72.67	66.75	52.36	62.30	96.51	66.95	57.33	67.15	46.36	61.88	49.39
Be	ppm	1.72	2.45	2.08	1.82	1.76	2.56	1.77	4.68	2.19	7.51	9.40	3.70	2.52	3.27	2.33	2.13	3.25	2.79	3.67	2.82	2.91	4.10	2.89
Sc	ppm	12.13	11.05	8.35	8.73	14.75	11.28	6.89	9.47	13.05	9.01	9.14	17.78	16.35	17.49	8.39	11.68	16.58	15.68	10.11	11.93	11.44	13.49	9.01
V	ppm	89.07	75.33	53.98	60.33	106.64	78.67	44.29	38.60	76.65	59.13	60.64	138.37	97.31	96.42	50.77	73.20	100.90	87.70	68.77	91.77	82.82	91.55	57.94
Cr	ppm	70.04	65.37	45.31	46.40	249.60	64.32	37.91	10.44	53.55	47.61	50.52	104.84	74.05	94.70	53.24	57.19	79.43	67.84	52.77	67.31	62.66	77.23	46.42
Co	ppm	33.71	54.56	41.14	43.28	60.26	39.94	29.84	21.07	57.21	53.60	53.27	43.67	42.66	34.72	47.66	42.61	64.11	35.87	88.36	70.17	33.80	57.52	47.45
Ni	ppm	35.03	27.12	20.73	21.14	101.34	31.58	20.41	26.22	29.93	23.58	24.71	45.07	38.24	49.27	16.96	29.21	40.86	34.35	24.14	49.01	28.88	31.84	20.90
Cu	ppm	9.53	11.22	11.86	12.98	46.50	8.40	75.48	19.76	24.31	9.75	11.01	25.61	7.33	12.85	6.65	10.39	6.62	39.13	20.86	39.98	7.32	13.00	14.95
Zn	ppm	93.19	79.23	53.87	55.19	134.28	82.12	42.52	41.54	75.06	63.55	64.99	126.22	100.74	101.49	54.62	81.64	102.38	84.86	70.17	68.59	76.52	90.05	59.62
Ga	ppm	16.25	15.00	12.93	12.79	18.73	15.47	10.67	24.43	18.21	16.56	17.78	24.56	21.93	21.94	13.85	18.55	21.72	18.88	17.45	20.28	15.95	20.35	16.87
As	ppm	1.13	1.38	1.10	0.82	1.22	0.62	0.96	0.75	2.37	0.70	1.01	1.14	1.43	1.04	1.88	1.13	1.15	0.67	1.05	0.53	0.35	0.84	0.79
Rb	ppm	170.75	40.44	105.75	80.98	6.50	139.98	74.42	180.60	158.99	165.15	156.57	204.30	181.15	171.45	151.82	145.22	224.65	179.94	162.78	176.60	137.34	162.84	169.54
Sr	ppm	244.69	208.45	119.34	171.67	2216.27	220.00	83.70	85.10	134.58	94.92	107.64	149.21	127.83	131.69	95.08	77.55	128.66	79.84	145.92	254.61	70.09	129.43	131.92
Y	ppm	32.08	41.52	25.85	28.41	13.91	31.06	22.14	47.95	26.59	26.55	64.32	43.48	26.83	32.75	24.64	32.71	29.47	23.32	52.54	18.52	30.61	37.81	32.27
Zr	ppm	153.92	371.01	267.24	248.95	208.72	163.22	171.89	203.09	154.19	198.92	178.98	198.72	142.18	153.84	177.97	145.62	163.86	138.06	242.47	178.20	131.42	243.79	173.22
Nb	ppm	13.82	16.79	11.62	11.56	11.18	13.01	8.78	13.57	16.38	13.41	12.55	15.94	15.67	17.99	12.68	14.27	18.17	18.32	13.48	9.81	12.26	13.48	12.12
Mo	ppm	2.00	0.69	0.25	0.31	0.65	0.20	0.29	0.21	0.19	1.18	0.12	0.14	0.35	9.38	0.19	0.73	0.29	0.24	0.10	0.05	0.22	0.11	0.31
Cd	ppm	0.13	0.17	0.07	0.13	0.08	0.10	0.04	0.06	0.05	0.06	0.05	0.06	0.05	0.05	0.05	0.05	0.05	0.04	0.09	0.07	0.04	0.09	0.07
Sn	ppm	3.72	3.27	2.57	2.63	2.46	3.24	2.25	4.50	4.96	5.38	5.69	5.04	10.40	5.65	4.92	4.26	5.63	9.07	4.17	2.35	2.03	8.63	3.74
Sb	ppm	0.92	2.02	0.09	0.17	0.97	0.49	0.06	0.18	0.19	0.28	0.36	0.03	0.63	0.41	0.20	0.04	0.11	0.25	0.09	0.02	0.01	0.12	0.15
Cs	ppm	7.78	2.85	11.05	3.91	0.70	32.95	7.47	13.49	8.83	12.02	12.02	33.99	12.27	8.79	9.96	17.43	13.36	15.99	7.06	9.90	10.09	9.94	9.79
Ba	ppm	1127.80	203.29	297.14	613.30	61.56	626.82	263.08	659.15	494.19	291.47	293.68	703.93	479.51	416.05	339.22	293.70	514.39	353.09	513.82	235.58	498.85	328.79	462.88
Ta	ppm	1.11	1.35	1.02	0.98	0.64	1.15	0.78	1.76	1.67	1.30	1.22	1.02	1.37	1.33	1.29	1.28	1.41	1.46	1.07	1.00	0.95	1.17	1.13
Tl	ppm	1.05	0.24	0.64	0.49	0.06	0.92	0.66	1.13	0.86	0.99	0.94	1.61	1.00	0.91	0.95	0.89	1.30	1.10	1.26	1.44	1.08	1.30	1.31
Pb	ppm	31.53	13.71	16.58	18.25	6.46	24.52	13.30	24.69	26.35	27.29	25.92	17.24	29.02	21.12	26.97	16.31	31.01	22.39	26.64	11.15	23.18	20.59	26.25
Th	ppm	13.12	15.02	11.73	8.77	8.03	12.35	10.02	38.31	12.94	18.29	16.23	16.09	14.78	15.26	11.91	14.76	16.04	14.19	11.97	4.10	11.77	12.24	9.55
U	ppm	3.70	4.52	2.67	2.39	2.14	3.35	2.40	7.94	3.22	4.32	4.98	2.82	3.66	2.68	4.09	4.40	3.52	4.52	3.11	1.13	2.40	3.40	1.95
La	ppm	36.37	44.16	35.20	29.48	51.41	36.16	25.73	54.54	37.77	41.15	37.04	37.34	36.60	42.28	31.44	39.01	39.47	34.63	30.82	13.62	30.49	33.69	22.60
Ce	ppm	72.59	91.51	71.14	61.62	122.69	71.76	53.39	119.69	74.17	82.95	75.28	101.80	74.89	86.28	63.48	80.27	81.26	71.11	66.67	30.23	65.49	74.02	54.75
Pr	ppm	8.89	11.31	8.51	7.66	15.73	8.87	6.29	14.34	9.15	9.86	8.92	10.17	8.78	9.97	7.61	9.67	9.54	8.42	8.22	3.79	7.56	8.86	5.99
Nd	ppm	33.67	43.52	31.48	29.48	60.49	33.04	23.67	55.39	34.72	36.48	33.38	37.99	32.83	36.92	28.01	35.94	35.92	31.07	31.67	15.08	29.17	33.51	22.65
Sm	ppm	6.92	8.74	6.29	6.03	9.11	6.65	4.85	12.02	6.90	7.28	7.18	8.15	6.62	7.11	5.60	7.35	7.16	6.29	7.36	3.73	6.13	7.50	4.96
Eu	ppm	1.36	1.57	1.07	1.23	2.34	1.25	0.83	1.64	1.26	1.01	1.10	1.42	1.20	1.32	0.95	1.19	1.29	1.02	1.25	0.92	1.22	1.32	1.02
Gd	ppm	6.21	7.83	5.40	5.36	6.36	5.97	4.27	9.80	5.97	6.14	7.33	7.07	5.67	6.24	4.84	6.47	6.24	5.37	6.84	3.38	5.34	6.42	4.56
Tb	ppm	1.01	1.25	0.85	0.87	0.75	0.97	0.69	1.60	0.92	0.95	1.43	1.19	0.90	1.00	0.79	1.04	0.96	0.83	1.22	0.56	0.85	1.05	0.81
Dy	ppm	5.97	7.36	4.91	5.13	3.43	5.73	4.13	9.85	5.12	5.17	9.78	7.27	5.11	5.91	4.63	6.11	5.49	4.67	7.99	3.25	5.16	6.38	5.00
Ho	ppm	1.19	1.47	0.95	1.03	0.54	1.15	0.83	2.01	0.98	0.95	2.18	1.62	0.97	1.18	0.91	1.19	1.08	0.89	1.86	0.70	1.12	1.41	1.15
Er	ppm	3.41	4.21	2.69	2.93	1.33	3.34	2.41	5.70	2.72	2.61	6.60	4.31	2.77	3.43	2.59	3.46	3.07	2.51	5.19	1.80	3.16	3.80	3.18
Tm	ppm	0.49	0.61	0.39	0.42	0.17	0.48	0.35	0.81	0.39	0.36	0.95	0.60	0.40	0.50	0.37	0.50	0.44	0.36	0.76	0.23	0.46	0.53	0.47
Yb	ppm	3.14	3.96	2.51	2.76	1.04	3.10	2.29	5.25	2.56	2.34	6.01	3.99	2.68	3.29	2.41	3.24	2.94	2.36	5.05	1.41	2.99	3.55	3.20
Lu	ppm	0.48	0.59	0.38	0.42	0.15	0.46	0.34	0.75	0.38	0.35	0.87	0.59	0.40	0.49	0.36	0.49	0.44	0.36	0.73	0.21	0.46	0.53	0.50
Hf	ppm	4.99	10.68	7.99	7.47	5.55	5.15	5.45	8.48	4.76	6.12	5.56	5.63	4.47	4.74	5.67	4.65	5.06	4.60	6.82	4.42	3.93	6.97	4.94
Sum LREE		158.45	199.24	152.62	134.28	259.43	156.48	113.94	255.97	162.71	177.74	161.80	195.44	159.72	182.55	136.14	172.23	173.34	151.52	144.74	66.45	138.85	157.59	110.95

Appendix 2

This digital appendix contains:

- Geochronology and mineral composition of zircon, monazite and titanite (Tables 1 to 6)
- Zr-in-titanite temperature (Table 7)
- Microprobe data for sample SQ17-034b (Table 8)

The digital files can be downloaded via the following link:

https://monash.figshare.com/s/8774799514ae4f6e0896

Appendix 3

Detailed petrography for Chapter 3

Al-rich siliciclastic rocks

Sample SM-003: Garnet-sillimanite metatexite

This migmatite crops out southwest of Santa Maria town. It has a mineral paragenesis characterized by Qtz-Bt-Grt-Sil-Pl-Kfs-Ms-Tur with zircon, apatite and monazite as accessory phases. The foliation is spaced zonal with 1-5 mm thick granoblastic microlithons that make around 30 % of the rock and are composed of coarse quartz-feldspar and isolated biotite and muscovite grains. The cleavage domains make ~70 % of the sample and are composed mostly by micas arranged in parallel and discrete domains. Plagioclase is the dominant feldspar and usually have myrmekite textures when in contact with Kfs. Garnet is scarce and forms 2-5 mm porphyroblasts with rims of fine-grained biotite, muscovite and sericite. Sillimanite is present in the core of large muscovite grains. Large 2-5 mm tourmaline grains are usually concentrically zoned. The retrograde mineralogy is defined by muscovite-sericite-chlorite. Muscovite is present as large 0.5-1 mm decussate grains in the relatively undeformed microlithons and as smaller grains in the cleavage domains. The sillimanite patches within the muscovite suggest retrogression of sillimanite to muscovite. Sericite alters around 20% of the feldspar grains and together with the muscovite form large haloes around garnets. Chlorite alters biotite.

The rock shows evidence of intense deformation recorded at outcrop-scale by stretched and boudinaged pegmatites, and in the micro-scale by mica fish and S/C-fabric indicative of simple shear. Additionally, some mineral aggregates formed by fine-grained unidentified minerals and garnet form σ-objects.

Samples LC-019 and SQ17-022: Grt-Sil-Kfs migmatites

These migmatite samples are part of relatively undeformed lithons, hundreds of metres across, where delicate migmatitic structures are better preserved than in the highly stretched surroundings. Within these lithons bedding is well preserved and so are leucosomes and melt pathways. Sample SQ17-022 represents one of these in-source leucosome and sample LC-019 is a nebulitic migmatite.

Melanosomes typically comprise Qtz-Bt-Pl-Kfs-Grt-Sil-Ms-Tur with zircon, apatite and monazite as accessory minerals. Some pelitic layers present 0.5-1 cm poikiloblasts of garnet with large eye-shaped haloes of fine-grained sericite, muscovite, sillimanite, biotite and quartz. Kfs is 0.5-1 cm long and has small rounded inclusions of quartz and biotite typically at the edge. Garnet has inclusions of rounded quartz and needles of fibrolite. Biotite is abundant and presents symplectitic intergrowth with quartz. In the quartz-feldspar microlithons, fibrolite forms “nests” that outline small crenulations and in some cases fibrolite grows at the edge of large biotite.

Leucosomes are comprised of 1-2 mm coarse-grained inequigranular Qtz-Bt-Pl-Kfs-Ms. They have scattered domains of large poikiloblastic Kfs with inclusions of round quartz and biotite, and in many cases myrmekites at the edge of the blast. In LC-019 there are large nebulitic leucosomes with parts rich in melanocratic residual mineral aggregates, mostly garnet, biotite and sillimanite.

Sample SQ17-049 : Filo granite

This body is elongated north-south and extends for at least 5 km. The rock is composed of Qtz-Pl-Kfs-Bt, traces of sillimanite, garnet and muscovite with Kfs phenocrysts with an average grain size of 0.5 cm (up to 1 cm), in a fine-grained quartz-feldspar matrix. It also has 10-15 cm long biotite-rich garnet-bearing schlieren oriented parallel to the foliation. Some of the Kfs phenocrysts have inclusions of corroded quartz and biotite and myrmekites at the edges. Sillimanite is scarce and found as small needles in the triple junction of quartz and feldspar grains and in contact with fine-grained muscovite. Retrogression is evidenced by sillimanite partially replaced by muscovite and by sericite in feldspars. The feldspar phenocrysts and the mafic schlieren define a magmatic foliation concordant to the metamorphic foliation defined by the preferred orientation of Kfs, biotite and muscovite.

Ca-rich siliciclastic rocks and ortho-amphibolite

Sample UMF: Ca-rich mylonite

This mylonite is part of the eastern flank of the Filo shear zone. It is composed of Qtz-Pl-Kfs-Hbl-Bt-Ep with allanite, titanite, apatite, ilmenite and magnetite as the main accessory phases. The rock has porphyroclasts of Kfs of ~ 2 cm and hornblende of up to 1 cm. The granoblastic matrix has an average grain size of 50-100 µm. Quartz defines ribbons, it has strong c-axis preferred orientation and it records grain boundary migration (GBM) microstructures. Kfs has a thin mantle of fine-grained recrystallized feldspar (core-and-mantle) and myrmekites at the edges. Biotite is preferably aligned in interconnected shear bands, usually smaller than 100 µm and with magnetite inclusions. Epidote has small metamict allanite cores. Epidote is euhedral when in contact with biotite and anhedral when in contact with quartz or feldspar. Titanite can be up to 2 mm long euhedral and in many cases with rounded ilmenite in the cores. Retrogression is evidenced by biotite partially replaced by chlorite and feldspars by sericite. The mylonitic foliation is defined by the preferred orientation of most minerals. Kinematic indicators like σ-objects and S/C shear bands indicate a strong simple shear component of deformation.

Sample SQ17-025: Ca-rich metatexite

This sample is from an area characterized by top-to-south shearing, and incipient in-situ partial melting marked by the presence of leucosomes. The bulk mineralogy of the gneiss is characterized by Qtz-Hbl-Bt-Kfs-Pl-Ms-Ep with accessory allanite, apatite, titanite and ilmenite. The gneiss has hornblende-rich layers and Bt-Kfs-rich layers. It has porphyroclasts of feldspar and muscovite with an average size of 0.5 mm. In the sheared Hbl-rich layers, fine-grained biotite, hornblende and opaques define a spaced anastomosed cleavage domains that separate quartz-feldspar microlithons. The Kfs porphyroclasts show dynamic recrystallization defined by core-and-mantle textures and myrmekites is common along their edges. Hornblende and biotite show intense grain size reduction and epidote has allanite cores, as in the previous sample.

Sample SQ17-046c: sheared ortho-amphibolite

This sample was collected in the southern end of the Filo shear zone, part of an elongated body, 3-5 m thick and ~ 1 km long in sharp contact with the Al-rich mylonite country-rock. It is composed of Hbl-Pl-Kfs-Qtz-Ttn, with 0.5-1 mm porphyroclasts of hornblende that makes 50 % of the sample and it is hosted in a finer grain granoblastic quartz-feldspar matrix. Plagioclase and quartz make 40 % of the sample and Kfs ~5%. The foliation is weak and typically defined by the preferred orientation of hornblende grains. This foliation defines an anastomosing spaced fabric visible at outcrop scale. Hornblende is usually bordered by finer angular fractions of the same mineral, suggesting grain size reduction. There is no sign of alteration or retrogression.

Samples SQ-213, SQ-108: thin Ca-rich schist hosted in Al-rich siliciclastic rocks

These are 0.5 to 1 m thick Ca-rich layers of schist hosted in a sheared Al-rich gneiss in the immediate footwall of the Pichao shear zone. These rocks are composed of Qtz-Pl-Kfs-Hbl-Bt-Ep-Ttn with accessory allanite, apatite and ilmenite. They have cm-scale compositional banding defined by different amounts of biotite and hornblende. Hornblende from 0.5-1 cm poikiloblasits with inclusions of quartz, plagioclase and biotite. Biotite and fine-grained Hbl form anastomosed cleavage domains that make 50% of the rock. Titanite can be up to 1 cm long euhedral grains mostly with ilmenite cores. Epidote is anhedral and in most cases have allanite cores.

Samples LC-028, SM-005: Ca-rich metatexites

These rocks are composed of Qtz-Pl-Kfs-Bt- Hbl-Ep-Grt±Scp±Cpx with accessory allanite, apatite, titanite, chlorite and calcite. They have an equigranular texture, and less commonly seriate texture with porphyroblasts of hornblende, feldspar and garnet. Compositional banding at cm-scale results from variable Hbl/Bt ratio. Plagioclase shows diffuse concentric zoning. Hornblende is 0.5-2 mm, subhedral and usually in contact with titanite and epidote-allanite. In the psammitic layers, hornblende is found as isolated, large 1-3 cm euhedral poikiloblasts with inclusions of quartz and plagioclase. Garnet is rare and usually located in the interface between Hbl-rich and the Bt-rich layers. It forms large 1-3 cm, inclusion-rich anhedral porphyroblasts with inclusions of quartz, plagioclase, biotite and epidote-allanite. Epidote is abundant (~20%), subhedral to euhedral, 0.5-1 mm grains that sometimes form aggregates with plagioclase, garnet or biotite, and have also allanite cores. SEM images with XRD reveals the presence of REE-rich epidote between the allanite core and a rim of REE-poor epidote. Titanite is euhedral and concentrated in the Hbl-rich layers. Meiolite (Ca-rich scapolite) is present in sample SM-005 as isolated subhedral grains in the quartz-felspathic layers. Sample LC-028 has Cpx which is typically in contact with Hbl and calcite. The feldspars are partially retrogressed to sericite, and biotite to chlorite.